ZDDP-Additive Interactions in Engine Lubricant Formulations

MICHAEL HEERAN

ZDDP-Additive Interactions in Engine Lubricant Formulations

Michael Heeran

Department of Chemistry

Durham University

This thesis is submitted for the degree of

Doctor of Philosophy

St Mary's College

2018

To my parents for teaching me the real basics.

Declaration

The work described in this thesis was carried out at Durham University between April 2015 and October 2018. This thesis is the work of the author, except where acknowledged by reference, and has not been submitted for any other degree. The copyright of this thesis rests with the author. No quotation from it should be published without the prior written consent and information derived from it should be acknowledged.

Parts of this work have been subject to the following publications:
1) **M. Heeran**, A. S. Batsanov, A. Beeby, J. C. Speelman, P. W. Dyer, 'Steric and electronic effects influencing the structure and thermochemistry of pyridine adducts of zinc dialkyl dithiophosphates (ZDDPs)' *manuscript in preparation*.
2) **M. Heeran**, A. S. Batsanov, J. C. Speelman, P. W. Dyer, 'The interaction of a commercial amine-based friction modifier with zinc dialkyl dithiophosphates (ZDDPs)' *manuscript in preparation*.

This work has been presented, in part, at:
1) Department of Chemistry Annual Postgraduate Research Symposium, 15th June 2017, Durham, UK, *oral presentation*.
2) Annual Meeting of the RSC Main Group Chemistry Interest Group, 1st September 2017, London, UK, *poster presentation*.
3) 15th European Workshop on Phosphorus Chemistry, 14th-16th March 2018, Uppsala, Sweden, *oral presentation*.
4) 22nd International Conference on Phosphorus Chemistry, 8th-13th July 2018, Budapest, Hungary, *oral presentation*.

Michael Heeran

2018

Acknowledgements

First and foremost, I would like to thank my supervisor, Dr Phil Dyer, for the opportunity to carry out my PhD under his supervision – it has been a pleasure! His immense knowledge, endless patience and sound advice made this thesis possible.

I would also like to thank Dr Joke Speelman for her insightful suggestions and constant, unwavering support of the project throughout. I am also grateful to Sarah Lundgren for MTM training and to Ulf Schröder for his help and support while in Sweden.

My research in Durham would not have been possible without the amazing help of the staff at Durham, in particular, the NMR staff, the glassblowers, the electrical and mechanical workshops, and Dr Andrei Batsanov for all of his crystallography work. A special thanks must go to Dr Juan A Aguilar Malavia for his time and expertise in developing, applying and explaining the NMR methodologies used in this thesis. Financial support from the EPSRC, SOFI CDT and AkzoNobel Specialty Chemicals (now Nouryon) are gratefully acknowledged.

Thanks to all members of the Dyer group (past and present), particularly Anna, Ben, Jack, Jas, Michael, Stephen, Claire, Dominikus, Kevin, Eder, Li Li, Alana, and Richard, who've made the group a fun and enjoyable place to work over the years. A special mention to Michael, Jas and Anna for their help, support and enthusiasm when I first started in the lab, it was much appreciated. I would also like to thank all members of "Cohort 1" in the SOFI CDT, for all of the laughs and entertainment at various points throughout our PhDs – I think the only thing to say is "Good work Alessandro!"

Finally, I would like to thank my family and friends for their love and support.

Abstract

This thesis describes the investigation of the solution phase interactions, and resulting coordination-, thermo- and tribo-chemistry, in binary antiwear (Zinc Dialkyl Dithio-Phosphate – ZDDP) and organic friction modifier (OFM) additive formulations. The work probed in particular, the importance of OFM structure in dictating the thermolysis and tribochemical performance of ZDDP-OFM formulations, with the aim of facilitating the selection or design of optimal additive combinations for engine lubricant applications. In this regard, Chapter 1 provides an introduction to the fundamentals of lubricant chemistry and lubricant formulation, with Chapter 2 briefly reviewing the current drivers that necessitate a more scientific approach to developing next-generation lubricant formulations.

Chapter 3 describes the investigation of model ZDDP-pyridine interactions, whereby the pyridine scaffold served as an easily tunable N-donor moiety. Both 1:1 and 1:2 ZDDP-Py' complexation reactions were identified, both of which occur *via* nitrogen-zinc coordination. Quantification of the contribution of steric ($\%V_{\mathrm{bur}}$) and electronic factors ($\mathrm{p}K_{\mathrm{aH}}$) on the propensity of solution complexation (K_{a}), was achieved using ^{31}P NMR spectroscopic titration data. Complexation was accompanied by a significant change in the zinc-bound dithiophosphate (DTP) binding mode, something that was monitored using Raman spectroscopy.

Chapter 4 identified that the nature of ZDDP-OFM interactions mirror those found in the previously studied ZDDP-Py' systems (*via* zinc-nitrogen complexation that is accompanied by a significant change in DTP binding bode). X-Ray crystallographic analysis of $[\mathrm{Zn}\{\kappa^1\text{-}S\text{-}\mathrm{S_2P(O}^i\mathrm{Bu)_2}\}_2(\mathrm{C_{18}\text{-}NH_2})_2]$ (**7**) unequivocally identified both the nitrogen-zinc coordination pathway and the OFM-induced change in binding mode previously inferred

from solution ^{31}P NMR spectroscopic data. The use of Raman spectroscopy for diagnosing DTP binding modes for ZDDP-OFM complexes was verified using the molecular structure of **7**. Subsequent ^{31}P NMR spectroscopic studies of other ZDDP-OFM combinations demonstrated that the strength of ZDDP-OFM solution interactions were highly dependent on the steric demands and presence of additional OFM donor sites.

Chapter 5 describes the impact of the complexation reactions discussed, on the thermolysis and tribological performance of ZDDP-OFM systems. Thermal degradation pathways were monitored using ^{31}P NMR spectroscopy, while the tribological performance was assessed using the mini traction machine-space layer interferometry method (MTM-SLIM). The presence of amine-functional OFMs was observed to enhance the rate of ZDDP thermal degradation in all cases studied, with the extent of the rate enhancement observed correlating with the strength of ZDDP-OFM interaction. Subsequently, it was found that the ZDDP tribofilm formation rate did not correlate to the observed thermal stability in ZDDP-OFM systems.

Chapter 6 explored some possible alternative synthetic methods for the preparation of zinc dialkyl diselenophosphates in an attempt to make use of the additional ^{77}Se NMR spectroscopic handle that they would provide. Finally, in Chapter 7, the results obtained in Chapters 3-5 are described in a holistic manner, with the benefits of studying simplified single-component ZDDP-additive systems highlighted.

Contents

Nomenclature

Abbreviations

2-EH	2-Ethylhexyl
δ	Chemical Shift
$\Delta\delta$	Change in Chemical Shift
μ	Friction Coefficient
AFM	Atomic Force Microscopy
ASAP-MS	Atmospheric Solids Analysis Probe Mass Spectrometry
Cys	L-Cysteine
DAB	1,4-Diaminobutane
DAP	1,3-Diaminopropane
DEA	Diethanolamine
DLC	Diamond-like Carbon
DOC	Diesel Oxidation Catalyst
DPF	Diesel Particulate Filter
DSP	Diselenophosphate
DTC	Dithiocarbamate
DTG	Differential Thermogravimetric Analysis

DTP	Dithiophosphate
EDA	Ethylenediamine
EDTA	Ethylenediaminetetraacetic Acid
EGR	Exhaust Gas Recirculation
EHL	Elastohydrodynamic Lubrication
EP	Extreme Pressure
FM	Friction Modifier
GMO	Glycerol Mono-oleate
HFRR	High Frequency Reciprocating Rig
HSD	Hydrogenated Styrene Dienes
ILSAC	International Lubricant Standardisation and Approval Committee
KDTP	Potassium Diisobutyl Dithiophosphate
MDAP	N-Methyl-1,3-diaminopropane
MDEA	N-Methyldiethanolamine
MoDDP	Molybdenum Dialkyl Dithiophosphate
MoDTC	Molybdenum Dialkyl Dithiocarbamate
MoS_2	Molybdenum Disulphide
MTM-SLIM	Mini Traction Machine-Spacer Layer Interferometry Method
NO_x	Oxides of Nitrogen
OCP	Olefin Copolymers
OFM	Organic Friction Modifier
PA	Polyacrylate

PAO	Poly(alphaolefin)
PDMS	Polydimethylsiloxane
PIB	Polyisobutylene
PMA	Polymethacrylate
PXRD	X-ray Powder Diffraction
SAPS	Sulfated Ash, Phosphorus and Sulfur
SCR	Selective Catalyst Reduction
Se-ZDDP	Zinc Dialkyl Diselenophosphate
TGA	Thermogravimetric Analysis
TGA-MS	Thermogravimetric Analysis-Mass Spectrometry
ToF-SIMS	Time-of-Flight Secondary Ion Mass Spectrometry
TWC	Three-Way Converter
VI	Viscosity Index
XPS	X-ray Photoelectron Spectroscopy
ZDDP	Zinc Dialkyl(aryl) Dithiophosphate
ZDTC	Zinc Dialkyl Dithiocarbamate

Glossary

Some of the terminology commonly used in the oil and lubricant industries is not as readily recognised within the chemistry field. The following therefore outlines definitions of such expressions.

Additive Package - A pre-formulated mixture of lubricant additives that is subsequently blended with a base oil (and potentially other additives) to give a fully formulated lubricant.

Base Oil - Mineral or synthetic base oil that an additive package is blended with to form a finished lubricant.

Cloud Point - The temperature at which paraffin wax or other solids begin to crystallise in a base oil, imparting a cloudy appearance.

Lubricant - Any substance interposed between two surfaces in relative motion for the purpose of reducing friction and wear.

NOACK Volatility - Standard test method (ASTM D5800) that determines the evaporation loss of lubricants in high temperature service. Found to correlate to oil consumption in passenger cars.

Pour Point - The lowest temperature at which a fluid will pour or flow.

Solvency - An oil's ability to dissolve polar additives.

Tribocontact - Collective term referring to rubbing components and their constituent contacting surfaces, together with any lubricant and other materials (wear debris, contaminants *etc.*) present in the interacting environment.

Tribofilm - Thin surface films generated as a consequence of sliding contact.

Viscosity Index (VI) - Relationship between the viscosity of a fluid and temperature. A high VI indicates that a fluid's viscosity is not as severley reduced by increasing temperature.

Wear - Progressive loss of material from the surface of a contacting body as a result of mechanical processes.

Chapter 1

An Introduction to Lubricant Chemistry

1.1 Tribology

Tribology is the science and technology of friction, wear and lubrication, derived from the Greek word *tribo*, meaning "I rub". The term was originally coined in a British study in the mid-1960s (The Jost Report), which highlighted the annual monetary loss in the UK ascribed to the consequences of friction and wear.[1] More precisely, tribology is the study of interacting surfaces in relative motion and spans multiple disciplines including chemistry, physics, mechanical engineering and materials chemistry.

In the field of tribology, *tribocontact* or *tribosystem* are collective terms referring to rubbing components and their constituent contacting surfaces, together with any lubricant and other materials (wear debris, contaminants, *etc.*), present in the interacting environment. A tribosystem is characterised by its operating conditions (*e.g.* load, velocity and type of motion), environmental conditions (*e.g.* temperature, humidity) and material parameters (*e.g.* surface material, hardness and surface roughness), Figure 1.1.

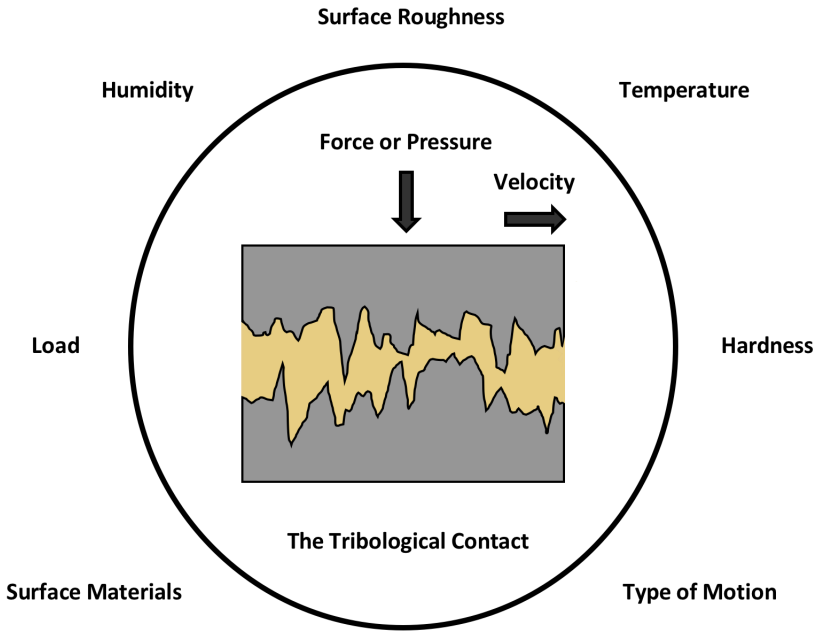

Figure 1.1: Summary of parameters affecting tribosystems. Adapted from ref. 2.

Tribology is a comparatively new branch of science that is essential in understanding the role of lubrication in automotive technologies. Hence, in the forthcoming chapter a brief introduction to the fundamental concepts of tribology, with a particular emphasis on its relationship to automotive lubrication, are presented.

1.1.1 Friction

Friction can be formally defined as the resistance a body meets while moving over another body in respect of transmitting motion.[3] The friction coefficient μ is defined in terms of the frictional force between two bodies (F_F) and the normal force pressing the same two bodies together (F_N) and may be written as:

$$\mu = \frac{F_F}{F_N}$$

Automotive technologies for transportation unsurprisingly involve mechanical motion. Naturally this entails variable degrees of contact between surfaces, often under extreme conditions. Contact between surfaces in relative motion inevitably produces a force that resists this motion; this force is friction. In terms of an internal combustion engine, friction is an undesired phenomenon that causes wear (Section 1.1.3) of various mechanical

components, in addition to contributing significantly to energy losses (Fig. 1.2).

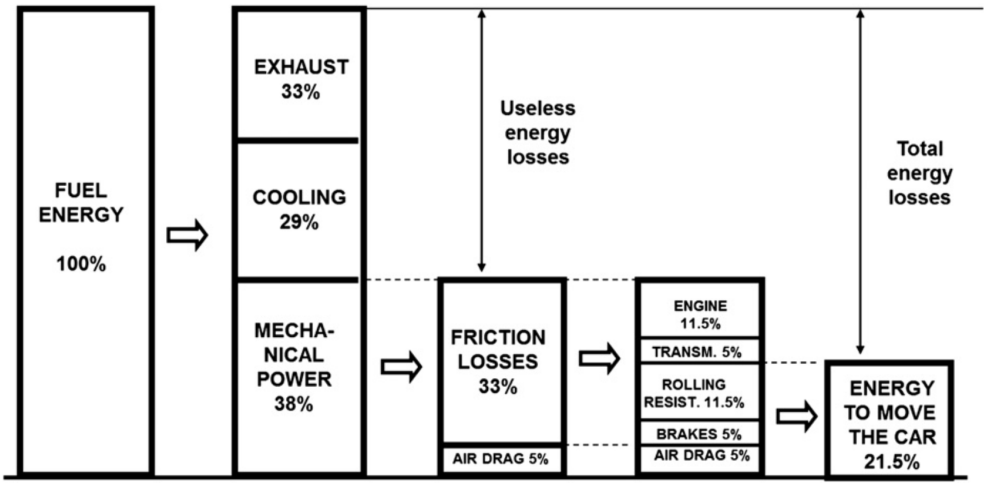

Figure 1.2: Breakdown of energy consumption in a typical passenger car. Reproduced with permission from ref. 4.

Indeed losses due to friction in an internal combustion engine constitute nearly 12% of the total fuel energy consumed; such losses occur in bearings, valve trains, piston assemblies, as well as from pumping and drag-related viscous losses.[4] It should be noted that while energy losses arising *via* viscous dissipation are strictly not friction losses, they are included here as viscosity is an extremely important parameter in automotive lubrication, contributing to fuel economy, friction and wear.

Transportation accounts for around 20% of the global primary energy consumption and around 18% of the anthropogenic greenhouse gas emissions.[5] Given that road transport accounts for 76% of this energy use and over 80% of the CO_2 emissions,[6] it is clear even relatively small improvements in engine efficiency would result in a substantial reduction in fuel consumption and thus emissions. In terms of mechanical losses (piston assembly, bearings, valve train and pumping losses) it has been estimated that a reduction in such losses of approximately 10% could lead to reductions in fuel consumption in excess of 1.5%,[4] and while this may seem relatively modest at best, when the scope of such an improvement is considered the significance is quickly realised.

In the absence of modifying engine design, friction (and wear) can be reduced primarily *via* surface modification/coating, and/or through the use of a conventional liquid lubric-

ant. The entirety of this thesis is confined to the latter scenario.

1.1.2 Lubricants and Lubrication

Lubrication can be defined as a process employed to control friction and wear between contacting surfaces in relative motion, by interposing a substance between them, namely a lubricant.[3] In this thesis the terms *lubricant* and *oil* are used interchangeably, but differ from the terms *base oil* and *base fluid*. Lubricant and oil pertain to finished lubricants, that is, they comprise base oil plus additives.

Friction and wear reduction between surfaces are unquestionably the primary, but not the only, functions required from a commercial lubricant. For engine applications a lubricant is required to perform a diverse array of functions, which include:[3]

Lubrication

The reduction of friction and wear - A lubricant essentially minimises surface-to-surface contact and reduces the force necessary to move a surface past another, thus reducing energy consumption and wear.

Cooling

Heat transfer - A lubricant is required to act as a heat sink to dissipate heat effectively away from critical components. The heat can be frictional heat or conducted and radiated heat, resulting from close proximity to a combustion source.

Cleaning and Suspending

Removal and suspension of potential harmful products, such as dirt and wear debris, ensuring component surfaces remain clean. This function is particularly important in operations that involve high temperature, such as that encountered in internal combustion engines.

Protection

Prevents metal damage due to oxidation, corrosion and wear. This is achieved by formation of protective films that are impervious to oxygen, water and acids

Transfer Power

Lubricants are used as a power transfer medium for some applications, such as in hydraulic systems. The lubricant is used to transmit force and motion from a single source to multiple sources.

1.1.2.1 Lubrication Regimes

In liquid lubrication, four distinct lubrication regimes are observed, and are defined by the relative thickness of the lubricant film interposed between component surfaces, to the surface roughness of such surfaces.[7] The distinct regimes are most conveniently represented graphically using a *Stribeck curve* (Fig. 1.3), which displays the variation in friction coefficient as a function of the dimensionless, Hersey number.[7,8]

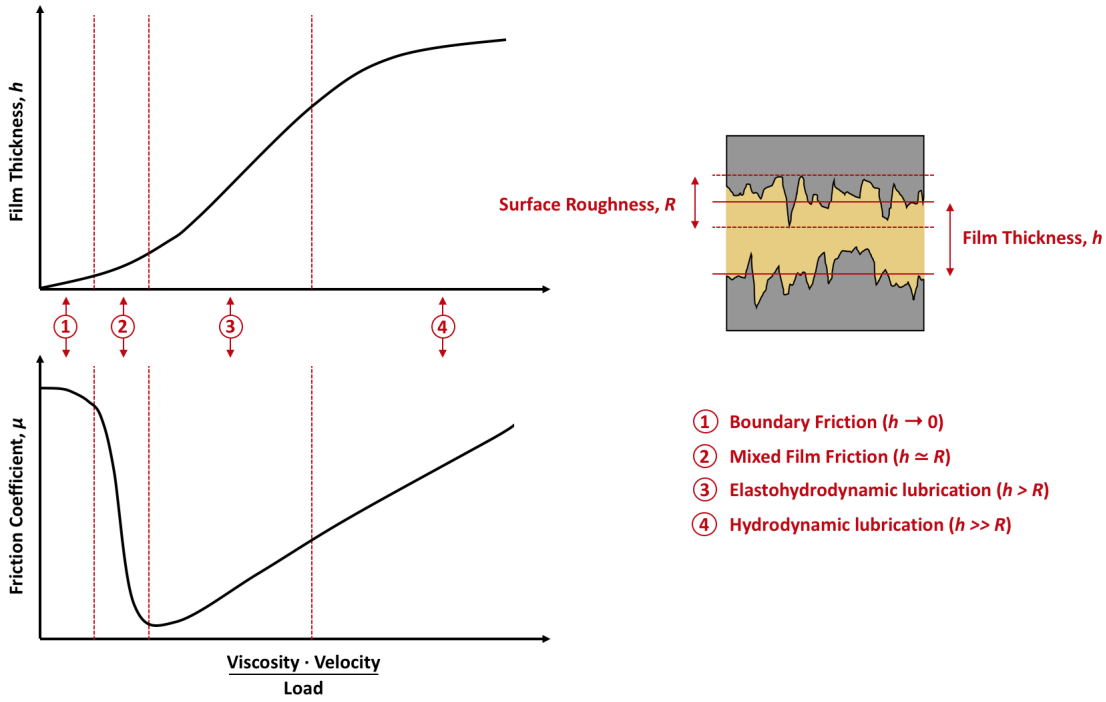

Figure 1.3: Stribeck curve displaying distinct lubrication regimes and associated lubricant film thickness. The x-axis on both plots are equivalent, but omitted on the top graph for clarity. Adapted from ref. 8.

The obvious conclusion from the Stribeck curve is that minimal friction is achieved when components operate in the elastohydrodynamic regime. However it is also apparent that when operating at the conditions associated with the minimum on the curve, the slightest change in contact conditions can result in a drastic increase in friction associated with

the transition away from the elastohydrodynamic regime into the mixed regime. The conditions associated with each lubrication regime are described below and summarised schematically in Figure 1.4.

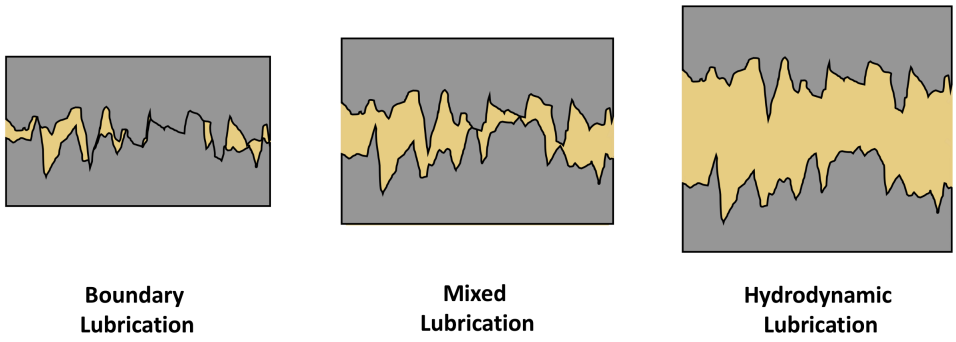

Figure 1.4: Schematic comparison of different lubrication regimes. Adapted from ref. 9.

Hydrodynamic Lubrication

In this regime, the two surfaces are completely separated by a continuous fluid film that supports the entirety of the contact load. As a result there is negligible contact between asperities (microscale protrusions) and thus friction arises only from the shearing of the lubricant; friction arising from shearing of the lubricant is directly relate to the lubricant viscosity.[7,10]

Elastohydrodynamic Lubrication

Elastohydrodynamic lubrication (EHL) is a form of hydrodynamic lubrication, associated with non-conformal surfaces (low contact area), where elastic deformation of the lubricated surfaces becomes significant. For contacts of high elastic modulus such as metals (hard EHL), elastic deformation and pressure-viscosity effects are equally important. The local elastic deformation (flattening) of surfaces enlarges the load-bearing area producing coherent fluid films where asperity contact is negligible; thus friction arises due to shearing of the lubricant.[7]

Mixed or Partial Lubrication

As implied by the name, this regime is governed by behaviour that is characteristic of both EHL and boundary lubrication regimes. Here, the lubricant film is thin enough to be penetrated by asperities giving rise to some asperity contact. However, the contact load is supported both partially by the lubricant and the contacting asperities.[7,10]

Boundary Lubrication

Under boundary lubrication conditions a considerable level of asperity contact occurs with the lubricant exhibiting minimal load-bearing capacity. Bulk properties of the lubricant, such as viscosity, are of little importance within this regime. Rather, the chemical and physical properties of substrate surfaces and thin surface films (tribofilms), dictate the level of friction and wear.[7]

1.1.3 Wear

Wear can be defined as the progressive loss of material from the surface of a contacting body as a result of mechanical processes, *i.e.* the contact and relative movement of a contacting solid, liquid or gas to the body.[8] Wear and friction are intimately related, with wear occurring as an almost inevitable consequence of friction, and while usually detrimental, in mild form, wear can be beneficial, *e.g.* during running-in (Section 1.1.3.1).

Multiple wear processes can occur simultaneously with the dominant mode of wear being subject to fluctuation as a result of the wear process itself. In addition, the multi-parameter sensitivity of the degree of wear highlights the need to understand the various wear processes that could occur in relation to system parameters. This sensitivity also highlights that wear is not a material property, but rather a system response. In other words, component operating conditions, as well as the nature of the material, affect the degree of wear. Four fundamental and widely recognised modes of wear exist: adhesive, abrasive, corrosive and fatigue wear, each of which will be briefly outlined in the forthcoming section.[11]

Adhesive Wear

Adhesive wear can be described as the localised welding of surface asperities in relative motion. When surface asperities come into contact under load, if sufficient heat is generated, micro-welding of the two contacting asperities and subsequent shearing results in material removal. The broken asperity tip either remains adhered to an opposing surface or may become entrained in the contact as wear debris and contribute to abrasive wear.

Metals are particularly susceptible to adhesive wear; for sliding metal contacts if the lubricant present does not provide satisfactory surface separation, adhesion and subsequent wear are inevitable.

Abrasive wear

This is the most common type of wear occurring in mechanical equipment, it arises due to the relative motion of either harder asperities or hard particles with respect to a softer surface. If abrasive wear occurs as a result of hard asperities of a mating surface, this is termed two-body abrasive wear. If hard, loose particles are present between component surfaces and cause abrasion of either component surfaces, this is termed three-body abrasive wear.

The problematic hard particles can originate from chemical (oxidation) or mechanical processes (wear), or from external contamination. A fundamental relationship exists between particle size of contaminants, lubricant film thickness and degree of component wear. The most detrimental particle size of contaminants, in terms of promoting wear, are particles with a size comparable to the thickness of the lubricant film.[12] Other factors such as hardness and shape also dictate particle abrasivity.

Fatigue Wear

Fatigue wear is surface failure resulting from asperity contact that produces very high local stresses. Repeated stress cycles cause nucleation and growth of cracks, at or close to, the substrate surface. Eventually this leads to generation of wear particles from the fatigue-propagated cracks. Fatigue wear normally occurs when contact conditions are not severe enough to give adhesive or abrasive wear.

Corrosive Wear

Corrosive wear is a general term relating to the combination of a chemical or corrosive process and any form of mechanical wear (adhesive, abrasive, fatigue, *etc.*). When surfaces are in relative motion, especially in the presence of corrosive materials, reaction products are formed on the component surfaces mainly by chemical or electrochemical interaction. If the reaction products formed are more readily worn than the bulk material, this leads to a greater extent of wear. In isolation, the corrosive action or mechanical

action may not be too detrimental; it is the combination of a corrosive process and tribological action (relative motion) that can exacerbate wear. Tribological action not only serves to remove any reacted material from the surface, it also accelerates chemical reaction; high temperatures and pressures found in the tribocontact enhance reaction rate.

1.1.3.1 Stages of Wear

Throughout component life, wear can be categorised into three basic regimes, namely, break-in, steady state and catastrophic wear (Fig. 1.5).

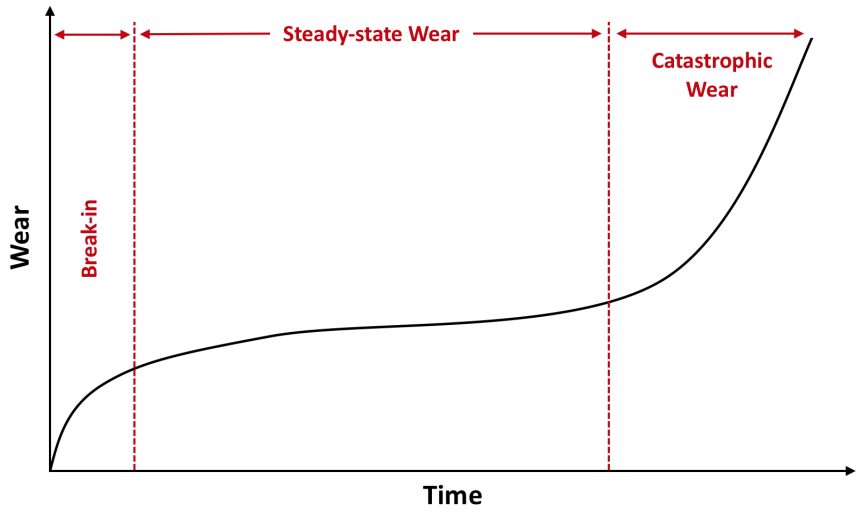

Figure 1.5: Evolution of wear as a function of time. Adapted from ref. 2.

The break-in, or running-in, stage is often associated with relatively high wear rates, but as surface asperities are flattened the surfaces become smoother (conformal mating of surfaces), so the load becomes more favourably distributed and the rate of wear decreases. For lubricated systems, the break-in period is also associated with the chemical reaction of lubricant components to form surface films, known as tribofilms. Such surface films are crucial in reducing wear and extending service life. Break-in is usually brief in comparison to the service life of a component.

After the running-in period, friction and wear will reach a steady-state in which the wear rate remains almost constant. This corresponds to the useful working life of a component and is the best regime to study long-term tribological properties. Eventually, steady-state

wear alters the conditions in the tribosystem such that steady-state wear can no longer be maintained and the rate of wear drastically increases; this causes severe and irreversible damage, which is termed catastrophic wear. This signifies the end of the useful working life of a component, and usually the larger machinery of which it is part.

1.2 Lubricant Formulation

A summary of the fundamental concepts of tribology (friction, lubrication and wear) has been presented. This has included a description of the many diverse roles a lubricant must perform. In the upcoming section the constituent components of a lubricant will be discussed in detail, namely the *base oil* and *additive package*.

1.2.1 Base Oil

Originally, and up to the 1930s, base oils, a mineral or synthetic hydrocarbon oil, were used as the single component of a lubricant formulation. In this role they functioned to separate moving surfaces, remove heat and minimise friction. However, as base oil properties became insufficient to meet the greater demands (engine efficiency, durability, longer drain intervals, *etc.*) placed on the lubricant, the void between demands and current performance was overcome primarily through the addition of lubricant additives, with little change in base oil chemistry. Such additives are used to tailor and/or enhance particular characteristics of a lubricant in order to meet the performance specific requirements for a given application. The topic of lubricant additives will be covered in detail in Section 1.2.2. The use of lubricant additives remained the only strategy for optimising lubricant performance for a long time, that was until significant improvements in base oil technology became available.[13] To maximise the performance of modern lubricant formulations, the base oil, not unlike the additive package, needs to be optimised.

1.2.1.1 Base Oil Characteristics

There are several important parameters to be considered when selecting an optimal base oil, these include: oxidative stability, viscosity index (VI), pressure-viscosity index,

low-temperature fluidity, pour point and volatility, The significance of such parameters is outlined in Table 1.1, specifically in terms of automotive lubrication. Base oil performance is heavily affected by the concentration and nature of impurities present, of particular significance is the level of aromatic species present. A high aromatic content yields a poor quality base oil as i) aromatic species impart oxidative instability to the base oil, and ii) the viscosity of aromatics is more sensitive to temperature, and thus their presence lowers the VI of a base oil.[3]

Table 1.1: Important base oil characteristics.[3]

Parameter	Automotive Significance
Oxidative Stability	Excessive oxidation can result in oil thickening and the formation of acids (corrosive), sludge and varnish. Improved oxidative stability equates to longer service life and better additive stability
Viscosity Index (VI)	A high VI indicates that viscosity is not as severely affected (reduced) by temperature. The VI of a base oil is a useful parameter to predict if sufficient protection will be maintained over a range of service temperatures.
Pressure Viscosity Index	Describes how an oil's viscosity varies under load. Useful for predicting performance in highly loaded contacts.
Pour Point	The lowest temperature at which an oil is readily pumped in an engine.
NOACK Volatility	Found to correlate with oil consumption in passenger car engines.

Once an appropriate base oil has been chosen, based on a consideration of the above characteristics, then an additive blend will be added to the base oil to provide or enhance particular properties for a given application. Therefore a further caveat for a base oil is that it must be able to solubilise any additives under normal service conditions.

Despite the major improvements in base oil properties that results from the removal of aromatic components, a significant drawback is incurred in terms of solvency. That is, highly processed oils, containing only trace aromatics, have a diminished ability to dissolve additives, many of which are polar in character. A similar issue is found when

using synthetic hydrocarbon oils such as poly(alphaolefins) (PAOs). One way in which lubricant formulators have overcome this issue is to add back in some polar compounds, *e.g.* alkylnaphthalenes. Although this method initially appears counter intuitive in terms of oxidative stability, if the new aromatic species are more oxidatively stable than the previously removed aromatics, then the new composition will have superior properties. Using alkylnaphthalenes containing a tertiary alkyl group, the formulation will have even better oxidative stability due to the lack of easily oxidisable benzylic protons.[14]

1.2.1.2 API Base Oil Classifications

Advances in the processing of base oils in the early 1990s meant that lubricant base oils made by hydrocracking and early wax isomerisation technologies showed favourable, differentiated performance. The availability of these superior base oils prompted the API to categorise base oils by their composition (Table 1.2).[13]

Table 1.2: API base oil categories.[15]

Group	Sulfur Content	Saturates Content	Viscosity Index (VI)
I	> 0.03 wt.%	< 90 wt.%	80-119
II	≤ 0.03 wt.%	≥ 90 wt.%	80-119
III	≤ 0.03 wt.%	≥ 90 wt.%	≥ 120
IV	All poly(alphaolefins) (PAOs)		
V	All others not included in above groups		

Group I Base Oils

Group I base oils are manufactured by solvent refinement. They are characterised by high levels of impurities, *i.e.* aromatics and sulfur.

Group II Base Oils

Group II oils differ from their group I counterparts in terms of containing significantly lower levels of impurities (≤ 10 wt.% aromatics, ≤ 0.03 wt.% sulfur). This is achieved *via* hydroprocessing and results in a base oil that is more inert and forms less oxidation by-products. Such by-products causes detrimental increases in viscosity and can react

adversely with additives.[13]

Group III Base Oils

Group III oils contain the same level of impurities as that of a group II oil, but have a higher VI. That is, the viscosity of a group III oil is less adversely affected by temperature in comparison to a group II oil. This higher VI is achieved by increasing the time or temperature in the hydrocracker, which reduces aromatic compounds to saturated cycloparaffins, that can subsequently rearrange to normal and branched paraffins. Hydrocracking also removes sulfur- and nitrogen-containing species to give a base oil that is comprised almost exclusively of saturated paraffins.[13]

Group IV Base Oils

Polyalphaolefins (PAOs) are synthetic hydrocarbon polymers. One of the reasons for their popularity in the lubricant industry is their similarity to mineral oils, but without the presence of impurities, such as aromatics, that can impact VI, volatility and oxidation stability. PAOs have superior low and high temperature properties relative to a mineral base oil of similar viscosity. Their major application is in automotive engine oils that require low pour point, low volatility and good thermo-oxidative properties.[3] A drawback is that synthetic oils are typically more expensive than mineral oils.

More recently with advances in the conversion of natural gas to liquids, several commercial Gas to Liquid (GTL) products have also become available, including GTL base oils. GTL base oils contain almost no sulfur or aromatic impurities, possess extremely high VIs, have high oxidation resistance, and low volatility. These characteristics make them perfect candidates for producing high quality lubricants. GTL base oils are primarily isoparaffinic in nature and typically classified as API Group III, displaying similar or superior performance to the more traditional Group III oils.[3,15]

Further background information on base oils and details about the refinement processes used can be found in a review by Kramer *et al*. on the evolution of base oil technology.[13]

1.2.2 Lubricant Additives

Despite the advances in base oil technologies, it is inconceivable that a base oil alone could perform all the functions required of a modern day automotive lubricant. Therefore, lubricant formulators use additive packages to improve and tune the property set of a lubricant to those required for a given application.

Typically, an additive package makes up 5-25 wt.% of a final lubricant formulation (Table 1.3), where additive components are classified by their primary function only, despite some being multifunctional. The nature and properties of each of the components present, in a representative engine oil additive package, will be described in detail in the forthcoming section.

Table 1.3: Typical automotive lubricant formulation.[16]

Function	Component	Concentration (wt.%)
	Base Oil	75-95
Reduce Friction and Wear	Viscosity Modifier	0-6
	Antiwear Additive	0.5-2
	Friction Modifier	0-2
	Corrosion Inhibitor	0-1
Contamination and Cleanliness	Dispersant	1-10
	Dispersant	1-10
	Detergent	2-8
Maintain Fluid Properties	Pour Point Depressant	0-0.5
	Foam Inhibitor	0-0.001

1.2.2.1 Detergents

Detergents have been used in engine oil applications since the 1940s. They are primarily used to suspend/disperse oil-insoluble species, *e.g.* soot, sludge and oxidation products,

and to neutralise acidic contaminants.[17] Because of this, detergents control rust, corrosion and resinous build up in an engine. The basic structure of such detergents consists of a surface-active polar head group and an oleophilic hydrocarbon tail, with an appropriate number of carbons to ensure solubility. The polar head group (commonly sulfonate, phenate or salicylate) contains a metal cation, typically calcium or magnesium. Historically, barium was used, however it has gradually been replaced due to environmental concerns associated with the use of heavy metals. The mechanism by which detergents suspend oil-insoluble species is *via* the formation of inverse micelles as depicted in Figure 1.6.[17]

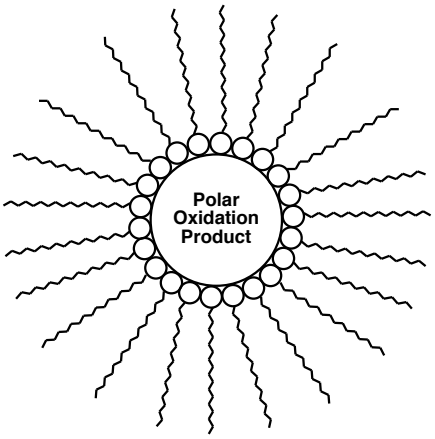

Figure 1.6: Oil suspension of a polar oxidation product by detergent aggregation.

Depending on the level of inorganic base (*e.g.* metal hydroxide, metal oxide or carbonate) used in their synthesis two different types of detergent can be formed. If a stoichiometric level of inorganic base is used, the detergent is *neutral*, whereas if an excess is used the detergent is termed *basic* or *over-based*. In over-based detergents, the excess base is present in colloidal form and can act as a base reserve to neutralise acidic contaminants, produced during fuel combustion and oil oxidation. Excess base is stabilised in solution by a monolayer of detergent, where the polar head group is associated with the basic core (commonly a metal carbonate) and the hydrocarbon tails extend into the bulk oil (Fig. 1.7).[18–20]

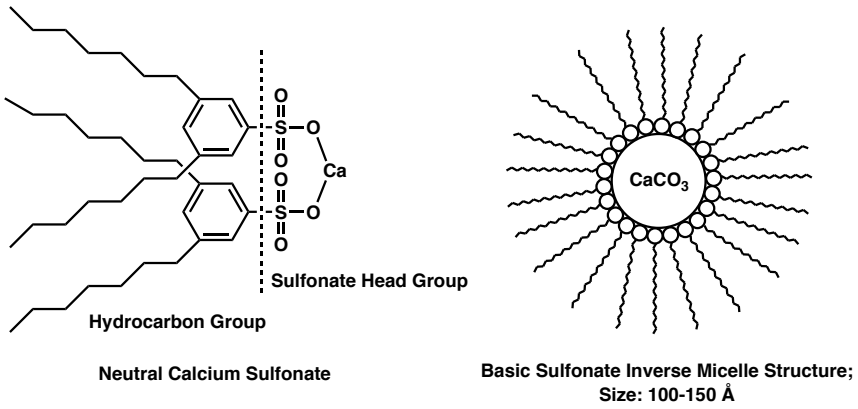

Figure 1.7: Neutral and over-based detergents.[17]

Detergents contain metals, and thus have the potential to form ash (tiny, solid, metallic salt particles). This is particularly relevant when considering the recent compositional constraints enforced on lubricant formulations in terms of achieving low sulfated ash, phosphorus and sulfur (SAPS) contents, a subject that is introduced more thoroughly in Section 2.1. These restrictions mean that the use of metal-containing additives such as over-based calcium salts of sulfonates is restricted, and a balance must be struck between other metal-containing species, *e.g.* zinc dialkyl(aryl) dithiophosphates (Section 1.2.2.8). Reduced detergent levels can somewhat be mitigated through the use of ashless dispersants (Section 1.2.2.2), but this change can have a significant, potentially detrimental, effect on other lubricant properties.[21]

1.2.2.2 Dispersants

In the 1960s ashless dispersants became commercially available. These species have a similar structure and perform in a similar way to detergents (Section 1.2.2.1), but contain no metal. Their polar head is derived from an organic functionality, usually comprising nitrogen- or oxygen-containing moieties, while the tail is hydrocarbon-based. Typically these two fragments are linked by a connecting group that is most often a succinimide or phenol group.

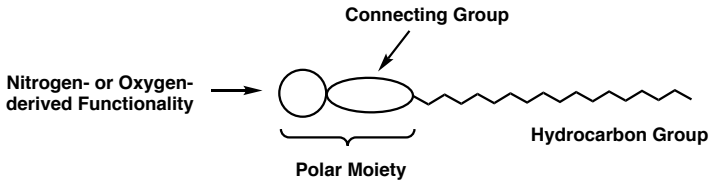

Figure 1.8: Schematic of a typical dispersant molecule.

Dispersants differ from detergents in three significant ways:[22]

1. Dispersants do not contain metals, and therefore do not form ash upon combustion.
2. Dispersants have little or no acid-neutralising ability. This is because dispersants do not contain reserves of strong bases, which can neutralise acidic contaminants.
3. Dispersants are typically much higher molecular weight (approx. 4-15 times greater) than the organic segment of a detergent. This makes dispersants much more efficient in their suspending and cleaning functions in comparison to detergents.

Dispersants are particularly useful in preventing the agglomeration of soot particles, a particular problem in diesel engines.[23,24] They hinder this agglomeration through a combination of steric and electrostatic stabilisation mechanisms. In addition, they are more efficient at suspending oil insoluble components at lower temperatures in comparison to detergents. The dominant dispersant structures in engine oil formulations are based on succinimides, succinate esters and Mannich bases (Fig. 1.9), with polyisobutylene (PIB) being the most commonly used hydrocarbon tail.

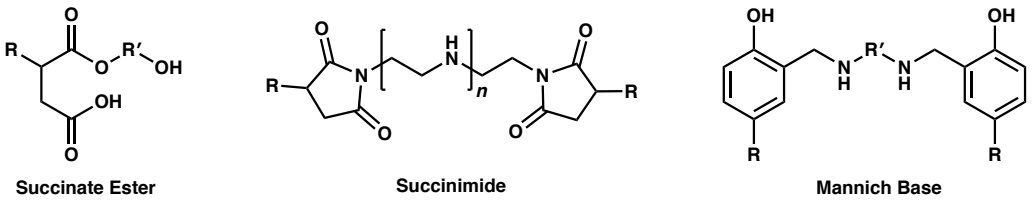

Figure 1.9: Chemical structures of some common dispersants molecules.

1.2.2.3 Oxidation Inhibitors (Antioxidants)

Oxidation inhibitors are added to a lubricant to slow the rate of oxidation, in order to extend service life and lubricant drain intervals. Oxidation of oil leads to the formation of insoluble sludge, soot and corrosive acids that are detrimental to engine performance.

The process of hydrocarbon oil oxidation can be described by the well known free-radical mechanism, which takes place *via* alkyl and peroxide radicals (Fig. 1.10).[15] The mechanism can be categorised into three steps: initiation, propagation and termination. Initiation starts the oxidation process *via* radical formation caused by oxygen. The propagation step involves radical attack on hydrocarbons, forming new radicals. This is a chain reaction resulting in an exponential increase in radical formation. The process is terminated by either radical combination or through the use of antioxidants. There are three types of antioxidants: radical scavengers (primary antioxidants), peroxide decomposers (secondary antioxidants) and metal deactivators.[25]

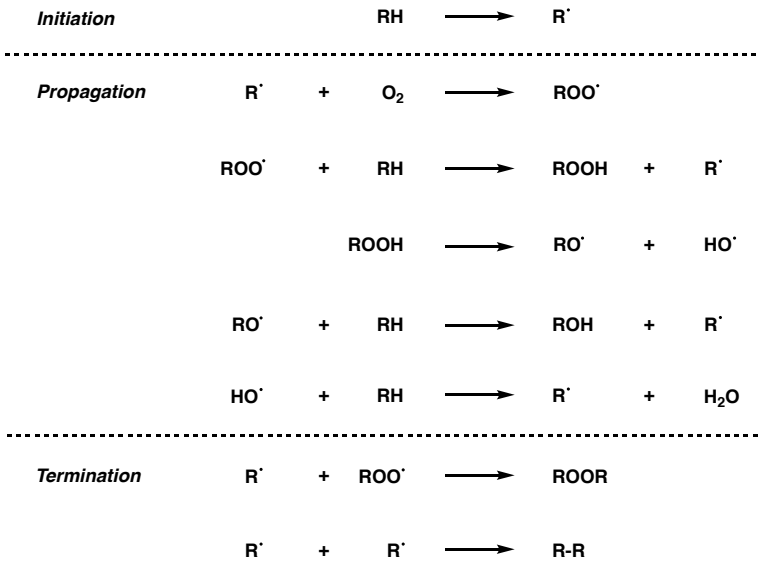

Figure 1.10: Mechanism of hydrocarbon oxidation.[15]

Radical scavengers compete effectively with base oil hydrocarbon species to intercept deleterious free radicals to form hindered, resonance-stabilised radicals, that are not prone to propagation. Hindered phenols and aromatic amines are the two main classes of primary antioxidants used in lubricants,[3] although ZDDPs are also known to function as radical scavengers.[26]

Peroxide decomposers function by converting peroxides to non-radical products, and hence prevent radical chain propagation. Organophosphorus, organosulfur and compounds containing both phosphorus and sulfur, *i.e.* ZDDPs, are well known peroxide decomposers (Fig. 1.11).[3]

Transition metal ions are able to catalyse both radical initiation and hydroperoxide decomposition *via* a redox mechanism.[27] The activation energies for such processes are lowered and thus, initiation and propagation occur at lower temperatures. Metal deactivators are used to suppress this phenomenon and reduce the catalytic activity of metals present. Two functioning mechanisms are known, surface passivators and chelators.[25] Surface passivators act by forming protective layers on a metal surface (*e.g.* ZDDP) and thus prevent metal-hydrocarbon interaction, and simultaneously serve to minimise corrosive attack. Chelators, in comparison, function in the bulk and trap metal ions to form inactive species or species with significantly diminished activity.

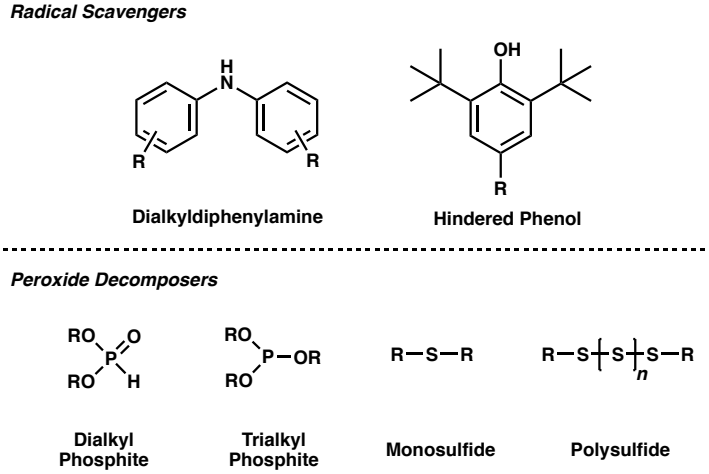

Figure 1.11: Chemical structures of common antioxidants.

1.2.2.4 Rust and Corrosion Inhibitors

Rust and corrosion inhibitors prevent corrosion and rusting of metal surfaces that are in contact with the lubricant. Rust/corrosion inhibitors can function by two mechanisms, film formation and acid neutralisation.[3] Acid-neutralising agents simply neutralise acidic contaminants and render them innocuous. In contrast, film-formers generate protective surface films by physical or chemical adsorption and thereby isolate the metal surface from the attack of harmful species. For engine oil applications, multifunctional, over-based sulfonates that are primarily deployed as detergents (Section 1.2.2.1), fulfil the corrosion inhibition needs of the system.[28] Such detergents function by both acid neutralisation and protective film formation. Another multifunctional additive present in engine oil formulations are ZDDPs. The primary function of ZDDPs are as antiwear

additives (Section 1.2.2.8), but they also function as corrosion inhibitors.[3,15,29]

1.2.2.5 Foam Inhibitors

The presence of additives in lubricating oils can slow the release of dissolved or generated gases. This can result in gas entrainment and/or foaming. In engine oils, foam can result in reduced oil pressure, while gas entrainment can result in cavitation of the oil film in bearings and may cause failure; these effects necessitate the use of foam inhibitors, such as polydimethylsiloxane (PDMS), in engine oil formulations (Fig. 1.12). Such compounds are sparingly soluble in oil and separate onto the surface of air bubbles, causing them to rupture by reducing surface tension. Loadings are very low, typically < 20 ppm.[15,30]

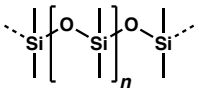

Figure 1.12: Chemical structure of PDMS.

1.2.2.6 Pour Point Depressants

Pour point depressants were the first commercially used lubricant additives dating back to the the early 1930s.[29] These additives function to reduce the lowest temperature at which an oil will pour or flow, *i.e.* the pour point. A low pour point is particularly critical to lubricant performance in cold climates. At low temperatures, wax (linear hydrocarbon species) in a lubricant base oil can crystallise and produce a gel-like structure (cloud point). This gel-like, three-dimensional network can trap the remaining lubricant fluid and render the lubricant oil immobile. For an engine oil, this can result in insufficient flow of oil to critical engine components and cause engine failure.

Pour point depressants work by providing seeds for wax crystallisation as well as co-crystallising with the wax. Co-crystallising with a pour point depressant separates the wax crystals by steric hindrance, thus inhibiting network formation. This effect, in combination with a greater number of nucleation sites, results in the formation of a multitude of small crystals, which may still impede the lubricant flow, but critically do

not immobilise the oil.[31] The most common materials used as pour point depressants are polyacrylates (PAs) and polymethacrylates (PMAs) (Fig. 1.13).[15]

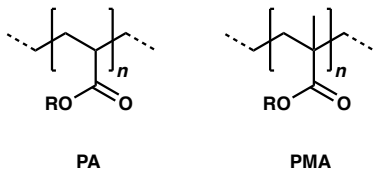

PA PMA

Figure 1.13: Chemical structures of PA and PMA.

It should be noted that the low-temperature fluidity of a lubricant oil is not only governed by wax crystal growth. All fluids become more viscous as temperature decreases, eventually reaching a viscosity where the fluid will no longer flow. The temperature at which the fluid no longer flows under gravity, solely due to the viscosity increase caused by decreasing temperature, is known as the viscous pour point. A pour point depressant has no effect on the viscous pour point.

1.2.2.7 Viscosity Modifiers

Viscosity modifiers are materials that decrease the sensitivity of a base oil's viscosity to temperature. The advent of such additives allowed the formulation of multi-grade engine lubricants, which meet both low temperature (winter) and high (summer) temperature oil requirements (Fig 1.14). This marked the end of seasonal oil changes. Multi-grade oils provide low viscosity at low temperatures, this facilitates cold starting and minimises viscous losses. At higher temperatures, the viscosity of a multi-grade oil is less sensitive than a single-grade oil (demonstrated by the lower gradient in Figure 1.14), and thus the viscosity remains high enough to provide sufficient surface separation and hence provide adequate wear protection.[15,32,33]

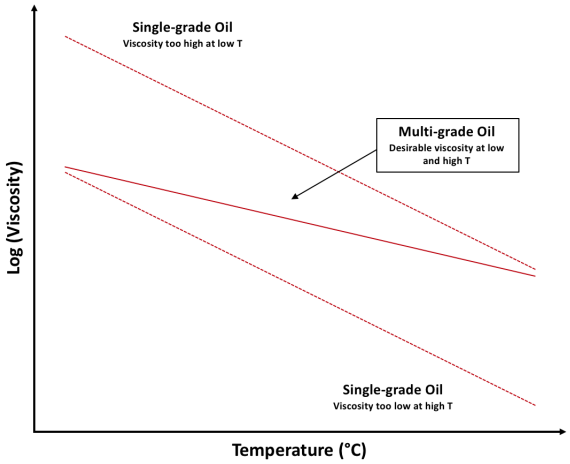

Figure 1.14: Temperature effects on viscosity for single- and multi-grade engine oils. Adapted from ref. 15.

Viscosity modifiers are typically high molecular weight polymers (> 10,000 g/mol), with common chemistries employed being olefin copolymers (OCPs), hydrogenated styrene dienes (HSDs), polyisobutylenes (PIB) (Fig. 1.15), and the previously mentioned polymethacrylates (PMAs), which were outlined in Section 1.2.2.6 on pour point depressants.[32,33]

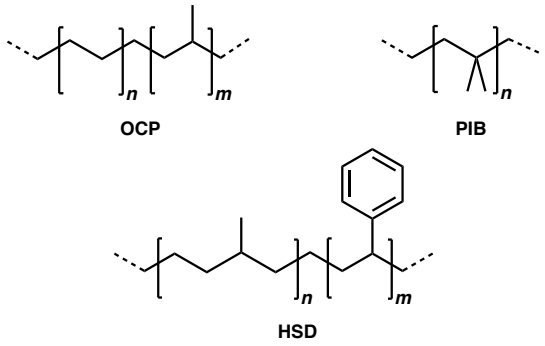

Figure 1.15: Chemical structure of some common viscosity modifiers.

The dual action of PMA as a viscosity modifier and pour point depressant highlights the potential multifunctional nature of viscosity modifiers, and more generally, of all lubricant additives. Aside from also acting as pour point depressants, viscosity modifiers have also been shown to provide additional benefits as friction modifiers and dispersants.[33] Considering the current trends in lubricant design, *i.e.* the use of ultra-low viscosity oils for improved fuel economy, development and understanding of viscosity modifier chemistries remains extremely important. A more in-depth coverage of the use

of viscosity modifiers, their mechanism of action and their multifunctional nature can be found in a recent review by Martini *et al.*[33]

1.2.2.8 Antiwear Additives – Zinc Dialkyl Dithiophosphate (ZDDP)

Studies assessing wear in engines have concluded that the majority of engine wear occurs during the brief start-up and acceleration periods.[3] This is essentially due to lubricant starvation of engine components, a situation where there is insufficient lubricant fluid to prevent metal-to-metal contact, *i.e.* within the boundary lubrication regime. Wear is minimised in this regime through the addition of antiwear additives, sometimes known as boundary lubricants. Such additives are effective in minimising wear in both the boundary and mixed lubrication regimes, in which asperity contact occurs.[29,34]

Zinc Dialkyl(aryl) Dithiophosphates (ZDDPs) were first introduced in the late 1930s, and are still ubiquitous in engine oil formulations today. The persistence of such additives is particularly striking given that alternatives have been actively sought. However, a cost effective alternative, showing comparable antiwear performance has yet to be identified. In part, today, the search for ZDDP alternatives results from modern legislation that limits sulfated ash, phosphorus and sulfur (SAPS) species in engine oil formulations, due to their deleterious effect on exhaust after-treatment systems.[35] The topic of legislation-imposed SAPS limits in engine lubricant formulations is covered in more detail in Section 2.1.

1.2.2.8.1 Chemical Structure and Properties of ZDDPs

ZDDPs are multifunctional lubricant additives (Fig. 1.16); they function not only as antiwear agents, but also inhibit corrosion and oxidation in lubricant formulations.[29] The molecular nature and behaviour of ZDDPs in solution is more complex than suggested by their most simple and common chemical representation (Fig. 1.16); this is something that will be discussed below.

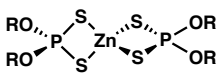

Figure 1.16: Chemical structure of ZDDP (neutral-monomeric form).

The organic groups can be either alkyl or aryl and are required to impart solubility in the lubricant base oil. The nature of this hydrocarbon group has a significant impact on various chemical properties and ultimately the antiwear performance of a given additive. Early work by Dickert and Rowe showed that the thermal stability of an alkyl ZDDP is dependent on the number of β-hydrogen atoms present in the alkyl substituents, *i.e.* the lower the number of β-hydrogens, the greater the thermal stability.[36] Hence, the use of primary alkyl groups yields ZDDPs of higher thermal stability than their secondary and tertiary analogues. Further studies related the thermal stability of alkyl ZDDPs to their antiwear effectiveness. It was found that in general there was an inverse relationship between thermal stability and antiwear activity, arising from more efficient degradation and hence protective antiwear tribofilm formation.[37,38]

Since engine oils are expected to perform for long service intervals, typically a blend of both primary and secondary alkyl ZDDPs are used. Secondary alkyl ZDDPs provide quick, efficient antiwear protection, whilst the more thermally stable primary alkyl ZDDPs provide more sustained wear protection ensuring the availability of antiwear chemistry towards the end of service life.

Neutral ZDDPs

Early solid-state structural data available for two alkyl ZDDPs (ethyl and isopropyl) show that ethyl ZDDP exhibits a one-dimensional polymeric structure in which each zinc atom is chelated by one dithiophosphate (DTP) ligand and bridged by a second DTP ligand that connects zinc atoms in the chain.[39] The isopropyl analogue has a dimeric rather than polymeric structure, where again each zinc atom is chelated by one DTP ligand, but in this case the two zinc atoms of the dimer are bridged by the two remaining DTP ligands.[40] More recent solid-state structural data revealed that isobutyl-substituted ZDDP exhibits the same dimeric structure (Fig. 1.17).[41]

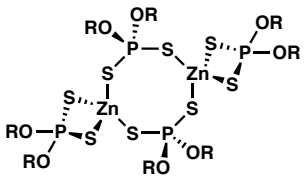

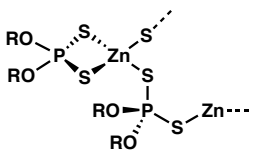

Figure 1.17: Dimeric (R = ^{i}Pr or ^{i}Bu) and polymeric (R = Et) structures of neutral ZDDPs.

In solution, NMR spectroscopy has been used to show that neutral ZDDPs exist in equilibrium between a monomeric and a dimeric form (Scheme 1.1).[42,43] Both structures contain zinc atoms in a tetrahedral environment. However, in the monomeric form the central zinc atom is coordinated by two equivalent, chelating DTP ligands, whereas in the dimer the two zinc atoms are coordinated by one chelating and one bridging DTP ligand. At room temperature, the ^{31}P NMR spectra of neutral, alkyl ZDDPs, display a singlet spectroscopic resonance, albeit broad, indicating that exchange between the three inequivalent phosphorus atoms is in the fast exchange regime on the NMR spectroscopic timescale (*i.e.* the system is above its coalescence temperature).[42,43]

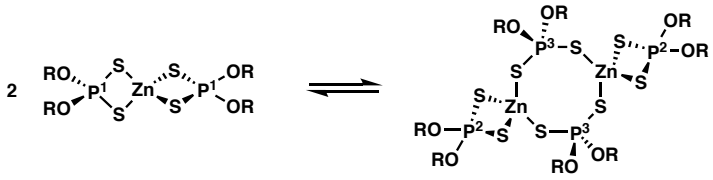

Scheme 1.1: Monomer-dimer equilibrium of neutral ZDDPs.[42,43]

Recently, Harrison *et al.* performed variable-temperature ^{31}P NMR spectroscopic studies with line-shape analysis for several alkyl ZDDPs, the results of which support the long-held view of the monomer-dimer equilibrium in solution.[43] At low temperatures (-52 °C) three distinct peaks were observed in the ^{31}P NMR spectrum of 2-ethylhexyl ZDDP, which broaden and coalesce as the temperature is increased to yield a single resonance (Fig. 1.18). Below -40 °C the spectra collected displayed three signals; 103.0 ppm, assigned to the bridging phosphorus (P^3) of the dimer, 99.0 ppm, assigned to the chelating position (P^2) in the dimer and 96.0 ppm, assigned to the chelating phosphorus (P^1) in the monomer (Scheme 1.1).

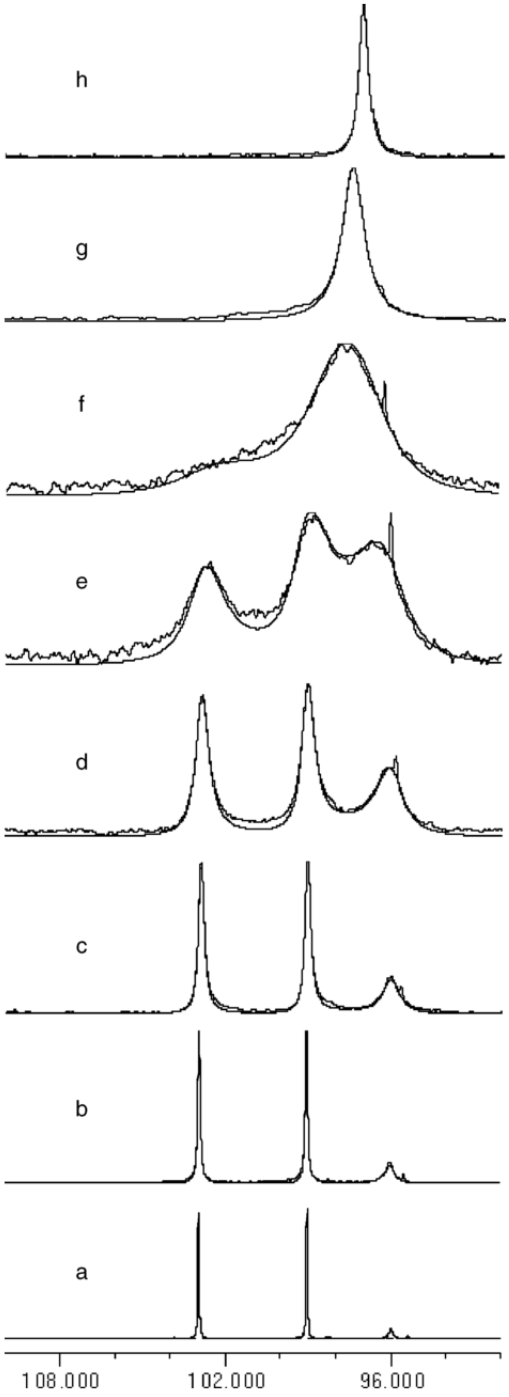

Figure 1.18: Full ^{31}P NMR spectroscopic line-shape analysis of 2-ethylhexyl ZDDP (0.0465 M). (a) Experimental and fitted spectrum at -52 °C, (b) -42 °C, (c) -33 °C, (d) -18 °C, (e) -4 °C, (f) 11 °C, (g) 25 °C and (h) 44 °C. Reproduced with permission from ref. 43.

Dynamic light scattering studies have suggested that for neutral isobutyl ZDDP, there may be tetrameric or even higher order oligomeric structures present in low polarity mineral oils.[44] This idea is supported by the observation that some ZDDP derivatives form

polymeric species in the solid-state, as outlined above. However, variable-temperature ^{31}P NMR spectroscopic results obtained by Harrison *et al.* for isobutyl ZDDP were not consistent with this presence of the proposed tetramer.[43]

Basic ZDDPs

Although their use dates back at least to the 1940s, structure of basic ZDDPs remained a matter of speculation for a long time, until Woollins *et al.* reported the crystal structure of basic isobutyl ZDDP, $Zn_4O[S_2P(O^iBu)_2]_6$ (Fig. 1.19).[41] The structure is analogous to that of beryllium acetate, consisting of a Zn_4O core with a tetrahedron of zinc atoms about a central oxygen, and the six edges of the Zn_4 tetrahedron bridged by DTP ligands.

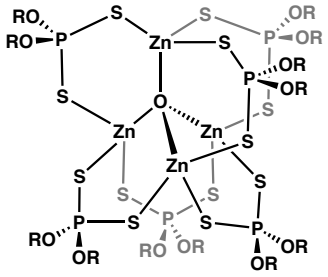

Figure 1.19: Chemical structure of basic ZDDP.[41]

Detailed studies of the solution behaviour of neutral and basic ZDDPs using ^{1}H and ^{31}P NMR spectroscopy reported by Harrison and Kikabhai, show that the two forms are in equilibrium (Scheme 1.2), with higher temperatures and more polar solvents favouring the neutral form.[42]

$$Zn_4O[S_2P(OR)_2]_6 \rightleftharpoons 3\ Zn[S_2P(OR)_2] + ZnO$$

Scheme 1.2: Equilibrium between the neutral and basic forms of ZDDP.

In terms of the practical significance of this neutral-basic equilibrium, a number of studies have compared the antiwear,[45] film-forming[46] and antioxidant[47] properties of the basic and neutral forms. The general conclusion is that, despite slight differences in reactivity, the mechanisms by which they function are essentially the same.[29] Indeed, the interconversion of neutral and basic forms in solution may contribute to their equivalent performance. Furthermore, the presence of a nitrogen donor such as pyridine, has been

shown to irreversibly convert basic ZDDP to its neutral ZDDP-pyridine adduct.[42] Such a reaction could conceivably occur in an engine oil formulation given the presence of nitrogen donors in the form of dispersants (Section 1.2.2.2) and/or amine-functional organic friction modifiers (Section 1.2.2.10.2) and hence may also contribute to the equivalent performance observed for neutral and basic ZDDPs.

1.2.2.8.2 Antiwear Mechanism of ZDDPs

The general view on the wear prevention properties of ZDDPs is that they function by forming surface films that act as a mechanically-protective barrier.[29] These films can be classified into two types:[48]

1. Antiwear films, which are formed under "normal" operating conditions and thereby reduce the rate of continuous moderate wear.

2. Extreme pressure (EP) films in contrast, are formed under extreme contact conditions at high local temperature. They function through rapid reaction with a surface under severe distress and inhibit more catastrophic modes of failure, *i.e.* scuffing and seizure.

Various studies report that the antiwear behaviour of ZDDP is derived from the formation of phosphate films, while its EP behaviour arises from its ability to form iron sulfide.[49,50] This agrees with other reports that sulfur-free phosphorus additives are effective antiwear, but ineffective EP additives.[51] ZDDPs are considered potent antiwear additives, and mild EP additives. The antiwear aspect of ZDDP behaviour will be the focus of this work.

Thermal Degradation of ZDDPs

As previously mentioned, it has long been recognised that there was an inverse relationship between the thermal stability and the antiwear effectiveness of ZDDPs,[37,38] with the thermal behaviour dictated by the nature of the alkyl substituents of ZDDP. The observed thermal degradation of ZDDPs between 130-230 °C has been long known,[29] however the mechanism of this degradation process remained a matter of debate for a considerable length of time.

The matter was mostly resolved in a paper by Jones and Coy using ^{1}H and ^{31}P NMR spectroscopies to identify thermal degradation products of various ZDDP derivatives (*n*-butyl, isobutyl and *sec*-butyl).[52] In all cases the final degradation products were similar (described below), although present in different proportions, which is evidence to support a common degradation mechanism that is applicable to both primary and secondary ZDDPs.

The decomposition of primary alkyl ZDDPs (*i.e.* *n*-butyl ZDDP) can be described by a sequential alkyl transfer mechanism from oxygen to sulfur (Fig. 1.3). The major (non-volatile) degradation products described are a zinc polypyrophosphate-type species (with a low sulfur and alkyl content), *S,S,S*-trialkyl tetrathiophosphate and dialkyl sulfide.[52,53] The nature of the final oil-soluble, phosphorus-containing product is still a matter of contention however, as Marshall *et al.* have reported the final soluble phosphorus-containing product to be *O,O,S*-trialkyl dithiophosphate in the degradation of isobutyl ZDDP, based on gas-liquid chromatography and mass spectrometry data.[54] This matter was also raised in the appended discussion of the work by Coy and Jones by Barber and Yamaguchi.[53] The discussers noted that in engine sequence tests they observe the major oil-soluble, phosphorus-containing end products to be oxygenated materials, in this case of fully formulated engine oils. It must also be noted that an exceptionally high ZDDP concentration was used (25 wt.% in mineral oil) in these studies by Coy and Jones compared to a standard 0.5 wt.% ZDDP that is very typical in engine oil formulations.[53]

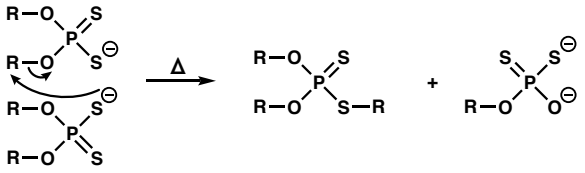

Scheme 1.3: Decomposition of alkyl ZDDP *via* an alkyl transfer mechanism. Zinc cations are omitted for clarity but may be assumed present.

Importantly however, the proposed alkyl transfer mechanism accounts for the relative thermal stabilities observed for different (primary) alkyl substituents (branched primary alkyl > primary alkyl) and agrees with the well-established correlation between decreasing the number of β-hydrogens and increasing thermal stability.[36] This thermal stability

trend is explained in terms of increasing steric hindrance inferred by the β-substituents, which inhibit nucleophilic attack at the α-carbon.

The decomposition of branched primary alkyl ZDDPs (*i.e.* isobutyl ZDDP) is reported to occur principally *via* the same alkyl transfer mechanism outlined above, but at a much slower rate. A relative increase in olefin formation is observed, however, compared to *n*-butyl ZDDP, and can be explained based on the slowed rate of alkyl transfer, thereby increasing the proportion of olefin *versus* other degradation products that arise from the alkyl transfer pathway.[52] Others have also observed olefin formation[36,54] during decomposition, a process that is suggested to occur by a β-hydrogen transfer elimination mechanism.[36,52] Recent theoretical studies have provided evidence in favour of olefin formation *via* β-hydrogen transfer,[55] specifically through a concerted mechanism (Scheme 1.4).[56] The phosphorus-containing degradation product can further decompose by loss of more olefin and/or various sulfur-containing species, including hydrogen sulfide.

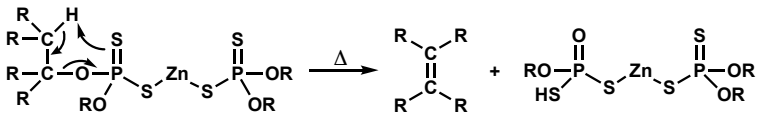

Scheme 1.4: Concerted olefin elimination from alkyl ZDDPs.

Thermal decomposition studies of *sec*-butyl ZDDP, have shown the decomposition mechanisms are similar to that of *n*-butyl and isobutyl ZDDPs previously outlined, but with the distinction that the olefin elimination mechanism dominates and occurs more readily than alkyl transfer.[52] This can be ascribed to increasing alkyl substitution, which inhibits nucleophilic attack as a result of steric inhibition, and accelerates elimination. The rate enhancement of the elimination pathway enables faster degradation of secondary ZDDPs, compared to their primary counterparts, and thus completes the previously observed trend in thermal stabilities for different alkyl substituents (branched primary alkyl > primary alkyl > secondary alkyl). Likewise, the thermal instability of tertiary alkyl ZDDPs can be ascribed to the ease with which they undergo olefin elimination, even at modest temperatures, hence making their commercial use prohibitive.

ZDDP Tribofilm Formation and Properties

Extensive macroscopic studies have shown that ZDDP molecules decompose at rubbing interfaces, and form protective films that minimise wear by providing a mechanical barrier and act in a sacrificial manner.[29,34,57] Such films can be generated thermally (thermal films) at elevated temperatures (typically > 150 °C), even in the absence of rubbing,[58] or they are formed within a rubbing contact (tribofilms), where they form at much lower temperatures even, albeit slowly, at room temperature.[58,59] The chemistry of thermal and tribofilms have been shown to be similar, although tribofilms are mechanically stronger.[46,60,61]

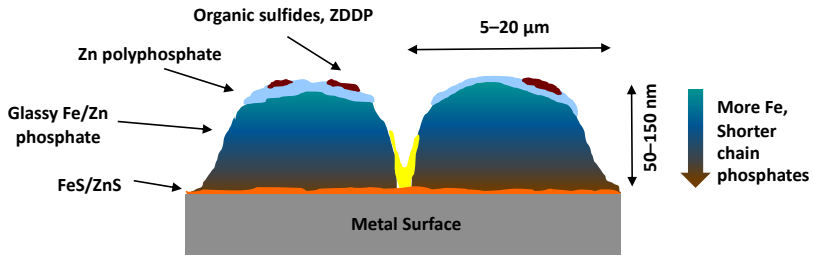

Figure 1.20: Schematic of a ZDDP tribofilm on steel.

Most research has focussed on the nature of ZDDP tribofilm formation on steel surfaces, though it has also been shown that ZDDPs can form thermal and tribofilms on other materials, such as other metals, ceramics, silicon and diamond-like carbon (DLC) coatings.[57] The chemical and structural details known specifically for ZDDP tribofilms on steel surfaces (Fig. 1.20) can be summarised as follows:

1. Tribofilms only form if actual sliding contact occurs – they do not form in rolling contacts or if the hydrodynamic film thickness is much greater than the surface roughness.[58]

2. Film growth appears self-limiting; ZDDP tribofilms tend to reach a stable thickness of around 50-150 nm on steel surfaces.[59,62,63]

3. Tribofilms initially form as separate patches on steel surfaces that gradually expand to form almost continuous, but still pad-like structures.[64]

4. The pad-like films are primarily composed of glassy phosphate, with a thin layer of zinc polyphosphate (~10 nm) grading to pyro- and ortho-phosphate in the bulk.[65,66]

5. The exterior of the tribofilm pads comprise mainly zinc cations with an increasing proportion of iron towards the metal surface.[66]

6. Within the pads there is negligible thiophosphate, rather sulfur is present as zinc sulfide.[67]

7. Directly on the metal surface there may be a sulfur-rich layer of zinc or iron sulfide,[68] though this has been contested by some.[66]

8. The presence of a viscous gel-like layer of alkyl phosphate material, up to 1 μm thick, covering islands of solid polyphosphate has been described recently.[68] This layer had gone un-noticed for a long time due to solvent washing and use of analytical techniques that require vacuum.

Experimental evidence has shown that increased operating temperature correlates to an increased rate of tribofilm formation (other parameters such as film thickness and friction coefficient are also affected).[69] This supports the long-standing view that faster tribofilm formation caused by lower thermal stability ZDDPs is the underlying reason for their superior antiwear performance (*i.e.* secondary ZDDPs form tribofilms faster than primary ZDDPs under the same conditions).

Tribofilm formation is believed to occur *via* a mechanism akin to the thermal degradation process that occurs in thermal films, but with formation being induced at lower temperatures, and films only forming on rubbing tracks. Whether the cause of this lower activation temperature is primarily dictated by flash temperature rise, pressure, triboemission or another factor, has been a matter of particular speculation. However, a recent innovative approach by Gosvami *et al*., using atomic force microscopy (AFM), provided real insight into the underlying mechanisms of ZDDP tribofilm formation.[70]

Gosvami's novel approach involves sliding an AFM tip against a substrate at temperatures from 80-140 °C while immersed in a ZDDP base stock solution, to monitor *in situ* the growth and properties of ZDDP tribofilms, in well-defined (known contact area and pressure), single-asperity contacts. The observed growth of a patchy (pad-like) tribofilm is consistent with macroscopic studies,[59,64] and the rate of tribofilm forma-

tion was found to increase exponentially with temperature or compressive stress; these results are consistent with a stress-assisted thermally activated reaction rate model.[70] Subsequently, Zhang and Spikes have demonstrated tribofilm formation in full film elastohydrodynamic (EHD) conditions (Section 1.1.2.1), where no surface contact occurs, effectively eliminating triboemission as a driver for tribofilm formation. In the same work it was also observed that a tribofilm is formed with a base oil that gives high shear stress, but not for a base oil that gives low shear stress, in otherwise identical conditions. This result strongly suggests applied shear stress rather than contact pressure is the driver for tribofilm formation. Additionally, the rate of tribofilm formation is in agreement with a stress-promoted thermally activated model, through which it is estimated that shear stress can reduce the thermal activation barrier to ZDDP film formation by half.[57]

The demonstration that shear stress (mechanochemistry) controls ZDDP tribofilm formation also explains several known features of ZDDP tribofilms, such as:

- No tribofilm formation is observed in pure rolling contacts;
- ZDDPs' relative indifference to surface composition;
- The pad-like structure of ZDDP tribofilms, which nucleate at asperity junctions (highest shear stress) and bear increasing proportions of the applied load as they grow, meaning the applied shear in the deep valleys is negligible inhibiting tribofilm growth;
- The self-limiting growth mechanism, which terminates when the shear stress is too low to drive the process (as the tribofilm modulus is lower than the substrates, contact stress at constant load decreases as the tribofilm thickens).

In the 1980s when fuel economy started to become an important issue, it was soon noticed that ZDDPs had a deleterious effect on friction, and hence fuel economy.[29] This is thought to arise from ZDDP inhibiting fluid entrainment within the contact zone, such that the contact remains in the boundary and mixed lubrication regimes to higher speeds than in the absence of ZDDP (see Stribeck curve in Figure 1.3).[71] The origin of this fluid entrainment inhibition however, is not currently clear. A simple mechanism is

that the deep valleys associated with the pad-like structure of ZDDP tribofilms act as drainage channels that inhibit fluid entrainment. Conversely, some work has suggested that even apparently smooth ZDDP tribofilms show an increase in friction and indicate that fluid entrainment may be prevented by another as yet unidentified mechanism.[72] Clearly, whichever mechanism does occur, it is apparent that ZDDP tribofilms have a negative effect on friction, and for this reason, it is essential to use ZDDPs in conjunction with an effective (and compatible) friction modifier in engine lubricant formulations, to reduce friction and improve fuel economy. It should also be noted that such a friction modifier will not necessarily be one that preferentially adsorbs on steel surfaces, but rather one that is able to adsorb and form friction-reducing films on a ZDDP-derived tribofilm.[73] Friction modifiers will be discussed in more detail in Section 1.2.2.10.

1.2.2.9 Low SAPS ZDDP Alternatives

Due to the compositional constraints enforced on modern engine lubricant formulations, in terms of achieving low SAPS content,[74] there is a significant level of research investigating alternative antiwear additives to ZDDP. In spite of the volume of research focused on identifying such additives, currently no cost effective additive showing comparable antiwear performance has been identified. ZDDP alternatives will not be the focus in this work; for a comprehensive overview on the potential low-SAPS ZDDP alternatives reported in the literature, the reader is directed to an excellent review on the matter by Spikes.[35]

1.2.2.10 Friction Modifiers

Friction modifiers (FMs) are lubricant additives that are commonly used to adjust friction characteristics and hence improve lubricity and energy efficiency. For engine oil applications FMs that reduce the friction coefficient are used and are effective in the boundary and/or mixed lubrication regimes (Table 1.4). At present there are two main families of friction modifiers in use in liquid lubricants: organic friction modifiers (OFMs) and organomolybdenum compounds.[75]

Table 1.4: Friction coefficients of different lubrication modes.[76]

Lubrication Mode	**Friction Coefficient**	**Comparison**
Non-lubricated Surface	0.5-0.7	Dragging an irregular rock over rocky ground
Antiwear/EP Films	0.12-0.18	Dragging a flat stone over a flat rock
Friction Modified Films	0.06-0.08	Ice Skating
Elastohydrodynamic	0.001-0.01	Hydroplaning

1.2.2.10.1 Organomolybdenum Compounds as Friction Modifiers

Initially recognised as EP additives in the 1950s,[77] oil-soluble organomolybdenum compounds were not recognised as FMs until the 1970s. Since then, organomolybdenum FMs have become one of the most important additives used in automotive engine lubricants to improve fuel economy.[75,77] Common organomolybdenum chemistries include molybdenum dialkyl dithiophosphates (MoDDPs) and molybdenum dialkyl dithiocarbamates (MoDTCs). These additives function by giving rise to the *in situ* formation of tiny, nano-sized platelets of low-friction molybdenum disulphide (MoS_2).[78,79] The friction-reducing ability of MoS_2 arises from its low shear strength, lattice-layer structure, in which there are strong covalent bonds between atomic species, but only weak van der Waals attractions between layers (Fig. 1.21).[69]

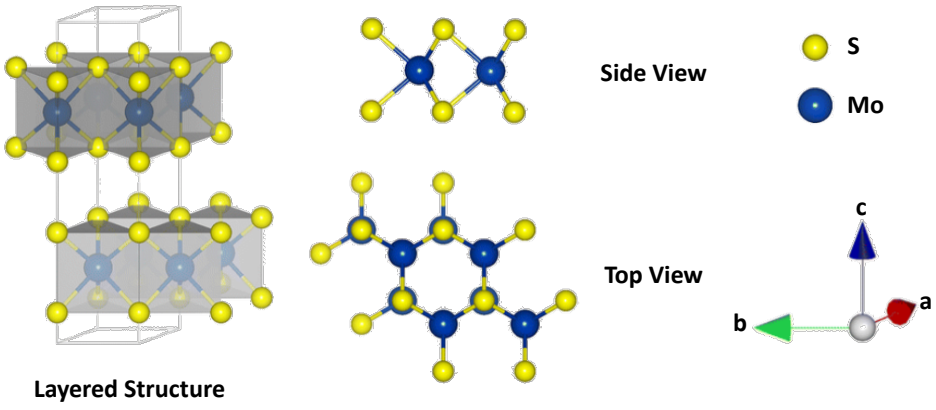

Figure 1.21: Structural representation of 2H-MoS_2. The side and top views of the layered structure are also shown. Adapted with permission from ref. 80.

By far the most prevalent organomolybdenum compounds used are MoDTCs. They have received significant attention not only because they function well as FMs, but also because they are one of the most efficient, non-phosphorus-containing antiwear additives,[81] shown to have a "synergistic" relationship with ZDDPs in reducing friction and wear.[81–85] The principle limitation of MoDTCs however, and organomolybdenum compounds in general, is recognised as the loss of their friction-reducing ability upon ageing or during engine operation.[77] Yagishita and Igarashi identified ligand exchange reactions between MoDTC and ZDDP,[86] reactions that have also been studied in detail by Korcek and co-workers, and lower the initial MoDTC concentration (Scheme 1.5).[87–90]

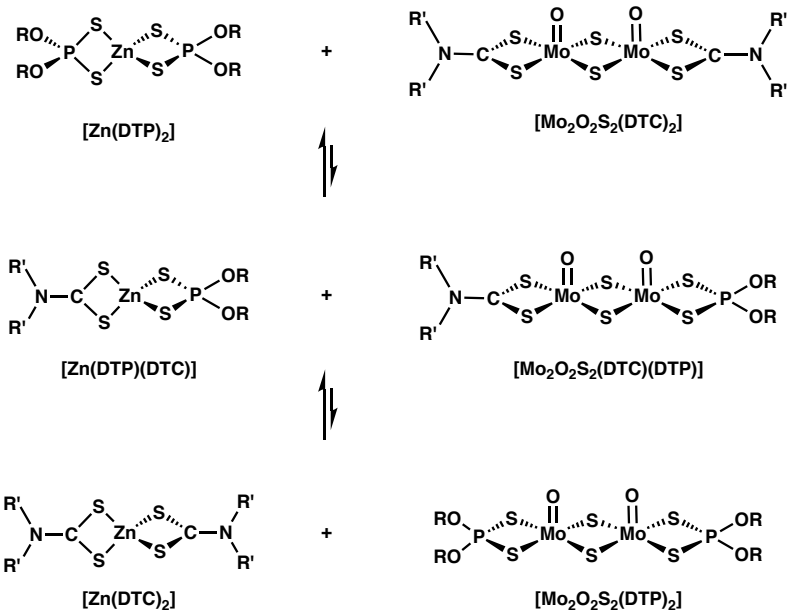

Scheme 1.5: Ligand exchange reactions between ZDDP and MoDTC. Exchange products become more favoured at higher temperatures.[87]

However, despite the initial lowering in MoDTC concentration due to ligand exchange reactions with ZDDP, it has been shown that the presence of ZDDP can reduce the decomposition rate of MoDTC, as well as improving the retention of friction-reducing capabilities. An explanation for this is that ZDDPs are more effective peroxide decomposers, and the double exchange products zinc dialkyl dithiocarbamates (ZDTCs) are better radical inhibitors (the single exchange product expected to have the capabilities of both) than their molybdenum analogues (Scheme 1.5), and hence serve to protect the

molybdenum compounds against decomposition and improve the retention of friction-reducing properties of MoDTCs. The eventual loss of friction-reducing properties is observed when the ZDDP present is fully consumed. This hypothesis is supported by the observation that other radical inhibitor and peroxide decomposer antioxidants slow MoDTC depletion, while other additives and the base oil employed influence the durability of the friction-reducing properties of MoDTC.[87–91]

Another aspect of MoDTC/ZDDP synergy that has been reported, is the ability of ZDDP to promote the formation of MoS_2,[92,93] by acting as a source of sulfur atoms.[93] Support for this idea comes from labelling studies from Iwasaki *et al*., who demonstrated using ^{34}S-labelled ZDDP and time-of-flight secondary-ion mass spectrometry (ToF-SIMS), that approximately 40% of the sulfur in the MoS_2 formed on rubbing surfaces was generated from sulfur from ZDDP.[94]

Recently Khaemba *et al.,* reported new insights regarding the decomposition mechanism of MoDTC using Raman spectroscopy. In this work, the authors utilised the ability of Raman spectroscopy to distinguish chemical compounds with the same oxidation state, something not possible by X-ray photoelectron spectroscopy (XPS); a spectroscopic method that has previously been used in an attempt to elucidate the mechanism of MoDTC degradation.[79] The main MoDTC decomposition products in steel/steel contacts were shown to be MoS_2, $FeMoO_4$ and sulfur-rich molybdenum compounds, MoS_x ($x > 2$),[95] in contrast to the previously reported MoS_2 and MoO_3.[79] The decomposition was shown to be highly dependent on test conditions (temperature, MoDTC concentration and contact pressure), while the formation of $FeMoO_4$ and MoS_x were shown to be conducive to high friction. Furthermore, based on the Raman analysis performed, a new decomposition pathway is proposed; one that involves shear-induced C-S bond cleavage and intramolecular sulfonation, to form amorphous MoS_x, which can subsequently be converted to MoS_2, or $FeMoO_4$ through reaction with iron oxides (Fig. 1.6).[95]

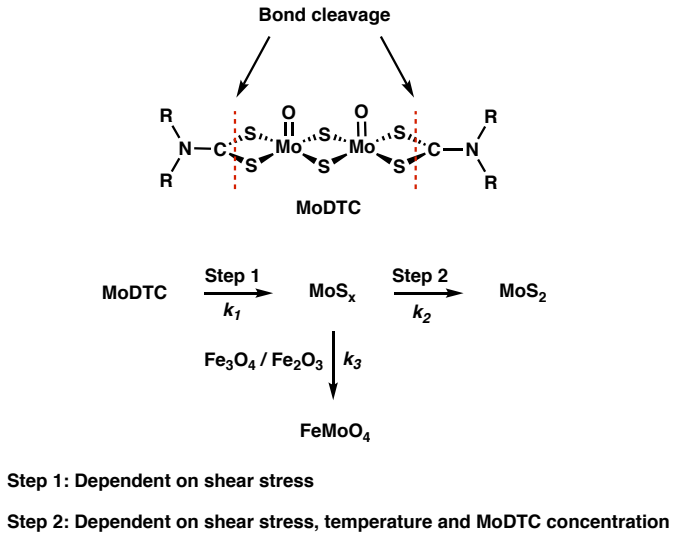

Scheme 1.6: Proposed decomposition pathway for MoDTC.[95]

1.2.2.10.2 Organic Friction Modifiers

Organic friction modifiers (OFMs) are surfactant-like molecules consisting of a polar head group (*e.g.* carboxylic acid, ester, alcohol, amine, amide and phosphate) and a long hydrocarbon chain. The traditional view on how OFMs function is that polar head group adsorption (physisorption) or chemical reaction (chemisorption) occurs with a metal surface to form vertically-oriented, dense monolayers (~ 2 nm thick) as shown in Figure 1.22.[75,77] These OFM monolayers serve to prevent asperity contact while also being easy to shear at the hydrocarbon tail interface between monolayers, thus giving rise to their lubricious nature. This view is supported by studies that have shown that both deposited[96,97] and self-assembled[98,99] monolayers on solid surfaces, can reduce friction. Their friction-reducing properties have been shown to be strongly dependent on the polar head group functionality, hydrocarbon chain length and configurations, as well as external factors such as temperature.[75,77]

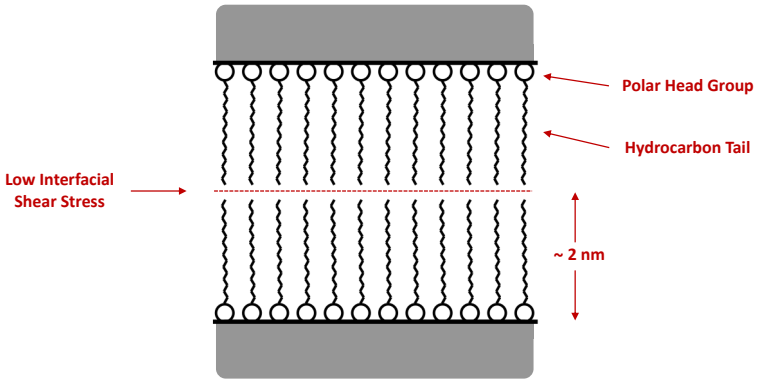

Figure 1.22: Monolayer model of adsorbed OFMs at metal surfaces. Adapted from ref. 100.

In spite of the general acceptance of the monolayer model, it has also been demonstrated that some FMs can form thicker more viscous layers that may be tens to hundreds of nanometres thick.[101–103] Ultrathin film interferometry is a particularly useful technique for studying these thicker layers, given that film thickness can be resolved on the nanometre scale *in situ*. FMs are "active" in low to medium load and low temperature conditions. Under more severe conditions, however, where the load and contact temperature increases within the tribochemical contact, the self-assembled film ruptures and the friction-reducing ability of the FM is lost. This limited film strength and thermal instability, necessitates the inclusion of other additives that are more effective under more severe conditions, namely antiwear and EP additives.[104]

In reference to the drive towards low SAPS lubricant formulations, some OFMs (*e.g.* amines, amides, fatty acids, *etc.*) have an intrinsic advantage over other FMs, in that they are intrinsically zero SAPS. This makes the use of such FMs particularly attractive in terms of meeting the compositional constraints enforced upon modern engine lubricant formulations.

1.2.3 Additive–Additive Interactions

The previous section has briefly outlined the components and functions of engine lubricant additives. However, much of the work investigating the behaviour of lubricant additives, is highly idealised, where the additives are studied in isolation, in the absence of other lubricant additives. Modern engine oil formulations however, contain a myriad

of additives (Table 1.3), all of which contribute, and tailor or modify the properties of the lubricant to meet application-specific requirements. These additives are likely to interact in bulk solution and/or compete at surfaces, thereby exhibiting antagonistic or synergistic effects. The lack of understanding regarding additive-additive interactions, and their ultimate effect on performance, has meant that much of the development of lubricant formulations has been empirical in nature, relying primarily on trial and error or past experience. A more systematic approach with an understanding of the underlying fundamental chemical and physical additive interactions would significantly aid the selection and design of additive combinations.

Chapter 2

Engine Lubricant Development and Thesis Aims

2.1 Current Trends in Engine Lubricant Development

Since their advent in the 1970s, exhaust after-treatment catalysts have been crucial in reducing air pollution, and thus, improving quality of life, particularly in major cities.[35] These catalysts function by removing harmful emissions such as oxides of nitrogen (NO_x), CO, unburned hydrocarbons and, in particular for diesel engines, soot particles. Their use has been driven primarily by increasingly stringent legislation, which permit progressively lower levels of harmful emissions.[105]

There are several different exhaust after-treatment systems currently available. However on a global basis, for gasoline engines, the most common is the three-way converter (TWC). This system oxidises CO and hydrocarbons to CO_2 and reduces NO_x to N_2.[106] For diesel engines, a diesel oxidation catalyst (DOC) and a diesel particulate filter (DPF) are typically used in combination with a NO_x removal system, such as exhaust gas recirculation (EGR), or to meet current emission standards, a selective catalytic reduction (SCR) system. The main function of DOCs is to oxidise hydrocarbons and CO to CO_2, whereas the DPF is used to collect particulate matter (predominantly soot), which is periodically burned off.[106]

It was however quickly realised, that some components of engine lubricants could produce emissions that reduce catalyst effectiveness. These contributed to the degradation of the exhaust after-treatment system during its operating life and result in the release of more harmful emissions into the environment.[107] In this regard, three components have been highlighted as being of particular concern: sulfated ash, phosphorus and sulfur (SAPS), all of which are present in or can be produced from ZDDP.[35]

Ash, which originates from the zinc present in ZDDP (also from magnesium- and calcium-based detergents and from wear of component surfaces), consists of tiny solid metallic salt particles. The main undesirable effect of this ash is its ability to build up in, and block DPFs,[108] in addition to contributing towards blocking TWCs.[109] The phosphorus-containing species that reach the catalyst are phosphorus oxide vapour and metal phosphate particulates. Phosphorus oxide vapour reacts with and blocks the porous matrix in which the active catalyst is deposited, while the metal phosphate particulates can deposit on catalyst surfaces and accumulate in DPFs.[110,111] Sulfur, is thought to be transferred to the after-treatment system *via* the exhaust gas, in the form of SO_2, which poisons oxidation catalysts. The majority of sulfur historically originated from fuel, but with the advent of ultra-low sulfur fuels a significant amount is now thought to come from ZDDP.[112,113]

The realisation that emissions originating from engine lubricants can have a detrimental effect on exhaust after-treatment systems, marked the beginning of legislation-imposed limits on SAPS levels.[74] SAPS levels in engine lubricants quickly became ever more stringent (Table 2.1); this legislation has ultimately limited the amount of ZDDP (a major source of SAPS) that can be incorporated into an engine oil formulation.

Table 2.1: Phosphorus and sulfur limits in engine oil specifications.[74]

Year	Specification	P and S limits
1989	SG	No P, S limits
1994	GF-1	$\leq$ 0.12 wt.% P
1997	GF-2	$\leq$ 0.10 wt.% P
2000	GF-3	$\leq$ 0.10 wt.% P
2004	GF-4	0.06 wt.% $\leq$ P $\leq$ 0.08 wt.%, $\leq$ 0.50 wt.% S†
2010	GF-5	0.06 wt.% $\leq$ P $\leq$ 0.08 wt.%, $\leq$ 0.50 wt.% S†

$^{\dagger}\leq$ 0.5 wt.% S for all viscosity grades except for 10W-30 (GF-4 $\leq$ 0.70 wt.% S, GF-5 $\leq$ 0.6 wt.% S)

It is currently not clear whether future SAPS limits will eventually lead to a phasing out of ZDDP in the long term. Although desirable, this would be an extremely difficult task given the current dependence of engine lubricants on ZDDPs, not only in terms of their antiwear, but also their antioxidant and corrosion inhibition properties. However, recently attention has turned to investigating the potential of replacing blanket limits on SAPS levels with a move towards a measure that better reflects the tendency of SAPS containing species to volatilise, and hence reach the after-treatment catalyst. This interest in replacing blanket SAPS limits is based on evidence that the volatility of SAPS-containing species *from* engine oil is more important than their concentration *in* engine oil, in terms of effect on catalyst efficiency.[114,115]

The volatility dependence of phosphorus-containing species on catalyst efficiency has been acknowledged in the current International Lubricant Standardisation and Approval Committee (ILSAC) GF-5 specification. The GF-5 specification requires no further reduction in the maximum phosphorus content permissible, in comparison to the previous GF-4 specification, but does introduce a new phosphorus volatility requirement. The GF-5 specification requires that engine oils retain a minimum of 79% of their original phosphorus content under standard test conditions (ASTM D7320).[74] This is born out of the recognition that differences in molecular chemistry and formulation result in phosphorus-containing species with different volatilities and consequently, can have different effects on emission catalysts at equal concentrations. Based on the GF-5 spe-

cification it appears that, currently at least, volatility requirements will be implemented as an additional safety measure to ensure minimal catalyst poisoning, rather than reduced volatility formulations providing a viable alternative to low SAPS formulations.

New performance standards for automotive lubricants are developed in response to changing consumer needs and legislative action from professional/governmental organisations. Current drivers for their future development include greater fuel economy (and fuel economy retention), reduced emissions and extended drain intervals.[3]

In the drive for improved fuel economy, modern lubricant formulations are now lower viscosity oils with good low temperature fluidity. The use of low-viscosity oils improves fuel economy by reducing energy consumption due to the reduction of friction and viscous losses that occur when cold starting and during stop-and-go type driving.[3] The proposed ILSAC GF-6A specification requires further improvements in fuel economy, fuel economy retention and oil robustness for spark-ignited engines, while minimising wear and low-speed preignition, beyond that required in GF-5. Additionally the new GF-6B category defines requirements for ultra-low viscosity (SAE 0W-XX, where XX is less than 20) engine oils, which would provide the same performance as GF-6A, but would potentially deliver further fuel economy improvements. The challenge in moving to lower viscosity oils however, is the increased likelihood of operation in the mixed and boundary lubrication regimes that are conducive to increased friction and wear (see Section 1.1.2.1).[116]

In terms of achieving reduced emissions targets, there are now strict legislation-imposed limits on the level of SAPS permitted in engine oil formulations, as evident from the data presented in Table 2.1. These limits, consequently restrict the level of ZDDP, the universal and often sole antiwear additive, used in engine oil formulations.

The convergence of these emissions and fuel economy trends reflects the need for automotive lubricants that can maintain engine durability whilst simultaneously enabling improved fuel economy and reduced emissions. The desire for improved fuel economy (move to ultra-low viscosity oils) would require increased SAPS levels to achieve equi-

valent antiwear performance (utilising current technology/chemistry). In contrast, emission regulations demand lower SAPS concentrations dictated by catalyst compatibility. Ultimately the drivers for the future development of automotive lubricants do not align and constitutes a significant challenge for the automotive lubricant industry.

2.2 Thesis Aims and Structure

Given the convergence of greater fuel economy and lower emissions trends previously described, the combination of lubricant additives that interact and perform in a synergistic manner is essential. Of particular importance in this regard is the combination of ZDDPs (antiwear additives) with effective FMs. It should be noted that, although many lubricant additives can be viewed as surface-active, that does not mean their bulk interactions are not of importance, and do not influence their surface function. However, work investigating these bulk interactions is relatively scarce and thus limits the design and development of next-generation lubricant formulations. This thesis aims to provide a fundamental understanding of any solution interactions, and the consequences thereof, between ZDDPs and FM additives, focusing in particular on OFMs with an amine functionality.

In regard to the above discussions, this thesis aims to answer three key questions:

1. How do ZDDP and OFMs interact in solution and what is the effect of OFM structure?

2. What is the impact of ZDDP-OFM interactions on subsequent thermal and tribological behaviour?

3. Can optimal additive combinations be selected and designed through an understanding of additive interactions occurring in bulk solutions?

In an attempt to answer these questions, Chapter 3 will investigate ZDDP-amine interactions more generally, studying the interactions between ZDDP and several substituted pyridines. The pyridine moiety in this case, serves as an easily tuneable scaffold to investigate the impact of sterics and electronics, on the strength and nature of ZDDP

solution interactions with amines. The knowledge gained here provides chemical understanding and grounding for later discussions.

Chapter 4 explores the solution interactions between ZDDPs and several OFMs and other model compounds where suitable; the effect of alkyl chain length, sterics and secondary donor sites are investigated. Building on the results outlined in Chapter 3, Raman spectroscopy is exemplified as a diagnostic tool for identifying DTP binding modes in ZDDP-OFM systems. The thermal and tribological behaviour of selected systems is then described in Chapter 5. From these data, attempts are made to rationalise the trends observed, based on the understanding gained regarding solution interactions, in previous chapters.

Attempted novel syntheses of the diselenophosphate, ZDDP analogues are discussed in Chapter 6, where the additional spectroscopic ^{77}Se handle would prove particularly useful for studying solution interactions. Finally, Chapter 7 provides a synoptic view of the results described in this thesis and outlines areas for future work.

Chapter 3

Exploring Steric and Electronic Effects in ZDDP-Pyridine Systems

3.1 Introduction

ZDDPs have been used as lubricant additives for over 60 years, and are still ubiquitous in engine oil formulations today, in spite of increasingly stringent legislation limiting the level of SAPS in such formulations (Section 2.1). Principally used as antiwear additives, ZDDPs function *via* the *in situ* formation of protective phosphate glass-based tribofilms under standard engine operating conditions (Section 1.2.2.8).[29,57,70,117] However, gaining further insight into the mechanism by which the antiwear films are obtained from ZDDP in commercial lubricant packages is complicated by the presence of a series of additional additives (*e.g.* friction modifiers, dispersants, detergents, antioxidants, *etc.*), which together tune the properties of the lubricant to meet the performance requirements of a given application.[16]

Amine derivatives are a prevalent class of compound featured in commercial lubricant additive packages, both as succinimide-based dispersants (Section 1.2.2.2) and as OFMs (Section 1.2.2.10.2). However, a little-explored scenario is that such functionalised amine derivatives react directly with key ZDDP complexes in (oil) solution, altering their physico-chemical degradation to the vital antiwear films, despite reports that nitrogen-containing additives can alter ZDDP tribofilm formation and composi-

tion.[73,118–120] Amine coordination at zinc is of particular interest, potentially altering the mode of DTP coordination and hence molecular structure, which will in turn affect thermal stability, and ultimately, tribological performance (friction, wear).

DTP ligands are known to be flexible in their coordination behaviour (Fig. 3.1), something that gives rise to a wide structural diversity for DTP complexes, with mono-, di-, tetra-, and poly-nuclear species having all been reported for zinc.[121,122] However, surprisingly, comparatively little is known about how any additive-induced changes in DTP coordination to zinc may impact the thermal and/or mechano-thermal breakdown of ZDDPs.

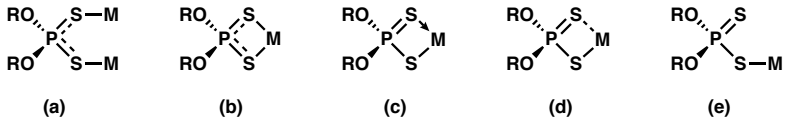

Figure 3.1: Coordination patterns observed for DTP ligands (a) symmetric bridging, (b) symmetric chelating (isobidentate), (c) anisobidentate chelating (dative), (d) anisobidentate chelating (semibonding), and (e) monodentate.

The relationship between the structure of a complexing amine and that of the resulting ZDDP-amine complex in the solid-state has been explored previously, with changes in DTP coordination noted.[123–129] However, the efficiency and performance of lubricant packages is likely determined by the strength and nature of amine-containing additive interactions with ZDDP in solution, and at least initially, on how the mechano-thermal degradation to the target antiwear film is affected.

In this chapter, a systematic investigation of how the steric and electronic properties of pyridine ligands affect the formation, structure and properties of ZDDP-amine complexes was undertaken. The pyridine-based moieties (Py') employed were chosen in order to provide a series of ligands in which the steric and Lewis basic properties can be varied in a systematic fashion. Subsequently, the structure of six mononuclear ZDDP-Py' complexes have been determined by X-ray crystallography, including five 1:1 ZDDP-amine adducts and the first 1:2 ZDDP-amine adduct. All complexes have been fully characterised, with association constants of several derivatives having been determined in hexane solution, thus providing a quantitative measure of the strength of solution inter-

action. The thermal behaviour of various adducts is investigated by thermogravimetric analysis-mass spectrometry (TGA-MS), which showed the mono- and di-(Py') ZDDP adducts followed subtly different degradation pathways. Finally, the use of Raman spectroscopy as a tool in determining DTP binding mode is demonstrated.

3.2 Results and Discussion

3.2.1 Binding Affinity and ZDDP Complex Formation with Pyridine Ligands

The reactions of zinc diisobutyl dithiophosphate (**^{i}Bu ZDDP**) with a series of variously-substituted pyridine ligands were monitored in hexane solution by ^{31}P NMR spectroscopy. Addition of Py' ligands was done incrementally in order to examine relative changes in the lineshape and chemical shift of the ^{31}P NMR spectroscopic resonance from the DTP ligands in each case. The ^{31}P NMR chemical shift variance was plotted as a function of ligand equivalents to **^{i}Bu ZDDP**, and where possible, the data fitted to a suitable binding model to afford binding constants.

^{i}Bu ZDDP presented a broad singlet resonance ($\nu_{\frac{1}{2}}$ = 72 Hz) by ^{31}P NMR spectroscopy at room temperature. This is a consequence of the established monomer-dimer equilibrium demonstrated by neutral ZDDPs in solution (Section 1.2.2.8.1, Scheme 1.1). Here, exchange between inequivalent phosphorus atoms is in the fast exchange regime on the NMR spectroscopic timescale (*i.e.* the system is above its coalescence temperature) and yields a single, averaged ^{31}P NMR spectroscopic resonance.[42,43] On subsequent incremental addition of pyridine, the proton-coupled,^{31}P[^{1}H], NMR resonance moves to higher frequency and sharpens to reveal coupling to the ^{i}Bu CH_2 units, thus indicating that all phosphorus-containing species present in solution are in rapid equilibrium on the NMR timescale and that the monomer-dimer equilibrium has been suppressed by amine complexation, shifting the equilibrium fully to the monomeric form (Scheme 3.1, Fig. 3.2).

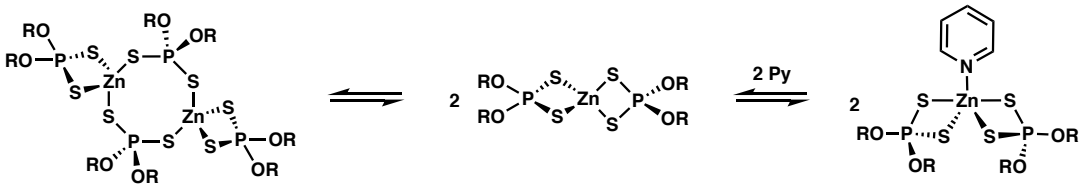

Scheme 3.1: Solution equilibria of ZDDP-pyridine complexes.

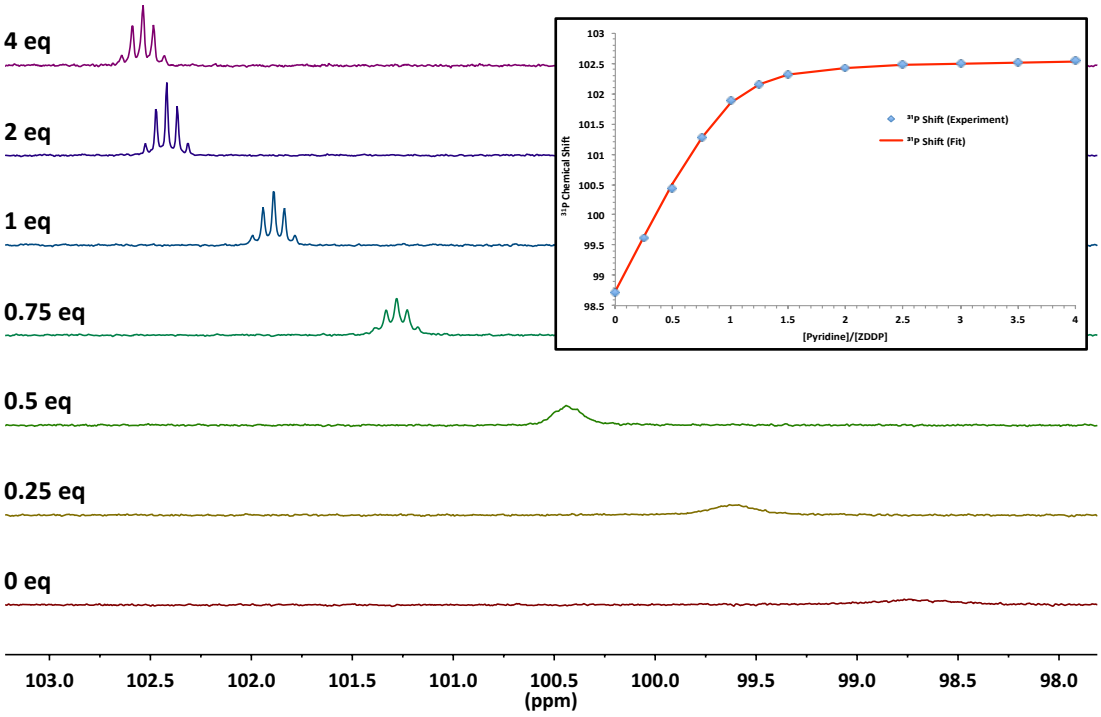

Figure 3.2: Evolution of the $^{31}P[^{1}H]$ NMR (162 MHz, hexane) spectrum of **^{i}Bu ZDDP** upon progressive addition of pyridine. Inset shows fit of observed chemical shifts to a 1:1 binding model. 0.006 M ZDDP (monomer), $CDCl_3$ insert spiked with PPh_3 to provide lock. Chemical shifts were referenced against PPh_3 in $CDCl_3$ (lit. -5.6 ppm[130]).

The observed shift to higher frequency is indicative of a change in the binding mode of DTP ligands(s), something that can be attributed to the complexation of pyridine *via* the zinc centre of ZDDP[42,124–126] and results in DTP ligands, which are now bound in an anisobidentate chelating fashion (Scheme 3.1), based on the ^{31}P NMR generalisations reported by Harrison and co-workers.[126] The change in dynamic behaviour is also in agreement with previous cryoscopic molecular weight measurements performed in benzene solution reported by Dakternieks and Graddon, which indicated that the molecular association of ZDDPs was disrupted in the presence of pyridine to form monomeric adducts.[131]

The measured ^{31}P chemical shift after each addition of Py to **^{i}Bu ZDDP** was plotted as a function of the number of Py equivalents, and fitted to a 1:1 binding model using the Bindfit web-tool (Fig. 3.2, inset).[132] These titration data fitted well to the 1:1 binding model, yielding an association constant (K_a) of 3760 ± 399 M^{-1}. This value provides a direct quantitative measure of the strength/extent of ZDDP-amine complexation in solution and can be compared directly with other related systems. The magnitude of the association constant obtained here is comparable to those measure spectrophotometrically for the binding of Py to a series of zinc-porphyrin complexes, which undergo a similar four to five-coordinate transition upon Py binding in toluene, though the geometry of the resulting complex differs slightly.[133]

Single crystals of [Zn{κ^2-*S,S*-$S_2P(O^iBu)_2$}$_2$(Py)] (**1**), from the reaction of **^{i}Bu ZDDP** with excess Py in hexane (ratio 1:3), were grown by slow evaporation.* The resulting structure confirmed the reaction product to be the mononuclear pyridine adduct of **^{i}Bu ZDDP** (Fig. 3.3). The zinc atom of this complex adopts an almost ideal trigonal bipyramidal geometry, with a value of the geometric parameter τ equal to 0.97 (0 for an ideal square pyramid and 1 for an ideal trigonal bipyramid).[134]

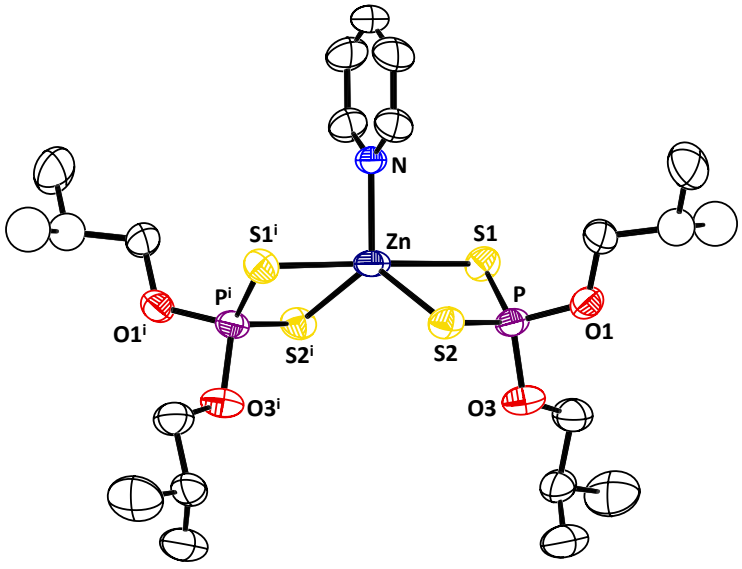

Figure 3.3: Molecular structure of [Zn{κ^2-*S,S*-$S_2P(O^iBu)_2$}$_2$(Py)] (**1**) with thermal ellipsoids at the 50% probability level; H atoms omitted for clarity. Selected bond distances: Zn-N, 2.014(3) Å; Zn-S1, 2.7085(7) Å, Zn-S2, 2.3226(7) Å; P-S1, 1.9703(10) Å; P-S2, 1.9988(11) Å. Selected bond angles: S-P-S, 113.16(4)°; S-Zn-S, 81.98(2)°.

*Identical crystals were also grown upon slow evaporation of a 1:1 ethanol solution

In complex **1** the zinc atom is coordinated by two equivalent chelating DTP ligands and a bound pyridine molecule. The chelation, however, is distinctly anisobidentate [Zn-S1 2.7085(7) Å, Zn-S2 2.3226(7) Å], as predicted from our ^{31}P NMR spectroscopic data (*vide supra*).[126] The structure of complex **1** differs from that previously determined for the related diisopropyl homologue, [Zn{κ^1-$S_2P(O^iPr)_2$}{κ^2-$S_2P(O^iPr)_2$}(Py)], in which the two DTP ligands were inequivalent, with one chelating (anisobidentate) and the other essentially monodentate.[124,125] The different DTP coordination modes observed between these two structures is attributed to the greater steric demands imposed by the ^{i}Pr substituents, which precludes chelation of both DTP ligands.

3.2.2 Steric Effects on ZDDP Complex Formation

As noted above, even small structural changes at the periphery of the alkyl substituents of the DTP ligands (R = ^{i}Pr *versus* R = ^{i}Bu) significantly affects the structure of the resulting ZDDP-pyridine adducts, in particular the nature of the DTP binding mode. Hence, changes in the steric demands of a pyridine derivative complexing directly to the zinc centre of the ZDDP complexes are likely to have a much greater effect on structure. Consequently, here, the correlation between pyridine steric demands and the nature of the resulting ZDDP-amine complexes is explored.

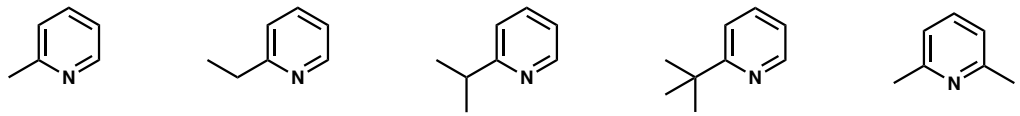

Figure 3.4: Structures of alkylpyridine ligands investigated.

To achieve a systematic variation in the steric demands of pyridine ligands, in the absence of gross electronic deviations, the coordination of the alkyl-substituted pyridine ligands 2-MePy, 2-EtPy, 2-^{i}PrPy, 2-^{t}BuPy and 2,6-Me_2Py with **^{i}Bu ZDDP** was investigated (Fig. 3.4). The steric influence of each of these different pyridines was determined using the percentage buried volume descriptor ($\%V_{bur}$) developed by Cavallo and co-workers, which measures the space occupied by a ligand in the first coordination sphere of a metal (represented by a sphere of radius, r) (Fig. 3.5).[135] Calculations were performed using

the Samb*V*ca 2 online tool,[136] using experimentally-determined crystal structure data of the complexes or free ligands in all cases, except for 2-^{t}BuPy where a DFT-optimised structure (B3LYP/6-31G(d)) was used in the absence of suitable crystal data (Table 3.1).

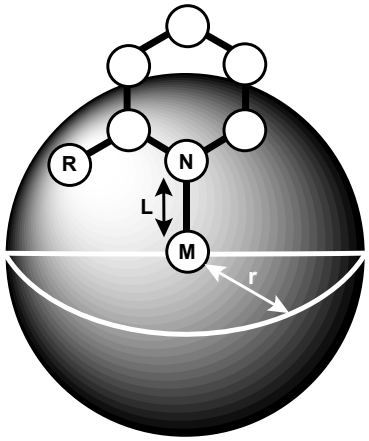

Figure 3.5: Schematic representation of the $\%V_{bur}$ descriptor. For the pyridine-based ligands analysed L = Zn-N bond distance (fixed at 2.11 Å), r = 3.5 Å, bond radii were scaled by 1.17, mesh spacing was 0.10 and all H atoms were included in calculations.

To remove any discrepancies in the $\%V_{bur}$ values originating from variation in the Zn-N bond distances (shorter bond lengths giving rise to larger values of $\%V_{bur}$), a fixed Zn-N bond length of 2.11 Å was used in all calculations. This value is the average Zn-N bond distance obtained from 24749 hits in the Cambridge Structural Database.[137]

Table 3.1: Calculated values of $\%V_{bur}$, association constants determined with **^{i}Bu ZDDP** in hexane and experimentally reported or theoretical pK_{aH} values.

Ligand	$\%V_{bur}$ **(%)**	K_a **(M^{-1})**	pK_{aH}[138,139]
Py	20	3760 ± 399	5.2
2-MePy	24	441 ± 23	6.0
2-EtPy	25	323 ± 20	5.9
2-^{i}PrPy	26	66 ± 1	5.8†
2,6-Me_2Py	29	-	6.7
2-^{t}BuPy	34	-	5.7†

†Calculated using ACD/Labs software, version 11.02; ACD/Labs 1994-2018.[140]

Thus to explore the impact of pyridine steric demands upon ZDDP-pyridine solution

interactions, hexane solutions of **^{i}Bu ZDDP** were titrated with aliquots of the various differently-substituted pyridines. Incremental addition of aliquots of 2-MePy, 2-EtPy, and 2-^{i}PrPy to **^{i}Bu ZDDP** under identical reaction conditions gave similar trends (Fig. 3.6) to that observed on addition of pyridine itself (Fig. 3.2). For each of these pyridines a 1:1 binding model was found to be followed; the resulting association constants are summarised in Table 3.1.

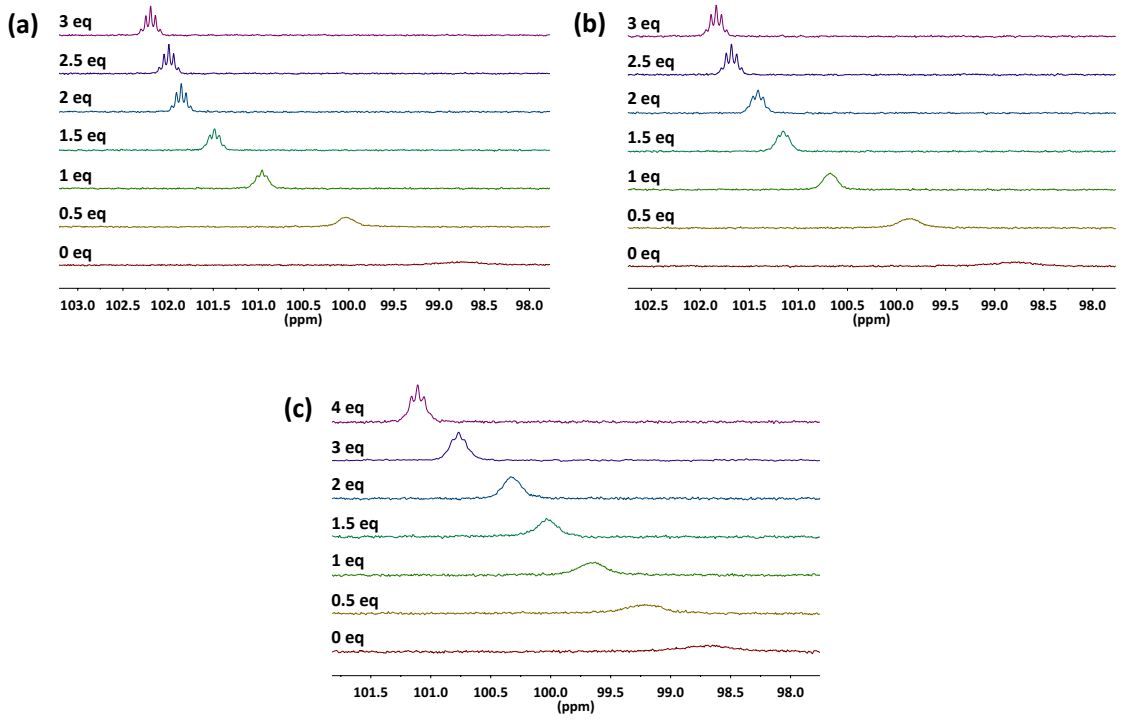

Figure 3.6: Evolution of the ^{31}P[^{1}H] NMR (162 MHz, hexane) spectrum of **^{i}Bu ZDDP** upon progressive addition of 2-alkylpyridine ligands (a) 2-MePy, (b) 2-EtPy and (c) 2-^{i}PrPy. 0.006 M ZDDP (monomer), $CDCl_3$ insert spiked with PPh_3 to provide lock. Chemical shifts were referenced against PPh_3 in $CDCl_3$ (lit. -5.6 ppm[130]).

From the calculated association constants (Table 3.1) and Figures 3.2 and 3.6, it can be seen that, the weaker the association constant of each alkyl-substituted pyridine ligands (lower K_a, smaller $\Delta\delta$), the less resonance sharpening that occurs, and the greater the concentration of ligand required before a reasonably resolved pentet is obtained. This observation further validates the idea that it is pyridine complexation to zinc in solution that disrupts the molecular association (monomer-dimer equilibrium) of **^{i}Bu ZDDP**.

As expected for the mono-substituted pyridines investigated, binding constants were smallest (Py >> 2-MePy > 2-EtPy > 2-^{i}PrPy > 2-^{t}BuPy) for the ligands with the largest

values of $\%V_{bur}$ due to the increased steric constraints imposed upon binding (Table 3.1). Taken to the extreme, the very sterically demanding 2-^{t}BuPy ligands with a $\%V_{bur}$ value of 34%, shows no evidence of interaction with **^{i}Bu ZDDP** by ^{31}P NMR spectroscopy in hexane solution (Fig. 3.7). In contrast to the comparatively strong binding of 2-MePy, only a very weak interaction is observed in solution by ^{31}P NMR spectroscopy ($\Delta\delta$ = 0.32 ppm after addition of 3 equivalents of amine) for the related disubstituted pyridine ligand, 2,6-Me_2Py, something that precluded the reliable estimation of an association constant. This weak interaction {estimated $0 < K_a << 66$ M^{-1} based on the observed $\Delta\delta$ (0.32 ppm) compared with the $\Delta\delta$ observed for 2-^{i}PrPy (2.08 ppm) after addition of 3 equivalents of amine in each case} correlates with the calculated values of $\%V_{bur}$ for 2,6-Me_2Py (29%), which lies between that of 2-^{i}PrPy and 2-^{t}BuPy, with $\%V_{bur}$ values of 26 and 34%, respectively.

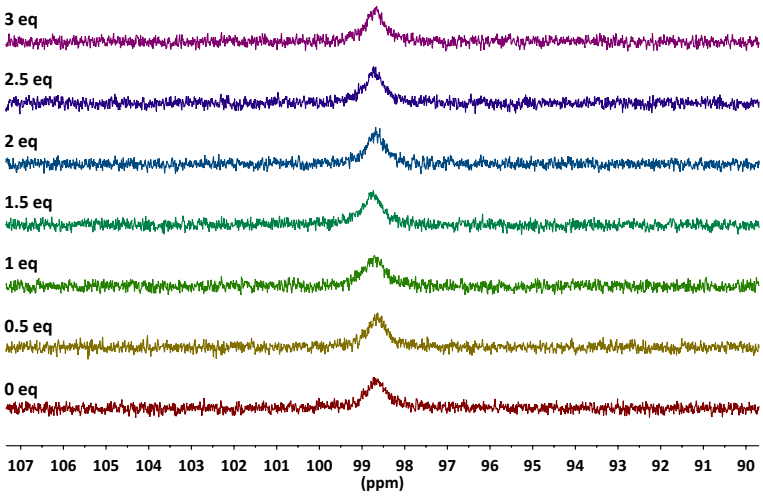

Figure 3.7: Evolution of the ^{31}P[^{1}H] NMR (162 MHz, hexane) spectrum of **^{i}Bu ZDDP** upon progressive addition of 2-^{t}BuPy. 0.006 M ZDDP (monomer), $CDCl_3$ insert spiked with PPh_3 to provide lock. Chemical shifts were referenced against PPh_3 in $CDCl_3$ (lit. -5.6 ppm[130]).

To explore how coordination of alkyl-substituted pyridines impacted on the structure and bonding of the **^{i}Bu ZDDP** moiety, single crystal X-ray crystallographic analysis of the resulting 2-alkylpyridine complexes [Zn{κ^2-*S*,*S*-S_2P(O^{i}Bu)$_2$}$_2$(L)] {L = 2-MePy (**2**), 2-EtPy (**3**) and 2-^{i}PrPy (**4**)} (see Appendix A) was undertaken. Complexes **2-4** all proved to be mononuclear 1:1 alkylpyridine adducts of **^{i}Bu ZDDP**, where the central zinc atom adopts a trigonal bipyramidal geometry and the pyridine moiety lies in the

equatorial plane in each case, as found for the parent pyridine complex **1** (Fig. 3.3). The two Zn-S bonds occupying the equatorial positions are shorter than those located in the two axial sites. The Zn-N bond distances vary somewhat [2.014(3)-2.0408(17) Å], with all 2-alkylpyridine adducts having longer Zn-N bond distances than that of complex **1**, though these variations do not correlate with the calculated values of $\%V_{bur}$. Alongside this Zn-N bond elongation, the 2-alkylpyridine ligands are tilted (evident from the Zn-N-C bond angles, Table A.1), which serves to orient the alkyl substituent of the pyridine ring away from the ZDDP framework, presumably to minimise steric effects (Fig. 3.8). All other key bond lengths and angles associated with the ZDDP frameworks of **1-4** were very similar and fell within narrow ranges (Table A.1, Appendix A).

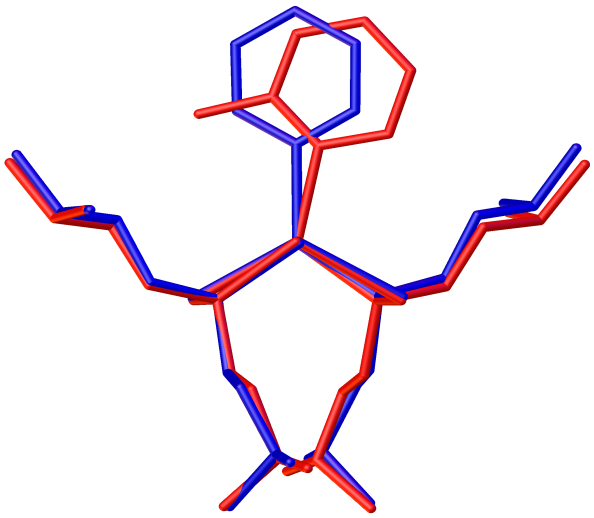

Figure 3.8: Overlaid molecular structures of complexes **1** (blue) and **2** (red) revealing the tilting of the 2-MePy ligands of **2**.

3.2.3 Electronic Effects on ZDDP Complex Formation

To study the effect of electronic factors on ZDDP-amine complex formation an investigation of the coordination of 2- and 3-fluoropyridine (2-FPy and 3-FPy, respectively) was undertaken, since the electron withdrawing nature of the fluorine atom, reduces the Lewis basicity of the pyridine ring to varying degrees depending on the substitution position.

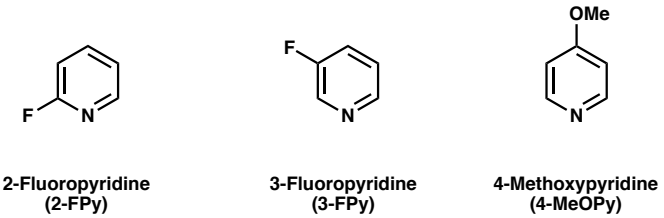

Figure 3.9: Structures of pyridine-based ligands investigated with varying electronic properties.

Fluorine was selected specifically as the electron withdrawing substituent since the small difference in size between hydrogen and fluorine atoms {van der Waals radii 1.20 (H) and 1.47 Å (F)},[141] minimises changes in steric demands upon substitution. Additionally, the binding of 4-methoxypyridine (4-MeOPy) was probed since this derivative provides considerably enhanced Lewis basicity, but with minimal change in steric demands (Fig. 3.9). The relative differences in Lewis basicity have been assessed from their pK_{aH} values, while the $\%V_{bur}$ descriptor was again used to confirm changes in steric demands, which proved minimal, thus allowing the effect of varying Lewis basicity to be investigated in isolation (Table 3.2).

Table 3.2: Calculated values of $\%V_{bur}$, association constants determined with **^{i}Bu ZDDP** in hexane and experimentally reported pK_{aH} values.

Ligand	**pK_{aH}** [138,142]	**K_a (M^{-1})**	**$\%V_{bur}$ (%)**
2-FPy	-0.4	-	22
3-FPy	3.0	286 ± 22	20
Py	5.2	3760 ± 399	20
4-MeOPy	6.6	-	20

Upon addition of aliquots of 2-FPy to a hexane solution of **^{i}Bu ZDDP**, no change in either the chemical shift or the lineshape of the ^{31}P NMR spectroscopic resonance was observed (Fig. 3.10a). This is attributed to the very weak Lewis basicity (*i.e.* low pK_{aH}) of 2-FPy, which precludes adduct formation in solution. However, with the fluorine substituent further removed from the pyridine nitrogen, *i.e.* 3-FPy, there is a notable shift to higher frequency of the phosphorus resonance, accompanied by significant sharpening to eventually display a resolved pentet following addition of ≥1.5 equivalents of the

fluoropyridine (Fig. 3.10b); this behaviour mirrors that observed for the alkyl-substituted pyridine ligands described above. The attenuated Lewis basicity of 3-FPy compared with Py however, gives rise to the expected decrease in association constant (>10 fold), despite comparable steric demands (Table 3.2).

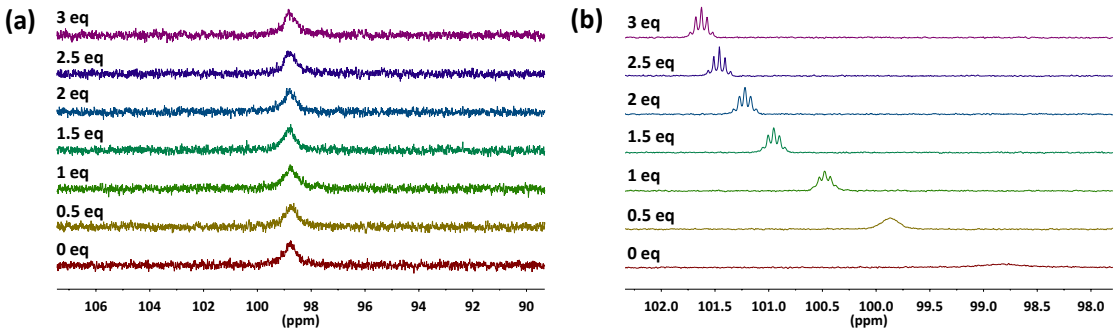

Figure 3.10: Evolution of the $^{31}P[^{1}H]$ NMR (162 MHz, hexane) spectrum of **^{i}Bu ZDDP** upon progressive addition of fluoropyridine ligands (a) 2-FPy and (b) 3-FPy. 0.006 M ZDDP (monomer), $CDCl_3$ insert spiked with PPh_3 to provide lock. Chemical shifts were referenced against PPh_3 in $CDCl_3$ (lit. -5.6 ppm[130]).

The solution-state spectroscopic data are supported in the solid-state by X-ray crystallographic studies, where only unreacted **^{i}Bu ZDDP** (dimeric form, Fig. 3.11) was isolated from a hexane solution of **^{i}Bu ZDDP** and 2-FPy (ratio 1:1 or 1:3) after recrystallisation (EtOH) (*cf.* identical crystals of complex **1** were obtained from hexane and EtOH solutions).

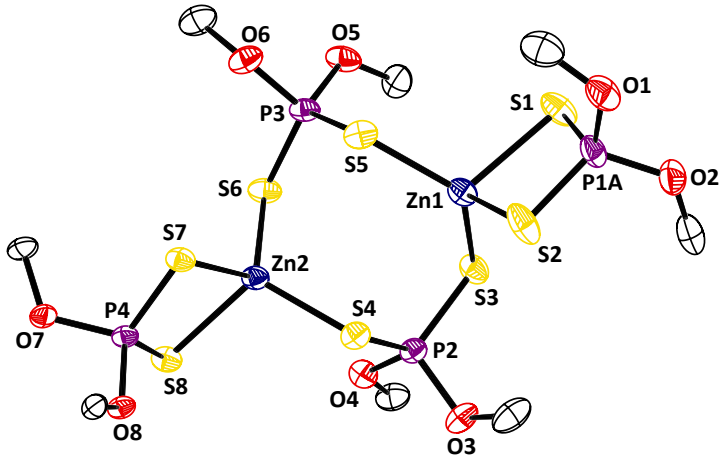

Figure 3.11: Molecular structure of **^{i}Bu ZDDP** (dimeric form) with thermal ellipsoids at the 50% probability level. Only the first carbon atom of the ^{i}Bu groups are shown and H atoms are omitted for clarity.

In contrast, single crystals of complex **5**, $[Zn\{\kappa^2\text{-}S,S\text{-}S_2P(O^iBu)_2\}_2(3\text{-FPy})]$, formed

upon slow evaporation of a hexane solution of **^{i}Bu ZDDP** and 3-FPy (ratio 1:3) (Fig. 3.12). Complex **5** once again adopts a trigonal bipyramidal geometry at zinc, but as expected has an elongated Zn-N bond length compared to that determined for **1** [2.034(2) *versus* 2.014(3) Å], based on the lower pK_{aH} of 3-FPy compared to Py.

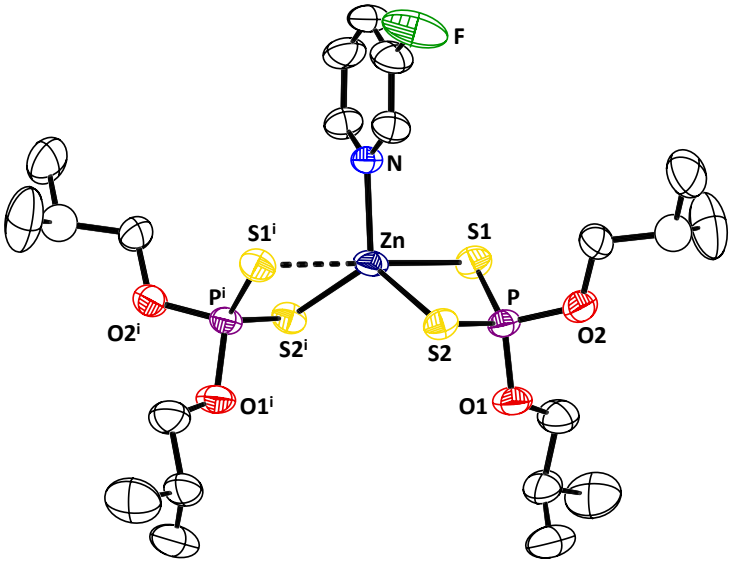

Figure 3.12: Molecular structure of [Zn{κ^2-*S,S*-$S_2P(O^iBu)_2$}$_2$(3-FPy)] (**5**) with thermal ellipsoids at the 50% probability level; H atoms are omitted for clarity. DTP ligands are related by a 2-fold rotation axis, however the zinc atom is disordered equally across two equivalent positions and does not lie on the 2-fold axis. The fluorine atom of 3-FPy is also disordered equally across two positions. Selected bond distances: Zn-N, 2.034(2) Å; Zn-S1, 2.525(3) Å, 2.896(3) Å; Zn-S2, 2.351(4), 2.285(4) Å; P-S1, 1.9770(9) Å; P-S2, 1.9957(9) Å. Selected bond angles: S-P-S, 113.55°; S-Zn-S, 78.82(10), 85.86(12)°.

For the most Lewis basic pyridine employed, 4-MeOPy, titration experiments with **^{i}Bu ZDDP** revealed that up to the addition of 1.5 equivalents of amine, similar increases in ^{31}P NMR chemical shift and resonance sharpening are observed to those discussed in detail above (Fig. 3.13). Addition of 4-MeOPy beyond 1.5 equivalents, however, led to the formation of a white precipitate. Subsequent analysis of the supernatant liquid by ^{31}P NMR spectroscopy showed that less than 10% of the phosphorus-containing species remained in solution and so, consequently, the association constant for 4-MeOPy could not be determined.

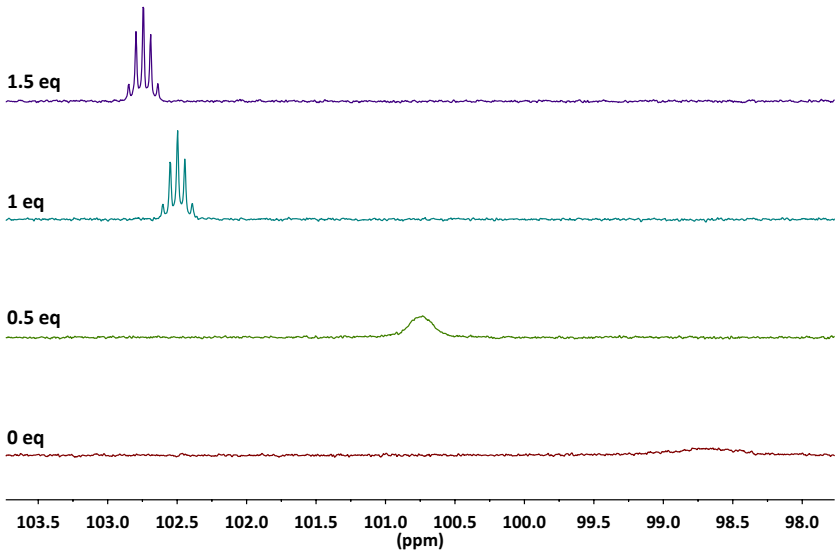

Figure 3.13: Evolution of the $^{31}P[^{1}H]$ NMR (162 MHz, hexane) spectrum of **^{i}Bu ZDDP** upon progressive addition of 4-MeOPy. 0.006 M ZDDP (monomer), $CDCl_3$ insert spiked with PPh_3 to provide lock. Chemical shifts were referenced against PPh_3 in $CDCl_3$ (lit. -5.6 ppm[130])

Single crystals suitable for X-ray crystallographic analysis, however, were grown *via* slow evaporation of a hexane solution of **^{i}Bu ZDDP** and 4-MeOPy when combined in a 1:1 ratio. The structure proved to be a mononuclear bis(4-MeOPy) complex of **^{i}Bu ZDDP**, $[Zn\{\kappa^1\text{-}S\text{-}S_2P(O^iBu)_2\}_2(4\text{-MeOPy})_2]$ (**6**), which is, to the best of our knowledge, the first isolated example of a mononuclear 1:2 ZDDP-amine complex (Fig. 3.14). Subsequent chemical and X-ray structural analysis of isolated complex **6** and the precipitate generated on addition of greater than 1.5 equivalents of 4-MeOPy are in excellent agreement and identified the two products to be identical (see Fig. 3.15).

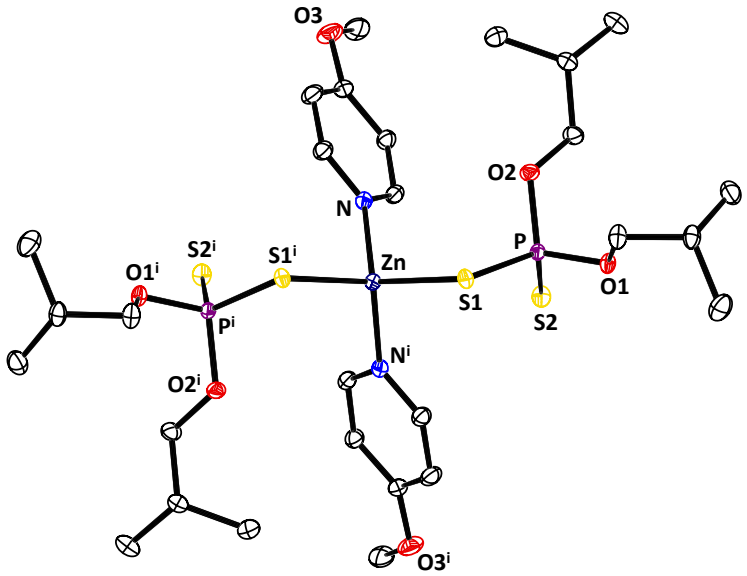

Figure 3.14: Molecular structure of [Zn{κ^1-*S*-$S_2P(O^iBu)_2$}$_2$(4-MeOPy)$_2$] (**6**) with thermal ellipsoids at the 50% probability level; H atoms are omitted for clarity. Selected bond distances: Zn-N, 2.0328(8) Å; Zn-S1, 2.3340(3) Å; P-S1, 2.0197(3) Å; P-S2, 1.9414(3) Å. Selected bond angles: S-P-S, 118.679(15)°.

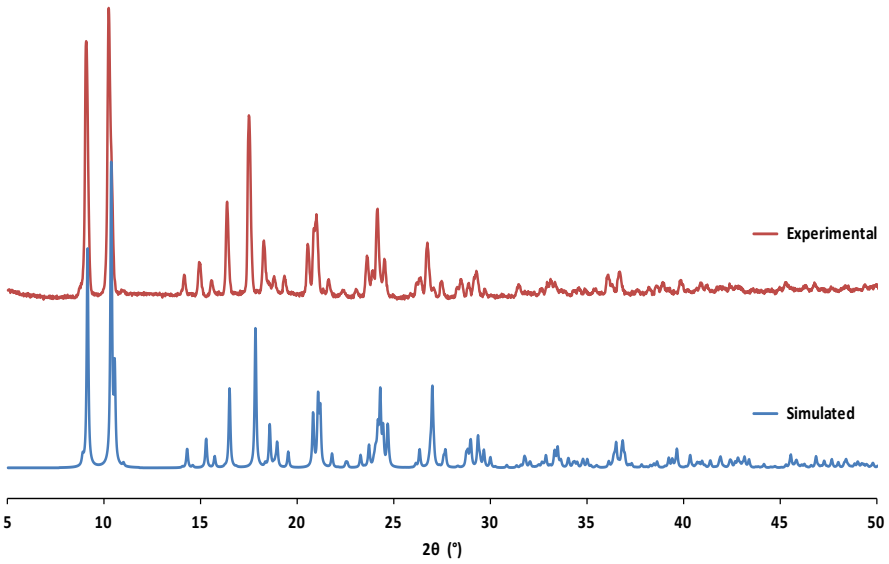

Figure 3.15: Experimental and simulated PXRD patterns obtained for complex **6**. The simulated PXRD pattern was produced using structural data from single-crystal X-ray crystallographic analysis with the aid of *Mercury* software.[143]

The structure of **6** contrasts with all the five-coordinate trigonal bipyramidal ZDDP-Py' complexes described previously in this work (**1-5**). Complex **6** contains a four-coordinate tetrahedral zinc centre resulting from the coordination of two 4-MeOPy ligands and two κ^1-*S*-DTP ligands. The adoption of this structure is attributed to the strongly Lewis basic

character of 4-MeOPy, which binds preferentially displacing the κ^2-*S,S* coordination of the DTP ligands. Monodentate DTP binding is clearly evidenced by the difference in Zn-S bond distances [Zn-S1 2.3340(3) Å, Zn-S2 3.7545(4) Å] and mirrored by the P-S bond lengths [P-S1 2.0197(3) Å, P-S2 1.9414(3) Å]. This mode of coordination is accompanied by a significant widening of the S-P-S bond angle [118.679(15)°] compared to a value of approximately 112° found for the chelating (anisobidentate) DTP ligands of the mono(Py') complexes **1-5** described above.

3.2.4 Thermal Behaviour of ZDDP-Py' Complexes

ZDDPs degrade *in situ*, under standard engine operating conditions (high T), to form protective antiwear tribofilms – a process attributed to a combination of thermal and mechanochemical drivers. Indeed, it has long been recognised that the thermal stability of ZDDPs is inversely related to antiwear effectiveness. This relationship is rationalised based on more efficient degradation and faster formation of a protective tribofilm (see Section 1.2.2.8.2).[144] It is therefore of significant interest to investigate the impact of the previously observed ZDDP-Py' complex formation on the thermal behaviour of ZDDP-amine systems.

Here, a study of the thermal behaviour of (RT-500 °C) of representative 1:1, 1:2 and pyridine-free complexes [Zn{κ^2-*S,S*-$S_2P(O^iBu)_2$}$_2$(Py)] (**1**), [Zn{κ^1-*S*-$S_2P(O^iBu)_2$}$_2$(4-MeOPy)$_2$] (**6**) and **^{i}Bu ZDDP** were performed by TGA-MS. Relative intensities associated with diagnostic *m/z* ratios of known (volatile) degradation products of ZDDPs were examined, specifically H_2S (*m/z* = 34) and C_4 olefins (*m/z* = 56),[54] as well as those of pyridine (*m/z* = 79) or 4-MeOPy (*m/z* = 109) where appropriate. Olefins are a primary degradation product of alkyl ZDDPs and are suggested to form through a concerted β-hydrogen transfer elimination mechanism (Section 1.2.2.8.2, Scheme 1.4).[56] The phosphorus-containing degradation product can further decompose by loss of more olefin and/or various sulfur-containing species, including hydrogen sulfide.[†]

[†]ZDDPs are known to undergo thermal degradation *via* a combination of two mechanisms, namely, sequential alkyl transfer and the olefin elimination pathway described briefly above. For a branched primary alkyl ZDDP, such as **^{i}Bu ZDDP** used in this work, both mechanisms are expected to contribute significantly to the thermal degradation (see Section 1.2.2.8.2).

The TGA, corresponding DTG curve, and MS responses of selected *m/z* ratios arising from thermolysis of **^{i}Bu ZDDP** are shown in Figure 3.16. These data show that **^{i}Bu ZDDP** degrades around 250 °C through a single well-defined mass loss event associated with the degradation of DTP ligands with the evolution of C_4 olefins (*m/z* = 56) and H_2S (*m/z* = 34). This is consistent with reports regarding the degradation of branched primary alkyl ZDDPs, with the slightly delayed onset of H_2S formation to higher temperature being expected, as it is known to be a later stage decomposition product compared to olefin formation, which is a primary degradation pathway.[36] The black residue remaining following thermal decomposition is ascribed to polymeric zinc (thio)phosphate {this assignment was confirmed by solid-state ^{31}P NMR spectroscopy (data not presented) and elemental analysis (*vide infra*)}.

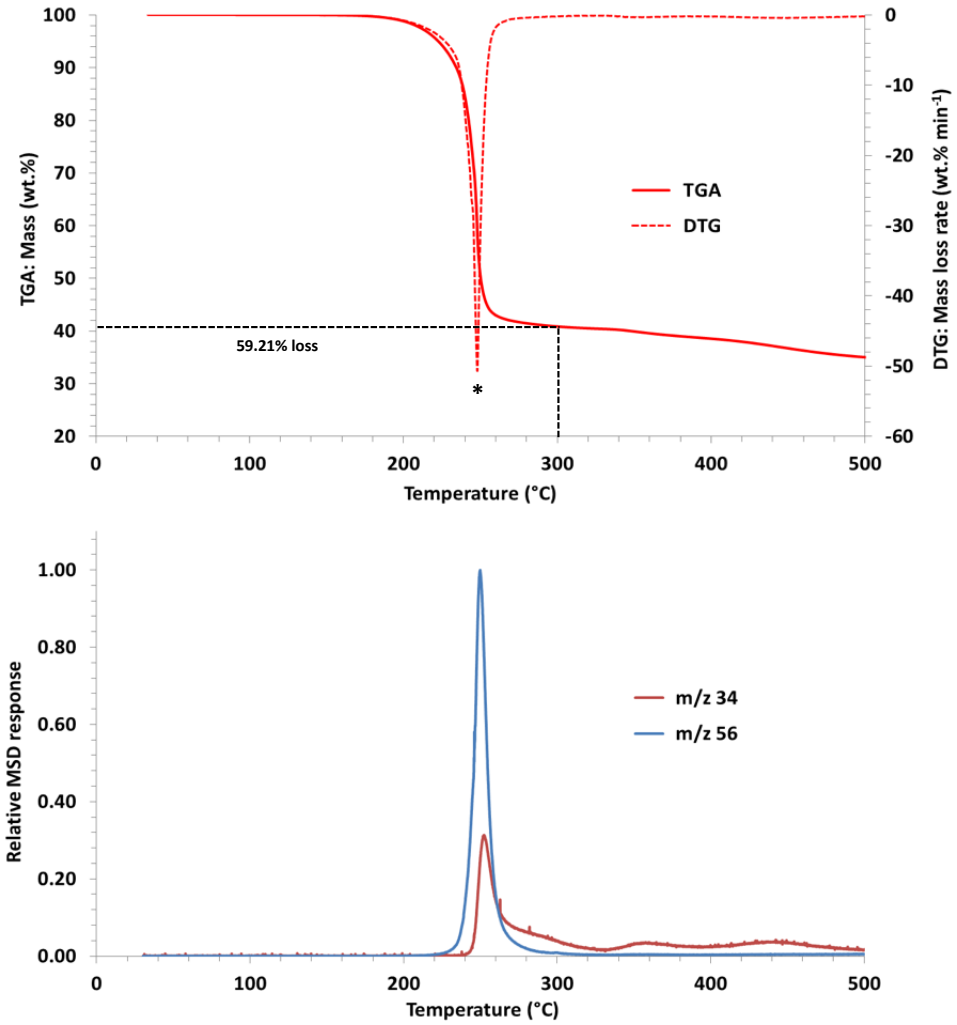

Figure 3.16: TGA and DTG thermograms for the degradation of **^{i}Bu ZDDP**, top, and the associated MS data, bottom. Significant mass loss events are marked with an asterisk.

In contrast, the thermal degradation of the related pyridine complex **1**, occurs *via* a two-stage process (Fig. 3.17). The first component of the thermolysis pathway occurs over the temperature range of 80-220 °C and accounts for a mass loss of 12.41%.

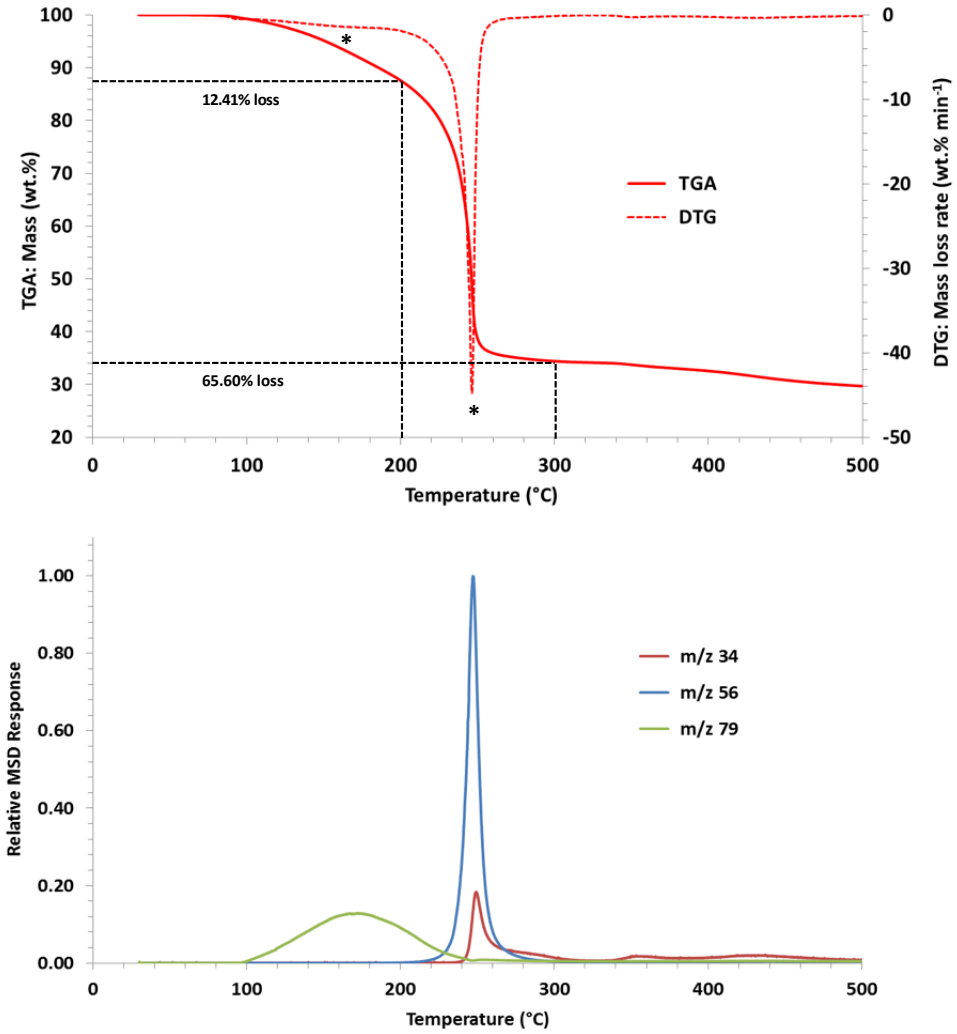

Figure 3.17: TGA and DTG thermograms for the degradation of [Zn{κ^2-*S,S*-$S_2P(O^iBu)_2$}$_2$(Py)] (**1**), top, and the associated MS data, bottom. Significant mass loss events are marked with an asterisk.

This primary mass loss event is then followed by a second much narrower event profile centred at ~250 °C. The MS data clearly identify the first event as liberation of coordinated pyridine (m/z = 79), producing **^{i}Bu ZDDP**, which undergoes thermal degradation in a manner exactly analogous to that of the parent **^{i}Bu ZDDP** (Fig. 3.16). The observed mass loss (RT-200 °C) of 12.41% is consistent with liberation of all coordinated Py ligands (calculated: 12.61%) providing additional support for the proposed degradation pathway. This discrete two-stage process is further confirmed through TGA-MS ex-

periments performed with a slower heating rate, whereby separation of thermal events becomes more distinct (Fig. 3.18).

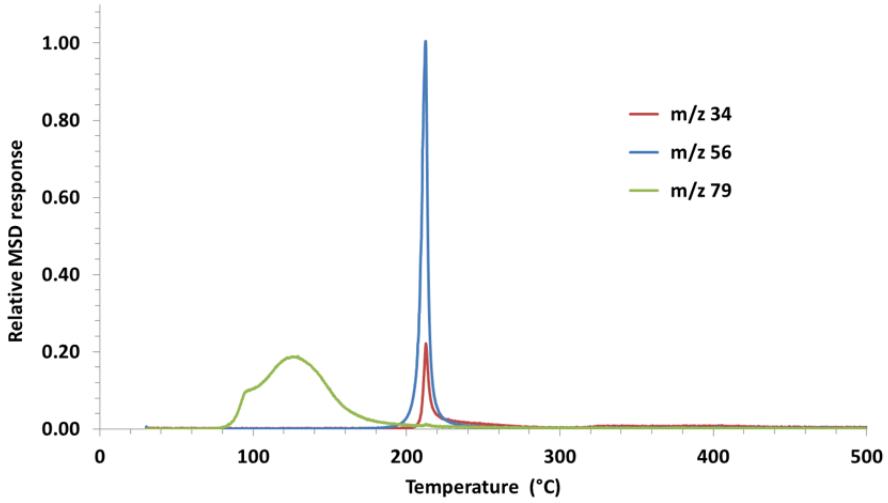

Figure 3.18: Associated MS data for the degradation of [Zn{κ^2-*S*,*S*-$S_2P(O^iBu)_2$}$_2$(Py)] (**1**) at a slower heating rate of 1 °C min^{-1}.

The thermal behaviour of [Zn{κ^1-*S*-$S_2P(O^iBu)_2$}$_2$(4-MeOPy)$_2$] (**6**) was also investigated by TGA-MS (Fig. 3.19). In contrast to the behaviour of the five-coordinate Py complex **1**, the associated MS data for **6** did not prove as diagnostic, with 4-MeOPy not being detected across the full temperature range studied (RT-500 °C). However, independent tests attribute this to a limitation of the TGA-MS system used, in which the heated transfer line linking the TGA and MS modules cannot be heated sufficiently to enable passage of the poorly volatile 4-MeOPy (b.p. 193 °C[138]). Despite this, the TGA/DTG data arising from the thermolysis of complex **6** offers some insight. The initial mass loss event spanning the window 75-160 °C (13.89% loss in mass), is consistent with the liberation of one 4-MeOPy ligand (calculated: 14.24%) from the bis(4-MeOPy) complex **6**. This mirrors what is observed by atmospheric solids analysis probe mass spectrometry (ASAP-MS),[145] where even under a range of different conditions only the mono(4-MeOPy) molecular ion (*m/z* 656.1 [MH–(4-MeOPy)]$^+$) was observed upon mass spectrometric analysis of complex **6**.

The origin of the second broader mass event during thermolysis of **6** is less obvious. However, from the MS data, it can be seen that the temperature ranges over which formation of C_4 olefins and H_2S are liberated are the same as those arising from the

degradation of **^{i}Bu ZDDP** alone. Based on this observation, the broadened mass loss event (160-270 °C) can be explained by the slow loss of the second 4-MeOPy, an event that then overlaps with the degradation of the DTP ligands of **^{i}Bu ZDDP** or the monoadduct [Zn{κ^1-*S*-$S_2P(O^iBu)_2$}$_2$(4-MeOPy)]. These data are consistent with the greater Lewis basicity of 4-MeOPy compared with that of Py (Table 3.2), which renders the methoxy-substituted derivative less labile.

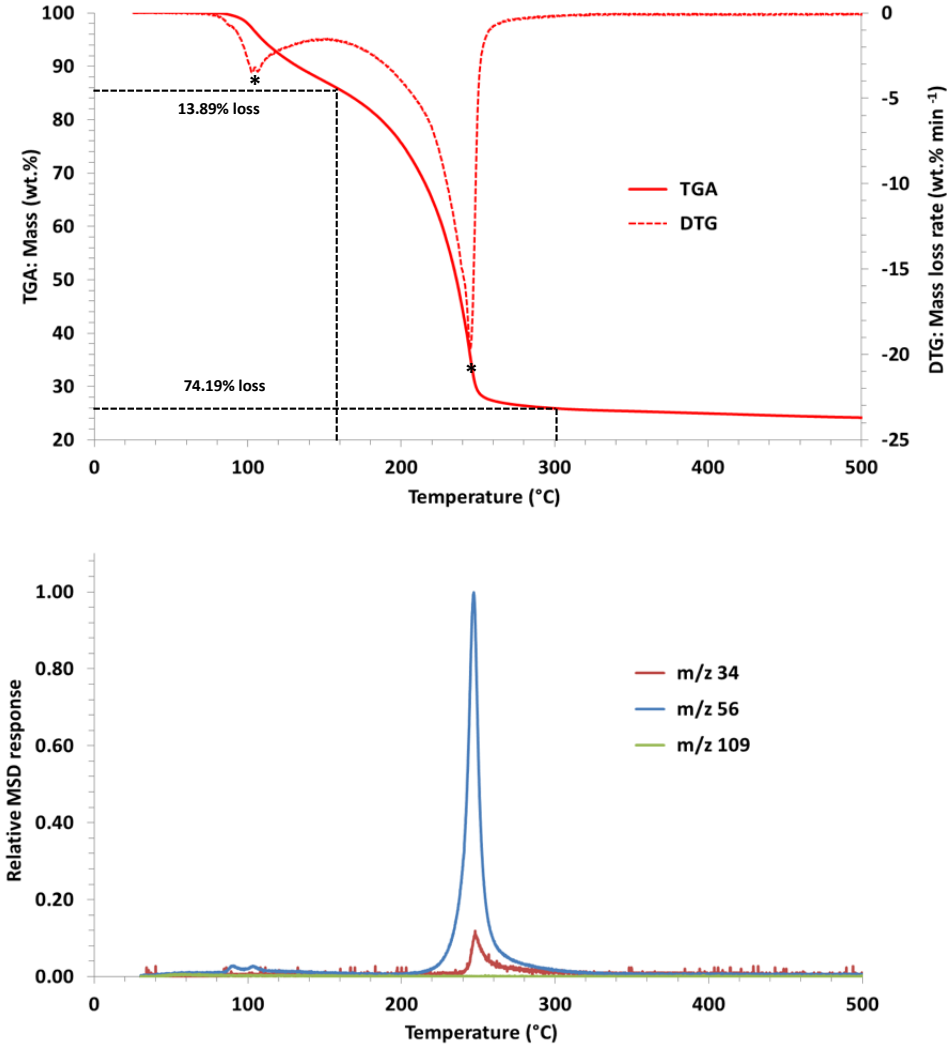

Figure 3.19: TGA and DTG thermograms for the degradation of [Zn{κ^1-*S*-$S_2P(O^iBu)_2$}$_2$(4-MeOPy)$_2$] (**6**), top, and the associated MS data, bottom. Significant mass loss events are marked with an asterisk.

Subsequently, the residual non-volatile decomposition residues remaining post TGA-MS studies were investigated further by elemental analysis (Table 3.3), as it is these residues that are likely to be closely related to the target ZDDP-derived antiwear films. From

these analytical data, it is evident that the residue from thermolysis of the bis(4-MeOPy) complex **6** is significantly more sulfur-rich (11.33 wt.% S) than the residues obtained from the decomposition of **^{i}Bu ZDDP** and the mono(Py) complex **1** (8.09 and 8.68 wt.% S, respectively). These observations are consistent with less H_2S (relative to C_4 olefin, *m/z* = 56) being produced in the thermolysis of **6** (Fig. 3.19). Furthermore, the decomposition residue was determined to possess a significant nitrogen content, which most likely indicates that some 4-MeOPy remains bound to zinc during the thermal decomposition process, giving rise to the formation of 4-MeOPy complexes of the resulting polymeric zinc (thio)phosphate species. The formation of such zinc/nitrogen-containing species from the thermolysis of ZDDP-amine complexes has been reported previously, but only for multidentate amines under milder thermolytic conditions.[146] Finally, the elemental analysis data for the residue following thermolysis of complex **1** were in reasonable agreement with those found for **^{i}Bu ZDDP** and thus supports the two-stage decomposition proposed from TGA-MS data, though carbon contents appear slightly reduced, which may suggest olefin formation is promoted somewhat.

Table 3.3: Elemental composition of the ultimate thermal degradations residue products from TGA-MS studies (RT-500 °C, 10 °C min^{-1}, helium flow (30 ml min^{-1})).

Complex	%C	%H	%N	%S	%P	%Zn
^{i}Bu ZDDP	8.12	1.04	0.00	8.09	18.98	25.62
1	5.72	1.47	0.00	8.68	18.28	27.40
6	7.42	0.96	1.35	11.33	16.96	30.04

As a whole, thermal analysis studies have revealed that complexation of a pyridine base forming mono(Py) ZDDP complexes such as **1**, has little to no effect on the ultimate non-volatile residue products. This is justified based on the two-stage decomposition pathway proposed following TGA-MS studies. In contrast, for the bis(4-MeOPy) complex **6**, the resulting decomposition residue proved to be more sulfur-rich and likely contains residual, bound 4-MeOPy. An explanation for this is that the less labile, methoxy-substituted pyridine disfavours H_2S formation, resulting in a more sulfur-rich decomposition residue that also contains residual nitrogen.

3.2.5 Identifying DTP Binding Modes Using Raman Spectroscopy

Since DTP ligands can coordinate to metals in a variety of different binding modes that significantly impact upon the reactivity of the complex (Fig. 3.1), attempts have been made to probe the nature of the metal-DTP interaction using IR and ^{31}P NMR spectroscopies, for systems where suitable crystal data are not available.[122,124,125,147] However, IR spectroscopy has proved of little use in this regard since although some variations in key vibrations are observed, attempts to correlate these changes with structural differences has been relatively unsuccessful, leading some to conclude that IR is not a suitable diagnostic tool for determining the nature of DTP binding.[122,125,131,148]

In contrast, ^{31}P NMR spectroscopy has proved much more diagnostic, with early correlations by Glidewell showing that the chemical shift of phosphorus in DTP ligands is sensitive to ligand binding mode,[147] despite some doubts regarding the universal applicability of the generalisations made.[149] This work has been extended to ZDDPs and ZDDP-amine adducts more specifically, in order to develop a method to readily detect DTP binding modes for such systems.[42,124,126] Indeed, Drew *et al.* have shown that for a series of nitrogen base adducts of ZDDPs there is a strong correlation between the solution-state ^{31}P NMR chemical shift and DTP binding mode.[124] Subsequently, Harrison and Kikabhai have established that amine-induced changes in ^{31}P NMR chemical shift in solution arise from a variation in the S-P-S bond angle, a parameter that correlates well with DTP binding mode. Ultimately, widening of the S-P-S angle gave rise to high frequency shifts in the ^{31}P NMR spectrum.[42] Further to this, using a combination of ^{31}P MAS-NMR and X-ray crystallography, Harrison and Sebald have established typical ^{31}P NMR chemical shift values for the various DTP binding modes displayed in ZDDP-amine complexes (Table 3.4).[126]

However, although quite useful generalisations, as noted by the authors themselves, exceptions to the correlations made are only too apparent. Indeed, the DTP binding mode of $[Zn\{\kappa^1\text{-}S\text{-}S_2P(O^iBu)_2\}_2(4\text{-MeOPy})_2]$ (**6**) would be wrongly assigned as symmetrically or, at best, anisobidentate chelating based on either solid- or solution-state ^{31}P NMR chemical shift data (δ 100.0 or 101.7 (0.05 M, $CDCl_3$), respectively). However,

the crystallographically-determined structure of **6** clearly confirms both DTP ligands to be equivalent and bound in a monodentate κ^1-*S* fashion (Fig. 3.14). Consequently, we have sought to establish an alternative complementary spectroscopic technique in order to unambiguously assign DTP binding modes, something we have achieved using Raman spectroscopy.

Table 3.4: Correlations between ^{31}P NMR chemical shift and DTP binding modes.[126]

^{31}P Chemical Shift (ppm)	**Binding Mode**	**Chemical Representation**
$\delta(^{31}P) < 100$	Symmetrically Chelating or Bridging	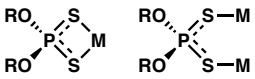
$100 \leq \delta(^{31}P) \leq 105$	Anisobidentate Chelating	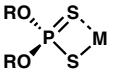
$\delta(^{31}P) \sim 106$	Monodentate	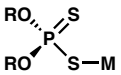
$\delta(^{31}P) > 110$	Ionic	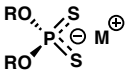

By comparing the IR and Raman vibrations of the PS_2 moiety of ZDDPs with other DTP-containing species, Paddy concluded that the absence of a strong vibration around 660 cm^{-1} ($\nu(PS_2)_{asym}$) in the Raman spectrum of ZDDPs indicated symmetrical DTP binding (chelating or bridging).[150] This is justified as the similarly positioned ν(P=S) vibration expected for a monodentate DTP ligand would have a strong Raman intensity. Based on this report, the utility of Raman spectroscopy as a diagnostic tool in determining DTP binding mode was explored for the ZDDP-amine adducts studied in this work, where the absence (or presence) of a Raman vibration near 660 cm^{-1} was investigated as an indicator of binding mode. To confirm the applicability of this method the Raman spectra of **^{i}Bu ZDDP** and the isolated complex **6** were initially investigated (Fig. 3.20).

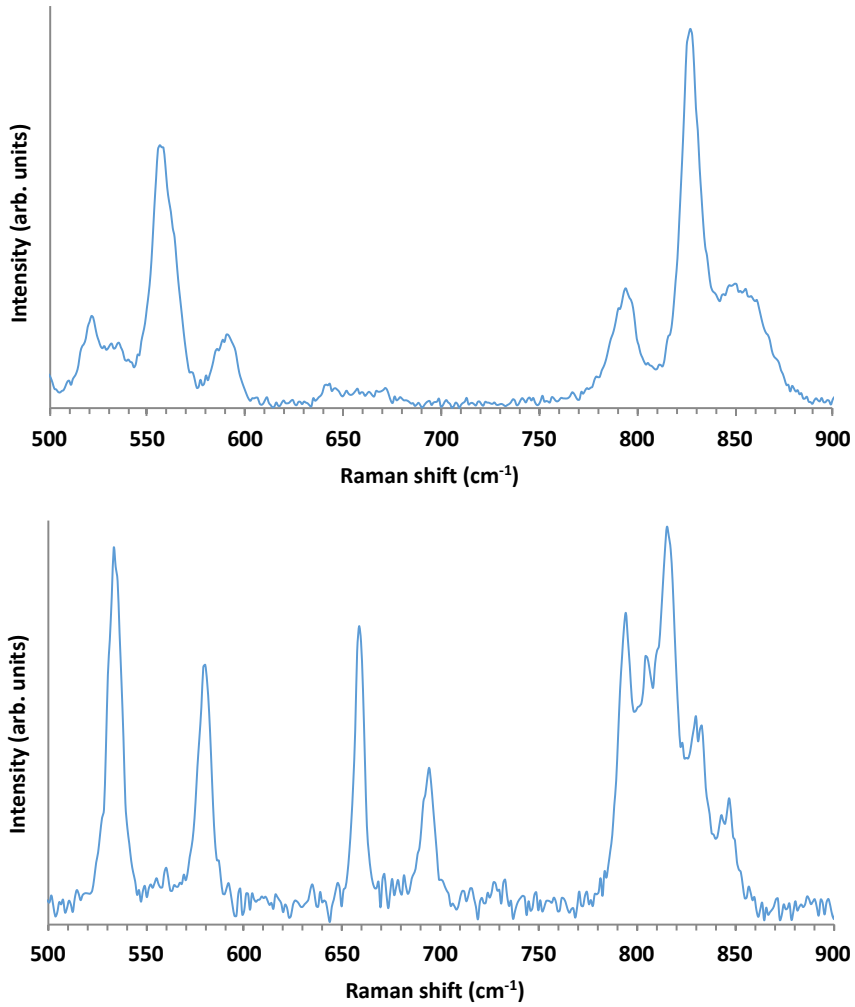

Figure 3.20: Solid-state Raman spectra (500-900 cm^{-1}) of **^{i}Bu ZDDP**, top, and $[Zn\{\kappa^1\text{-}S\text{-}S_2P(O^iBu)_2\}_2(4\text{-}MeOPy)_2]$ (**6**), bottom.

Focussing only on the region associated with PS_2 vibrations, it is apparent that for **^{i}Bu ZDDP** no Raman band is observed near 660 cm^{-1}, thus suggesting symmetrical DTP binding. This is in agreement with the known molecular structure of **^{i}Bu ZDDP**, which possesses symmetrically chelating and bridging DTP ligands as depicted in Figure 3.11, as previously reported by Woollins and co-workers.[41] In contrast, the Raman spectrum of complex **6** presents a strong band at 660 cm^{-1}, which has been attributed to ν(P=S), something therefore indicative of a monodentate mode of DTP binding. This is an important result as in the absence of crystal data, the DTP binding mode of this complex would be wrongly assigned using ^{31}P NMR chemical shift correlations alone.

In the intermediate case, where the DTP ligand binding mode lies somewhere between

symmetrical κ^2-*S,S* and κ^1-*S* binding modes (*i.e.* anisobidentate binding modes), the relative intensity of the $\nu(PS_2)_{asym}/\nu(P{=}S)$ is expected to lie somewhere between that observed for monodentate and symmetrically-bound κ^2-*S,S* DTP ligands, increasing as the difference in P-S bond lengths becomes larger and the two bonds progressively move closer to assuming P-S and P=S character. This expectation is consistent with the observed Raman spectrum of the complex [Zn{κ^2-*S,S*-$S_2P(O^iBu)_2$}$_2$(Py)] (**1**) (Fig. 3.21), where the DTP ligands are known to be anisobidentate (Fig. 3.3).

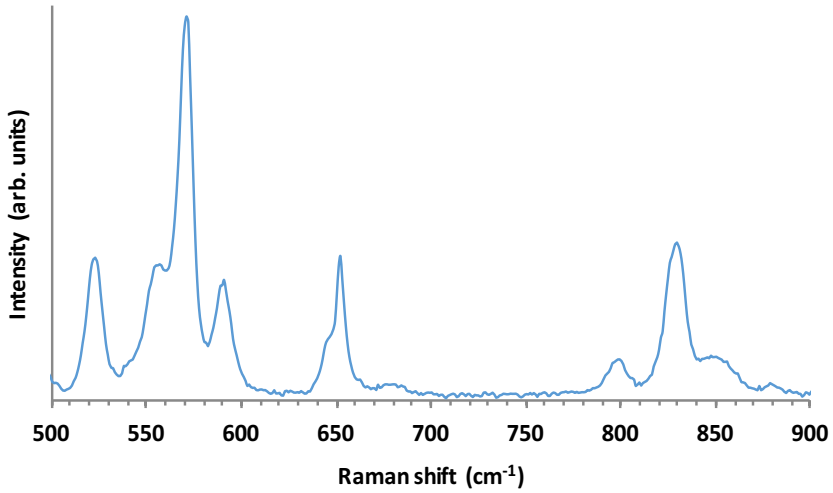

Figure 3.21: Solid-state Raman spectrum (500-900 cm^{-1}) of [Zn{κ^2-*S,S*-$S_2P(O^iBu)_2$}$_2$(Py)] (**1**).

Although currently this Raman spectroscopic analysis is qualitative, there is potential scope to develop it into a quantitative analysis by correlating the relative intensity of the 660 cm^{-1} Raman vibration to the DTP binding mode for compounds of known structure, akin to that previously performed using ^{31}P NMR spectroscopy. Finally, it should be noted that IR spectroscopy is not diagnostic for any of the complexes investigated in this work, with a relatively strong IR stretch near 660 cm^{-1} apparent for the symmetrical, anisobidentate and monodentate configurations of **^{i}Bu ZDDP**, and complexes **1** and **6**, respectively.

3.3 Conclusions

The use of ^{31}P NMR spectroscopic titration studies has shown that the propensity of ZDDP adduct formation with pyridine ligands is strongly dependent on the nature of

the Lewis bases employed. This has been quantified through the estimation of association constants in solution and subsequently correlated to steric ($\%V_{bur}$) and electronic (pK_{aH}) parameters for the various nitrogenous bases. Pyridine, 3-FPy and various 2-alkyl pyridine ligands form mononuclear adducts with **^{i}Bu ZDDP**; they possess a trigonal bipyramidal structure with DTP ligands bound in an anisobidentate chelating fashion. Contrastingly, the more electron-rich 4-MeOPy forms a mononuclear di-adduct, which displays a distorted tetrahedral structure, with DTP ligands bound in the far less commonly reported, monodentate κ^1-*S*-$S_2P(O^iBu)_2$ fashion.

TGA-MS studies have demonstrated that the thermal degradation of mono(pyridine) adducts, such as complex **1**, occurs *via* initial liberation of coordinated pyridine to yield 'free' **^{i}Bu ZDDP**. This amine-free ZDDP subsequently breakdowns further to produce C_4 olefins and H_2S and occurs at the same temperature to that found for pure **^{i}Bu ZDDP**. The thermal degradation pathway of the di-adduct **6** is slightly more complex. However, it also appears to involve initial liberation of one pyridine ligand, while the second broader mass loss observed can be rationalised as slow displacement of the second 4-MeOPy ligand, a process that takes place at a temperature at which the degradation of the DTP ligands on either 'free' or 'complexed' **^{i}Bu ZDDP** also occurs. Elemental analysis on the ultimate degradation residues post TGA-MS studies shows that for complex **6** the ultimate decomposition products are more sulfur-rich and also contain a significant amount of nitrogen, most likely arising from the presence of residual 4-MeOPy bound to zinc, which appears to suppress H_2S formation.

Finally, the ability of Raman spectroscopy to function as a diagnostic tool for assigning DTP binding modes has been highlighted. Further work will seek to correlate the relative intensity of $\nu(PS_2)_{asym}/\nu(P{=}S)$ vibrations with DTP binding mode, in order to develop quantitative guidelines to aid in diagnosing DTP binding mode for complexes of unknown structure.

Together, this study highlights how components of lubricant additive packages containing Lewis basic nitrogen centres could cause unexpected performance alterations as a result of complexation with the key ZDDP component, which degrades to form the es-

sential anti-wear film. An understanding of how to modulate or control these interactions is desirable since this would allow for the future selection or design of optimal additive combinations – either preventing coordination or using zinc-amine binding to control ZDDP degradation.

3.4 Experimental

3.4.1 General Considerations

Chemicals and Solvents: Air/moisture sensitive manipulations were performed under an atmosphere of dry nitrogen using standard Schlenk line techniques with oven dried glassware. Dry solvents were obtained from an Innovative Technologies SPS facility and degassed prior to use by freeze-pump-thaw cycles. **^{i}Bu ZDDP** was synthesised using literature procedures and its purity verified by NMR spectroscopy (^{1}H and ^{31}P) and elemental analysis.[151] All other chemicals were purchased and used as received from commercial suppliers, unless otherwise stated.

NMR Spectroscopy: Solution-phase NMR spectra were collected on a Varian Mercury 400, Varian Inova 500, Varian VNMRS-700, Bruker Advance 400 or a Varian VNMRS-600 spectrometer at room temperature unless otherwise stated. All chemical shifts were referenced relative to residual solvent resonances (^{1}H, ^{13}C) or to external aqueous 85% H_3PO_4 (^{31}P). ^{1}H and ^{13}C NMR spectra were assigned with the aid of 2D COSY, HMBC and HSQC spectroscopic experiments. Solid-state ^{31}P NMR spectra were collected on a Varian VNMRS spectrometer room temperature and referenced to H_3PO_4.

Mass Spectrometry: ASAP mass spectra were collected using a LCT Premier XE (Waters Ltd, UK) while accurate mass measurements (ESI) were collected using a QToF Premier (Waters Ltd, UK) mass spectrometer. In most cases, softer ionisation conditions (typical modified conditions: temperature = 150 °C, cone voltage = 10 V) were necessary to observe the desired molecular ions of ZDDP-Py' complexes by ASAP-MS.

TGA-MS: Thermogravimetric Analysis-Mass Spectrometry (TGA-MS) experiments were

performed on a Perkin Elmer Pyris 1 TGA employing ceramic pans and a heating rate of 10 °C min^{-1}. The sample gas flow was helium (CP grade, BOC) at 30 mL min-1. Evolved sample gases were transferred directly to a Hiden HPR20 QIC mass spectrometer (which operates through an electron ionisation source at 70 eV and a quadrupole mass filter) via a ceramic-lined heated transfer line. The MS detector was configured for Selective Ion Monitoring (SIM) of certain diagnostic m/z ratios as required.

Raman Spectroscopy: Raman spectra were recorded using a Horiba Jobin-Yvon Lab-RAM HR spectrometer equipped with a 633 nm HeNe laser. Collected spectra were baseline corrected using an adaptive baseline correction in Spekwin32.[152]

PXRD: X-ray powder diffraction (PXRD) analysis was performed on a Bruker D8 Advance diffractometer utilising Cu Kα radiation (λ = 1.5406 Å) at scattering angles (2θ) from 5° to 50° with a step size of 0.02°.

Elemental Analysis: C, H and N contents were determined by combustion (Exeter Analytical CE440). Sulfur contents were also determined by combustion and performed by MEDAC Ltd. Phosphorus and zinc contents were determined (after dissolution in hot HNO_3) by inductively coupled plasma optical emission spectrometry (ICP-OES, Thermo Scientific iCAP 6000 Series).

DFT Calculations: The structure of 2-^{t}BuPy was geometry optimised by DFT at the B3LYP/6-31G(d) level of theory using Gaussian09 software.[153] No imaginary frequencies were found from frequency calculations on the optimised geometry and indicate the obtained geometry is a true minimum. The optimised geometry was then used to determine a value of percentage buried volume ($\%V_{bur}$).

3.4.2 Synthesis of 2-Alkyl Pyridine Ligands

2-^{i}PrPy and 2-^{t}BuPy were synthesised using the methods of Pasquinet *et al.* with slight modifications.[154]

Preparation of 2-isopropylpyridine (2-^{i}PrPy)

A stirred solution of 2-ethylpyridine (5.62 g, 52.4 mmol) in dry, degassed THF (35 cm^3) was cooled to -30 °C in a dried, nitrogen-flushed three-necked round bottom flask. *n*-BuLi (22 cm^3, 55.0 mmol) was added dropwise over a period of 30 minutes, with the temperature being maintained between -30 °C and -20 °C, to give a deep red solution. The solution was then allowed to stir for a further 1 hour before cooling to -50 °C. Methyl iodide (8.18 g, 57.6 mmol) in dry, degassed THF (10 cm^3) was then added slowly between -50 °C and -40 °C to give an orange solution. After stirring for a further 30 minutes at -40 °C and subsequent hydrolysis (25 cm^3 of water), the reaction mixture was made acidic with 6 cm^3 of conc. HCl and extracted with ether (50 cm^3). The aqueous layer was treated with solid K_2CO_3 (pH 8) and extracted with DCM (3×40 cm^3). After drying ($MgSO_4$) and filtration, the volatile components were removed *in vacuo* at room temperature. Twice distillation (155-157 °C / 760 mmHg) gave the title compound as a pale yellow liquid (3.21 g, 51% yield).

^{1}H NMR (700 MHz, Chloroform-*d*) δ 8.52 (d, J = 4.8 Hz, 1H, 6-Py C*H*), 7.58 (td, J = 7.7, 1.9 Hz, 1H, 4-Py C*H*), 7.15 (d, J = 7.7 Hz, 1H, 3-Py C*H*), 7.07 (ddd, J = 7.7, 4.8, 1.2 Hz, 1H, 5-Py C*H*), 3.05 (hept, $^{3}J_{HH}$ = 6.9 Hz, 1H, 2-Py C*H*$(CH_3)_2$), 1.29 (d, $^{3}J_{HH}$ = 6.9 Hz, 6H, 2-Py CH(C*H*$_3)_2$).

^{13}C NMR (176 MHz, Chloroform-*d*) δ 167.4 (2-Py *C*), 149.2 (6-Pyr *C*H), 136.5 (4-Py *C*H), 121.1 (5-Py *C*H), 120.7 (3-Py *C*H), 36.5 (2-Py *C*H$(CH_3)_2$), 22.7 (2-Py CH(*C*H$_3)_2$).

HRMS (ESI) *m/z* Calc. for $[M+H]^+$ $C_8H_{12}N$ 122.0970; Found 122.0954.

Preparation of 2-*tert*-butylpyridine (2-^{t}BuPy)

A stirred solution of potassium *tert*-butoxide (0.70 g, 6.2 mmol) and diisopropylamine (0.63 g, 6.2 mmol) in dry, degassed THF (10 cm^3) was cooled to -70 °C in a dry, nitrogen-flushed two-necked round bottom flask. *n*-BuLi (2.8 cm^3, 6.2 mmol) was then added slowly, before warming to -50 °C over 15 minutes and addition of 2-isopropylpyridine (0.50 g, 4.1 mmol) to give a deep red solution. The solution was then stirred for a further 30 minutes and cooled to -75 °C. Methyl iodide (1.8 g, 12.4 mmol) in dry, degassed THF (3 cm^3) was slowly added and allowed to react for a further 2 hours at -75 °C. After

hydrolysis (10 cm^3 of water), DCM extraction (3 × 15 cm^3) and drying ($MgSO_4$), the volatile components were removed *in vacuo* at room temperature. The crude product was purified by column chromatography on silica gel using hexane/ethyl acetate (99:1) as the eluent to yield the title compound as a colourless liquid (0.34 g, 61% yield).

^{1}H NMR (600 MHz, Chloroform-*d*) δ 8.56 (d, J = 4.9 Hz, 1H, 6-Py C*H*), 7.59 (td, J = 7.8, 2.0 Hz, 1H, 4-Py C*H*), 7.33 (d, J = 7.8 Hz, 1H, 3-Py C*H*), 7.07 (ddt, J = 7.8, 4.9, 0.8 Hz, 1H, 5-Py C*H*), 1.37 (s, 9H, 2-Py C(CH_3)$_3$).

^{13}C NMR (151 MHz, Chloroform-*d*) δ 169.4 (2-Py *C*), 148.7 (6-Py *C*H), 136.3 (4-Py *C*H), 120.7 (5-Py *C*H), 119.2 (3-Py *C*H), 77.2 (2-Py *C*(CH_3)$_3$), 30.3 (2-Py C(*C*H_3)$_3$).

HRMS (ESI) *m/z* Calc. for $[M+H]^+$ $C_9H_{14}N$ 136.1126; Found 136.1116.

3.4.3 Synthesis of 1:1 ZDDP-Py' Complexes

General Procedure

ZDDP-pyridine complexes were obtained by adding either a stoichiometric amount or excess pyridine-based ligand (ratio 3:1) to a solution of **^{i}Bu ZDDP** (0.15 g, 0.27 mmol) in hexane or ethanol (10 cm^3). After stirring for 30 minutes and allowing the mixture to stand at room temperature, colourless, crystalline complexes formed over the period of hours to days. The resulting crystalline materials were isolated by filtration, washed with hexane and dried in air.

[Zn{κ^2-*S,S*-$S_2P(O^iBu)_2$}$_2$(Py)] (1)

^{1}H NMR (400 MHz, Chloroform-*d*) δ 9.05 – 9.02 (m, 2H, 2,6-Py C*H*), 7.99 (tt, J = 7.7, 1.7 Hz, 1H, 4-Py C*H*), 7.61 – 7.54 (m, 2H, 3,5-Py C*H*), 3.88 (dd, $^3J_{PH}$ = 8.3 Hz, $^3J_{HH}$ = 6.7 Hz, 8H, OCH_2CH(CH_3)$_2$), 2.00 (nonet, $^3J_{HH}$ = 6.7 Hz, 4H, OCH_2C*H*(CH_3)$_2$), 0.95 (d, $^3J_{HH}$ = 6.7 Hz, 24H, OCH_2CH(CH_3)$_2$).

^{31}P{^{1}H} NMR (162 MHz, Chloroform-*d*) δ 100.6 (s).

^{31}P{^{1}H} SSNMR (162 MHz) δ 101.8 (s).

^{13}C{^{1}H} NMR (151 MHz, Chloroform-*d*) δ 149.3 (2,6-Py *C*H), 139.9 (4-Py *C*H), 125.3

(3,5-Py *C*H), 73.8 (d, $^{2}J_{CP}$ = 7.6 Hz, O*C*H_2CH(CH_3)$_2$), 29.0 (d, $^{3}J_{CP}$ = 8.6 Hz, OCH_2*C*H(CH_3)$_2$), 19.1 (OCH_2CH(*C*H_3)$_2$).

MS (ASAP) *m/z* 626.1 (100%, $[M+H]^+$), 547.0 (32%, $[M\text{-}Py+H]^+$), 384.0 (4%, $[M\text{-}(DTP)^-]^+$).

(Calc.: C, 40.22; H, 6.59; N, 2.23. Found: C, 40.05; H, 6.54; N, 2.13).

[Zn{κ^2-*S,S*-$S_2P(O^iBu)_2$}$_2$(2-MePy)] (2)

^{1}H NMR (400 MHz, Chloroform-*d*) δ 8.93 (ddd, *J* = 5.4, 1.8, 1.1 Hz, 1H, 6-Py C*H*), 7.81 (td, *J* = 7.7, 1.8 Hz, 1H, 4-Py C*H*), 7.41 – 7.29 (m, 2H, 3,5-Py C*H*), 3.83 (dd, $^{3}J_{PH}$ = 8.4 Hz, $^{3}J_{HH}$ = 6.7 Hz, 8H, OC*H*$_2$CH(CH_3)$_2$), 2.90 (s, 3H, 2-Py C*H*$_3$), 1.97 (nonet, $^{3}J_{HH}$ = 6.7 Hz, 4H, OCH$_2$C*H*(CH_3)$_2$), 0.92 (d, $^{3}J_{HH}$ = 6.7 Hz, 24H, OCH$_2$CH(C*H*$_3$)$_2$).

^{31}P{^{1}H} NMR (162 MHz, Chloroform-*d*) δ 100.3 (s).

^{31}P{^{1}H} SSNMR (162 MHz) δ 101.2 (s).

^{13}C{^{1}H} NMR (151 MHz, Chloroform-*d*) δ 158.9 (2-Py *C*), 149.5 (6-Py *C*H), 139.6 (4-Py *C*H), 125.7 (3-Py *C*H), 122.1 (5-Py *C*H), 73.8 (d, $^{2}J_{CP}$ = 7.4 Hz, O*C*H_2CH(CH_3)$_2$), 28.9 (d, $^{3}J_{CP}$ = 8.5 Hz, OCH$_2$*C*H(CH_3)$_2$), 24.7 (2-Py *C*H_3, 19.0 (OCH$_2$CH(*C*H_3)$_2$).

MS (ASAP) *m/z* 640.1 (100%, $[M+H]^+$), 547.0 (75%, $[M\text{-}(2\text{-MePy})+H]^+$).

(Calc.: C, 41.21; H, 6.76; N, 2.18. Found: C, 41.24; H, 6.76; N, 2.13).

[Zn{κ^2-*S,S*-$S_2P(O^iBu)_2$}$_2$(2-EtPy)] (3)

^{1}H NMR (400 MHz, Chloroform-*d*) δ 8.92 (ddd, *J* = 5.4, 1.8, 0.8 Hz, 1H, 6-Py C*H*), 7.84 (td, *J* = 7.9, 1.8 Hz, 1H, 4-Py C*H*), 7.37 (d, *J* = 7.9 Hz, 1H, 3-Py C*H*), 7.35 – 7.29 (m, 1H, 5-Py C*H*), 3.85 (dd, $^{3}J_{PH}$ = 8.4 Hz, $^{3}J_{HH}$ = 6.7 Hz, 8H, OC*H*$_2$CH(CH_3)$_2$), 3.23 (q, $^{3}J_{HH}$ = 7.6 Hz, 2H, 2-Py C*H*$_2$CH$_3$), 1.98 (nonet, $^{3}J_{HH}$ = 6.7 Hz, 4H, OCH$_2$C*H*(CH_3)$_2$), 1.39 (t, $^{3}J_{HH}$ = 7.6 Hz, 3H, 2-Py CH$_2$C*H*$_3$), 0.93 (d, $^{3}J_{HH}$ = 6.7 Hz, 24H, OCH$_2$CH(C*H*$_3$)$_2$).

^{31}P{^{1}H} NMR (162 MHz, Chloroform-*d*) δ 100.0 (s).

^{31}P{^{1}H} SSNMR (162 MHz) δ 101.2 (s).

^{13}C{^{1}H} NMR (151 MHz, Chloroform-*d*) δ 164.0 (2-Py *C*), 149.4 (6-Py *C*H), 139.4 (4-Py *C*H), 123.6 (3-Py *C*H), 122.1 (5-Py *C*H), 73.8 (d, $^{2}J_{CP}$ = 7.4 Hz, O*C*H$_2$CH(CH$_3$)$_2$), 31.2 (2-Py *C*H$_2$CH$_3$), 28.9 (d, $^{3}J_{CP}$ = 8.6 Hz, OCH$_2$*C*H(CH$_3$)$_2$), 19.0 (OCH$_2$CH(*C*H$_3$)$_2$), 13.8 (2-Py CH$_2$*C*H$_3$).

MS (ASAP) *m/z* 654.1 (35%, [M+H]$^+$), 547.0 (100%, [M-(2-EtPy)+H]$^+$), 412.0 (6%, [M-(DTP)$^-$]$^+$), 108.1 (97%, [(2-EtPy)+H]$^+$).

(Calc.: C, 42.16; H, 6.92; N, 2.14. Found: C, 41.97; H, 6.88; N, 2.03).

[Zn{κ^2-*S,S*-S$_2$P(O^{i}Bu)$_2$}$_2$(2-^{i}PrPy)] (4)

^{1}H NMR (400 MHz, Chloroform-*d*) δ 8.85 (ddd, *J* = 5.4, 1.8, 1.0 Hz, 1H, 6-Py C*H*), 7.82 (td, *J* = 7.7, 1.8 Hz, 1H, 4-Py C*H*), 7.37 (dt, *J* = 7.7, 1.2 Hz, 1H, 3-Py C*H*), 7.28 (ddd, *J* = 7.7, 5.4, 1.2 Hz, 1H, 5-Py C*H*), 3.87 (dd, $^{3}J_{PH}$ = 8.4 Hz, $^{3}J_{HH}$ = 6.7 Hz, 8H, OC*H*$_2$CH(CH$_3$)$_2$), 3.60 (hept, $^{3}J_{HH}$ = 6.9 Hz, 1H, 2-Py C*H*(CH$_3$)$_2$), 2.00 (nonet, $^{3}J_{HH}$ = 6.7 Hz, 4H, OCH$_2$C*H*(CH$_3$)$_2$), 1.37 (d, $^{3}J_{HH}$ = 6.9 Hz, 6H, 2-Py CH(C*H*$_3$)$_2$), 0.94 (d, $^{3}J_{HH}$ = 6.7 Hz, 24H, OCH$_2$CH(C*H*$_3$)$_2$).

^{31}P{^{1}H} NMR (162 MHz, Chloroform-*d*) δ 99.7 (s).

^{31}P{^{1}H} SSNMR (162 MHz) δ 101.9 (s), 99.9 (s) (ratio 1:1). Two resonances arising from two inequivalent DTP ligands – consistent with molecular structure.

^{13}C{^{1}H} NMR (151 MHz, Chloroform-*d*) δ 168.3 (2-Py *C*), 149.0 (6-Py *C*H), 139.2 (4-Py *C*H), 122.2 (5-Py *C*H), 121.8 (3-Py *C*H) 74.0 (d, $^{2}J_{CP}$ = 7.4 Hz, O*C*H$_2$CH(CH$_3$)$_2$), 36.8 (2-Py *C*H(CH$_3$)$_2$), 28.9 (d, $^{3}J_{CP}$ = 8.7 Hz, OCH$_2$*C*H(CH$_3$)$_2$), 23.2 (2-Py CH(*C*H$_3$)$_2$), 19.0 (OCH$_2$CH(*C*H$_3$)$_2$).

MS (ASAP) *m/z* 668.1 (43%, [M+H]$^+$), 547.0 (79%, [M-(2-^{i}PrPy)+H]$^+$), 426.1 (3%, [M-(DTP)$^-$]$^+$), 122.1 (100%, [(2-^{i}PrPy)+H]$^+$).

(Calc.: C, 43.08; H, 7.08; N, 2.09. Found: C, 43.03; H, 7.05; N, 2.02).

[Zn{κ^2-*S,S*-S$_2$P(O^{i}Bu)$_2$}$_2$(3-FPy)] (5)

^{1}H NMR (400 MHz, Chloroform-*d*) δ 8.89 (ddd, *J* = 2.6, 1.9, 0.6 Hz, 1H, 2-Py C*H*), 8.83

(dt, J = 5.1, 1.2 Hz, 1H, 6-Py C*H*), 7.72 – 7.65 (m, 1H, 4-Py C*H*), 7.60 – 7.53 (m, 1H, 5-Py C*H*), 3.90 (dd, $^{3}J_{PH}$ = 8.3 Hz, $^{3}J_{HH}$ = 6.7 Hz, 8H, OCH_2CH(CH$_3$)$_2$), 2.03 (nonet, $^{3}J_{HH}$ = 6.7 Hz, 4H, OCH$_2$CH(CH$_3$)$_2$), 0.97 (d, $^{3}J_{HH}$ = 6.7 Hz, 24H, OCH$_2$CH(CH_3)$_2$).

^{31}P{^{1}H} NMR (162 MHz, Chloroform-*d*) δ 99.6 (s).

^{31}P{^{1}H} SSNMR (162 MHz) δ 101.2 (s).

^{13}C{^{1}H} NMR (151 MHz, Chloroform-*d*) δ 160.0 (d, $^{1}J_{CF}$ = 256.4 Hz, 3-Py *C*), 145.6 (d, $^{4}J_{CF}$ = 4.3 Hz, 6-Py *C*H), 138.4 (d, $^{2}J_{CF}$ = 28.5 Hz, 2-Py *C*H), 126.6 (d, $^{2}J_{CF}$ = 17.9 Hz, 4-Py *C*H), 126.1 (d, $^{3}J_{CF}$ = 5.1 Hz, 5-Py *C*H), 74.0 (d, $^{2}J_{CP}$ = 7.6 Hz, O*C*H$_2$CH(CH$_3$)$_2$), 29.0 (d, $^{3}J_{CP}$ = 8.6 Hz, OCH$_2$*C*H(CH$_3$)$_2$), 19.0 (OCH$_2$CH(*C*H$_3$)$_2$).

MS (ASAP) *m/z* 644.1 (100%, [M+H]$^{+}$), 547.0 (45%, [M-(3-FPy)+H]$^{+}$).

(Calc.: C, 39.10; H, 6.25; N, 2.17. Found: C, 39.01; H, 6.23; N, 2.07).

3.4.4 Synthesis of 1:2 ZDDP-Py' Complex

General Procedure

A stoichiometric amount of 4-MeOPy was added to a solution of **^{i}Bu ZDDP** (0.15 g, 0.27 mmol) in hexane (10 cm^3) and the reaction mixture was stirred for 30 minutes. Upon standing at room temperature, a colourless crystalline solid formed and was subsequently isolated by filtration, washed with hexane and dried in air.

[Zn{κ^1-*S*-S$_2$P(O^{i}Bu)$_2$}$_2$(4-MeOPy)$_2$] (6)

^{1}H NMR (400 MHz, Chloroform-*d*) δ 8.70 – 8.67 (m, 2H, 2,6-Py C*H*), 6.95 – 6.90 (m, 2H, 3,5-Py C*H*), 3.90 (s, 3H, 4-Py OCH_3), 3.81 (dd, $^{3}J_{PH}$ = 8.2 Hz, $^{3}J_{HH}$ = 6.7 Hz, 8H, OCH_2CH(CH$_3$)$_2$), 1.95 (nonet, $^{3}J_{HH}$ = 6.7 Hz, 4H, OCH$_2$CH(CH$_3$)$_2$), 0.92 (d, $^{3}J_{HH}$ = 6.7 Hz, 24H, OCH$_2$CH(CH_3)$_2$).

^{31}P{^{1}H} NMR (162 MHz, Chloroform-*d*) δ 101.7 (s).

^{31}P{^{1}H} SSNMR (162 MHz) δ 100.0 (s).

^{13}C{^{1}H} NMR (151 MHz, Chloroform-*d*) δ 167.4 (4-Py *C*), 151.2 (2,6-Py *C*H), 110.7

(3,5-Py *C*H), 73.4 (d, $^{2}J_{CP}$ = 7.8 Hz, O*C*H_2CH(CH_3)$_2$), 55.8 (4-Py O*C*H_3), 28.9 (d, $^{3}J_{CP}$ = 8.7 Hz, OCH_2*C*H(CH_3)$_2$), 19.1 (OCH_2CH(*C*H_3)$_2$).

MS (ASAP) *m/z* 656.1 (39%, [M-(4-MeOPy)+H]$^+$), 547.0 (29%, [M-2(4-MeOPy)+H]$^+$), 523.1 (72%, [M-(DTP)$^-$]$^+$), 110.1 (100%, [(4-MeOPy)+H]$^+$). (*N.B.* molecular ion not observed despite softer ionisation conditions employed).

(Calc.: C, 43.89; H, 6.58; N, 3.66. Found: C, 43.97; H, 6.58; N, 3.59).

Chapter 4

Understanding ZDDP-OFM Solution Interactions

4.1 Introduction

Since ZDDPs are known to extend the range of contact conditions where boundary lubrication occurs (high friction regime) in lubricant packages, of particular interest, and importance, is their combination with effective friction modifiers.[73] Currently there are two main classes of friction modifiers in use in liquid lubricants: organic friction modifiers (OFMs) and organomolybdenum compounds (Section 1.2.2.10). Generally it is regarded that OFMs offer an intrinsic advantage over their molybdenum counterparts, in that typically they are zero SAPS, thus making them particularly attractive in terms of meeting compositional constraints enforced upon modern lubricant formulations (Section 2.1).

Previously-published work investigating the interaction between ZDDP and OFMs (and ZDDP-additive interactions in general) has been concerned primarily with rationalising the tribological performance (friction, wear) and tribofilm properties (growth rate, composition, thickness, morphology) based on the chemical structure of the additives present, normally referenced against a ZDDP studied in isolation.[73,118,120,155] However, despite many reporting the possibility of interaction or complex formation in solution between ZDDPs and nitrogen-containing additives (OFM and dispersant additives), which would

conceivably occur prior to a formulation being exposed to conditions associated with an engine, studies investigating these bulk interactions are comparatively scarce.[123,155,156] Should ZDDP and friction modifier additives form complexes in solution then it is the properties of the complex, not the individual components, likely to dictate the tribological performance. Hence an understanding of, and how to tune or modulate such interactions is extremely desirable.

In Chapter 3 we investigated in detail the interaction in solution between ZDDP and various pyridine-based ligands (pyridine ligands serving as model amines) where the formation of both 1:1 and 1:2 mononuclear ZDDP-amine adducts were observed. Steric and electronic properties of the interacting amine were shown to dictate both the extent and type of interaction observed. Complex formation was also associated with a change in DTP binding mode, a change that could be monitored using Raman spectroscopy. In this Chapter, our work extends to evaluate whether commercial amine-based OFMs interact with ZDDPs in a similar manner, assessing effects on solution behaviour and structure. Initially, the interaction between **^{i}Bu ZDDP** and a monodentate primary alkyl amine was examined in detail, before other factors such as steric effects and secondary donor sites were subsequently investigated. The chapter concludes with a brief insight into ZDDP interactions with some alternative FMs, specifically MoDTC and glycerol mono-oleate (GMO).

4.2 Results and Discussion

4.2.1 Monitoring ZDDP-OFM Interactions

Initial experiments performed involved the reaction of **^{i}Bu ZDDP** with the commercial OFM, Armeen18D (octadecylamine, **OFM1**) in hexane solution. The reaction was monitored by ^{31}P NMR spectroscopy in a similar manner to that described previously (Section 3.2.1), examining relative changes in the lineshape and chemical shift of the ^{31}P spectroscopic resonance from the DTP ligands. Prior to amine addition, **^{i}Bu ZDDP** presents a broad singlet resonance by ^{31}P NMR spectroscopy, which arises as a result of the established ZDDP monomer-dimer equilibrium in solution (Section 1.2.2.8.1,

Scheme 1.1). Upon sequential addition of octadecylamine, a single $^{31}P[^{1}H]$ NMR resonance is observed in all cases, which moves to higher frequency and sharpens to reveal coupling to the ^{i}Bu CH_2 units with increasing amine concentration (Fig. 4.1); this mirrors the trend observed for the pyridine-based ligands reported in Chapter 3. Such changes indicate all phosphorus-containing species present in solution are in rapid equilibrium (on the NMR timescale) and the monomer-dimer equilibrium of **^{i}Bu ZDDP** has been suppressed by ZDDP-amine complexation, favouring a monomeric species. However, for the ZDDP-octadecylamine case, a much greater chemical shift change ($\Delta\delta$ = 8.28 ppm after addition of 3 equivalents of amine) is observed (*cf.* $\Delta\delta$ = 3.77 ppm after addition of 3 equivalents of pyridine), consistent with a stronger zinc-nitrogen interaction and, as a result, a greater change in DTP binding mode. This has tentatively been assigned as monodentate coordination based on the ^{31}P NMR spectroscopic data generalisations outlined by Harrison and Sebald (Section 3.2.5, Table 3.4).[126]

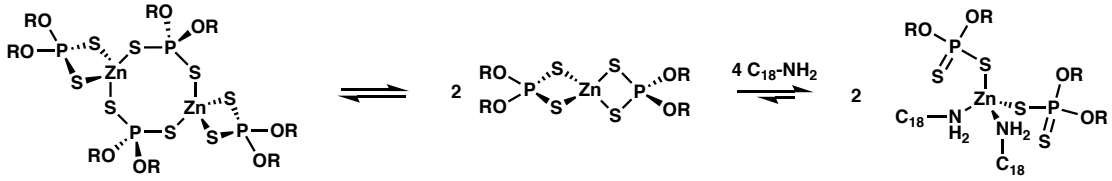

Scheme 4.1: Proposed solution equilibria between ZDDP and octadecylamine (C_{18}-NH_2, **OFM1**).

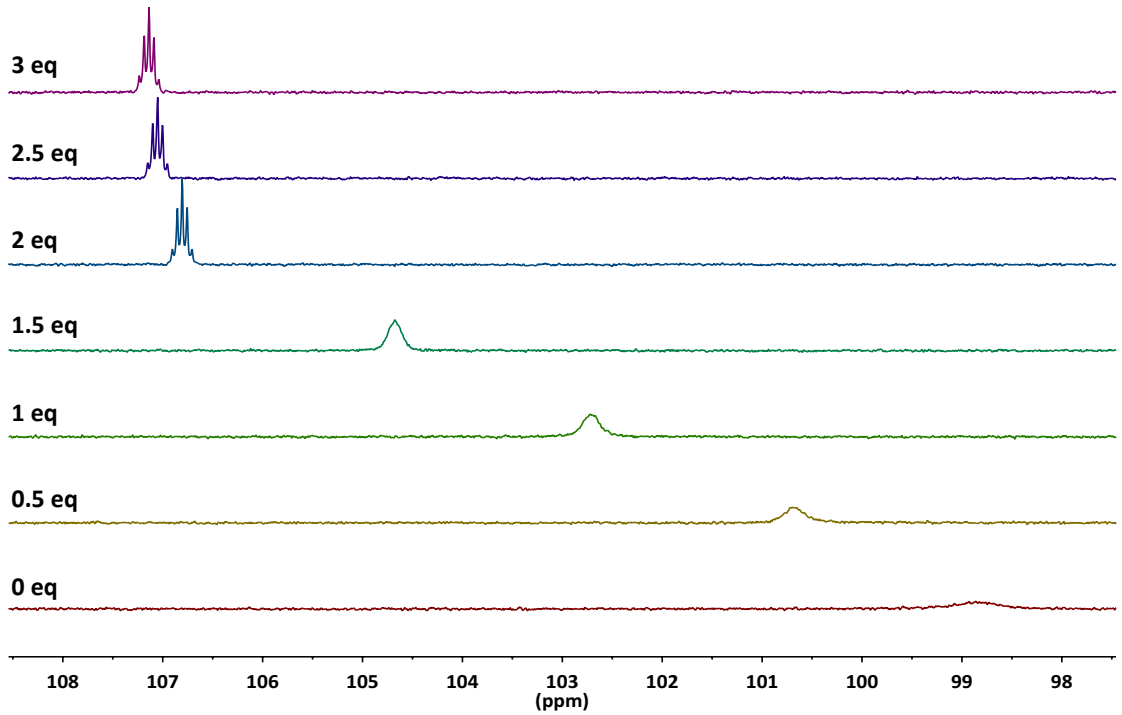

Figure 4.1: Evolution of the $^{31}P[^{1}H]$ NMR (162 MHz, hexane) spectrum of **^{i}Bu ZDDP** upon progressive addition of octadecylamine (**OFM1**). 0.006 M ZDDP (monomer), $CDCl_3$ insert spiked with PPh_3 to provide lock. Chemical shifts were referenced against PPh_3 in $CDCl_3$ (lit. -5.6 ppm [130]).

Particularly, at an amine:ZDDP ratio of 2 (Fig. 4.1), a sharp plateau in chemical shift change is apparent, that coincides with the resolution of the pentet resonance. Together, the ^{31}P NMR spectroscopic data are consistent with the formation of a monomeric, 1:2 ZDDP-amine complex (Scheme 4.1). Identical experiments were performed with a group III mineral oil solvent (Nexbase 3043) and gave almost identical results, thus suggesting identical interactions occur in an engine oil formulation (Fig. 4.2). However, the resonances observed in mineral oil are slightly broader, and a fully resolved pentet is never observed. The broader spectral features can be attributed to viscosity-induced resonance broadening, caused by the higher viscosity of the mineral oil solvent, in comparison to hexane. The higher viscosity causes an increase in NMR spectral line-width based on a decrease in T_2 (spin-spin) relaxation time caused by slower molecular tumbling.

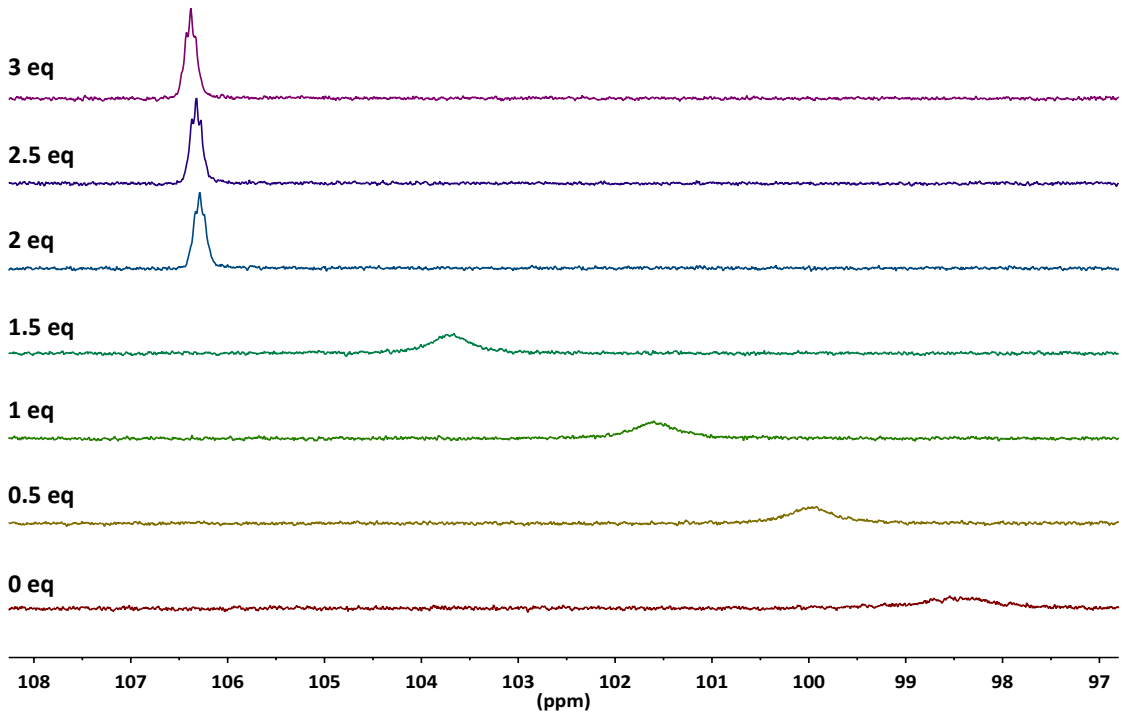

Figure 4.2: Evolution of the $^{31}P[^{1}H]$ NMR (162 MHz, mineral oil) spectrum of **^{i}Bu ZDDP** upon progressive addition of octadecylamine (**OFM1**). 0.006 M ZDDP (monomer), $CDCl_3$ insert spiked with PPh_3 to provide lock. Chemical shifts were referenced against PPh_3 in $CDCl_3$ (lit. -5.6 ppm[130]).

Confirmation of monomer-dimer equilibrium suppression was achieved *via* dilution experiments, on hexane solutions of **^{i}Bu ZDDP**-octadecylamine (ratio 1:2) and **^{i}Bu ZDDP** for reference (Fig. 4.3). Over the concentration range studied, for the amine-containing system only a very small change in chemical shift change was observed ($\Delta\delta = 0.19$ ppm), meaning the observed ^{31}P NMR chemical shift is largely concentration-independent. This supports the idea that the dynamic monomer-dimer equilibrium of **^{i}Bu ZDDP** is suppressed by the presence of octadecylamine. In contrast, for **^{i}Bu ZDDP** alone, a significant chemical shift change was observed ($\Delta\delta$ = 1.31 ppm), over the same concentration range studied. Subsequent fitting of the concentration-dependent ^{31}P NMR spectroscopic data to a dimerisation model (using the Bindfit web-tool[132]) yielded a dimerisation constant (K_{dim}) of 24 ± 1 M^{-1}; a value that is in good agreement with previous data obtained for **^{i}Bu ZDDP** in non-polar media.[157]

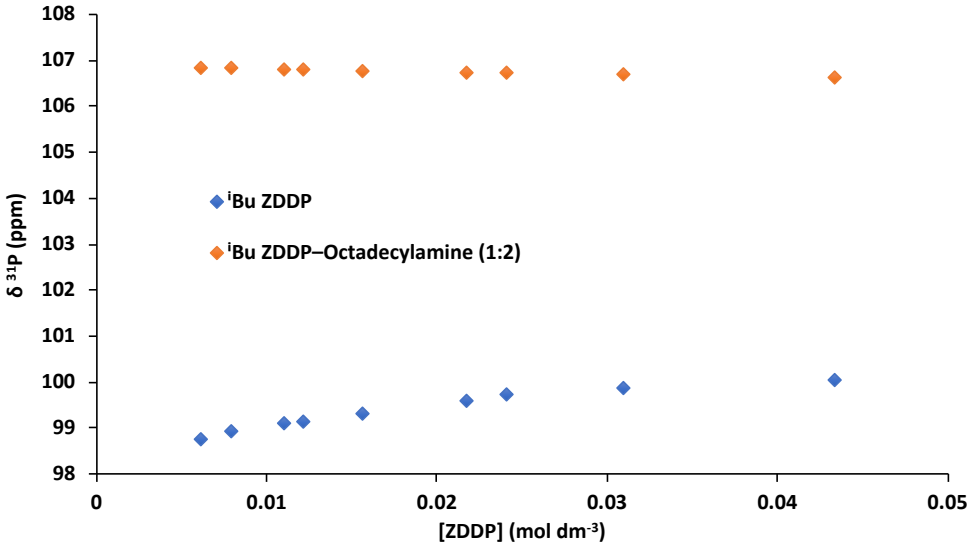

Figure 4.3: Plot of ^{31}P NMR (162 MHz, hexane) chemical shifts as a function of ZDDP concentration (monomer). $CDCl_3$ insert spiked with PPh_3 to provide lock. Chemical shifts were referenced against PPh_3 in $CDCl_3$ (lit. -5.6 ppm[130]).

Attempts to quantify the strength of the ZDDP-octadecylamine interaction by fitting an appropriate 1:2 binding model to the observed chemical shift changes proved unsuccessful. Although visual inspection of the titration data clearly indicates a 1:2 binding event (Fig. 4.1), fitting of the obtained data gave K_as with very large uncertainties (> 100%), suggesting the fitting results are meaningless. The inability to achieve suitable fitting is possibly a consequence of the strong ZDDP-amine interaction observed, meaning the association constant lies well above the practical limit where ^{31}P NMR titrations work reliably.* To obtain an accurate binding constant, it is important to perform titrations under equilibrium conditions, where both free *host* and *guest* are present throughout the titration. Non-equilibrium, high affinity binding curves are often characterised by linear titration curves with hard breaks at the ligand concentration present in the resulting complex. Under such conditions only a very crude estimation of the lower limit for K_a can be obtained.[158,160] Although it should also be noted that, for the ZDDP-octadecylamine system studied in this work, higher loadings of amine (> 3 equivalents) could not be confidently achieved due to poor solubility in hexane, which also limited the analysis.

*The upper limit for ^{1}H NMR titrations is often quoted as $K_a < 10^5$ M^{-1}, though with modern NMR instruments good quality ^{1}H NMR spectra can be obtained with sub-millimolar concentrations, suggesting K_a values up to and even above 10^6 M^{-1} may be possible.[158] However, with the reduced sensitivity of ^{31}P NMR (6.63×10^{-2} in comparison to ^{1}H NMR[159]), the upper limit for ^{31}P NMR titrations is therefore lower.

For the same reason an analysis using Job's method to confirm reaction stoichiometry could not be carried out.

Additional ^{31}P NMR spectroscopic titration studies however, have shown that the alkyl chain length of a primary amine had little to no effect on the observed ZDDP-amine interaction in solution. For example, the titration data for the closely related hexylamine with **^{i}Bu ZDDP** in hexane (Fig. 4.4), can be seen to be almost identical to that observed for octadecylamine (Fig. 4.1), with a slightly sharper plateau that possibly arises due to improved solubility of the liquid hexylamine. Once again, the fitting of a 1:2 binding model proved unsuccessful for similar reasons to those outlined above. However, in this case, due to the improved solubility of the liquid hexylamine, greater loadings of amine could be achieved. At sufficiently high loadings of amine (> 5 equivalents of amine), deviations away from the linear plateau in chemical shift with increasing amine concentration are evident, suggesting that some ionisation of DTP ligands may occur given a sufficient concentration of amine being present (Figure 4.4, inset). Fitting of the data obtained below 5 equivalents, to remove any ionisation effects, though again unsuccessful, yields crude estimates of the association constants, $K_{11} > 10^7$ and $K_{12} > 10^4$.

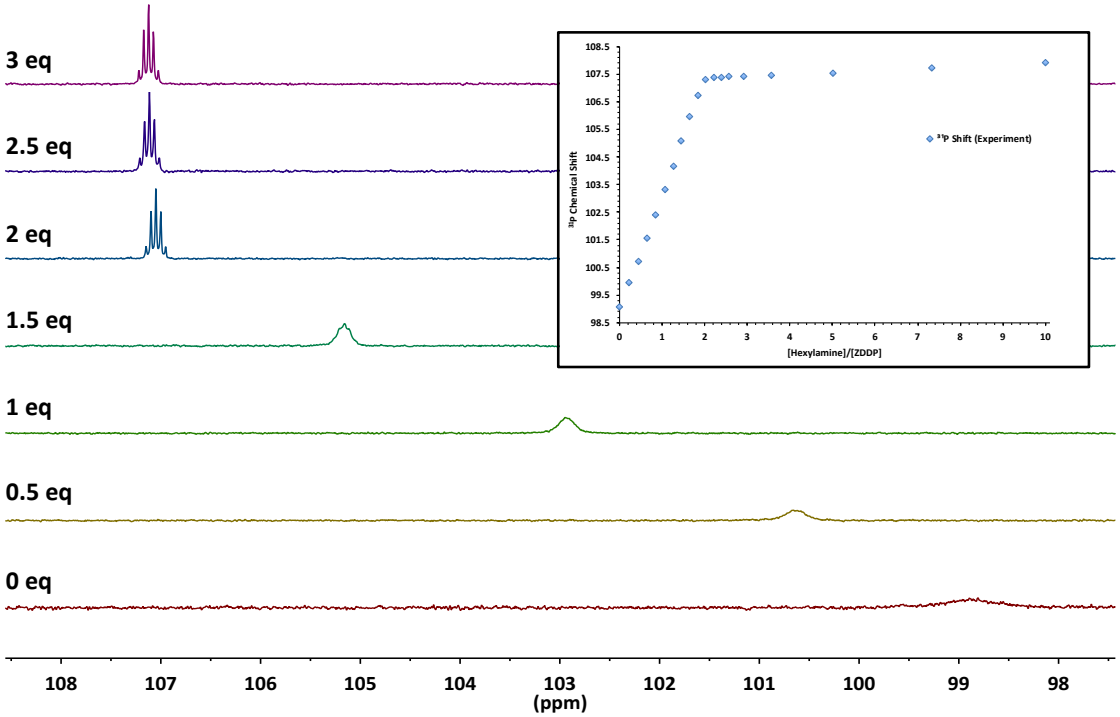

Figure 4.4: Evolution of the $^{31}P[^{1}H]$ NMR (162 MHz, hexane) spectrum of **^{i}Bu ZDDP** upon progressive addition of hexylamine. Inset shows a graph of ^{31}P chemical shift against hexylamine equivalents over the full range studied. 0.006 M ZDDP (monomer), $CDCl_3$ insert spiked with PPh_3 to provide lock. Chemical shifts were referenced against PPh_3 in $CDCl_3$ (lit. -5.6 ppm [130]).

Given the improved solubility of hexylamine in hexane, a Job's method analysis could be performed for this amine (Fig. 4.5). The Job's plot for **^{i}Bu ZDDP** and hexylamine displays a maximum at ~0.33 mole fraction of **^{i}Bu ZDDP**, something that is consistent with a 1:2 (ZDDP:amine) binding stoichiometry, and with the sharp plateau that is observed in the ^{31}P NMR spectroscopic titration data (Fig. 4.4).

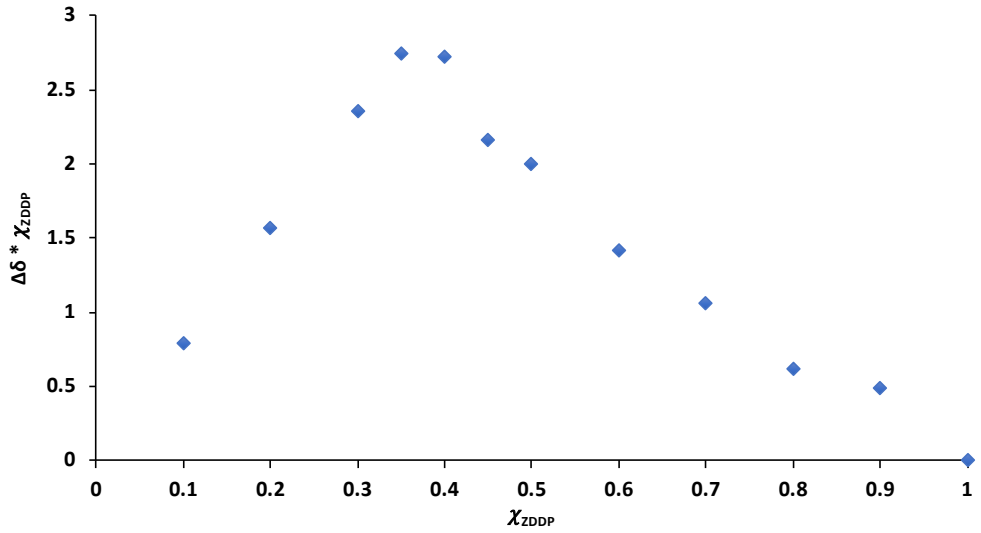

Figure 4.5: ^{31}P NMR continuous variation Job Plot for **^{i}Bu ZDDP** and hexylamine in hexane. Total concentration = 0.015 M. χ_{ZDDP} is the mole fraction of ZDDP.

Further verification of the complexation reaction pathway proposed (Scheme 4.1) comes from ^{31}P DOSY NMR spectroscopic experiments (Table 4.1). These DOSY experiments indicate an increase in molecular weight (decrease in diffusion coefficient) as octadecylamine is progressively added to **^{i}Bu ZDDP**, thus corroborating that the ^{31}P NMR spectroscopic changes observed arise due to a ZDDP-amine complexation reaction.

Table 4.1: Diffusion coefficients measured by ^{31}P DOSY NMR spectroscopy as a function of octadecylamine (**OFM1**) equivalents added to **^{i}Bu ZDDP**. 0.06 M ZDDP (monomer) in hexane, acetone-d_6 insert to provide lock.

Equivalents of Amine†	**Diffusion Coefficient (10^{10} m^{2}s^{-1})**
0	16 ± 2
1	7.83 ± 0.04
2	6.24 ± 0.04

†Greater loadings of amine could not be confidently achieved due to solubility reasons.

4.2.2 X-Ray Crystallographic Analysis of [Zn{κ^1-*S*-$S_2P(O^iBu)_2$}$_2$ (C_{18}-NH_2)$_2$] (7)

To unambiguously prove the nature of ZDDP-OFM complexation for amine-functional OFMs, and in particular the effect on DTP binding mode, single crystal X-ray crystallo-

graphic analysis of the resulting ZDDP-octadecylamine complex was undertaken. The zinc-amine complex [Zn{κ^1-*S*-$S_2P(O^iBu)_2$}$_2$(C_{18}-NH_2)$_2$] (**7**) was prepared by addition of 2 equivalents of octadecylamine (C_{18}-NH_2) to **^{i}Bu ZDDP** in hexane to yield a clear oil that solidified slowly on standing. Subsequent recrystallisation (slow evaporation of a chloroform/acetonitrile (1:1) solution) yielded single crystals suitable for X-ray crystallographic analysis. Complex **7** proved to be a mononuclear bis(octadecylamine) complex of **^{i}Bu ZDDP** and to the best of our knowledge is the first isolated example of a ZDDP-OFM complex (Fig. 4.6).

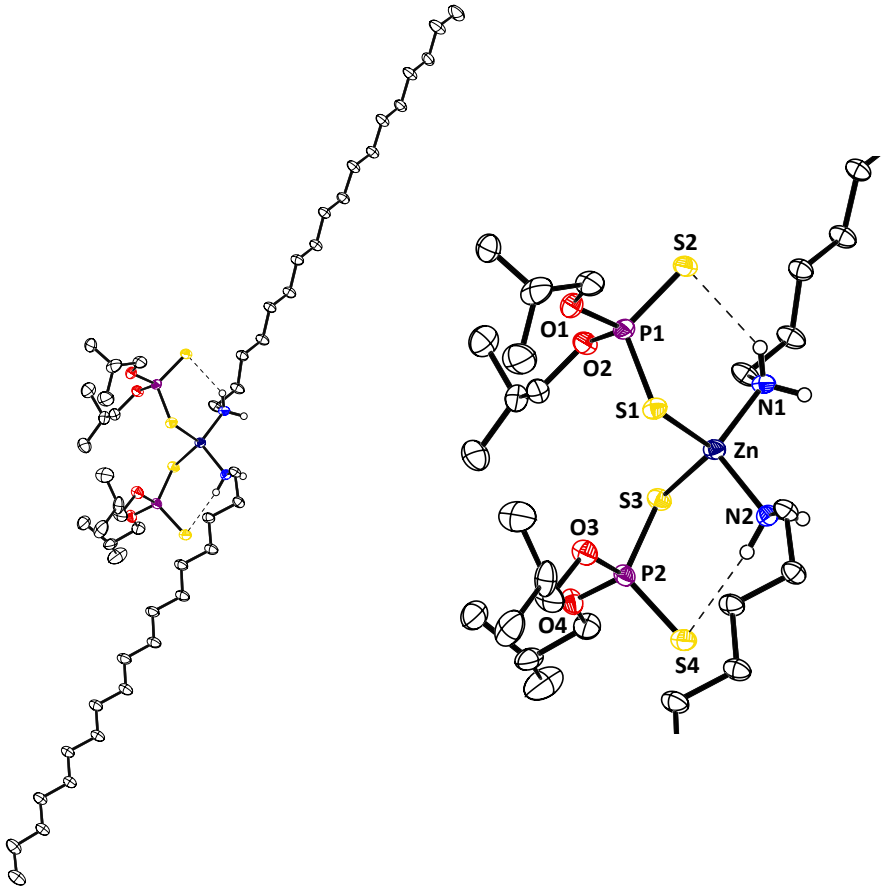

Figure 4.6: Molecular structure of [Zn{κ^1-*S*-$S_2P(O^iBu)_2$}$_2$(C_{18}-NH_2)$_2$] (**7**) with thermal ellipsoids at the 50% probability level; alkyl H atoms are omitted for clarity. Inset shows zoom of the zinc coordination sphere. Selected bond distances: Zn-N1, 2.0441(19) Å; Zn-N2, 2.0348(19) Å; Zn-S1, 2.3192(7) Å; Zn-S3, 2.3764(7) Å; P1-S1, 2.0248(8) Å; P1-S2, 1.9482(9) Å; P2-S3, 2.0062(8) Å; P2-S4, 1.9628(9) Å. Selected bond angles: S1-P1-S2, 117.38(4)°; S3-P2-S4, 116.69(4)°.

The structure is very similar to that of complex **6**, [Zn{κ^1-*S*-$S_2P(O^iBu)_2$}$_2$(4-MeOPy)$_2$], reported in Chapter 3, with a four-coordinate tetrahedral zinc centre containing two

bound octadecylamine ligands and two now monodentate, κ^1-*S*-DTP ligands; a binding mode that is in agreement with that predicted from our ^{31}P NMR spectroscopic data (*vide supra*).[126] The preference for this coordination environment is rationalised based on the high Lewis basicity of the octadecylamine ligands, which preferentially bind to zinc and hence displace the κ^2-*S,S* coordination of the DTP ligands. Furthermore, the formation of weak hydrogen bonds between the uncoordinated sulfur atoms and the amino hydrogen atoms likely promotes monodentate DTP coordination. Meanwhile, the crystal packing diagram of complex **7**, viewed along the *a*-axis (Fig. 4.7), shows the efficient packing of the long alkyl chains in the solid-state. The C_{18} alkyl chains are arranged in an interdigitated, bilayer fashion that maximises interchain interactions.

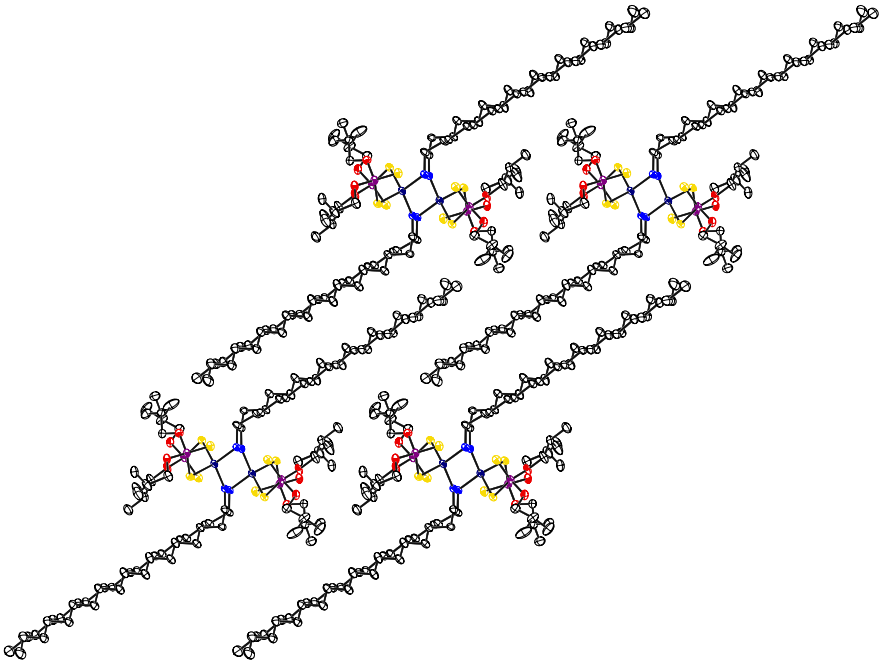

Figure 4.7: Crystal packing of complex **7** viewed along the *a*-axis.

Most importantly, the structure of complex **7** unequivocally identifies complexation to occur *via* nitrogen coordination to zinc, not a zinc-phosphorus interaction as suggested by some.[161] In addition, the resulting change in DTP coordination mode following amine addition likely increases the nucleophilicity/basicity of the DTP ligands and may impact the thermal and/or tribological behaviour of ZDDPs (see Chapter 5).

4.2.3 Raman Spectroscopic Analysis of [Zn{κ^1-*S*-$S_2P(O^iBu)_2$}$_2$ (C_{18}-NH_2)$_2$] (7)

In Chapter 3, the use of Raman spectroscopy as a diagnostic tool for the determination of DTP binding mode for a series of ZDDP-pyridine complexes of known structure was examined. In that work it was demonstrated that the presence (or absence) of a Raman band near 660 cm^{-1} (assigned to ν(P=S)/$\nu(PS_2)_{asym}$) was an indicator of the DTP binding mode in the studied complexes (Fig. 4.8). The intensity of the ~660 cm^{-1} band increases as the DTP binding mode is progressively shifted from symmetrically bridging or chelating through to monodentate. The Raman intensity for intermediate binding modes lies somewhere in between the two extreme cases, increasing as the two P-S bond lengths progressively assume P-S and P=S character. Here we expand this method to encompass the ZDDP-OFM complex **7**, to validate the method's wider applicability to ZDDP-amine complexes more generally, and specifically for ZDDP-OFM complexes relevant to engine oil formulations.

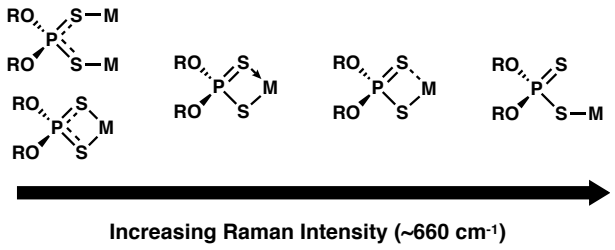

Figure 4.8: Relative intensity of the Raman band at ~660 cm^{-1} as a function of DTP binding mode.

The Raman spectrum of complex **7** clearly presents a strong band centred around 670 cm^{-1} that is attributed to ν(P=S) (Fig. 4.9). This peak is indicative of a monodentate binding mode and is thus consistent with the molecular structure obtained for **7** (Fig. 4.6). Moreover, this result is verification that Raman spectroscopy is a useful diagnostic tool for assigning DTP binding modes for amine-functional OFM complexes of ZDDPs, and could be applied to similar species where suitable crystal data cannot be attained.

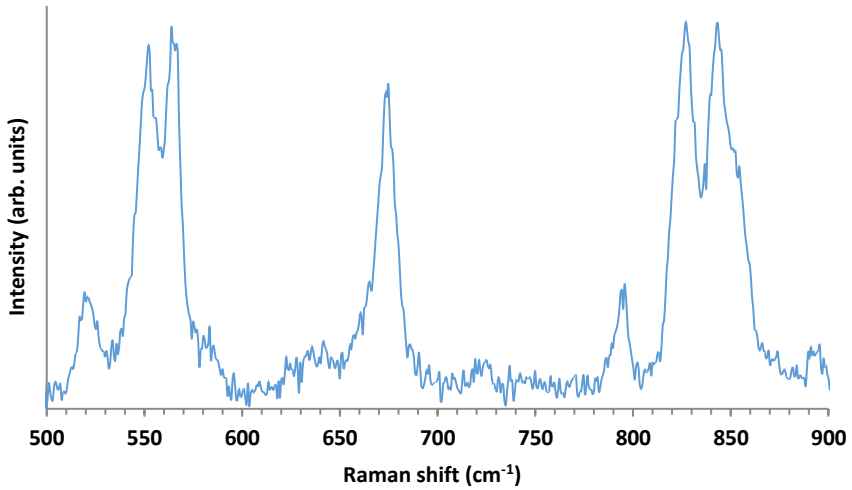

Figure 4.9: Solid-state Raman spectrum (500-900 cm^{-1}) of [Zn{κ^1-*S*-$S_2P(O^iBu)_2$}$_2$(C_{18}-NH_2)$_2$] (**7**).

4.2.4 Variable-Temperature ^{31}P NMR Spectroscopic Analysis of [Zn{κ^1-*S*-$S_2P(O^iBu)_2$}$_2$(C_{18}-NH_2)$_2$] (7)

Given the temperature cycling that occurs in an engine, it is of particular interest to assess how the previously identified complex formation is affected by elevated temperatures. To achieve this, initial variable-temperature ^{31}P NMR spectroscopy experiments were performed on complex **7** in heptane solution, rather than hexane, so that higher temperatures could be reached (Fig. 4.10).

From the data presented in Figure 4.10 it can be seen that an increase in temperature causes a low frequency shift alongside significant broadening of the ^{31}P spectroscopic resonance of complex **7**.[†] This trend is the inverse of that observed in previous titration experiments and implies that higher temperatures disfavour ZDDP-amine complex formation. The result of this decomplexation is broader spectral resonances; these arise from loss of the monomer-dimer equilibrium suppression previously observed (confirmed by dilution studies, see Fig. 4.3) and/or reasonably slow exchange between complexed, partially complexed (*i.e.* 1 bound octadecylamine ligand) and 'free' ZDDP. However, upon return to ambient temperature the spectroscopic resonance returns to its original

[†]To get absolute values for the temperature effect on chemical shift, a correction should be applied for the PPh_3 reference in toluene-d^8.

form and chemical shift, thus suggesting that, over the temperature range studied at least, that the decomplexation observed is reversible.

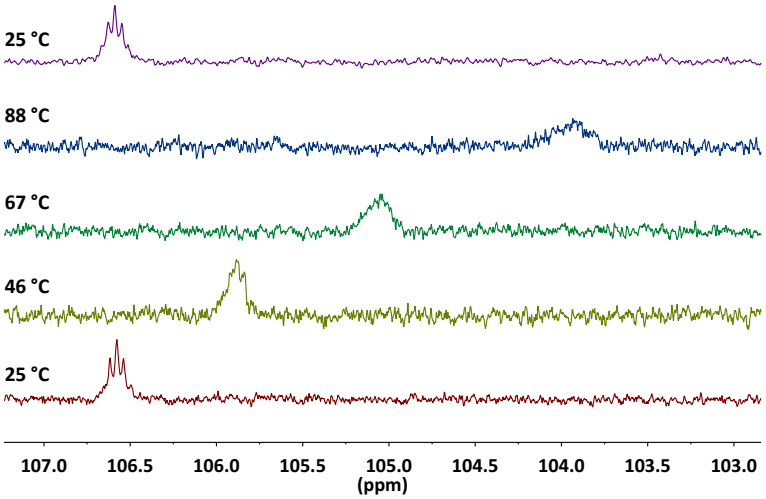

Figure 4.10: Evolution of the $^{31}P[^{1}H]$ NMR (202 MHz, heptane) spectrum of complex **7** as a function of temperature. 0.006 M ZDDP (monomer), toluene-d_8 insert spiked with PPh_3 to provide lock. Chemical shifts were referenced against PPh_3 in toluene-d_8 (lit. -5.4 ppm[162]).

For this spectroscopic study (Fig. 4.10), the use of protio heptane necessitated the use of a toluene-d_8 capillary insert to provide a lock solvent. Difficulties obtaining sufficient lock and adequate shimming with the capillary insert, especially at higher temperatures, contributed to the poor NMR spectral quality, and made it difficult to determine to what extent the resonance broadening observed was a consequence of the chemistry involved or other external factors *i.e.* poor shimming.

As a consequence of these potentially detrimental factors, subsequent high-temperature ^{31}P NMR spectroscopic studies of complex **7** were performed in toluene-d_8 and acquired with proton-decoupling to improve signal quality and aid the interpretation of results. As a capillary insert containing a deuterated solvent was no longer needed when using toluene-d_8, this facilitated the use of an alternative reference material, *e.g.* H_3PO_4, that was added to the NMR tube in a sealed capillary. This reference material was chosen specifically as its chemical shift has been reported to be essentially unaffected by temperature.[163] However due to the intensity of the H_3PO_4 signal, some method to modulate the signal intensity of the reference had to be employed, so as to not overwhelm

the signal of interest. This was achieved by using a radio frequency pulse with a sinc profile (Fig. 4.11), where truncation of the sinc wave positioned one of the smaller, local maxima at or close to the reference signal, thus giving a reference signal with a modulated intensity.

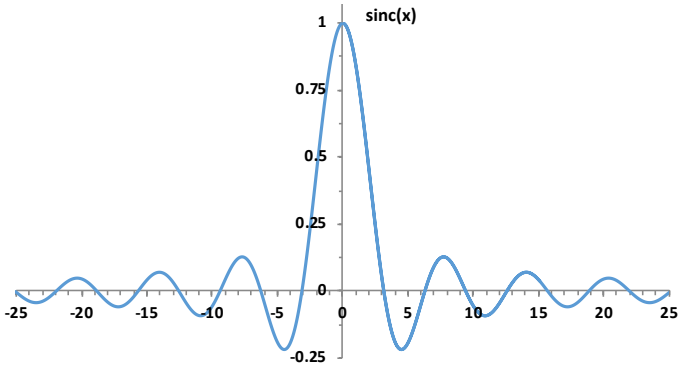

Figure 4.11: Sine cardinal, or sinc, wave function.

This signal attenuation was particularly important given the resonance broadening that occurs at high temperatures, which increases the likelihood that the signal of interest could potentially be lost into the NMR spectral baseline. An example of the use of the tailored excitation profile is given in Figure 4.12.

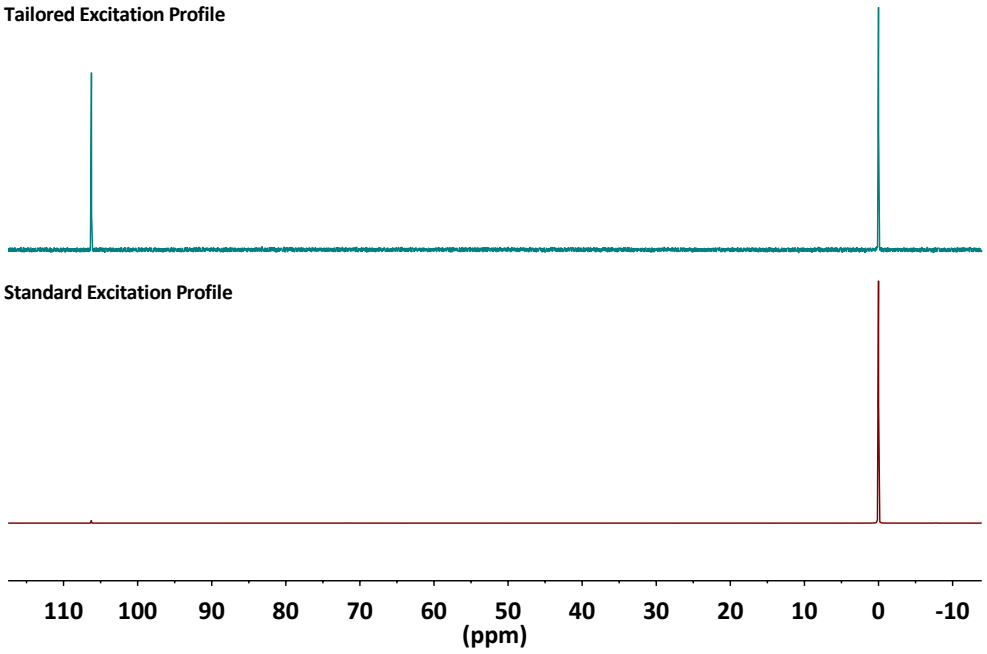

Figure 4.12: $^{31}P\{^{1}H\}$ NMR (202 MHz, toluene-d_8, 32 °C) spectrum of complex **7** using a tailored excitation profile, top, and a standard excitation profile, bottom. 0.006 M ZDDP (monomer), chemical shifts were referenced internally against a H_3PO_4 capillary insert (lit. 0.00 ppm).

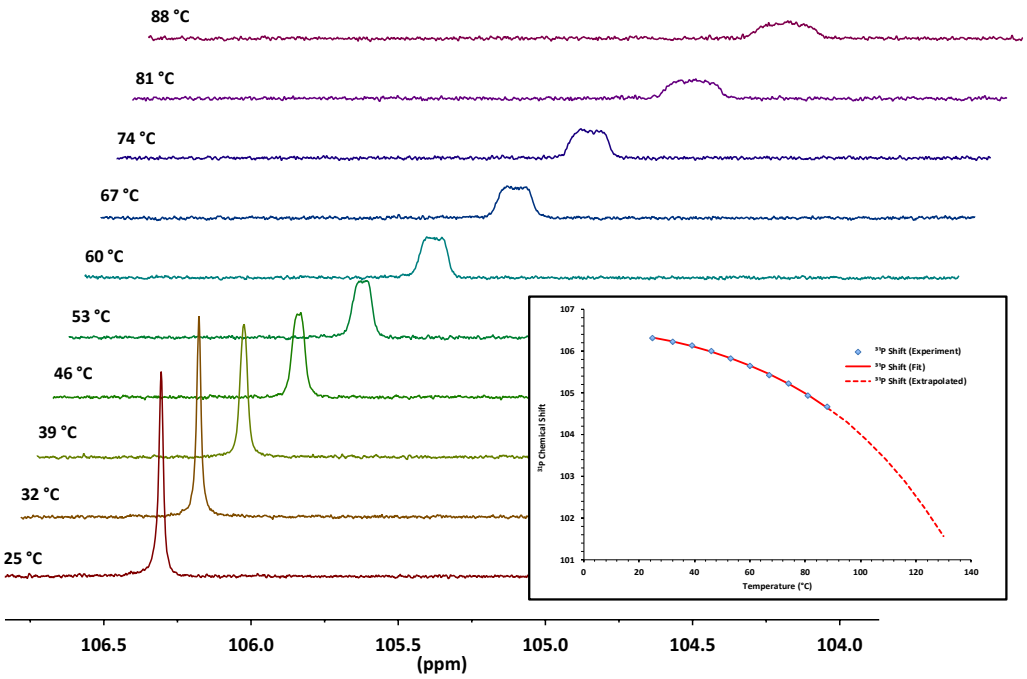

Figure 4.13: Evolution of the $^{31}P\{^{1}H\}$ NMR (202 MHz, toluene-d_8) spectrum of complex **7** as a function of temperature, using a tailored excitation profile to modulate the H_3PO_4 reference intensity (see above). 0.006 M ZDDP (monomer), chemical shifts were referenced internally against a H_3PO_4 capillary insert (lit. 0.00 ppm). Inset shows the fit to an exponential decay. Decomplexation was again found to be fully reversible over the temperature range studied (data not presented).

Again, from the data summarised in Figure 4.13, an increase in temperature is shown to cause a low frequency shift alongside significant broadening of the ^{31}P spectroscopic resonance, consistent with the previous results obtained in heptane solution. The square-like resonances at higher temperatures suggest the presence of multiple species, which are likely to be complexed, partially complexed and amine-free ZDDP. The obtained data were fitted to a single-exponential decay of the form:

$$y = y_0 + Aexp(-T/\tau)$$

where T is temperature, y is chemical shift, and y_0, A and τ are constants. The resulting fit was very good (R^2 = 0.9989) and extrapolation of the fit to 130 °C (engine sump temperatures can be as high as 130 °C under heavy load[164]), yields a predicted chemical shift of 101.6 ppm. This value, when compared to the known chemical shift of **^{i}Bu ZDDP** (δ_P 97.3 and 97.4 at 25 °C and 88 °C, respectively), suggests that significant

ZDDP-amine complex persists even at the extreme of sump temperatures. This observation highlights the persistence of ZDDP-OFM complexes at elevated temperatures, and therefore emphasises the potential impact of solution interactions on the thermal and tribological performance of lubricant formulations, a topic that is discussed in Chapter 5.

4.2.5 Steric Effects on ZDDP-OFM Complexation

In Chapter 3, a correlation between increasing steric demands ($\%V_{\mathrm{bur}}$) and ZDDP-amine complex formation in solution (K_{a}) for several pyridine-based ligands was identified. Subsequently, in this chapter, a detailed understanding of the behaviour of the ZDDP-octadecylamine OFM system has been attained. With this knowledge and understanding in hand, our attention then shifted to investigate how steric factors affected the complexation of ZDDPs with other commercial amine-based OFMs. To probe these steric factors, we investigated both secondary and tertiary commercial alkyl amines, Armeen1M1618D (a mixture of octadecylmethylamine and hexadecylmethylamine, **OFM2**) and Armeen DM18D (octadecyldimethylamine, **OFM3**) (Fig. 4.14).

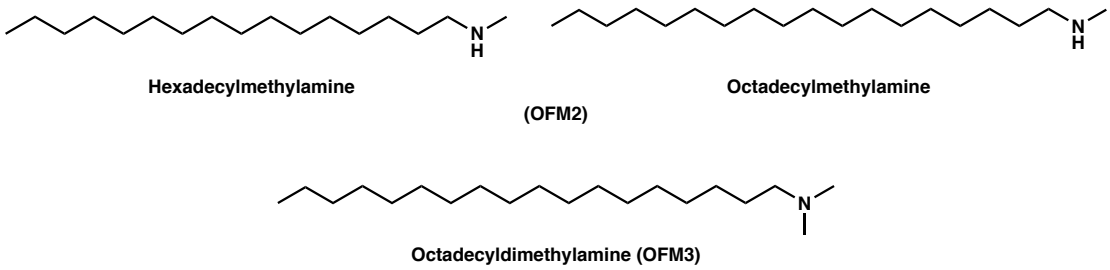

Figure 4.14: Chemical structures of commercial OFMs studied.

In a similar manner to that outlined above, hexane solutions of **^{i}Bu ZDDP** were titrated with aliquots of the aforementioned amine-functional OFMs. Incremental addition of aliquots of **OFM2** and **OFM3**, to **^{i}Bu ZDDP** under identical reaction conditions gave similar trends (Fig. 4.15) to that observed on addition of the 1° amine, octadecylamine (**OFM1**). As expected however, the change in chemical shift is modulated and decreases as the steric demands of the OFM increases. Notable resonance sharpening occurs for both **OFM2** and **OFM3** though a resolved pentet is never observed for **OFM2**, something likely arising from the fact that **OFM2** contains a mixture of alkyl chain lengths.

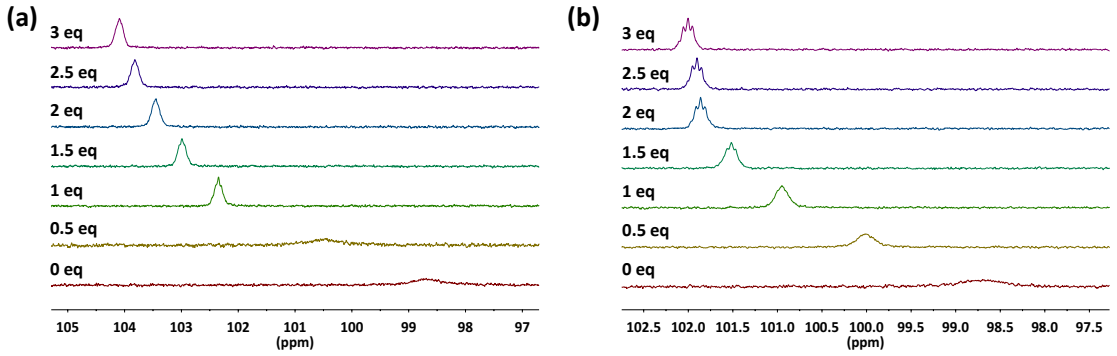

Figure 4.15: Evolution of the $^{31}P[^{1}H]$ NMR (162 MHz, hexane) spectrum of **^{i}Bu ZDDP** upon progressive addition of OFMs (a) **OFM2** and (b) **OFM3**. 0.006 M ZDDP (monomer), $CDCl_3$ insert spiked with PPh_3 to provide lock. Chemical shifts were referenced against PPh_3 in $CDCl_3$ (lit. -5.6 ppm[130]).

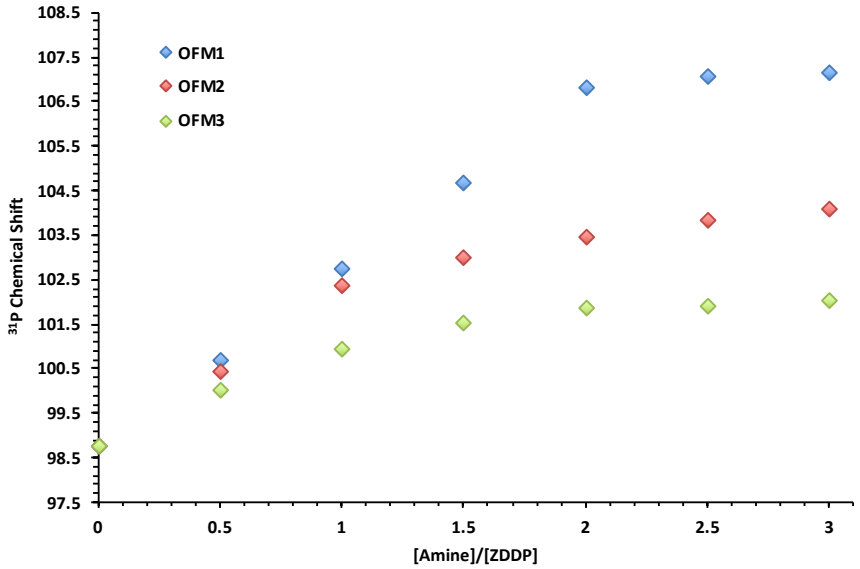

Figure 4.16: Plot of ^{31}P NMR (162 MHz, hexane) chemical shifts upon progressive addition of OFMs **1-3**. $CDCl_3$ insert spiked with PPh_3 to provide lock. 0.006 M ZDDP (monomer), chemical shifts were referenced against PPh_3 in $CDCl_3$ (lit. -5.6 ppm[130]).

It is also apparent from the chemical shift increases observed with increasing amine concentration (Fig. 4.16), that the binding stoichiometry for **OFM2** and **OFM3** with **^{i}Bu ZDDP** cannot be deduced by simple inspection as was previously possible, and subsequently confirmed, for **OFM1**. Analyses by Job's methods for **OFM2** and **OFM3** binding were performed in an attempt to identify the binding stoichiometry in each case (Fig. 4.17). For both systems the maximum observed is close to 0.45, something that is indicative of a composite binding stoichiometry, *i.e.* both 1:1 and 1:2 ZDDP:amine

complexes were present in solution, and hence a a maximum at a mole fraction of ZDDP somewhere between 0.33 and 0.5 is observed.[165] This is consistent with the observed chemical shift changes by ^{31}P NMR spectroscopy (Fig. 4.16), where smaller chemical shift changes indicate weaker ZDDP-amine interaction for 2° and 3° OFMs (**OFM2** and **OFM3**, respectively), and greater steric demands disfavours complete 1:2 complex formation.

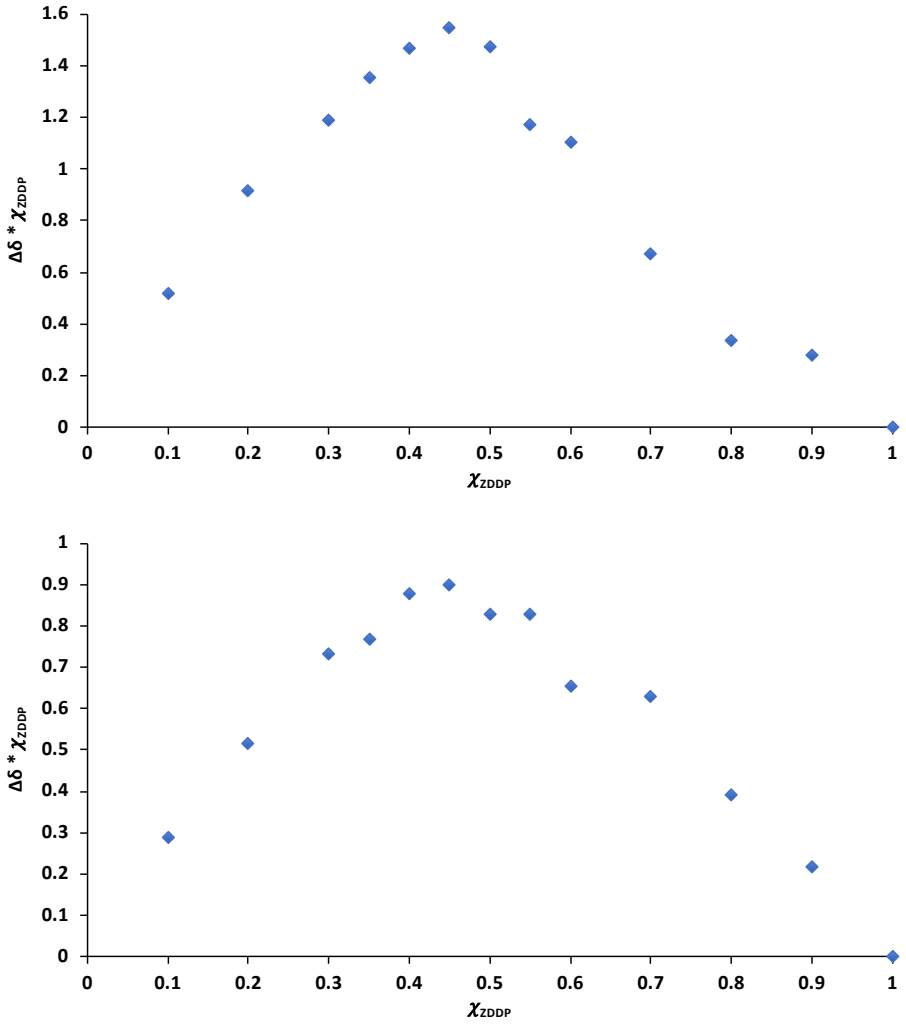

Figure 4.17: ^{31}P NMR continuous variation Job Plot for ^{i}**Bu ZDDP** with **OFM2**, top, and **OFM3**, bottom, in hexane. In both cases, total concentration = 0.015 M.

Variable-temperature ^{31}P NMR studies on the most sterically demanding amine **OFM3** with ^{i}**Bu ZDDP** (Fig. 4.18), displays similar decomplexation behaviour to that observed for **OFM1** (Fig. 4.13). A low frequency shift is apparent and the decomplexation showed reversibility over the temperature range studied (1 cycle), though in this case the ob-

served change in chemical shift fit well to a straight line, rather than an exponential decay. The absolute change in chemical shift observed ($\Delta\delta$ = 3.12 ppm) is almost twice that observed for **OFM1** ($\Delta\delta$ = 1.65 ppm), something that is consistent with a greater degree of decomplexation at elevated temperature. However, the final chemical shift value at 88 °C for the **^{i}Bu ZDDP-OFM3** (δ_P 99.5 ppm) compared to that of **^{i}Bu ZDDP** at the same temperature (δ_P 97.4 ppm) demonstrates that some ZDDP-amine complex still persists at this temperature for the more substituted system.

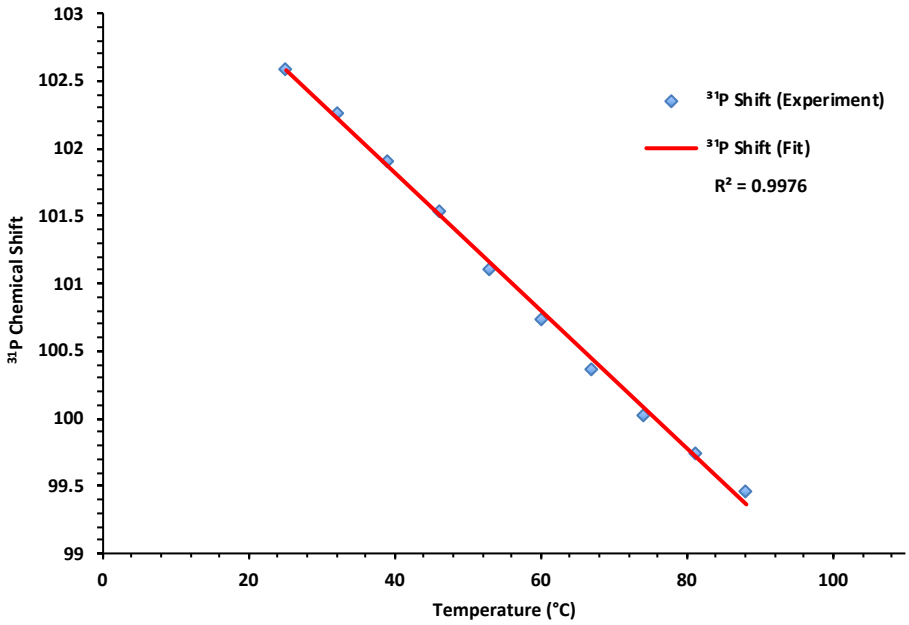

Figure 4.18: Plot of $^{31}P\{^{1}H\}$ NMR (202 MHz, toluene-d_8) chemical shifts of **^{i}Bu ZDDP-OFM3** solution (ratio 1:2) as a function of temperature. ^{31}P NMR spectra were recorded using a tailored excitation profile to modulate the H_3PO_4 reference intensity (see above). 0.006 M ZDDP (monomer), chemical shifts were referenced internally against a H_3PO_4 capillary insert (lit. 0.00 ppm). Decomplexation was found to be fully reversible over the temperature range studied (data not presented).

Extrapolation of the obtained fit to a temperature of 130 °C, as performed previously for **OFM1**, yields a predicted chemical shift of 97.2 ppm. This value very closely resembles the chemical shift of **^{i}Bu ZDDP** at 88 °C (δ_P 97.4 ppm), which also appears to be unaffected by increasing temperature {*cf.* δ_P (**^{i}Bu ZDDP**) = 97.3 ppm at 25 °C}. Together, the aforementioned experimental and predicted ^{31}P NMR spectroscopic data suggest that complete ZDDP-OFM decomplexation may occur for the ZDDP-**OFM3** system, at temperatures approaching values similar to that experienced at the extreme

of engine sump temperatures (130 °C[164]). This result directly contrasts that observed for the ZDDP-**OFM1** system (Section 4.2.4), where complexation is stronger and more persistent at high temperature. This difference in solution behaviour for **OFM1** and **OFM3** infers that tuning OFM steric demands is a useful design strategy in order to modulate ZDDP-OFM interactions in engine lubricant formulations. That said, as yet, the full impact of these differences in terms of lubricant performance are not known and hence, will be addressed in Chapter 5.

4.2.6 ZDDP Interactions with Multi-Donor OFMs

Thus far, our investigations have focussed only on monodentate amine-containing systems. However commercial OFMs often contain at least one other donor site, commonly nitrogen- or oxygen-based. In this regard, another factor of interest to us was the impact of these secondary donor site(s) on the strength and nature of ZDDP-OFM interactions. Consequently, in this section, our investigations focus on diamine-based and ethoxylated OFMs, as well as some model amine compounds, where applicable, to aid understanding and inform subsequent discussions regarding commercial OFMs.

4.2.6.1 ZDDP-Diamine Interactions

Shiomi *et al.* previously published work examining ZDDP-diamine interactions and reported the impact of alkyl chain length. Short chain aliphatic diamines such as ethylenediamine were proposed to form 1:1 chelate complexes, whereas longer chain, more hindered diamines formed bridging 2:1 ZDDP-amine adducts, as a result of entropic effects. However, it should be noted that, in their work no X-ray structural characterisations were performed and the conclusions were made based on ^{1}H NMR and elemental analyses only.[123] More recent work, focussing on dipyridyl-type ligands, has demonstrated, *via* X-ray crystallographic studies, that the steric requirements of both the dipyridyl ligand and the dithiophosphate-bound organic substituents of ZDDP control the degree of aggregation in such systems and thus, monomeric, dimeric and polymeric species can be formed.[127–129]

Additionally, Harrison and co-workers have investigated the effect of increasing amine

denticity on ZDDP-amine complex formation in the solid-state, demonstrating that progressive displacement of DTP ligands occurs with increasing amine denticity. Taken to the extreme, in the case of tetraethylenepentamine, the ability of a multidentate amine to effectively sequester the zinc dication, leaving two anionic DTP ligands was demonstrated.[125]

To build our chemical understanding and provide grounding before attempting to study commercial diamine-based OFMs, our initial work focussed on a simpler diamine, namely ethylenediamine (EDA). Titration experiments were performed for **^{i}Bu ZDDP** with EDA in hexane and the change in ^{31}P NMR chemical shift observed is plotted and compared with that of the monodentate **OFM1** (Fig. 4.19). For EDA a distinctly different trend is observed; an initial sharper increase in chemical shift is observed between 0 and 1 equivalents of added amine, most likely a consequence of the bidentate nature of EDA, and a sharp plateau at 1 equivalent, rather than 2 equivalents of amine, is also apparent.

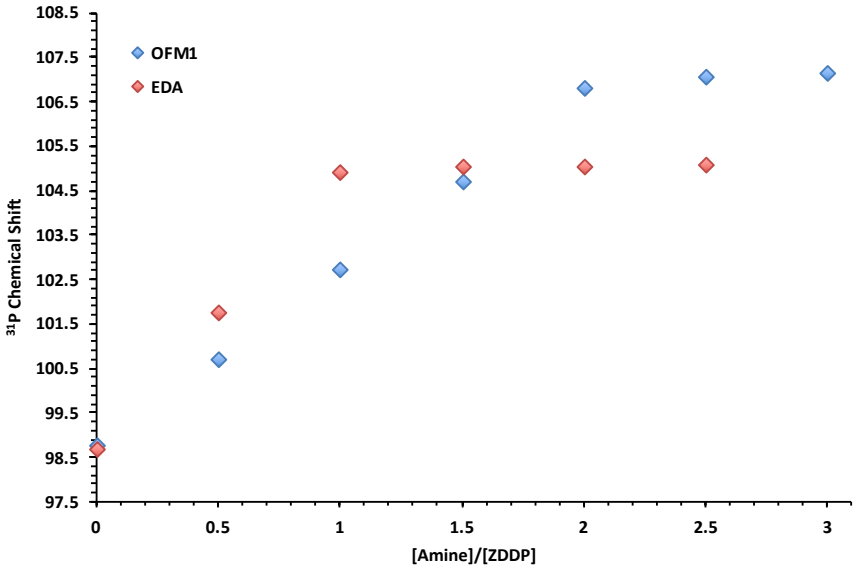

Figure 4.19: Plot of ^{31}P NMR (162 MHz, hexane) chemical shifts upon progressive addition of EDA and **OFM1** to **^{i}Bu ZDDP**. $CDCl_3$ insert spiked with PPh_3 to provide lock. 0.006 M ZDDP (monomer), chemical shifts were referenced against PPh_3 in $CDCl_3$ (lit. -5.6 ppm[130]).

These observations are consistent with the formation of a 1:1 complex between ZDDP and EDA (with two nitrogen atoms bound to zinc) and one would predict a ZDDP complex not dissimilar to that identified previously with **OFM1**, complex **7** (Fig. 4.6),

and the bis(4-MeOPy) complex **6** (Fig. 3.14), except that the two nitrogen centres would now be connected by an alkyl linker. X-Ray crystallography confirmed this to indeed be the case, with the complex [Zn{κ^1-*S*-$S_2P(O^iBu)_2$}$_2$(κ^2-EDA)] (**8**) being isolated from a 1:1 mixture of **^{i}Bu ZDDP** and EDA in ethanol (Fig. 4.20). In the solid-state the zinc centre of **8** adopts a distorted tetrahedral configuration, and is bound by a chelating EDA ligand and two DTP ligands. The DTP ligands are inequivalent, but are both bound in a monodentate fashion. One DTP ligand is stabilised by an intramolecular hydrogen bond between the uncoordinated sulfur atom and an amino hydrogen, something that may explain its slightly wider S-P-S angle. The structure is comparable to the related diisopropyl homologue previously reported by Drew *et al.*[124]

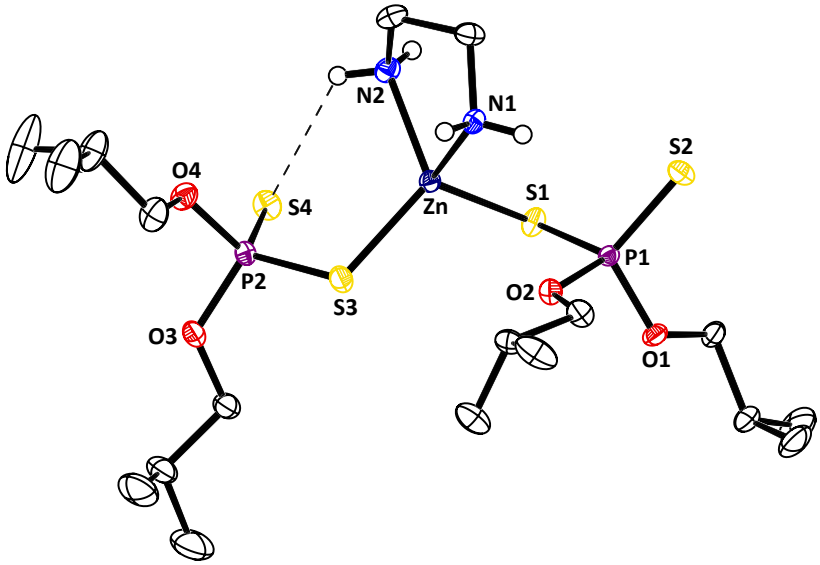

Figure 4.20: Molecular structure of [Zn{κ^1-*S*-$S_2P(O^iBu)_2$}$_2$(κ^2-EDA)] (**8**) with thermal ellipsoids at the 50% probability level; some H atoms are omitted for clarity. Selected bond distances: Zn-N1, 2.0631(13) Å; Zn-N2, 2.0596(13) Å; Zn-S1, 2.3279(5) Å; Zn-S3, 2.3013(5) Å; P1-S1, 2.0193(5) Å; P1-S2, 1.9488(6) Å; P2-S3, 2.0151(6) Å; P2-S4, 1.9494(6) Å. Selected bond angles: S1-P1-S2, 116.37(2)°; S3-P2-S4, 117.51(3)°.

Addition of 3 equivalents of EDA to **^{i}Bu ZDDP** in hexane instantly yielded a white precipitate. Subsequent ^{31}P NMR spectroscopic analysis of the supernatant liquid showed that no phosphorus-containing species were retained in solution, and so, consequently, a data point cannot be obtained for this amine:ZDDP ratio. ^{31}P NMR spectroscopic analysis of the precipitate is indicative of ionic DTP ligands {δ 108.3 ($CDCl_3$) or 111.2 (D_2O)}. The plateau in the ^{31}P NMR spectroscopic data between 1 and 2.5 equivalents

of EDA (Fig. 4.19) also indicates that $[Zn(EDA)_2][S_2P(O^iBu)_2]_2$ is not formed and 3 equivalents of EDA are required to sequester the zinc cation and ionise the DTP ligands. The chemical shift in this region of around 105 ppm is also not characteristic of ionic DTP. X-ray crystallographic analysis corroborated the solution NMR data and proved the precipitate to be a salt of the form $[Zn(EDA)_3][S_2P(O^iBu)_2]_2$ (**9**), containing anionic DTP ligands (Fig. 4.21). A summary of the complexation behaviour between **^{i}Bu ZDDP** and EDA is depicted in Scheme 4.2.

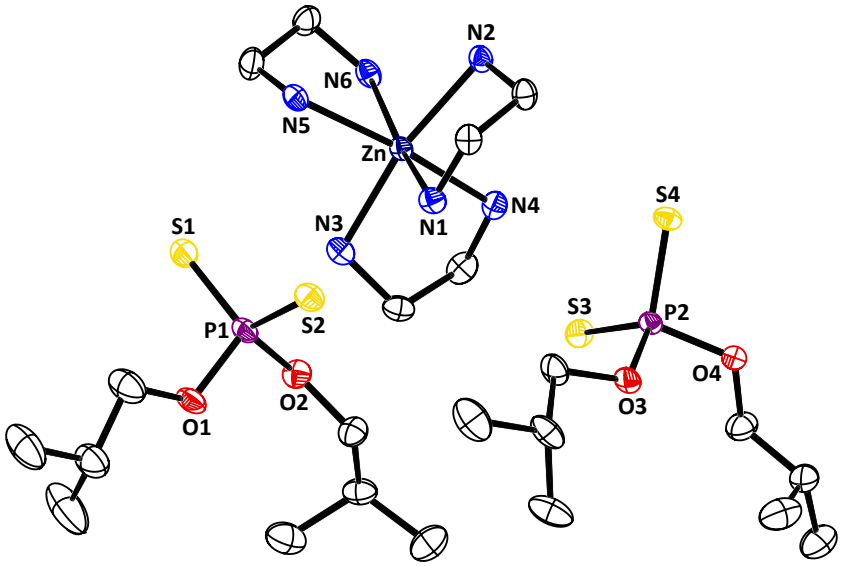

Figure 4.21: Molecular structure of $[Zn(EDA)_3][S_2P(O^iBu)_2]_2$ (**9**) with thermal ellipsoids at the 50% probability level; H atoms omitted for clarity. Selected bond distances: Zn-N, 2.1738(19)-2.2047(18) Å; P1-S1, 1.9625(9) Å; P1-S2, 1.9818(8) Å; P2-S3, 1.9689(8) Å; P2-S4, 1.9670(8) Å. Selected bond angles: S1-P1-S2, 119.60(4)°; S3-P2-S4, 117.38(4)°.

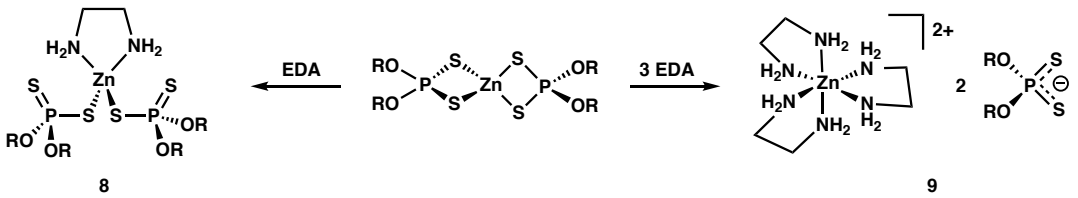

Scheme 4.2: Summary of the complexation behaviour observed between **^{i}Bu ZDDP** and EDA (R = ^{i}Bu).

The symmetrical nature of the ionic DTP ligands in **9** is reflected in the similar P-S bond lengths that are almost equivalent, something that contrasts with the monodentate DTP ligands of complex **8**. Since the structures of **8** and **9** provided two model

compounds, which displayed monodentate and ionic DTP configurations, respectively, Raman spectra were recorded of both complexes to determine if Raman spectroscopy could also distinguish between ionic and monodentate DTP ligands, a task that is often difficult to achieve using ^{31}P NMR spectroscopy, as the chemical shift guidelines for ionic and monodentate DTPs are not well-defined (Table 3.4). Previously in this thesis, it was demonstrated that the presence (or absence) of a Raman band near 660 cm^{-1}(assigned to ν(P=S)/$\nu(PS_2)_{asym}$) was an indicator of DTP binding mode, and could distinguish between symmetrically chelating/bridging, anisobidentate and monodentate binding modes, with the intensity of the 660 cm^{-1} increasing as the difference in P-S bond lengths increased (see Fig. 4.8). Therefore, extending this idea to encompass ionic DTP ligands, which have almost equivalent P-S bonds, means that Raman spectroscopy should be able to effectively distinguish between ionic and monodentate DTP species (where the difference in P-S bond lengths are greatest).

The Raman spectra of **8** and **9** are presented in Figure 4.22 and clearly distinguish between the two binding modes, with a strong Raman band being observed near 660 cm^{-1} for the monodentate DTP complex **8**, and no Raman vibration present in the same region for the ionic DTP complex **9**. This result again highlights the potential use of Raman spectroscopy for identifying DTP binding modes for species of unknown structure where suitable crystallographic data cannot be attained. The method is complementary to previously-established ^{31}P NMR spectroscopic generalisations[126] and the combination of both techniques should aid unambiguous assignment.

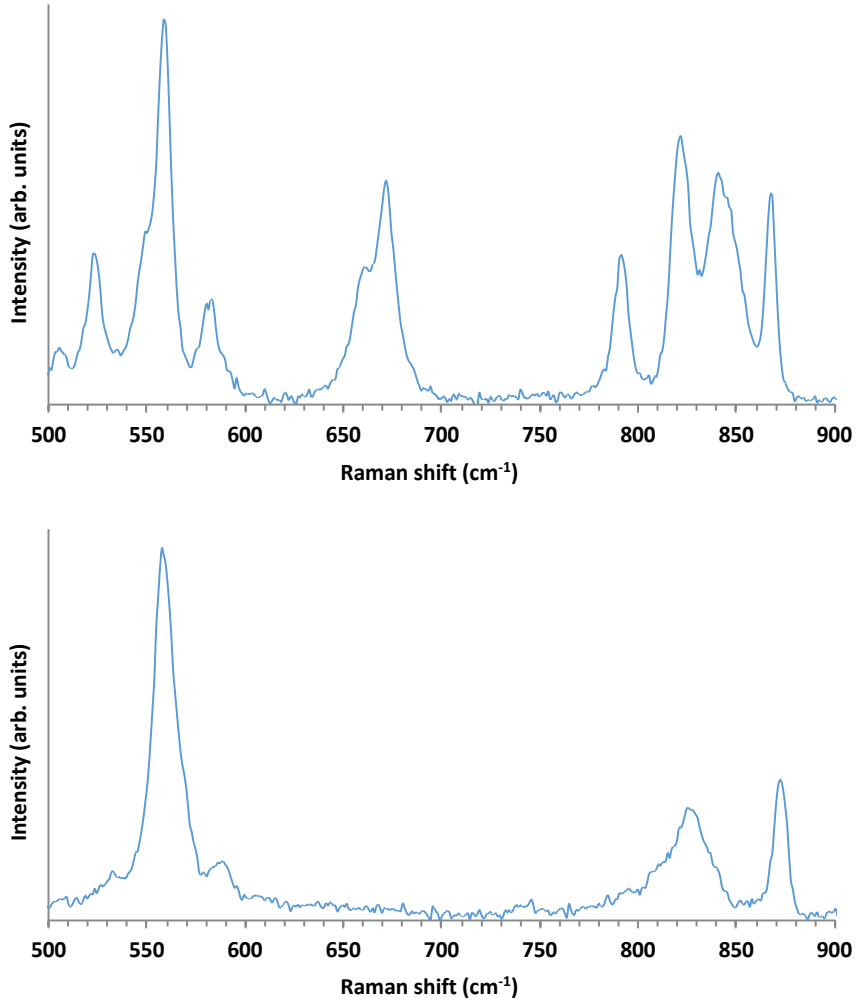

Figure 4.22: Solid-state Raman spectra (500-900 cm^{-1}) of $[Zn\{\kappa^1\text{-}S\text{-}S_2P(O^iBu)_2\}_2(\kappa^2\text{-}EDA)]$ (**8**), top, and $[Zn(EDA)_3][S_2P(O^iBu)_2]_2$ (**9**), bottom.

4.2.6.1.1 Effect of Alkyl Linker Chain Length on ZDDP Complexation

Based on the previous work by Shiomi *et al.*, outlined briefly above (Section 4.2.6.1), a key parameter in dictating the type of ZDDP-diamine interaction was reported to be the alkyl linker chain length. In addition, the most commercially relevant alkyl linker chain length, in terms of AkzoNobel's portfolio of OFMs at least, is a C_3 linker. As such, it was of significant interest to study the effect of increasing the alkyl chain linker from C_2 on ZDDP-diamine interactions.

Towards achieving this aim, our work then focussed on the simplest C_3 diamine, 1,3-diaminopropane (DAP) and titration studies with **^{i}Bu ZDDP** were again attempted. However, no phosphorus-containing species remained in hexane solution after the ad-

dition of just 2 equivalents of DAP to **^{i}Bu ZDDP**, meaning this analysis could not be completed. ^{31}P NMR spectroscopic analysis of the precipitate formed {δ 106.4 ($CDCl_3$)} was not conclusive in determining the nature of the DTP species as monodentate or ionic. In contrast, the Raman spectrum of the formed precipitate was conclusive in its assignment (Fig. 4.23), and in combination with ^{1}H NMR spectroscopic and elemental analysis data it is possible to conclude specifically that the precipitate is $[Zn(DAP)_2][S_2P(O^{i}Bu)_2]_2$ (**10**) (Scheme 4.3).

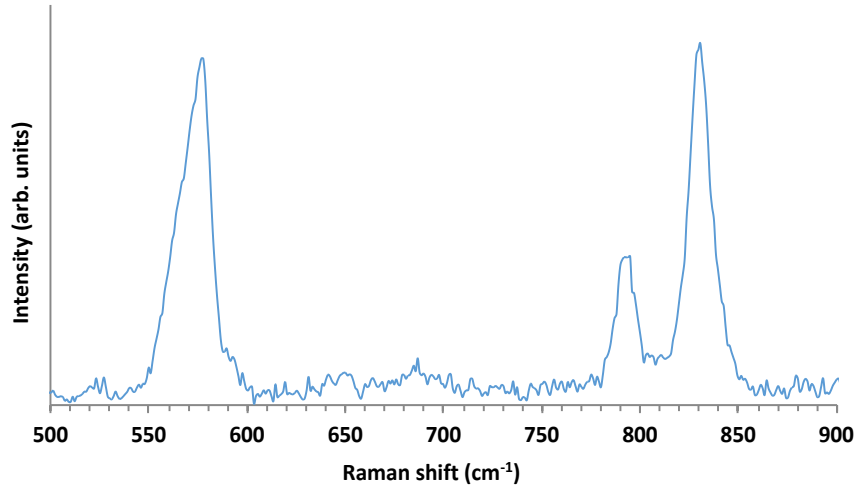

Figure 4.23: Solid-state Raman spectrum (500-900 cm^{-1}) of $[Zn(DAP)_2][S_2P(O^{i}Bu)_2]_2$ (**10**).

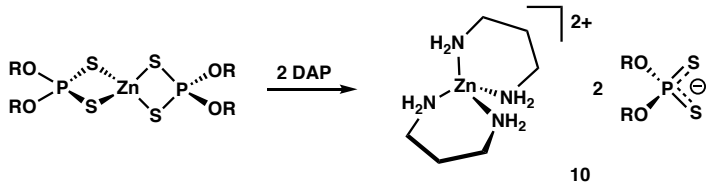

Scheme 4.3: Complexation pathway for **^{i}Bu ZDDP** with DAP (R = ^{i}Bu).

This result shows that DAP is more efficient than EDA in removing the zinc from **^{i}Bu ZDDP**, something likely to result from its improved flexibility and natural bite angle making it better able to wrap around and sequester the zinc dication. Similar behaviour with zinc has previously been identified by others, in which, EDA is reported to form complexes of the form $[Zn(EDA)_3]X_2$, while DAP is reported to form $[Zn(DAP)_2]X_2$ {X = Cl^-, Br^-, $\frac{1}{2}SO_4^{2-}$}.[166] The predicted molecular structure of **10** was subsequently confirmed upon isolation of single crystals suitable for X-ray crystallographic analysis

from hexane solution upon standing (Fig. 4.24). The solid-state structure of **10** consists of two equivalent DTP anions and a zinc-based dication. The zinc-based cation adopts a tetrahedral environment and is sequestered by two equivalent DAP ligands. The two DTP anions are equivalent and display almost identical P-S bond lengths as would be expected. The DTP sulfur atoms and an alkoxy oxygen atom form stabilising hydrogen bonds with the amino hydrogens of the zinc cation.

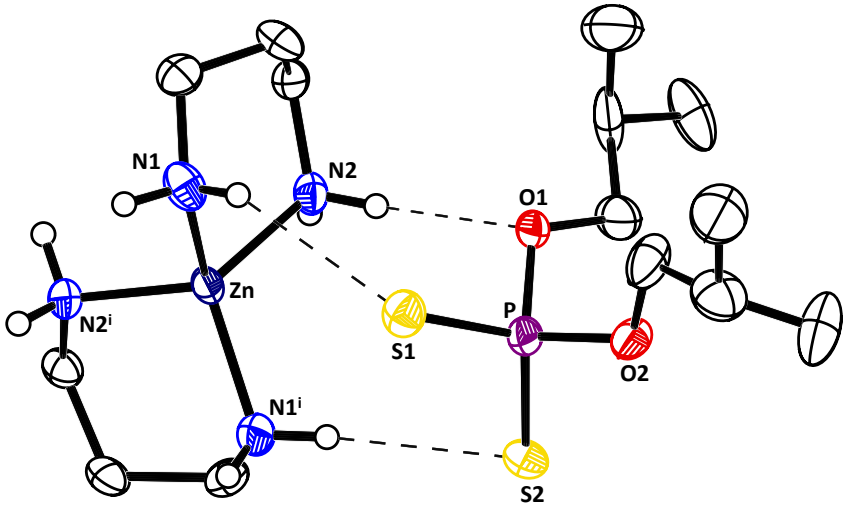

Figure 4.24: Molecular structure of $[Zn(DAP)_2][S_2P(O^iBu)_2]_2$ (**10**) with thermal ellipsoids at the 30% probability level; some H atoms are omitted and only one of two equivalent DTP ligands are shown for clarity. Selected bond distances: Zn-N1, 2.033(8) Å; Zn-N2, 2.044(7) P-S1, 1.951(4) Å; P-S2, 1.955(4) Å. Selected bond angles: S1-P-S2, 118.25(18)°.

This investigation was extended further to study the C_4 diamine, 1,4-diaminobutane (DAB), though yet again titration studies were unsuccessful due to precipitate formation, in this case after addition of 1 equivalent of DAB to **^{i}Bu ZDDP**. Once again, no phosphorus-containing species remained in solution and ^{31}P NMR {δ 103.9 ($CDCl_3$)} and Raman spectroscopic analysis of the precipitate (Fig. 4.25) would suggest an anisobidentate/monodentate binding configuration of the DTP ligands.

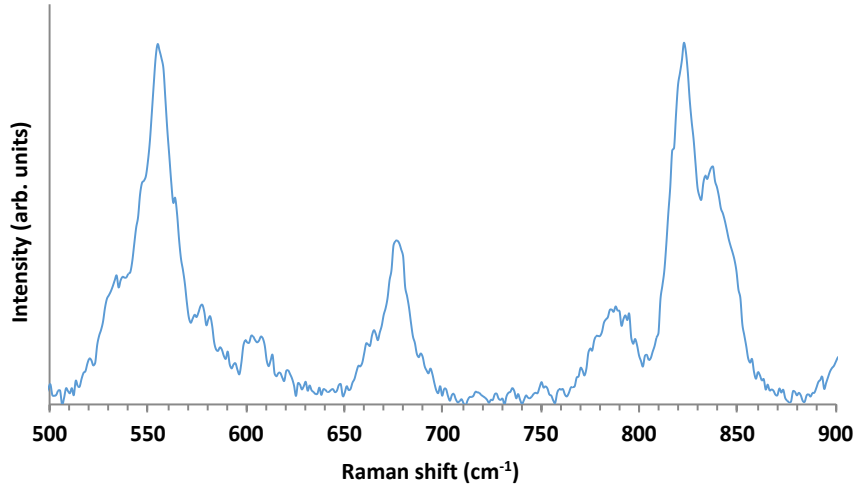

Figure 4.25: Solid-state Raman spectrum (500-900 cm^{-1}) of $[Zn\{\kappa^1\text{-}S\text{-}S_2P(O^iBu)_2\}_2(\mu\text{-}DAB)]_n$ (**11**).

However, such a DTP configuration would be possible for DAB bound in a chelating or a bridging fashion (with increasing alkyl linker length, chelation becomes increasingly disfavoured due to entropic effects and at some point one would expect a bridging rather than chelating diamine configuration). However, these two binding configurations are not easily distinguished by NMR spectroscopy or elemental analysis (Scheme 4.4).

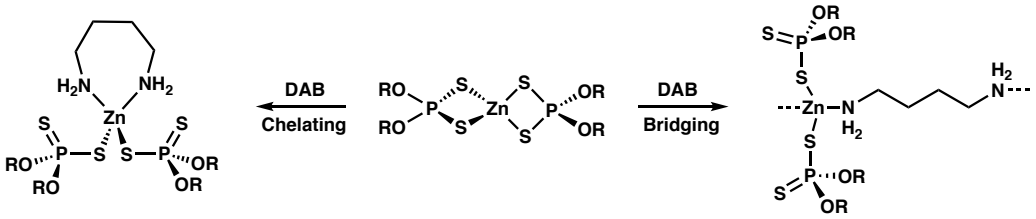

Scheme 4.4: Chelating and bridging configurations possible for ZDDP-DAB complex **11** (R = ^{i}Bu).

To distinguish between these two different modes of coordination, crystals of **11** were grown from hexane solution upon standing. Subsequent X-ray crystallographic analysis unequivocally proved that the DAB ligands bind in a bridging, rather than a chelating fashion. This is illustrated in the molecular structure of $[Zn\{\kappa^1\text{-}S\text{-}S_2P(O^iBu)_2\}_2(\mu\text{-}DAB)]_n$ (**11**) depicted in Figure 4.26. Complex **11** has a polymeric structure with zinc atoms present in a distorted tetrahedral environment, bound by two monodentate κ^1-*S*-DTP ligands and two bridging μ-DAB ligands, which connect zinc atoms in the polymeric chain. This structure resembles some of the polymeric ZDDP-bipyridyl struc-

tures reported by Tiekink *et al.*,[127–129] but to the best of our knowledge is the first reported polymeric ZDDP-diamine molecular structure with an aliphatic diamine. More importantly, it demonstrates the drastic impact on complex formation and structure a small change in the nature of the complexing amine can have in ZDDP-amine systems, something that likely translates to ZDDP-OFM formulations for amine-based OFMs.

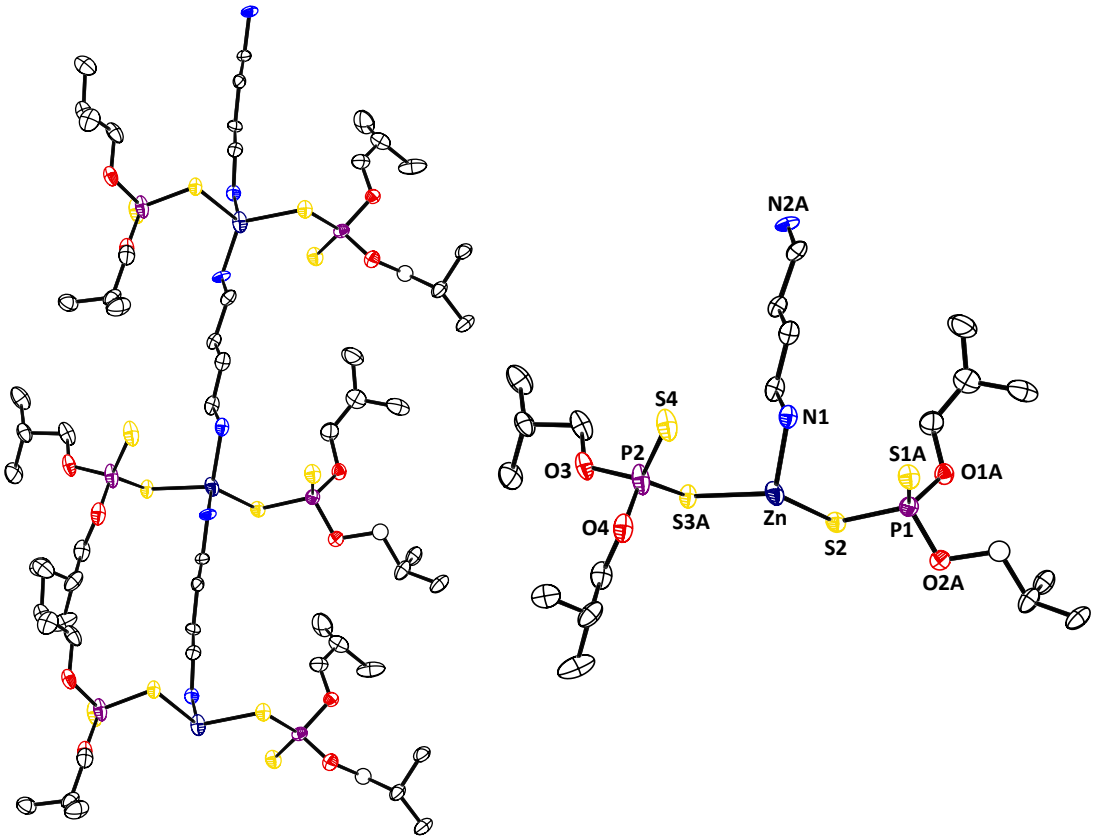

Figure 4.26: Molecular structure of $[Zn\{\kappa^1\text{-}S\text{-}S_2P(O^iBu)_2\}_2(\mu\text{-DAB})]_n$ (**11**) with thermal ellipsoids at the 50% probability level. Inset shows the asymmetric unit. Selected bond distances: Zn-N1, 2.021(4) Å; Zn-N2A, 1.901(9); Zn-S2, 2.3259(15) Å; Zn-S3A, 2.392(4) Å; P1A-S1A, 1.940(5) Å; P1A-S2, 2.029(6) Å; P2-S3A, 2.004(4) Å; P2-S4, 1.951(2) Å. Selected bond angles: S1A-P1A-S2, 117.0(3)°; S3A-P2-S4, 116.46(15)°.

4.2.6.1.2 Interaction of a Diamine-Based OFM with ZDDP

Having already studied 1,3-diaminopropane (DAP), our focus then moved towards the commercially available, N-tallow-1,3-diaminopropane (Duomeen T, **OFM4**) (Fig. 4.27).

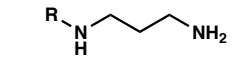

N-Tallow-1,3-Diaminopropane

Figure 4.27: Chemical structure of **OFM4**, where R is tallow (mixture of saturated and unsaturated alkyl chains from C_{12}-C_{18}, predominantly C_{18}).

Titration experiments were performed for **^{i}Bu ZDDP** with **OFM4** in hexane, the resulting change in ^{31}P chemical shift is plotted in Figure 4.28 and compared with that obtained using the monodentate **OFM1**. For **OFM4** two clear regimes can be observed; between 0-1 equivalents of amine an initial sharp increase in chemical shift occurs, then beyond this point the chemical shift continues to increase, but with a lower gradient up to the addition of 3 equivalents of amine.

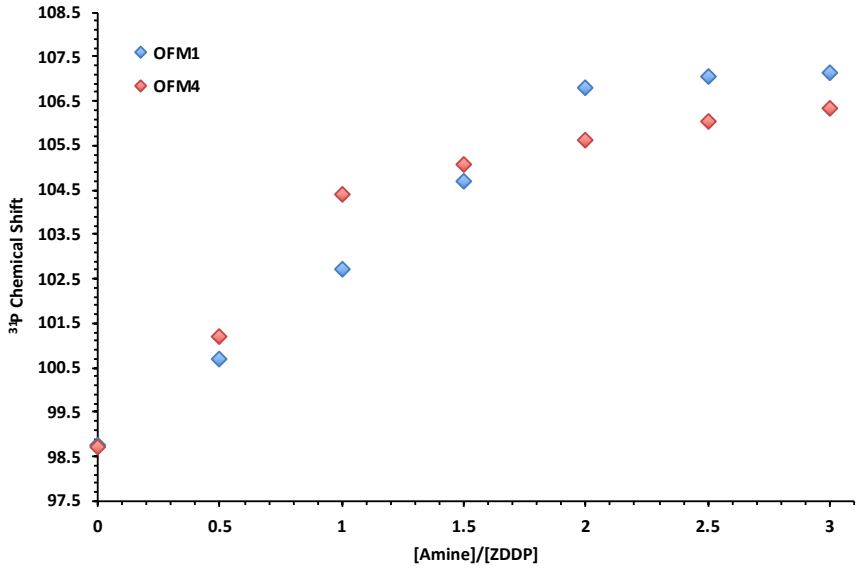

Figure 4.28: Plot of ^{31}P NMR (162 MHz, hexane) chemical shifts upon progressive addition of **OFM4** and **OFM1** to **^{i}Bu ZDDP**. $CDCl_3$ insert spiked with PPh_3 to provide lock. 0.006 M ZDDP (monomer), chemical shifts were referenced against PPh_3 in $CDCl_3$ (lit. -5.6 ppm[130]).

The trend observed is rationalised by initial chelation of one diamine ligand, which would yield a four-coordinate complex of the form [Zn{κ^1-*S*-$S_2P(O^iBu)_2$}$_2$(κ^2-**OFM4**)], analogous to those characterised previously in this work and by others.[124,125] Subsequently, upon further additions beyond 1 equivalent of amine, ionisation of the DTP ligands begins to occur and the degree of ionised DTP progressively increases as the concentration of amine increases, causing further increases in chemical shift (Scheme 4.5).

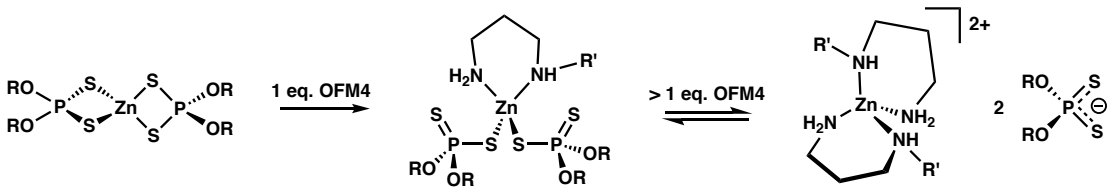

Scheme 4.5: Proposed reaction pathway for **^{i}Bu ZDDP** with **OFM4** (R = ^{i}Bu, R' = tallow).

Support for this rationalisation comes from studies of the model compound, N-methyl-1,3-diaminopropane (MDAP), which compared to DAP, more effectively mimics the steric requirements and the unsymmetrical nature of **OFM4,** but without the greasy alkyl chain that hinder crystallisations. In addition, MDAP is not a mix of alkyl chain lengths and is of higher purity than the commercial OFM making subsequent analysis much easier. Upon reacting MDAP with **^{i}Bu ZDDP** it was found that when combined in a 1:1 ratio, crystals suitable for X-ray crystallography could be isolated from a hexane/pentane solution on cooling and were subsequently identified as the MDAP chelate complex of the form [Zn{κ^1-*S*-$S_2P(O^iBu)_2$}$_2$(κ^2-MDAP)] (**12**) (Fig. 4.29, Scheme 4.6).

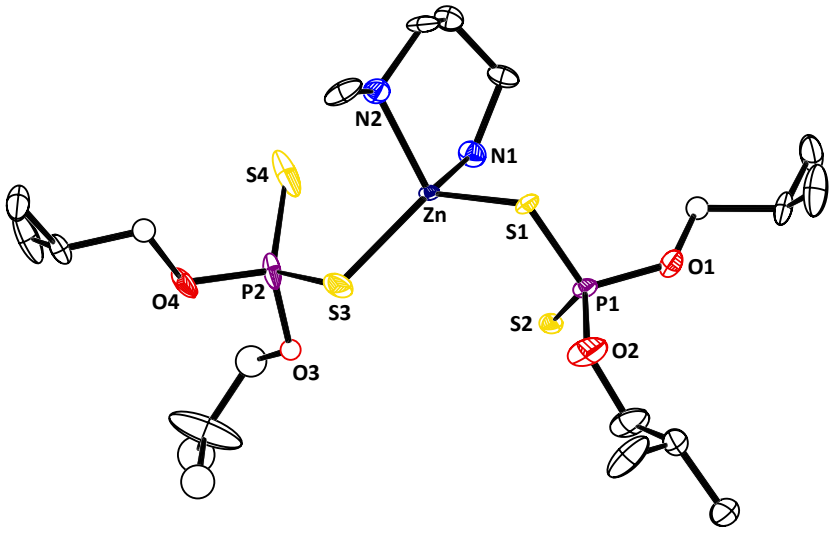

Figure 4.29: Molecular structure of [Zn{κ^1-*S*-$S_2P(O^iBu)_2$}$_2$(κ^2-MDAP)] (**12**) (one of two independent molecules) with thermal ellipsoids at the 30% probability level. The structure displays molecular connectivity but reliable bond lengths and bond angles can not be quoted (R-factor = 11.57%).

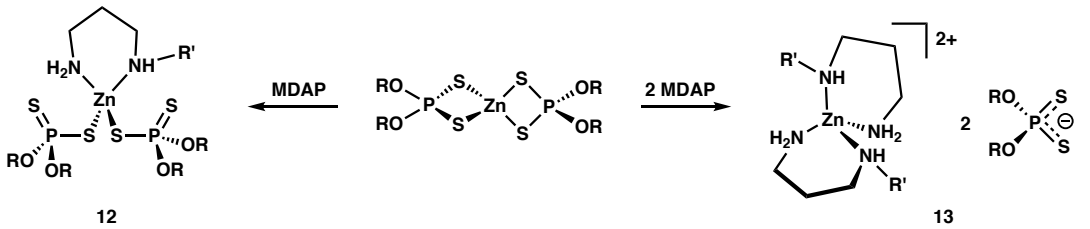

Scheme 4.6: Reaction pathways observed for MDAP with **^{i}Bu ZDDP** when combined in 1:1 and 1:2 ZDDP:amine ratios (R = ^{i}Bu, R' = Me).

At a greater MDAP:ZDDP ratio however, specifically 2:1, a white solid was obtained and although crystals suitable for X-ray crystallography could not be isolated, Raman spectroscopic analysis of this solid clearly identified the DTP ligands in this complex to be ionic, based on the absence of a Raman band near 660 cm^{-1} (Fig. 4.30). Full characterisation of the complex identifies it as $[Zn(MDAP)_2][S_2P(O^iBu)_2]_2$ (**13**) (Scheme 4.6), with an expected molecular structure similar to that of $[Zn(DAP)_2][S_2P(O^iBu)_2]_2$ (**10**) shown previously in Figure 4.24. The isolation of both the 1:1 chelate complex **12** and the salt **13**, isolated at different MDAP:ZDDP molar ratios clearly supports the two step chelation/ionisation pathway proposed for **OFM4** with increasing concentration. The ability of a commercial diamine-based OFM to ionise DTP ligands and produce anionic DTP ligands in solution, something not observed for monodentate amine-based OFMs at commercially relevant loadings, is something likely to significantly affect ZDDP thermal degradation and in turn the tribological behaviour of ZDDP-OFM systems; this topic will be discussed in more detail in the Chapter 5.

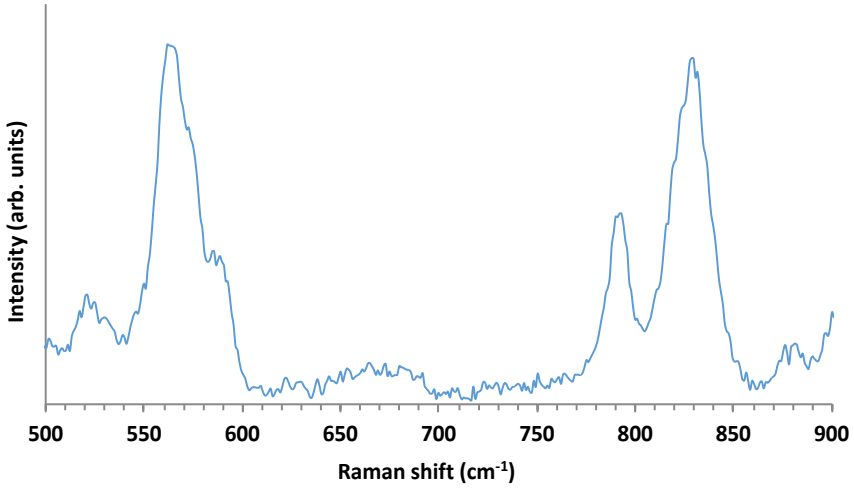

Figure 4.30: Solid-state Raman spectrum (500-900 cm^{-1}) of $[Zn(MDAP)_2][S_2P(O^iBu)_2]_2$ (**13**).

4.2.6.2 Interaction of an Ethoxylated OFM with ZDDP

Another structural motif that provides a secondary donor site, present in some commercial amine-based OFMs, is the ethoxylate chain. Ethoxylated amines such as Ethomeen HT/12 (hydrogenated tallow amine ethoxylate, **OFM5**) are produced by alkoxylation of a primary amine with ethylene oxide. These amine ethoxylates contain two oxygen-based secondary donor sites in addition to the nitrogen-based centre, as shown in Figure 4.31.

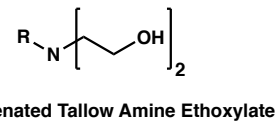

Figure 4.31: Chemical structure of **OFM5**, where R is hydrogenated tallow (mixture of alkyl chains from C_{12}-C_{18}, predominantly C_{18}).

To begin to determine if the aforementioned oxygen donor sites also participate in or effect ZDDP-OFM interactions, ^{31}P NMR spectroscopic titration studies were performed on **^{i}Bu ZDDP** with the ethoxylated amine **OFM5** (Fig. 4.32). Upon sequential addition of **OFM5**, a single $^{31}P[^1H]$ NMR resonance is observed in all cases alongside a notable high frequency chemical shift, something that mirrors the trend observed with all previously studied amines. However in this case, although initially a notable resonance sharpening is observed up to the addition of 1 equivalent of amine, addition of more than

1 equivalent of amine results in progressive resonance broadening, something in stark contrast to that previously observed with all other amines and OFMs.

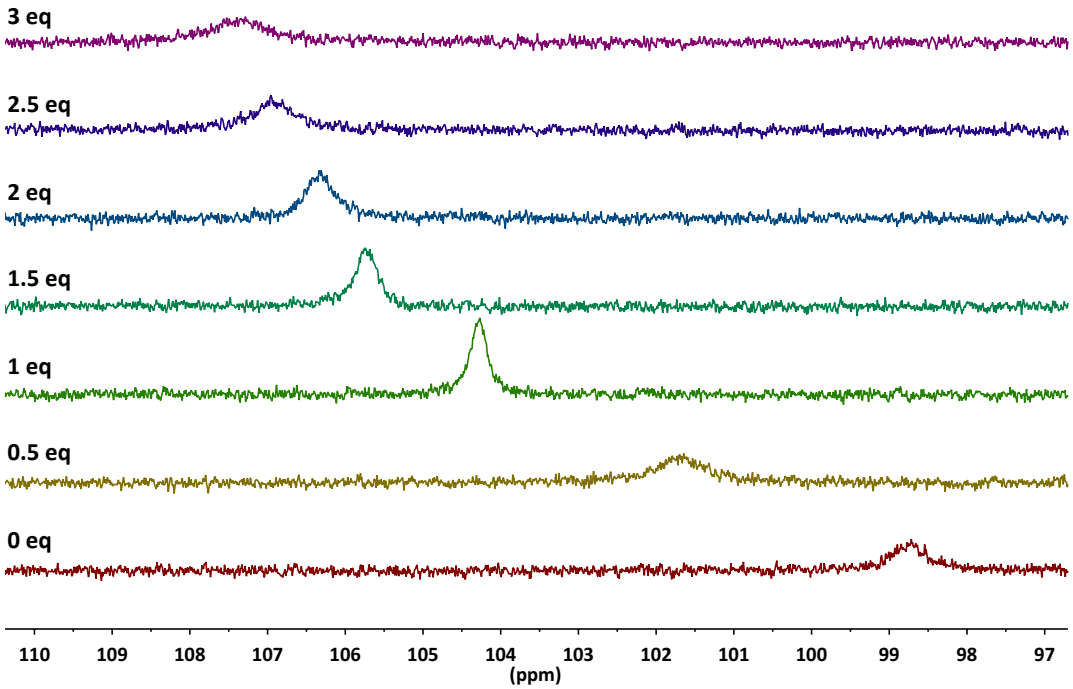

Figure 4.32: Evolution of the $^{31}P[^{1}H]$ NMR (162 MHz, hexane) spectrum of **^{i}Bu ZDDP** upon progressive addition of **OFM5**. 0.006 M ZDDP (monomer), $CDCl_3$ insert spiked with PPh_3 to provide lock. Chemical shifts were referenced against PPh_3 in $CDCl_3$ (lit. -5.6 ppm[130]).

Furthermore, the chemical shift changes observed for **^{i}Bu ZDDP** upon progressive addition of **OFM5**, is significantly greater than that observed upon sequential addition of an alkyl-substituted tertiary amine with no propensity to chelate, such as octadecyldimethylamine **(OFM3)** described previously (Fig. 4.33).

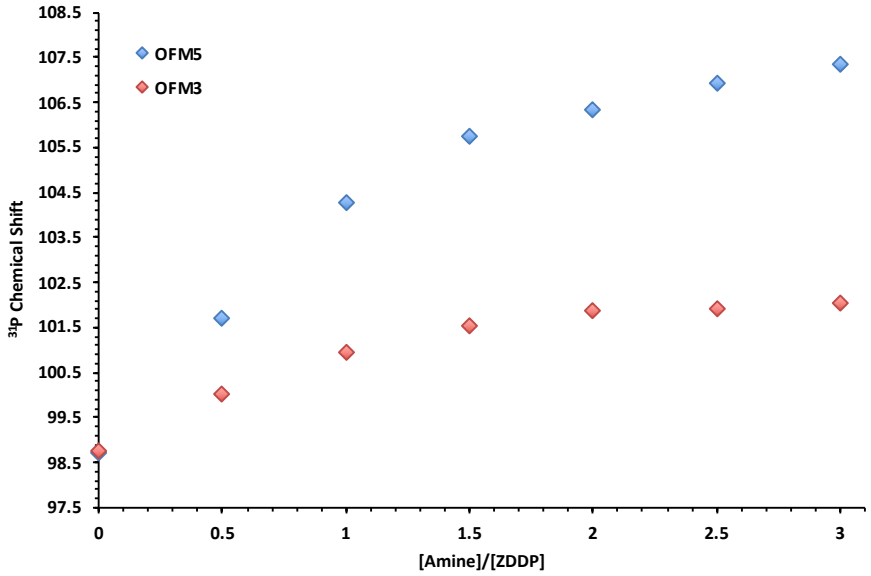

Figure 4.33: Plot of ^{31}P NMR (162 MHz, hexane) chemical shifts upon progressive addition of **OFM5** and **OFM3** to **^{i}Bu ZDDP**. $CDCl_3$ insert spiked with PPh_3 to provide lock. 0.006 M ZDDP (monomer), chemical shifts were referenced against PPh_3 in $CDCl_3$ (lit. -5.6 ppm[130]).

This disparity in chemical shift change observed between the **^{i}Bu ZDDP-OFM5** and **^{i}Bu ZDDP-OFM3** systems (Fig. 4.33) strongly suggests some coordination of the secondary hydroxyl donors of **OFM5** to the zinc centre of **^{i}Bu ZDDP**, resulting in a greater change in DTP binding mode and hence a larger change in chemical shift. Given the structure of **OFM5** it would be expected to bind to ZDDPs in a tridentate fashion, analogous to that observed in the diethanolamine (DEA) complex of zinc acetate, $[Zn(OAc)_2(DEA)]$ (Fig. 4.34).[167]

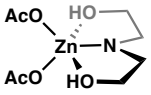

Figure 4.34: Chemical structure of $[Zn(OAc)_2(DEA)]$.

Further evidence to support hydroxyl group coordination to zinc was sought *via* ^{1}H NMR spectroscopic titrations, where the ^{1}H NMR chemical shifts of **OFM5** were recorded in the presence of increasing concentrations of **^{i}Bu ZDDP**. Particular attention was given to the CH_2 units of the ethoxylate chains and those adjacent to the amine nitrogen (see Fig. 4.35).

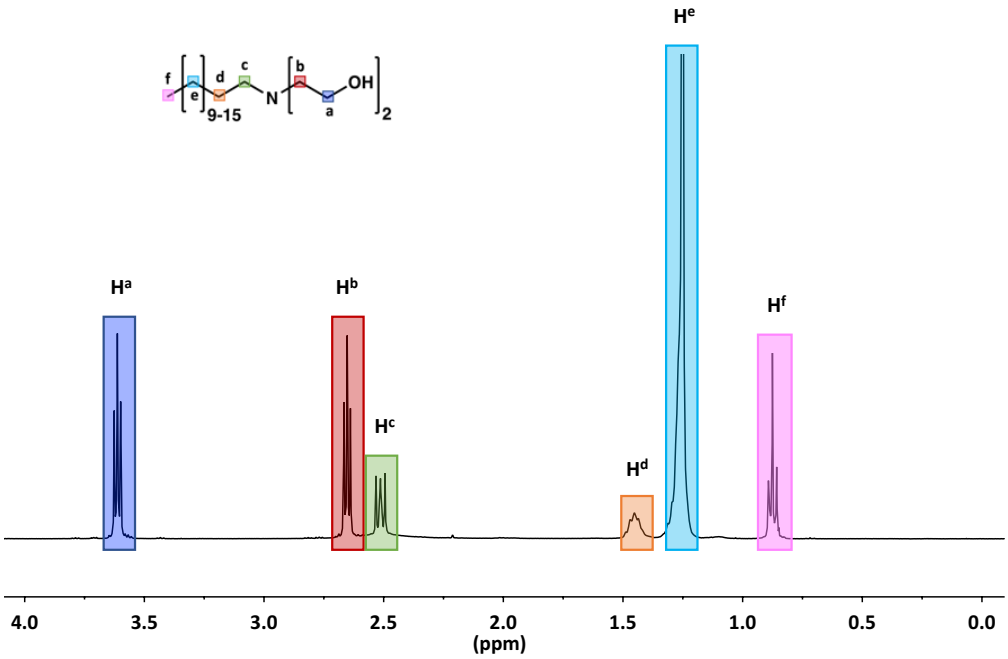

Figure 4.35: ^{1}H NMR (400 MHz, $CDCl_3$) spectrum and assignments for **OFM5**.

The change in chemical shift observed ($\Delta\delta$) with increasing **^{i}Bu ZDDP** concentration for the hydrogen environments H^a-H^d of **OFM5** are shown in Figure 4.36. The data presented shows that the proton environments $H^b$and H^c experience the greatest $\Delta\delta$ upon sequential addition of **^{i}Bu ZDDP**. This is unsurprising given their proximity to the nitrogen atom of **OFM5**, being the most Lewis basic donor present, hence these protons would be expected to experience the greatest deshielding effect. For the proton environments H^a and H^d, both of which are two carbons removed from the nitrogen centre, there is a large disparity in the $\Delta\delta$ observed, with environment H^a experiencing a significantly larger change in chemical shift. The larger $\Delta\delta$ observed for H^a is evidence to support hydroxyl group coordination to the zinc, which means the H^a protons experience a much greater deshielding effect compared to H^d. It is also noteworthy that high frequency shifts of the OH signal were also observed during the titration, though the signals were naturally broad and broadened further during the course of the titration.‡

‡In some cases the peaks of interest were found to partially overlap with signals from **^{i}Bu ZDDP**, this meant locating the centre of a given peak was sometimes difficult. Future experiments would utilise "pure shift" techniques to remove spin-spin coupling and render all ^{1}H NMR peaks as singlets (in the absence of heteronuclear couplings) and/or higher fields to help to decongest busy regions and make peak picking much easier.

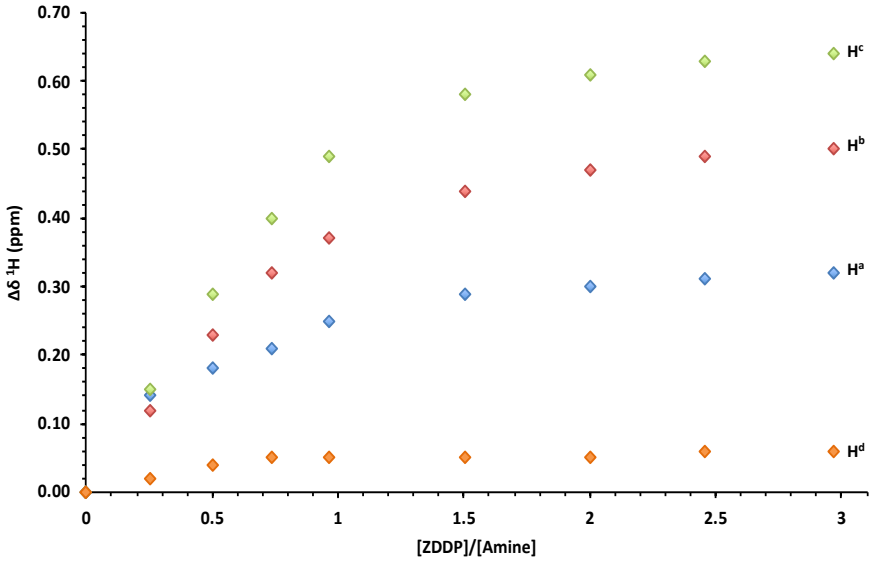

Figure 4.36: Plot of ^{1}H $\Delta\delta$ (400 MHz, $CDCl_3$) for the proton environments H^a-H^d of **OFM5** (see Fig. 4.35) upon progressive addition of **^{i}Bu ZDDP**.

Additional binding studies using the model compound N-methyldiethanolamine (MDEA), provided further verification of the proposed tridentate coordination mode of **OFM5**. Upon reacting MDEA with **^{i}Bu ZDDP** it was found that crystals suitable for X-ray crystallography could be isolated from a 1:2 ZDDP-amine solution. Somewhat unexpectedly, the isolated complex proved to be a tetrametallic zinc cluster, $Zn_4(MDEA)_2\{S_2P(O^iBu)_2\}_4$ (**14**) (Figs. 4.37 and 4.38).

The structure of **14** consists of four zinc atoms alternated with four oxygen atoms to form an exterior, eight-membered cycle, but with two zinc-oxygen bonds present between the central species to form three adjacent four-membered rings. The zinc atoms alternate in either a distorted trigonal bipyramidal or distorted tetrahedral environment, while the DTP ligands are present in monodentate κ^1-*S*-DTP or bridging μ-*S*,*S*-DTP configurations, with the difference in binding mode reflected in Zn-S and the associated P-S bond lengths. Adopting the notation used by Conterosito *et al.* for triethanolamine in its complexation reactions with zinc acetate,[168] for use with MDEA; neutral MDEA is denoted $MDEAH_2$, singly deprotonated MDEA is $MDEAH^-$, and doubly deprotonated MDEA is $MDEA^{2-}$.

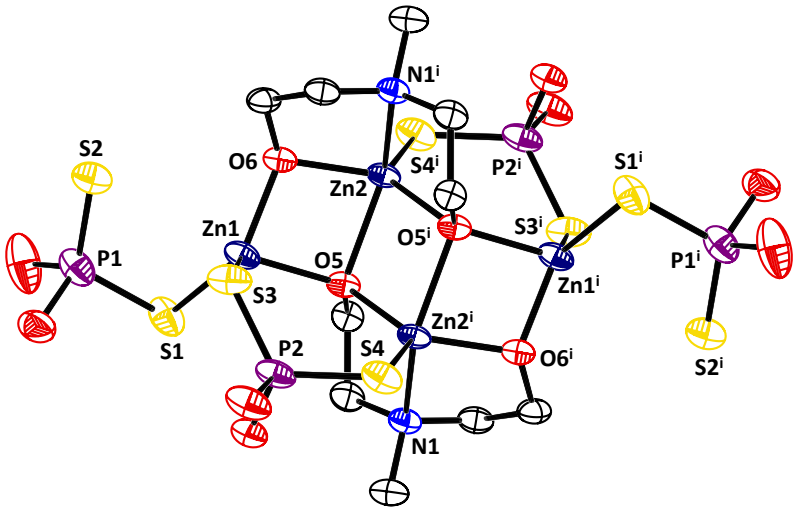

Figure 4.37: Molecular structure of $Zn_4(MDEA)_2(S_2P(O^iBu)_2)_4$ (**14**) with thermal ellipsoids at the 50% probability level; H atoms and the carbon atoms of the DTP ligands are omitted for clarity. Selected bond distances: Zn2-N1, 2.177(4) Å; Zn1-S1, 2.2995(16) Å; Zn1-S3, 2.3493(15) Å; Zn2-S4, 2.308(2) Å; P1-S1, 2.021(2) Å; P1-S2, 1.930(2) Å; P2-S3, 1.983(3) Å; P2-S4, 1.987(2) Å. Selected bond angles: S1-P1-S2, 115.47(11)°; S3-P2-S4, 117.80(10)°.

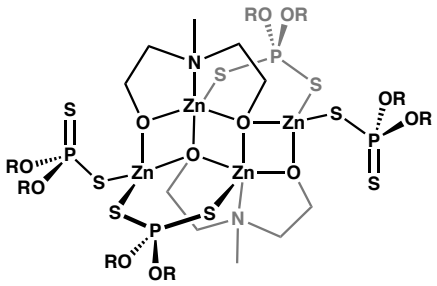

Figure 4.38: Chemical structure of $Zn_4(MDEA)_2(S_2P(O^iBu)_2)_4$ (**14**) (R = ^{i}Bu).

Based on charge balance considerations, the structure is made up of four Zn^{2+} ions, balanced by four DTP^- ligands and by two doubly deprotonated $MDEA^{2-}$ species. $MDEA^{2-}$ ligands are shown to bind zinc through the nitrogen atom, as expected, while one deprotonated hydroxyl, bridges two zinc atoms (μ-O), the other bridges three zinc atoms (μ_3-O).

Although more complex than anticipated, the structure of **14** unequivocally proves the chelation and involvement of the pendant ethanol branches in binding to zinc of ZDDP, thus explaining the stronger interaction observed for **OFM5** by ^{31}P NMR spectroscopy compared to a tertiary, alkyl-substituted equivalent. The solution ^{31}P NMR spectrum of the isolated complex **14** however, was observed to consist of multiple broad reson-

ances, likely reflecting the flexible nature of the cluster and/or reasonably slow exchange between phosphorus environments (relative to the NMR timescale). In contrast, solid-state ^{31}P NMR spectroscopy of **14** displays two singlet resonances, at 104.0 and 102.3 ppm (ratio 1:1), assigned to monodentate and bridging DTP configurations, respectively (Fig. 4.39); a result that is consistent with the two DTP environments observed in the molecular structure of **14** (Fig. 4.37).

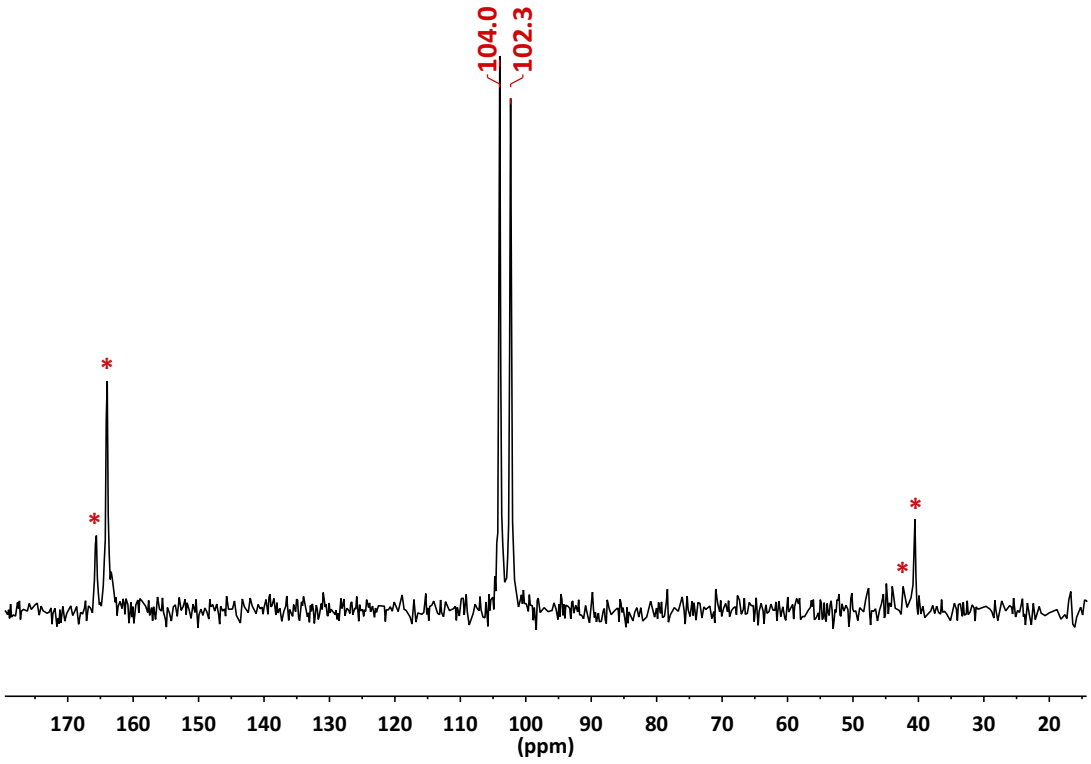

Figure 4.39: ^{31}P CP-MAS NMR (162 MHz) spectrum of $Zn_4(MDEA)_2\{S_2P(O^iBu)_2\}_4$ (**14**) measured at a spin-rate of 10 kHz. Asterisks indicate spinning sidebands.

The isolated complex **14** however, does not account for the full stoichiometry of the initial reagents present (1:2 ZDDP:amine ratio). Each **^{i}Bu ZDDP** molecule provides one zinc atom and two DTP ligands, therefore for a tetrametallic Zn_4 cluster, one would expect eight DTP ligands and, for a 1:2 ZDDP:MDEA ratio, eight MDEA ligands. Complex **14** contains only four DTP and two MDEA ligands, meaning four DTP ligands and six MDEA ligands are unaccounted for. Given the DTP ligands have been completely displaced from zinc they are expected to be in their ionic form, likely present with a MDEA-based ammonium counter cation, with the proposed reaction pathway presented in Scheme 4.7.

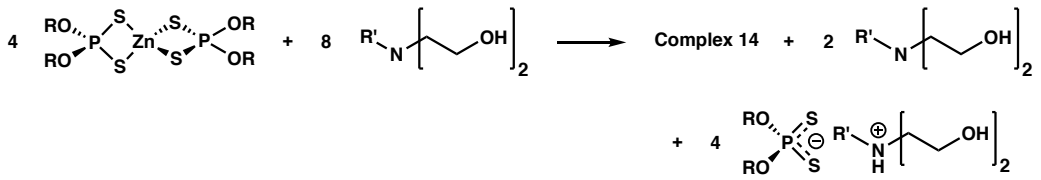

Scheme 4.7: Proposed reaction pathway for MDEA with **^{i}Bu ZDDP** (R = ^{i}Bu, R' = Me).

Initial attempts to verify the presence of ionic DTP were sought *via* the addition of an authentic sample of ionic DTP, potassium diisobutyl dithiophosphate (KDTP) {δ_P 110.4 ($CDCl_3$)}, to a solution of **^{i}Bu ZDDP** and **OFM5** (ratio 1:2) (Scheme 4.8, Fig. 4.40).

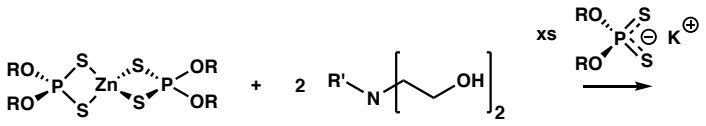

Scheme 4.8: Reaction scheme for the addition of excess KDTP to a solution of **^{i}Bu ZDDP** and **OFM5** (ratio 1:2) (R = ^{i}Bu, R' = tallow).

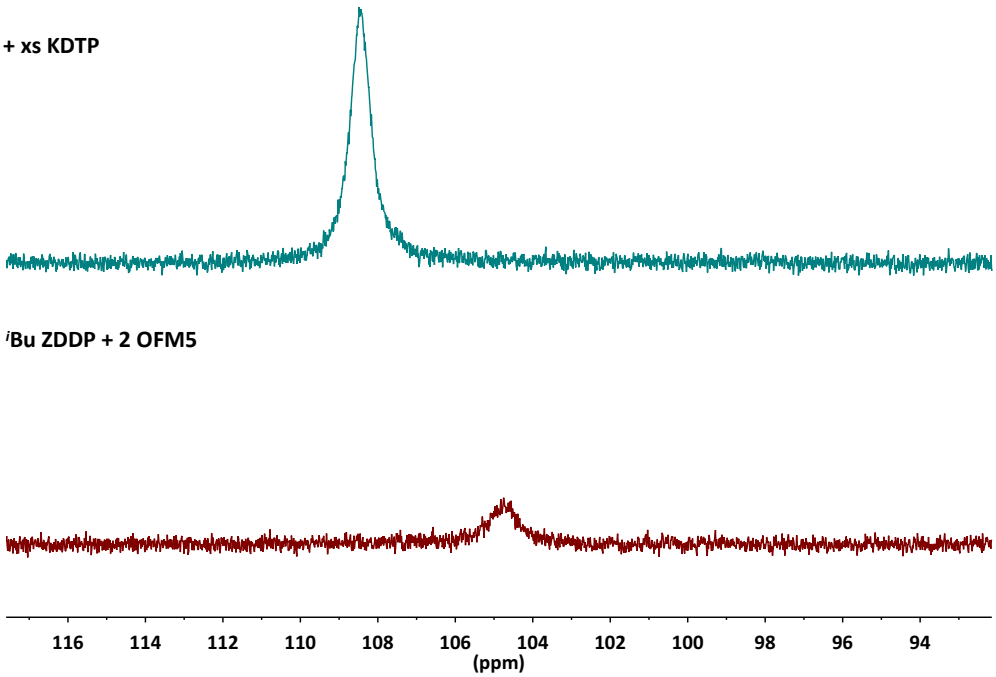

Figure 4.40: Evolution of the $^{31}P[^{1}H]$ NMR (162 MHz, $CDCl_3$) spectrum of **^{i}Bu ZDDP** upon addition of excess KDTP.

The presented data (Fig. 4.40) showed that upon addition of excess KDTP, the initial, broad signal (δ_P 104.7) sharpened and shifted to higher frequency (δ_P 108.4), towards the value known for the authentic KDTP sample. Given the observation of only a single ^{31}P

spectroscopic resonance and the high frequency shift towards that of KDTP, the results suggested that ionic DTP is in equilibrium with the other DTP-containing species and supports both the presence of ionic DTP in solution and the proposed reaction pathway (Scheme 4.7).

Subsequently, further evidence supporting the presence of ionic DTP in solution was achieved by low temperature variable-temperature ^{31}P NMR studies on a solution of **^{i}Bu ZDDP** and **OFM5** (ratio 1:2), the results of which are shown in Figure 4.41. At room temperature, a single, broad spectroscopic resonance is observed and upon lowering the temperature, the resonance broadens further and ultimately splits to reveal the presence of two signals, best observed at -20 °C. The higher frequency resonance is assigned to ionic DTP based (δ_P 109.1) while the second (δ_P 104.7) is rationalised as a cluster complex not dissimilar to complex **14**, by drawing comparison to the related **^{i}Bu ZDDP**-MDEA system previously studied (Figs. 4.37 and 4.38 and Scheme 4.7) . Subsequent lowering of the temperature below -20 °C further slows the exchange between the phosphorus environments and results in significant sharpening of the ionic DTP signal, something that ultimately means the spectroscopic resonance for the assigned zinc-containing cluster species is lost into the NMR baseline at -40 °C, and so only one spectroscopic resonance is observed. These data confirm the presence of anionic DTP in solution and demonstrates the ability of an ethoxylated amine-based OFM to complex with, and ionise the DTP ligands of a ZDDP, similar to what was observed for the diamine-based OFM (**OFM4**), something that may ultimately effect thermal and/or tribological performance in a lubricant formulation.

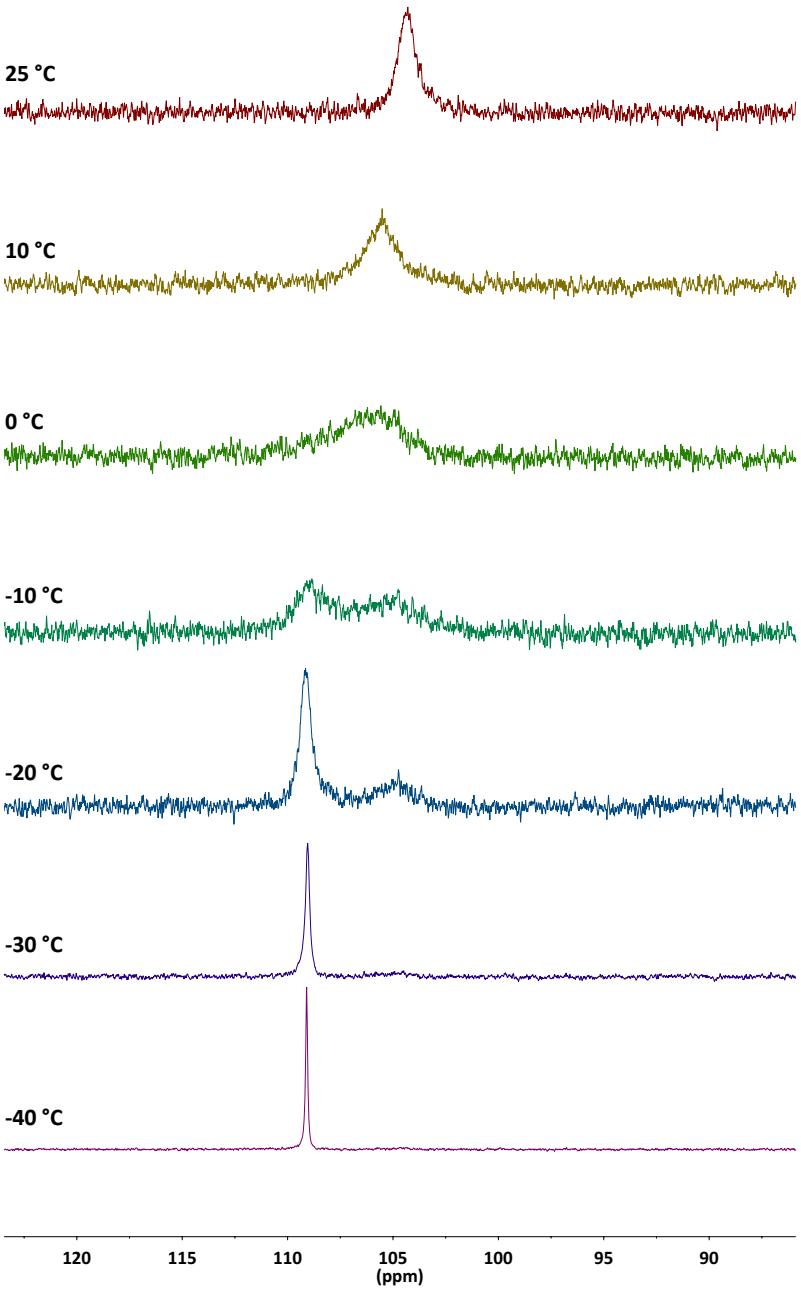

Figure 4.41: Evolution of the $^{31}P\{^{1}H\}$ NMR (202 MHz, $CDCl_3$) spectrum of a solution of **^{i}Bu ZDDP** and **OFM5** (ratio 1:2) as a function of temperature. 0.006 M ZDDP (monomer).

4.2.7 Investigating the Solution Interactions in Tertiary ZDDP-OFM-MoDTC Systems

To this point, the focus of this work has exclusively been concerned with binary ZDDP-amine or ZDDP-OFM systems. Though in a commercial lubricant formulation, ZDDPs

and OFMs are used in combination with a myriad of other additives (see Section 1.2.2). A key type of additive, often used and reported to synergise well with ZDDPs, are MoDTCs, previously introduced in Section 1.2.2.10.1. Given reports that ZDDPs synergise with MoDTCs, and that some ligand exchange reactions have been identified between the two species (see Scheme 1.5), it was of interest to us to determine if the presence of MoDTC had any effect on the complexation reactions observed between ZDDPs and amine-based OFMs.

However, to study this area reliably a pure, single-component form of MoDTC was required. Commercial sources often contain a mixture of MoDTCs and are of low purity, thus making the use of a commercial MoDTC sample unfeasible. Synthesis of a pure, single-component MoDTC was achieved *via* synthesis of the $Mo_2O_2S_2$ core in the form of the L-cysteine (cys) complex, $Na_2[Mo_2O_2S_2(cys)_2]$,[169] which was then subject to a ligand exchange reaction with the sodium salt of the desired dithiocarbamate (DTC) ligand (Scheme 4.9). This route is much more convenient that the more traditional approach based on substitution of $MoCl_5$, which itself is moisture sensitive, and requires subsequent treatment of the reaction product with H_2S gas to transform the di-μ-oxo complex into the di-μ-thio analogue.[170]

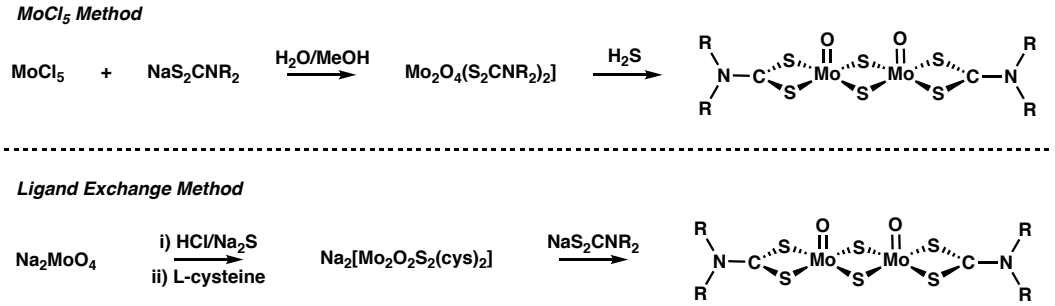

Scheme 4.9: Synthetic routes for the preparation of MoDTC complexes.

Initial synthesis of the isopropyl derivative, $[Mo_2O_2S_2(^iPr_2DTC)_2]$ (**^{i}Pr MoDTC**) was performed. However, the solubility of **^{i}Pr MoDTC** in non-polar media was poor, and therefore synthesis of the 2-ethylhexyl derivative, $[Mo_2O_2S_2(2\text{-}EH_2DTC)_2]$ (**2-EH MoDTC**), was subsequently performed and used for further studies. Single crystals of **2-EH MoDTC** were grown by layering a concentrated DCM solution with MeOH. The molecular structure of **2-EH MoDTC** is depicted in Figure 4.42.

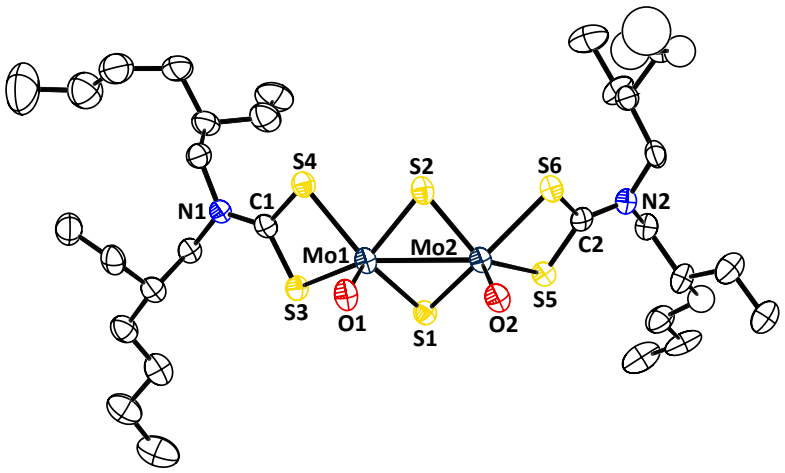

Figure 4.42: Molecular structure of **2-EH MoDTC** with thermal ellipsoids at the 50% probability level; H atoms and solvate DCM molecule are omitted for clarity. Selected bond distances: Mo1-Mo2, 2.8199(5) Å; Mo1-O1, 1.666(3) Å; Mo2-O2, 1.679(3) Å; C1-S3, 1.720(4) Å; C1-S4, 1.732(4); C2-S5, 1.731(4) Å; C2-S6, 1.723(4) Å; N1-C1, 1.309(5) Å; N2-C2, 1.306(5) Å. Selected bond angles: S3-Mo1-S4, 70.87(4)°; S5-Mo2-S6, 70.96(4)°; S3-C1-S4, 111.5(2)°; S5-C2-S6, 111.3(2)°.

As a brief insight into whether the presence of MoDTC modulates, changes or interferes with the previously observed ZDDP-amine interactions, ^{31}P NMR spectroscopic titration studies were performed by progressive addition of the previously studied hexylamine (Fig. 4.4) to a 1:1 mixture of **^{i}Bu ZDDP** and **2-EH MoDTC** (Fig. 4.43). Comparison of the data presented in Figures 4.4 and 4.43 demonstrated that the high frequency shift and resonance sharpening trends observed for the MoDTC-containing system mirrored those observed in the absence of MoDTC. This result implies that MoDTC does not interfere with the previously observed complex formation between ZDDP and amines, at room temperature at least. That said, ligand exchange is more pronounced at higher temperatures and therefore may have a greater impact at such temperatures.[87]

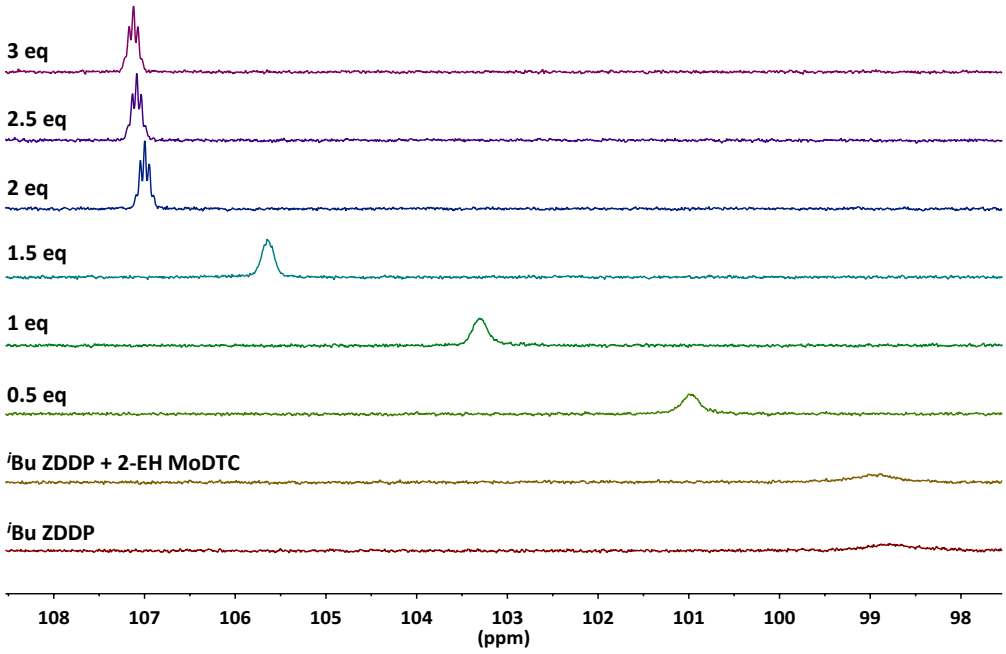

Figure 4.43: Evolution of the $^{31}P[^{1}H]$ NMR (162 MHz, hexane) spectrum of ***i*Bu ZDDP** upon initial addition of 1 equivalent of **2-EH MoDTC** and then progressive addition of hexylamine. 0.006 M ZDDP (monomer), $CDCl_3$ insert spiked with PPh_3 to provide lock. Chemical shifts were referenced against PPh_3 in $CDCl_3$ (lit. -5.6 ppm[130]).

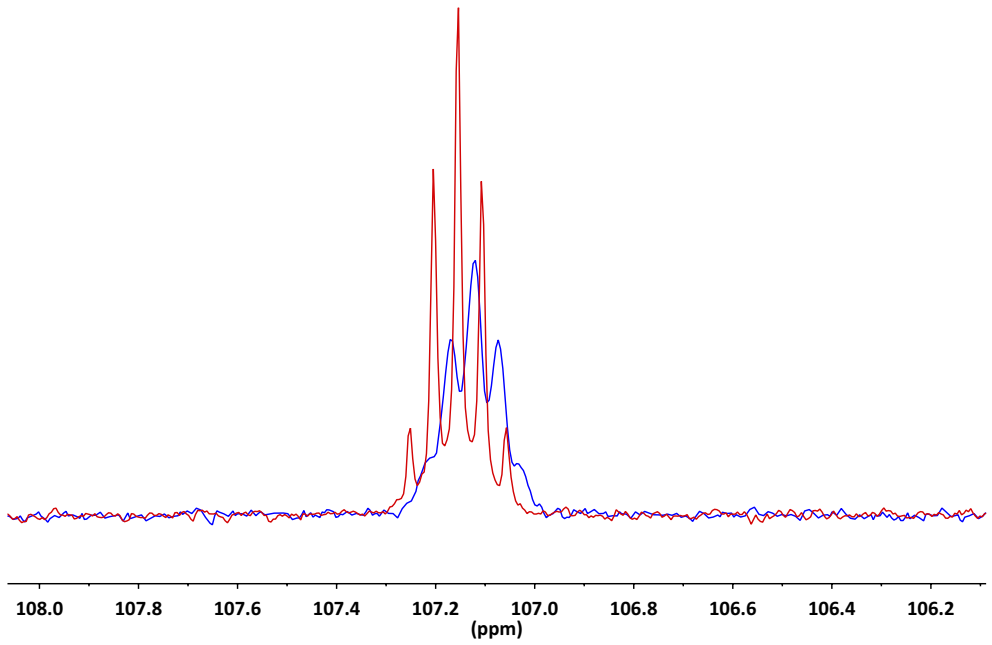

Figure 4.44: $^{31}P[^{1}H]$ NMR (162 MHz, hexane) spectra upon addition of 3 equivalents of hexylamine to ***i*Bu ZDDP** (red) and a 1:1 solution of ***i*Bu ZDDP** and **2-EH MoDTC** (blue). 0.006 M ZDDP (monomer), $CDCl_3$ insert spiked with PPh_3 to provide lock. Chemical shifts were referenced against PPh_3 in $CDCl_3$ (lit. -5.6 ppm[130]).

Closer inspection and comparison of the ^{31}P NMR spectra obtained from addition of

3 equivalents of hexylamine to **^{i}Bu ZDDP** and a 1:1 mixture of **^{i}Bu ZDDP** and **2-EH MoDTC** (Fig. 4.44) reveals that while the chemical shifts obtained are almost identical, a slightly broader spectroscopic resonance is apparent for the MoDTC-containing system, something that likely arises due to the paramagnetic nature of the Mo^{V} species.

4.2.8 Investigating ZDDP-OFM Interactions for Amine-Free OFMs

The final aspect of ZDDP-OFM interactions addressed in this chapter is whether the previously observed ZDDP-OFM interaction and complex formation pathways identified are limited and unique to amine-based OFMs, or are in fact, a more universal feature of ZDDP-OFM formulations. Glycerol mono-oleate (GMO), the reaction product of glycerin and oleic acid, is one the most common OFMs used in lubricant formulations (Fig. 4.45).[171] GMO also contains two potential hydroxyl-based donor sites that may bind to the zinc of ZDDP and so made a suitable candidate to begin to assess if other OFM-types interact with ZDDPs in a similar manner to that observed for amine-based OFMs.

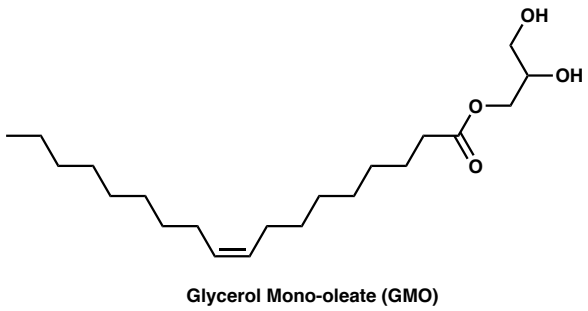

Figure 4.45: Chemical structure of GMO.

Similar ^{31}P NMR spectroscopic titration experiments, as described previously, were performed with incremental addition of GMO to an **^{i}Bu ZDDP** solution in hexane. The presented data (Fig. 4.46) showed that there is negligible change in the form or chemical shift of the **^{i}Bu ZDDP** spectroscopic resonance, even up to the addition of 10 equivalents of GMO, a loading that far exceeds commercially relevant ones. This result demonstrates that GMO does not interact with **^{i}Bu ZDDP** in solution and no change in DTP binding mode occurs, presumably as the hydroxyl donors of GMO are not strong enough Lewis bases to even partially displace the κ^2-*S*-*S*-DTP coordination. The solution ^{31}P NMR

spectroscopic data are supported in the solid-state by X-ray crystallographic studies, where crystals of unreacted **^{i}Bu ZDDP** (dimeric form, Fig. 3.11) formed upon standing and slow evaporation of the final ZDDP-GMO titration solution (ratio 1:10).

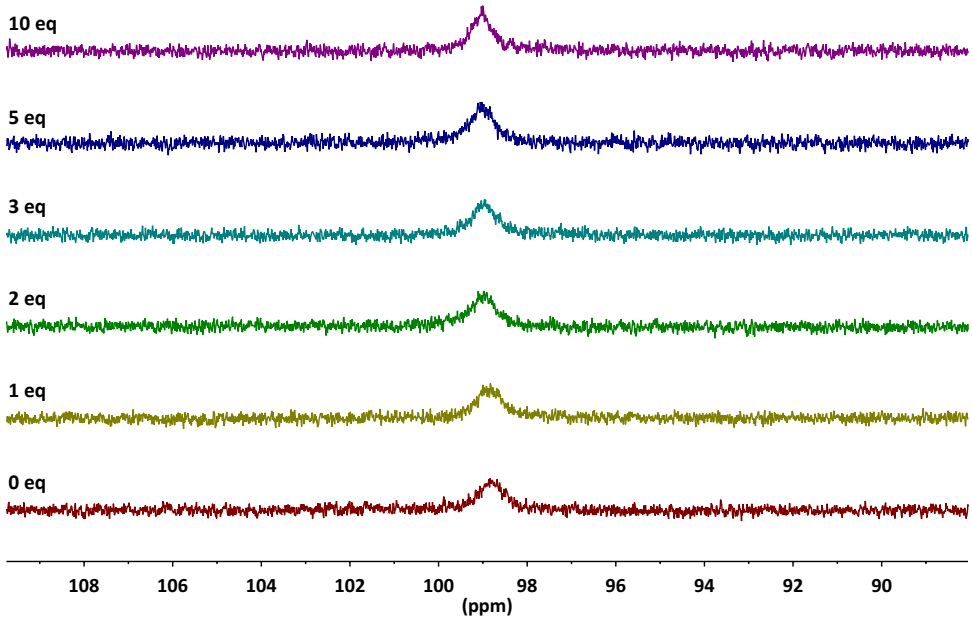

Figure 4.46: Evolution of the $^{31}P[^{1}H]$ NMR (162 MHz, hexane) spectrum of **^{i}Bu ZDDP** upon progressive addition of GMO. 0.006 M ZDDP (monomer), $CDCl_3$ insert spiked with PPh_3 to provide lock. Chemical shifts were referenced against PPh_3 in $CDCl_3$ (lit. -5.6 ppm [130]).

4.3 Conclusions

Following on from Chapter 3, through a combination ^{31}P NMR spectroscopic titration, X-ray crystallographic and Raman spectroscopic studies it has been demonstrated that amine-based OFMs interact with ZDDPs in a similar manner to that proven for ZDDP-Py' systems. X-Ray crystallography of complex **7** unequivocally identified the nature of ZDDP-OFM interaction for amine-based OFMs as a nitrogen-zinc complexation pathway, something that coincides with a change in DTP binding mode, and is to the best of our knowledge the first ZDDP-OFM complex isolated. Based on this, given the known structure of complex **7**, the use of Raman spectroscopy was subsequently extended and verified as a diagnostic tool for identifying DTP binding mode in ZDDP-OFM complexes.

The use of ^{31}P NMR spectroscopic titration studies then demonstrated that the propensity for ZDDP-OFM complex formation is strongly dependent on the steric demands of the complexing amine, with the strength of complex formation following the trend of amine substitution, 1° > 2° > 3°. Variable-temperature NMR spectroscopic studies showed that at higher temperatures, some decomplexation (reversible) occurs, though for 1° amine OFMs in particular, significant ZDDP-amine complex likely persists even at the extreme of engine sump temperature (130 °C).

Attention then moved on to investigate amines containing additional donor sites in the form of diamines and ethoxylated amines. For EDA it was demonstrated that depending on the molar ratio of amine present, either a ZDDP-EDA chelate complex, [Zn{κ^1-*S*-$S_2P(O^iBu)_2$}$_2$(κ^2-EDA)] (**8**), or a salt complex [Zn(EDA)$_3$][$S_2P(O^iBu)_2$]$_2$ (**9**) was formed. These two structures were then used to demonstrate how Raman spectroscopy could distinguish between monodentate and ionic DTP configurations, something that is often difficult using ^{31}P NMR spectroscopy alone.

The importance of alkyl linker chain length for diamines was revealed and it was found that upon moving from EDA (C_2 linker) to a C_4 linker as in DAB, the polymeric complex **11** is formed where the diamine ligands are bound in a bridging, rather a chelating fashion. For the intermediate C_3 linker, the diamine PDA was found to be more efficient in sequestering the zinc atom of ZDDP than EDA, requiring only 2 equivalents of PDA to form the salt complex [Zn(PDA)$_2$][$S_2P(O^iBu)_2$]$_2$ (**10**).

In terms of commercial OFMs, the ability of both ethoxylated and diamine-based OFMs to complex and ionise the DTP ligands of ZDDP, *via* subtly different pathways, was demonstrated using understanding gained while studying model amine systems. The diamine-based **OFM4** sequesters the zinc atom of ZDDP by chelation of 2 equivalents of **OFM4** and therefore produces a salt complex containing a zinc-based dication and two ionic DTP ligands. In contrast, the ethoxylated amine **OFM5** is thought to form a tetranuclear zinc cluster species, similar to complex **14**, which results in the formation of anionic DTP ligands that have an associated **OFM5**-based ammonium counter cation.

Finally, this chapter concluded with a brief insight into ZDDP interactions with alternative FMs, where it was apparent that MoDTC did not interfere with or effect the previously observed ZDDP-amine interactions (at room temperature), while GMO, one of the most commonly employed OFMs, did not interact with **^{i}Bu ZDDP** even up to the addition of 10 equivalents of GMO as proven by ^{31}P NMR spectroscopy.

Additive-additive interactions in bulk solution has been an area that has been largely neglected and scarcely studied, however this chapter highlights how such components of lubricant additive packages, specifically amine-based OFMs and ZDDPs, interact in bulk solution principally by a zinc-nitrogen interaction. As might be expected, the interaction observed is shown to be heavily dependent on the nature of the complexing amine and has the potential to cause significant, unexpected performance alterations. Though as yet, the full impact of the observed interactions are not known and hence, this will be the focus of the forthcoming chapter, where the thermal and tribological behaviour of selected ZDDP-amine systems will be assessed. Attempts to rationalise the trends observed will be made, based on the understanding gained regarding solution interactions in this, and previous chapters.

4.4 Experimental

4.4.1 General Considerations

Solvent purification and compound characterisation was performed as detailed in Chapter 3. All commercial OFMs and Nexbase 3043 mineral oil (Neste) were kindly supplied by AkzoNobel, while all other chemicals were purchased and used as received from commercial suppliers, unless otherwise stated. $Na_2[Mo_2O_2S_2(cys)_2]\cdot 4H_2O$[169] and $NaS_2CN(2\text{-}EH)_2$[172] were prepared according to literature methods.

IR Spectroscopy: Infra-red (IR) spectra were recorded on a Perkin Elmer FTIR Two^{TM} spectrometer fitted with an ATR probe.

^{31}P DOSY NMR Spectroscopy: A 700 MHz Varian spectrometer with an Agilent OneNMR probe able to deliver a maximum pulsed field gradient of 62 G cm^{-1} was used

to acquire ^{31}P Diffusion-Ordered SpectroscopY (DOSY) experiments using a convection compensated DBPPSTE pulse sequence. 20 pulse amplitudes ranging from 3.78 to 45.75 G cm^{-1} in equal steps of gradient squared, 148 transients, 1 dummy scan and 131852 complex data points covering 29 kHz were used. The diffusion-encoding pulsed gradient duration was 0.5 ms. The diffusion time was 0.5 s. The gradient stabilisation delay was 190 ms. The repetition time was 3.2 s, of which, 2.2 s comprised the acquisition time. The results were analysed using mono-exponential fittings.

Pulse sequence: convection compensated DBPPSTE (bipolar gradient pulses simulated echo sequence).[173,174]

4.4.2 Synthesis of ZDDP-amine complexes

General Procedure

ZDDP-amine complexes were obtained by adding the desired stoichiometry of amine to a solution of **^{i}Bu ZDDP** (0.15 g, 0.27 mmol) in hexane or ethanol (10 cm^3). Precipitate formation either occurred immediately, or in some cases, it was necessary to reduce the solvent volume by slow evaporation and/or cool the solution in the freezer to give the desired precipitate. The resulting materials were isolated by filtration, washed with cold hexane or ethanol and dried in air.

$[Zn\{\kappa^1\text{-}S\text{-}S_2P(O^iBu)_2\}_2(C_{18}\text{-}NH_2)_2]$ (7)

^{1}H NMR (700 MHz, Chloroform-*d*) δ 3.78 (dd, $^3J_{PH}$ = 7.9 Hz, $^3J_{HH}$ = 6.7 Hz, 8H, OCH_2CH(CH$_3$)$_2$), 2.97 (t, $^3J_{HH}$ = 7.3 Hz, 4H, N-α-CH_2), 1.97 (nonet, $^3J_{HH}$ = 6.7 Hz, 4H, OCH$_2$CH(CH$_3$)$_2$), 1.61 (p, $^3J_{HH}$ = 7.3 Hz, 4H, N-β-CH_2), 1.39 – 1.17 (m, 60H, N-alkyl-CH_2), 0.95 (d, $^3J_{HH}$ = 6.7 Hz, 24H, OCH$_2$CH(CH_3)$_2$), 0.88 (t, $^3J_{HH}$ = 7.1 Hz, 6H, N-alkyl-CH_3).

^{31}P{^{1}H} NMR (162 MHz, Chloroform-*d*) δ 104.5 (s).

^{13}C{^{1}H} NMR (176 MHz, Chloroform-*d*) δ 73.4 (d, $^2J_{CP}$ = 8.5 Hz, OCH$_2$CH(CH$_3$)$_2$), 42.4 (N-α-CH$_2$), 32.5 (N-β-CH$_2$), 32.1, 29.9, 29.8, 29.8, 29.7, 29.7 (N-δ-CH$_2$), 29.5, 29.4, 29.1 (d, $^3J_{CP}$ = 8.6 Hz, OCH$_2$$C$H(CH$_3$)$_2$), 26.8 (N-$\gamma$-$CH_2$), 22.8,

19.2 ($OCH_2CH(CH_3)_2$), 14.3 (N-alkyl-CH_3).

HRMS (ASAP) *m/z* Calc. for $[M+H]^+$ $C_{52}H_{115}N_2O_4P_2S_4Zn$ 1085.6506; Found 1085.6522.

(Calc.: C, 57.46; H, 10.57; N, 2.58. Found: C, 57.53; H, 10.56; N, 2.54).

Crystals suitable for X-ray crystallographic analysis were formed upon slow evaporation of a $CHCl_3$/MeCN (1:1) solution.

$[Zn\{\kappa^1$-*S*-$S_2P(O^iBu)_2\}_2(\kappa^2$-EDA)] (8)

^{1}H NMR (700 MHz, Chloroform-*d*) δ 3.80 (dd, $^3J_{PH}$ = 7.9 Hz, $^3J_{HH}$ = 6.7 Hz, 8H, $OCH_2CH(CH_3)_2$), 3.33 (br. s, 4H, NH_2), 3.24 – 3.20 (m, 4H, $NH_2(CH_2)_2NH_2$), 1.96 (nonet, $^3J_{HH}$ = 6.7 Hz, 4H, $OCH_2CH(CH_3)_2$), 0.95 (d, $^3J_{HH}$ = 6.7 Hz, 24H, $OCH_2CH(CH_3)_2$).

^{31}P{^{1}H} NMR (162 MHz, Chloroform-*d*) δ 103.5 (s).

^{13}C{^{1}H} NMR (176 MHz, Chloroform-*d*) δ 73.6 (d, $^2J_{CP}$ = 8.4 Hz, $OCH_2CH(CH_3)_2$), 40.4 ($NH_2(CH_2)_2NH_2$), 29.1 (d, $^3J_{CP}$ = 8.6 Hz, $OCH_2CH(CH_3)_2$), 19.2 ($OCH_2CH(CH_3)_2$).

MS (ASAP) *m/z* 547.0 (100%, $[M-(EDA)+H]^+$) 365.0 (18%, $[M-(DTP)^-]^+$). (*N.B.* molecular ion not observed).

(Calc.: C, 35.55; H, 7.29; N, 4.61. Found: C, 35.52; H, 7.23; N, 4.61).

Crystals suitable for X-ray crystallographic analysis formed from a saturated ethanol solution upon standing.

$[Zn(EDA)_3][S_2P(O^iBu)_2]_2$ (9)

^{1}H NMR (700 MHz, Chloroform-*d*) δ 3.74 (dd, $^3J_{PH}$ = 7.7 Hz, $^3J_{HH}$ = 6.7 Hz, 8H, $OCH_2CH(CH_3)_2$), 2.99 (s, 12H, $NH_2(CH_2)_2NH_2$), 2.31 (s, 12H, NH_2), 1.94 (nonet, $^3J_{HH}$ = 6.7 Hz, 4H, $OCH_2CH(CH_3)_2$), 0.94 (d, $^3J_{HH}$ = 6.7 Hz, 24H, $OCH_2CH(CH_3)_2$).

^{31}P{^{1}H} NMR (162 MHz, Chloroform-*d*) δ 108.4 (s).

^{13}C{^{1}H} NMR (176 MHz, Chloroform-*d*) δ 72.9 (d, $^{2}J_{CP}$ = 8.6 Hz, O*C*H$_2$CH(CH$_3$)$_2$), 40.9 (NH$_2$(*C*H$_2$)$_2$NH$_2$), 29.1 (d, $^{3}J_{CP}$ = 8.7 Hz, OCH$_2$*C*H(CH$_3$)$_2$), 19.3 (OCH$_2$CH(*C*H$_3$)$_2$).

MS (ESI) *m/z* +ve, 365.1 (100%, [M-2(EDA)-(DTP)$^-$]$^+$); -ve, 241.1 (100%, (DTP)$^-$). (*N.B*. molecular ion not observed).

(Calc.: C, 36.28; H, 8.30; N, 11.54. Found: C, 35.91; H, 8.15; N, 11.19)

Crystals suitable for X-ray crystallographic analysis were grown from hot ethanol.

[Zn(DAP)$_2$][S$_2$P(O^{i}Bu)$_2$]$_2$ (10)

^{1}H NMR (700 MHz, Chloroform-*d*) δ 3.75 (dd, $^{3}J_{PH}$ = 7.9 Hz, $^{3}J_{HH}$ = 6.7 Hz, 8H, OC*H*$_2$CH(CH$_3$)$_2$), 3.18 (s, 8H, N*H*$_2$), 3.14 – 3.10 (m, 8H, N-α-C*H*$_2$), 1.95 (nonet, $^{3}J_{HH}$ = 6.7 Hz, 4H, OCH$_2$C*H*(CH$_3$)$_2$), 1.89 – 1.84 (m, 4H, N-β-C*H*$_2$), 0.94 (d, $^{3}J_{HH}$ = 6.7 Hz, 24H, OCH$_2$CH(C*H*$_3$)$_2$).

^{31}P{^{1}H} NMR (283 MHz, Chloroform-*d*) δ 106.4 (s).

^{13}C{^{1}H} NMR (176 MHz, Chloroform-*d*) δ 73.1 (d, $^{2}J_{CP}$ = 8.5 Hz, O*C*H$_2$CH(CH$_3$)$_2$), 42.2 (N-α-*C*H$_2$), 30.7 (N-β-*C*H$_2$), 29.1 (d, $^{3}J_{CP}$ = 8.7 Hz, OCH$_2$*C*H(CH$_3$)$_2$), 19.3 (OCH$_2$CH(*C*H$_3$)$_2$).

MS (ESI) *m/z* +ve, 695.2 (12%, [M+H]$^+$), 379.1 (100%, [M-(DAP)-(DTP)$^-$]$^+$); -ve, 241.1 (100%, (DTP)$^-$).

(Calc.: C, 37.95; H, 8.11; N, 8.05. Found: C, 37.57; H, 7.98; N, 8.02).

Crystals suitable for X-ray crystallographic analysis formed from a hexane solution on standing.

[Zn{κ^1-*S*-S$_2$P(O^{i}Bu)$_2$}$_2$(μ-DAB)]$_n$ (11)

^{1}H NMR (700 MHz, Chloroform-*d*) δ 3.79 (dd, $^{3}J_{PH}$ = 7.9 Hz, $^{3}J_{HH}$ = 6.7 Hz, 8H, OC*H*$_2$CH(CH$_3$)$_2$), 3.14 – 3.10 (m, 4H, N-α-C*H*$_2$), 1.96 (nonet, $^{3}J_{HH}$ = 6.7 Hz, 4H, OCH$_2$C*H*(CH$_3$)$_2$), 1.92 – 1.87 (m, 4H, N-β-C*H*$_2$), 0.94 (d, $^{3}J_{HH}$ = 6.7 Hz, 24H, OCH$_2$CH(C*H*$_3$)$_2$).

^{31}P{^{1}H} NMR (287 MHz, Chloroform-*d*) δ 103.9 (s).

^{13}C{^{1}H} NMR (176 MHz, Chloroform-*d*) δ 73.4 (d, $^{2}J_{CP}$ = 8.4 Hz, O*C*H$_2$CH(CH$_3$)$_2$), 42.0 (N-α-*C*H$_2$), 29.0 (d, $^{3}J_{CP}$ = 8.6 Hz, OCH$_2$*C*H(CH$_3$)$_2$), 28.0 (N-β-*C*H$_2$), 19.2 (OCH$_2$CH(*C*H$_3$)$_2$).

(Calc.: C, 37.76; H, 7.60; N, 4.40. Found: C, 37.46; H, 7.50; N, 4.37).

Crystals suitable for X-ray crystallographic analysis formed from a hexane solution on standing.

[Zn{κ^1-*S*-S$_2$P(O^{i}Bu)$_2$}$_2$(κ^2-MDAP)] (12)

^{1}H NMR (600 MHz, Chloroform-*d*) δ 4.09 – 4.01 (m, 3H, CH$_3$N*H*/N*H*$_2$), 3.80 (dd, $^{3}J_{PH}$ = 7.9, $^{3}J_{HH}$ = 6.7 Hz, 8H, OC*H*$_2$CH(CH$_3$)$_2$), 3.29 – 3.22 (m, 2H, NH$_2$C*H*$_2$), 2.99 (br. s, 2H, CH$_3$NHC*H*$_2$), 2.49 (d, $^{3}J_{HH}$ = 6.1 Hz, 3H, C*H*$_3$NH), 1.97 (nonet, $^{3}J_{HH}$ = 6.7 Hz, 4H, OCH$_2$C*H*(CH$_3$)$_2$)*, 0.95 (d, $^{3}J_{HH}$ = 6.7 Hz, 24H, OCH$_2$CH(C*H*$_3$)$_2$).

^{31}P{^{1}H} NMR (162 MHz, Chloroform-*d*) δ 103.6 (s).

^{13}C{^{1}H} NMR (151 MHz, Chloroform-*d*) δ 73.3 (d, $^{2}J_{CP}$ = 8.4 Hz, O*C*H$_2$CH(CH$_3$)$_2$), 53.3 (CH$_3$NH*C*H$_2$), 42.4 (NH$_2$*C*H$_2$), 37.3 (*C*H$_3$NH), 28.9 (d, $^{3}J_{CP}$ = 8.7 Hz, OCH$_2$*C*H(CH$_3$)$_2$), 27.7 (CH$_3$NHCH$_2$*C*H$_2$CH$_2$NH$_2$), 19.0 (OCH$_2$CH(*C*H$_3$)$_2$).

* Peak overlaps and masks CH$_3$NHCH$_2$C*H*$_2$CH$_2$NH$_2$ resonance, as observed in the HSQC spectrum.

Crystals suitable for X-ray crystallographic analysis were obtained by cooling a hexane/pentane solution in the freezer.

[Zn(MDAP)$_2$][S$_2$P(O^{i}Bu)$_2$]$_2$ (13)

^{1}H NMR (700 MHz, Chloroform-*d*) δ 3.78 (dd, $^{3}J_{PH}$ = 7.9 Hz, $^{3}J_{HH}$ = 6.7 Hz, 8H, OC*H*$_2$CH(CH$_3$)$_2$), 3.05 (t, $^{3}J_{HH}$ = 6.0 Hz, 4H, NH$_2$C*H*$_2$),* 2.84 (t, $^{3}J_{HH}$ = 6.0 Hz, 4H, CH$_3$NHC*H*$_2$), 2.46 (s, 6H, C*H*$_3$NH), 1.96 (nonet, $^{3}J_{HH}$ = 6.7 Hz, 4H, OCH$_2$C*H*(CH$_3$)$_2$), 1.86 (p, $^{3}J_{HH}$ = 6.0 Hz, 4H, CH$_3$NHCH$_2$C*H*$_2$CH$_2$NH$_2$), 0.94 (d, $^{3}J_{HH}$ = 6.8 Hz, 24H, OCH$_2$CH(C*H*$_3$)$_2$).

$^{31}P\{^{1}H\}$ NMR (162 MHz, Chloroform-*d*) δ 104.8 (s).

$^{13}C\{^{1}H\}$ NMR (176 MHz, Chloroform-*d*) δ 73.3 (d, $^{2}J_{CP}$ = 8.4 Hz, O*C*H_2CH(CH_3)$_2$), 52.0 (CH_3NH*C*H_2), 42.0 (NH_2*C*H_2), 37.1 (*C*H_3NH), 30.1 (CH_3NHCH_2*C*$H_2CH_2NH_2$), 29.0 (d, $^{3}J_{CP}$ = 8.7 Hz, OCH_2*C*H(CH_3)$_2$), 19.2 (OCH_2CH(*C*H_3)$_2$).

MS (ESI) *m/z* +ve, 723.2 (4%, $[M+H]^+$), 393.1 (100%, $[M-(DAP)-(DTP)^-]^+$); -ve, 241.1 (100%, $(DTP)^-$).

(Calc.: C, 39.80; H, 8.35; N, 7.74. Found: C, 39.54; H, 8.25; N, 7.68)

* Peak overlaps with and completely masks broad NH resonance. Confirmed by collecting an additional ^{1}H NMR spectrum at a lower frequency of 400 Hz.

$Zn_4(MDEA)_2\{S_2P(O^iBu)_2\}_4$ (14)

$^{31}P\{^{1}H\}$ SSNMR (162 MHz) δ 104.0 (s), 102.3 (s) (ratio 1:1). Two resonances arising from two DTP binding configurations - consistent with molecular structure.

(Calc.: C, 34.52; H, 6.48; N, 1.92. Found: C, 34.51; H, 6.47; N, 1.92).

Crystals suitable for X-ray crystallographic analysis were obtained by slow evaporation of an EtOH solution.

4.4.3 Synthesis of MoDTC

$[Mo_2O_2S_2(2\text{-}EH_2DTC)_2]$

$NaS_2CN(2\text{-}EH)_2$ (0.52 g, 1.56 mmol) was added to a MeOH/H_2O (1:1 v/v) solution of $Na_2[Mo_2O_2S_2(cys)_2]\cdot 4H_2O$ (0.5 g, 0.78 mmol). The resulting mixture was stirred for 1.5 h to yield a cloudy yellow solution. Volatile components were then removed *in vacuo* to yield a sticky, yellow semi-solid. The resulting material was treated with a small portion of hexane (15 cm^3) which produced an off-white precipitate. After filtration, volatile components were removed from the filtrate *in vacuo* to yield a yellow oil, which solidified on scraping (0.60 g, 85% yield).

HRMS (ASAP) *m/z* Calc. for $M^{+\cdot}$ $C_{34}H_{68}N_2O_2S_6Mo_2$ 912.1741; Found 912.1775.

IR (neat, cm^{-1}) $\nu_{C=N}$ 1525 (s); $\nu_{Mo=O}$ 957 (s), 967 (vs).

(Calc.: C, 44.33; H, 7.44; N, 3.04. Found: C, 44.12; H, 7.36; N, 3.01).

Crystals suitable for X-ray crystallographic analysis where grown by layering a concentrated DCM solution with MeOH.

Chapter 5

Thermolysis and Tribological Studies on ZDDP-OFM Systems

5.1 Introduction

The thermal stability of ZDDPs has long been recognised as a key parameter in dictating their antiwear performance and tribofilm formation rate. Specifically, an inverse relationship between thermal stability and antiwear activity is well known (dependent on the nature of alkyl groups - see Section 1.2.2.8.2).[144] This relationship is attributed to more efficient degradation leading to faster tribofilm formation. In the previous chapter, we highlighted how ZDDP and friction modifier additives present in a lubricant formulation can interact and undergo complex formation in solution. Hence, the ultimate performance of lubricant packages are likely to be dictated, in part, by the complexes formed in solution. But, as yet, the effect of the observed ZDDP-OFM complexation reactions is unknown. Based on the known correlation between thermal and tribological performance for ZDDPs when studied in isolation, it was of particular interest to investigate first the thermal stability and then the tribological performance of these binary ZDDP-OFM systems where complexation is known to occur.

Here, in this chapter, we first investigate the thermolysis of ZDDP and selected ZDDP-OFM systems, monitored by ^{31}P NMR spectroscopy. Subsequently, the tribological performance is tested using the Mini Traction Machine-Spacer Layer Interferometry

Method (MTM-SLIM), which measures film thickness development and Stribeck friction curves. MTM-SLIM testing was performed by the author at AkzoNobel in Stenungsund, Sweden. Surface analysis (SEM-EDX) on the MTM disk specimens was also performed (*ex situ*) to gain further insight into the tribofilms formed and complement the information gained using the MTM-SLIM method.

5.2 Results and Discussion

5.2.1 Thermolysis of ZDDP and ZDDP-OFM Systems

The thermal behaviour of **^{i}Bu ZDDP** and selected ZDDP-OFM systems in mineral oil (Nexbase 3043, group III) were assessed by heating samples of the material in an NMR tube, at the desired temperature, for the required length of time and ^{31}P[^{1}H] NMR spectra recorded periodically. Although the ^{31}P NMR spectra collected were not acquired so as to be quantitative, gross repetition time effects on the observed product integrations were ruled out by collecting intermediate thermal degradation spectra (where all P-containing species are present) with a standard relaxation delay (D1 = 2 s) and a long relaxation delay (D1 = 20 s).* Relative product ratios proved to be independent of the relaxation time used (within error), with the only difference observed being a greater recovery of the PPh_3 capillary reference signal, which does not affect the interpretation of the results.

Initial thermolysis experiments probed the degradation of **^{i}Bu ZDDP** at 160 °C, so as to provide a baseline for comparison to subsequent studies with OFM-containing systems (Fig. 5.1). Here it can be observed that the degradation of **^{i}Bu ZDDP** proceeds steadily and full degradation is achieved after 77 h to a single, oil-soluble, phosphorus-containing degradation product (δ_P 97.4). The low frequency shift of the broad ZDDP resonance is noteworthy, something that is expected based on a decrease in concentration as the degradation progresses (see Section 4.2.1, Fig. 4.3).

*Routinely for quantitative NMR (qNMR) measurements, the repetition time (τ) is set so that $\tau = 5T_1$, where T_1 is the longest longitudinal relaxation time. τ = relaxation delay + acquisition time. At $\tau = 5T_1$, 99.3% of the equilibrium magnetisation (signal) is measured. If two (or more) species have notably different T_1 relaxation times, and τ is not long enough to allow the species with the longest T_1 to relax to any great extent, then the subsequent integrations will not reflect the true product ratios.[175]

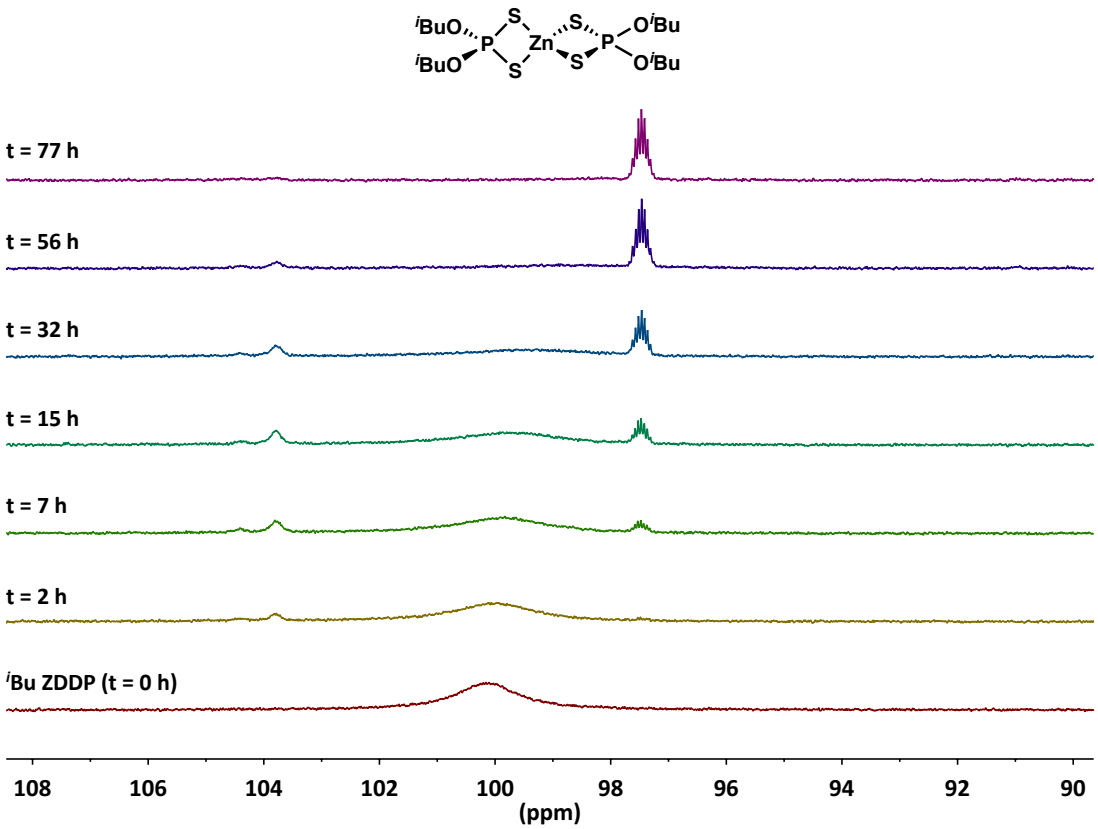

Figure 5.1: Evolution of the $^{31}P[^{1}H]$ NMR (162 MHz, mineral oil) spectrum of **^{i}Bu ZDDP** upon heating at 160 °C. 2.5 wt.% ZDDP, C_6D_6 insert spiked with PPh_3 to provide lock. Chemical shifts were referenced against PPh_3 in C_6D_6 (lit. -5.0 ppm[176]).

The degradation product observed is assigned to *O,O,S*-triisobutyldithiophosphate, consistent with reports from Marshall *et al.*,[54] (not *S,S,S*-triisobutyltetrathiophosphate as reported by Coy and Jones[53]) and has been validated by independent synthesis of the dithio and tetrathio derivates (Scheme 5.1, Fig. 5.2).

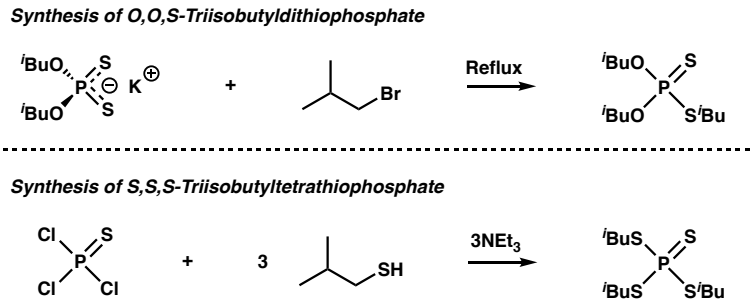

Scheme 5.1: Synthesis of two reported ZDDP thermal degradation products, *O,O,S*-triisobutyldithiophosphate and *S,S,S*-triisobutyltetrathiophosphate.

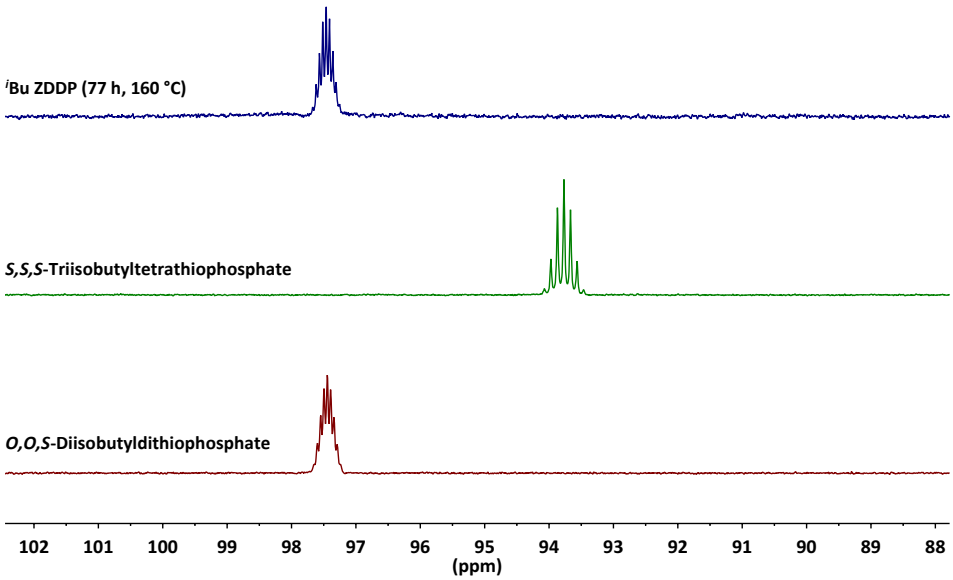

Figure 5.2: Comparison of the $^{31}P[^{1}H]$ NMR (162 MHz, mineral oil) spectra of the degraded **^{i}Bu ZDDP** sample after heating for 77 hours at 160 °C (top), *S,S,S*-triisobutyltetrathiophosphate (middle) and *O,O,S*-triisobutyldithiophosphate (bottom). C_6D_6 insert spiked with PPh_3 to provide lock. Chemical shifts were referenced against PPh_3 in C_6D_6 (lit. -5.0 ppm[176]).

In addition, high resolution-mass spectrometric analysis [HRMS (ASAP) *m/z* calc. for $[M+H]^+$ $C_{12}H_{28}O_2PS_2$: 299.1268. Found: 299.1270] was undertaken directly on the fully degraded sample in mineral oil, unequivocally proving the nature of the degradation product. Furthermore, the ability to perform HRMS studies directly from a mineral oil sample is potentially a very useful technique, especially for more complex mixtures where the synthesis of all possible degradation products becomes unfeasible.

Similarly, the degradation of an **^{i}Bu ZDDP**-hexylamine (ratio 1:2) mixture[†] proceeds to also yield *O,O,S*-triisobutyl-dithiophosphate (δ_P 97.4), but with full degradation occurring almost 4 times faster than for the **^{i}Bu ZDDP** system, after just 20 hours (Fig. 5.3). Some variation in the chemical shift of the ZDDP-amine resonance is observed; initially a low frequency shift is apparent (2 h spectrum, Fig. 5.3), that is attributed to a slowed return to equilibrium after cooling from elevated temperature. This is likely

[†]Initial experiments were attempted for the **^{i}Bu ZDDP**-octadecylamine (ratio 1:2) system, though the poor solubility of octadecylamine (**OFM1**) in mineral oil, at the higher loading required for the ^{31}P NMR spectroscopic thermolysis experiments, inhibited analysis. For this reason, **OFM1** was substituted for the closely related hexylamine, an amine which has previously been shown interact in an almost identical manner with **^{i}Bu ZDDP** in solution (Fig. 4.4).

caused by the high viscosity of the mineral oil that inhibits the return to equilibrium after rapid cooling and is consistent with previous variable temperature experiments that demonstrated ZDDP-amine systems underwent a reversible decomplexation at high temperatures (Section 4.2.4). Ultimately, this viscosity-inhibited return to equilibrium was confirmed by allowing sufficient time for the partially degraded thermolysis sample to return to equilibrium and reacquiring the ^{31}P NMR spectrum. Upon further heating of the **^{i}Bu ZDDP**-hexylamine (1:2) sample (Fig. 5.3), a high frequency shift of the ZDDP-amine resonance is observed. This opposing trend is rationalised based on a decrease in ZDDP concentration (caused by thermal degradation) and hence results in an effective increase in the ZDDP:amine ratio, something that is known to cause a high frequency shift of ZDDP resonances.

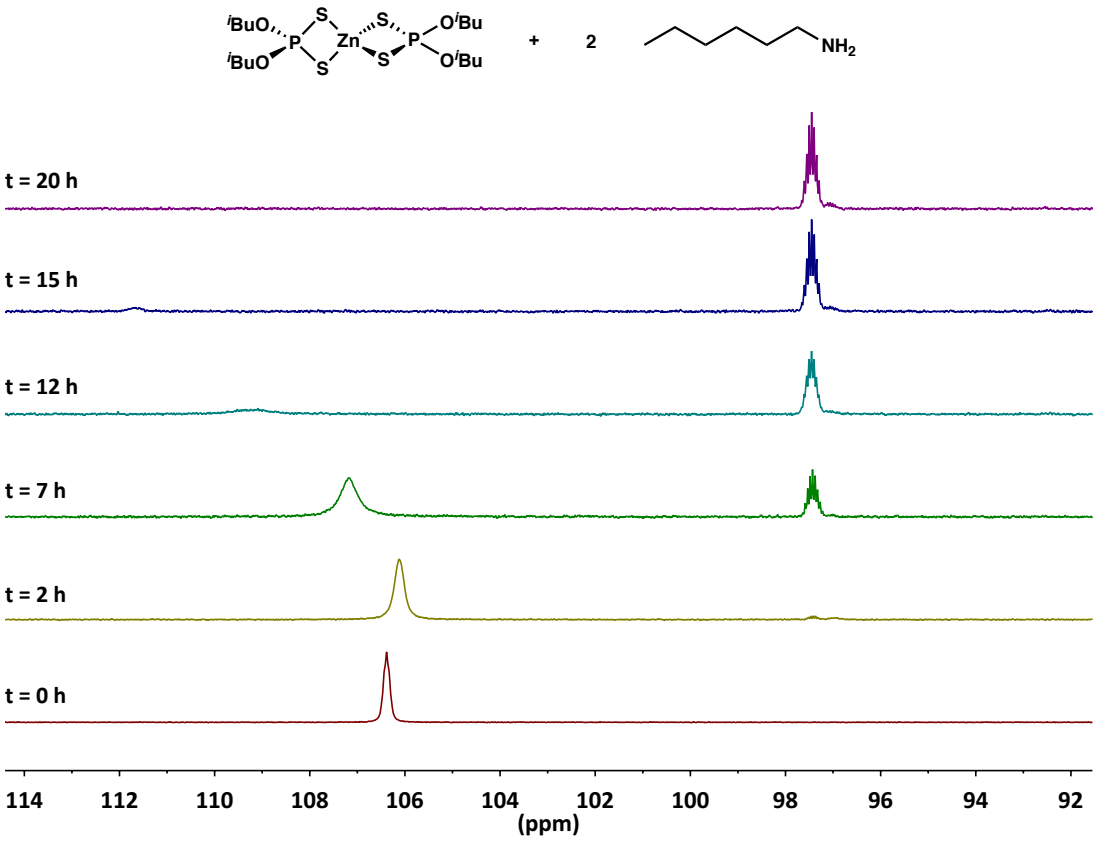

Figure 5.3: Evolution of the ^{31}P[^{1}H] NMR (162 MHz, mineral oil) spectrum of **^{i}Bu ZDDP**-hexylamine (1:2) upon heating at 160 °C. 2.5 wt.% ZDDP, C_6D_6 insert spiked with PPh_3 to provide lock. Chemical shifts were referenced against PPh_3 in C_6D_6 (lit. -5.0 ppm[176]).

The quicker decomposition of the hexylamine-containing **^{i}Bu ZDDP** system (Fig. 5.3)

compared that of **^{i}Bu ZDDP** when studied in isolation (Fig. 5.1) demonstrates the ability of amines to increase the rate of ZDDP degradation – something that one might expect to impact the antiwear behaviour of ZDDPs. Upon consideration of the previously identified ZDDP-amine complexation reactions (Chapters 3 and 4) and the known thermal degradation mechanisms associated with ZDDPs (Scheme 5.2),[52,55,56] it is perhaps not unsurprising that the presence of amine enhances ZDDP decomposition rate. In this thesis it has been demonstrated that 1° amine complexation to ZDDP is associated with a change in DTP binding mode from chelating/bridging to monodentate – a change that would be expected to augment both the alkyl transfer and β-hydrogen transfer elimination degradation pathways shown (Scheme 5.2), based on an increased nucleophilicity and enhanced basicity of the DTP ligands, respectively. The loss of DTP chelation to zinc is something that has been previously observed in molecular dynamics simulations of ZDDP monomers at elevated temperatures, where the dissociation of either one or two Zn-S bonds was observed.[55] This transient dissociation was observed for all the ZDDPs investigated by Mosey *et al.* and was found to persist for longer at higher temperatures. Therefore it follows that, if an amine favours this process and allows the (partially) dissociated species to persist at lower temperatures, then this likely enhances the rate of thermal degradation.

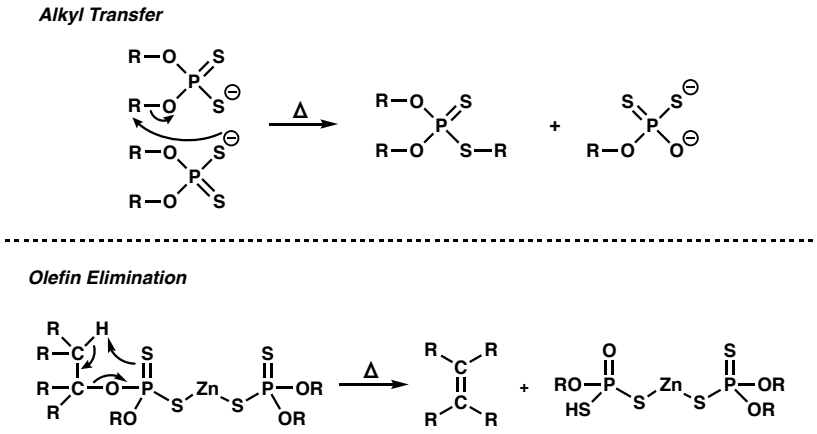

Scheme 5.2: Known thermal degradation mechanisms of ZDDPs.[52,55,56] For clarity, zinc is omitted in the alkyl transfer mechanism, but may be assumed present.

More generally, one might expect this amine-induced, thermolysis rate enhancement for ZDDPs to extend to other amine-containing systems, *i.e.* for a 3° amine, which we have previously shown to interact less strongly with ZDDPs than 1° amines, based on

increased steric demands (Section 4.2.5). This weaker interaction ultimately causes less change in the DTP binding mode, and as such the rate enhancement observed should not be as significant (Fig. 5.4).

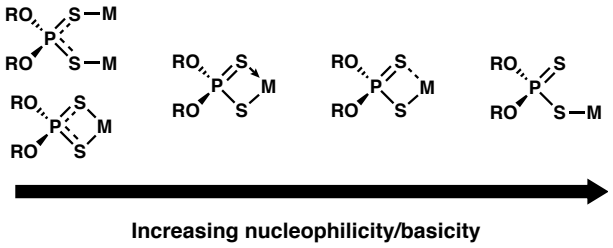

Figure 5.4: Relative changes in nucleophilicity/basicity as a function of DTP binding mode.

To test this hypothesis, similar thermolysis studies were performed for octadecyldimethylamine, ($C_{18}NMe_2$, **OFM3**) with **^{i}Bu ZDDP** at 160 °C. However, although a thermolysis rate enhancement was observed for the **OFM3**-containing system, in comparison to that of **^{i}Bu ZDDP** when degraded in the absence of amine (as would be expected based on the arguments made above), differentiating any obvious differences in thermal stability between the two ZDDP-amine formulations (hexylamine and **OFM3**) at the given temperature was not possible. In an attempt to better resolve any differences in thermal stability the temperature was reduced to 150 °C and thermolysis experiments repeated for the hexylamine and **OFM3** systems. At the new lower temperature, it was found that a slight difference in thermal stability could be identified by ^{31}P NMR spectroscopy. This is best displayed by comparing the spectra of the hexylamine and **OFM3** systems obtained after 32 h heating, as shown in Figure 5.5. It can be seen that after 32 h the ZDDP-hexylamine system (Fig. 5.5, bottom) has undergone complete degradation to yield a single degradation product, *O,O,S*-triisobutyldithiophosphate (δ_P 97.4). However, in contrast, for the **^{i}Bu ZDDP-OFM3** system (Fig. 5.5, top) a resonance from the ZDDP-amine adduct (δ_P 112.7) is still present after 32 h, indicating thermal degradation is not complete. This observation is consistent with a weaker ZDDP-amine interaction in solution for a tertiary amine-based OFM, that results in a smaller deviation in DTP binding mode, and hence the degree of thermolysis rate enhancement observed is reduced (Fig. 5.4). It is expected that if the temperature was reduced further, *i.e.* to 100-120 °C, then greater differences in the thermal stability of the two amine systems

may be observable. These lower temperatures are also closer to that expected in the bulk of an engine oil (maximum sump temperatures as high as 130 °C in passenger car engines[164]) though initial degradation tests at these temperature were extremely slow and would require exceptionally long degradation times.

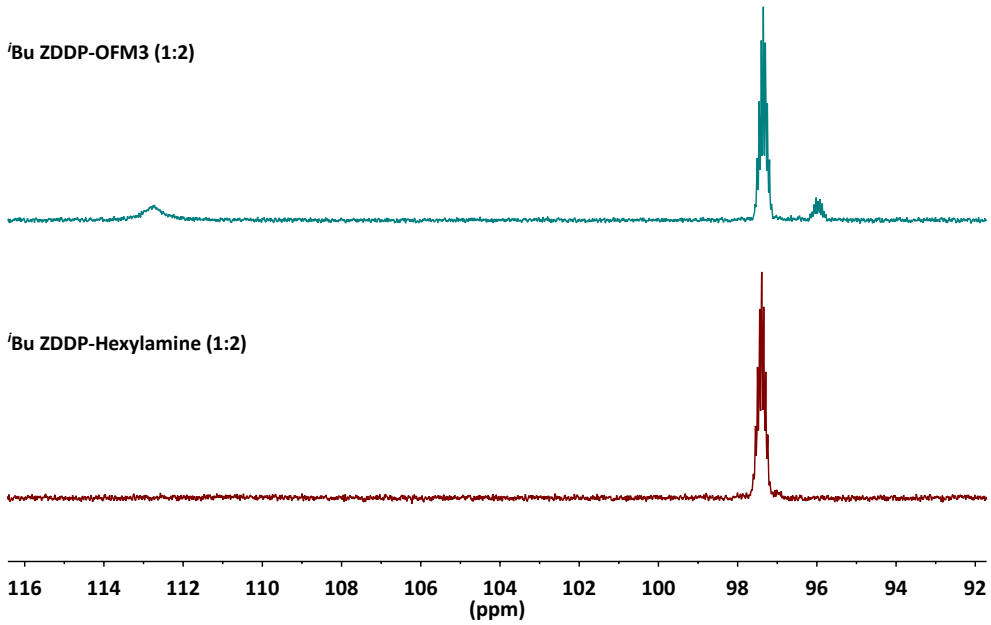

Figure 5.5: $^{31}P[^{1}H]$ NMR (162 MHz, mineral oil) spectra of **^{i}Bu ZDDP-OFM3** (1:2), top, and **^{i}Bu ZDDP**-hexylamine (1:2), bottom, after heating at 150 °C for 32 h. 2.5 wt.% ZDDP, C_6D_6 insert spiked with PPh_3 to provide lock. Chemical shifts were referenced against PPh_3 in C_6D_6 (lit. -5.0 ppm[176]).

In addition to the resonance assigned to *O,O,S*-triisobutyldithiophosphate (δ_P 97.4), a small additional resonance is observed for the **^{i}Bu ZDDP-OFM3** system (δ_P 96.0). Given the similar chemical shift to that observed for *O,O,S*-triisobutyldithiophosphate, the additional degradation product is likely to be very similar in structure, and is tentatively proposed to arise from *O,O*-diisobutyl-*S*-methyldithiophosphate. This species would conceivably form as a result of nitrogen to sulfur alkyl (methyl) transfer, something which we have shown to occur for a related system (see Scheme 5.4), though further work is needed to definitively assign this additional product.

Subsequently, we then decided to test the thermal behaviour of an ethoxylated amine system (**OFM5**), as our previous studies had suggested that ZDDP-amine complexation in this case likely produces anionic DTP species as a side product (Fig. 4.7). Anionic

DTP is the most nucleophilic form of DTP and therefore the thermolysis rate enhancement for this system would be expected to be even greater than that observed for the 1° alkylamine system (Fig. 5.3). As such, thermolysis studies were performed for the ethoxylated amine **OFM5** with **^{i}Bu ZDDP**, at the lower temperature of 150 °C, in an attempt to aid the resolution of any differences in thermal stability between the different OFM-containing systems studied (Fig. 5.6). For the **^{i}Bu ZDDP-OFM5** system (ratio 1:2, mineral oil) studied, initially (at t = 0) two broad, partially-coalesced resonances were visible {*cf.* in hexane solution at RT one broad signal was observed (Fig. 4.32), while in $CDCl_3$ solution at RT a single broad resonance was observed that split into two upon lowering the temperature (Fig. 4.41)}. The difference observed between hexane/$CDCl_3$ and mineral solutions is likely a viscosity effect, whereby the increased viscosity of the mineral oil solvent slowed exchange between the exchanging phosphorus species, such that the two signals become partially resolved at room temperature in mineral oil.

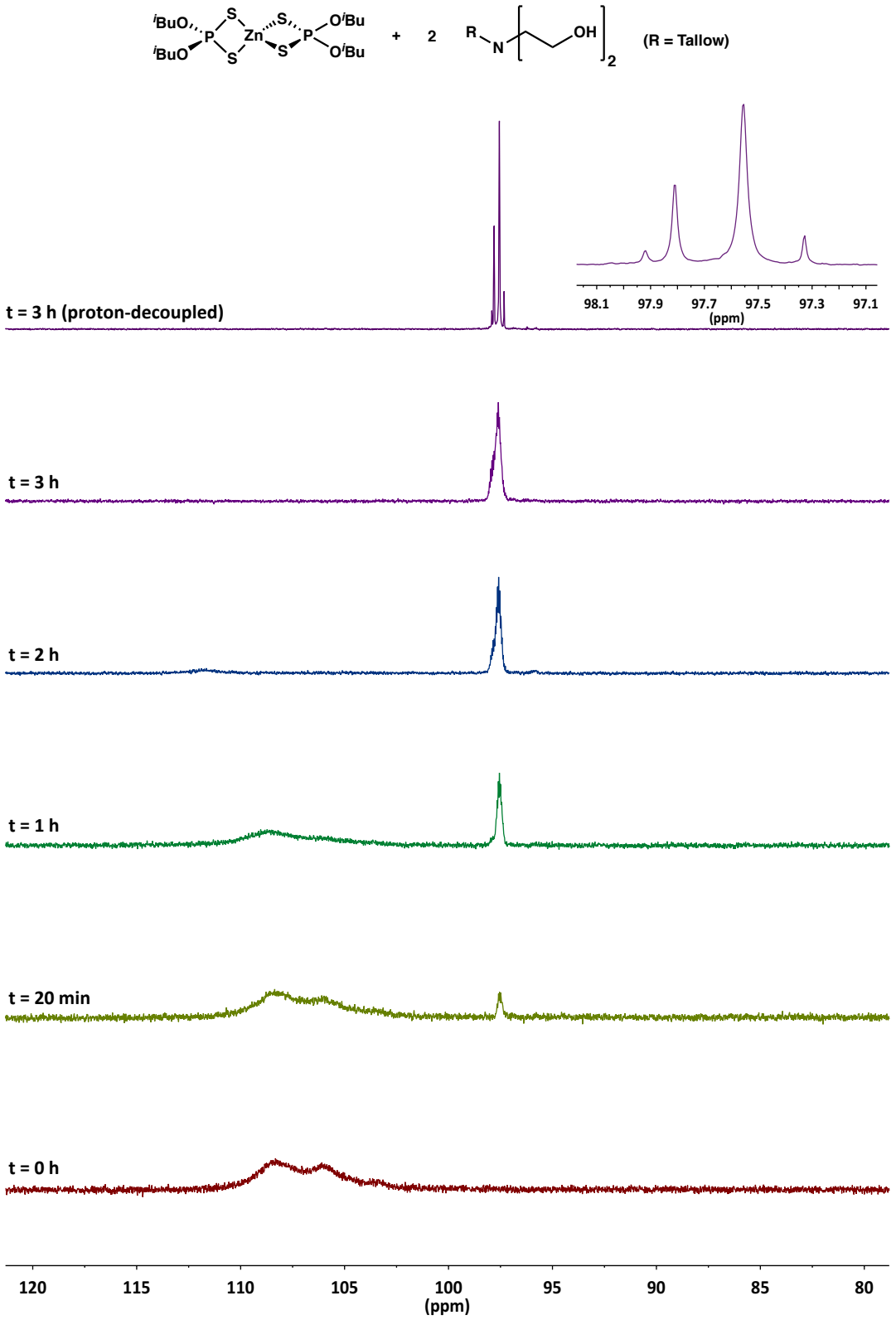

Figure 5.6: Evolution of the ^{31}P NMR (162 MHz, mineral oil) spectrum of **^{i}Bu ZDDP-OFM5** (1:2) upon heating at 150 °C. 2.5 wt.% ZDDP, C_6D_6 insert spiked with PPh_3 to provide lock. Chemical shifts were referenced against PPh_3 in C_6D_6 (lit. -5.0 ppm[176]).

From the data presented in Figure 5.6, it is apparent that thermal degradation for the ethoxylated amine system proceeds notably faster than any previously studied system, with full degradation having occurred after just 3 h at 150 °C. This observation is consistent with the presence of anionic DTP that is significantly more nucleophilic than any metal-bound DTP ligand, and is expected to considerably enhance the rate of thermolysis, based on the promotion of the alkyl transfer degradation mechanism known for ZDDPs (Scheme 5.2). Although a significant rate enhancement is observed, in this case the degradation product mixture is far more complex, with the $^{31}P\{^{1}H\}$ NMR spectrum revealing the presence of four, oil-soluble phosphorus-containing species (Fig. 5.6, inset). The chemical shifts of the products observed are all very similar, ranging from 97.3 to 97.9 ppm. These values are also very similar to that of the previously observed degradation product, *O,O,S*-triisobutyldithiophosphate (δ_P 97.4). The narrow range and absolute values of the chemical shifts observed highlights the similarity of the degradation products to each other, and to *O,O,S*-triisobutyldithiophosphate. The nature of these degradation products will be discussed further, later in this section.

To test our hypothesis regarding thermolysis rate enhancement being caused by the presence of anionic DTP, we performed thermolysis experiments on **^{i}Bu ZDDP** with the addition of an authentic sample of anionic DTP. Initially, we had potassium diisobutyldithiophosphate (KDTP) to hand, as it is an intermediate used for the synthesis of **^{i}Bu ZDDP**, however the solubility of this species in mineral oil was exceptionally poor, as would be expected. To circumvent this solubility problem, a cation exchange reaction was performed in which the potassium cation was exchanged for tetraalkylammonium, specifically $[NPr_4]^+$, to give tetrapropylammonium diisobutyldithiophosphate (ADTP) (Scheme 5.3, Fig. 5.7).

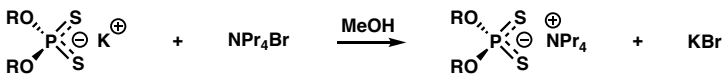

Scheme 5.3: Synthesis of tetrapropylammonium diisobutyldithiophosphate (ADTP).

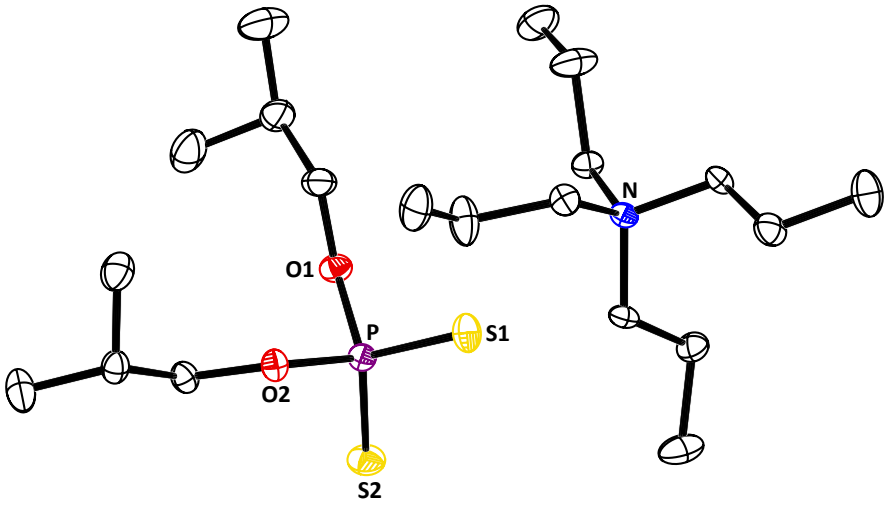

Figure 5.7: Molecular structure of tetrapropylammonium diisobutyldithiophosphate (ADTP) with thermal ellipsoids at the 50% probability level; H atoms are omitted for clarity. Selected bond distances: P-S1, 1.9594(4) Å; P-S2, 1.9586(4) Å. Selected bond angles: S1-P-S2, 119.81(2)°.

Now with ADTP in hand, thermolysis experiments were performed on a 1:1 mineral oil solution of **^{i}Bu ZDDP** and ADTP (sample formulated at 0.28 wt.% P to match the P content of a 2.5 wt.% **^{i}Bu ZDDP** solution) at 160 °C (Fig. 5.8). Here it can be seen that, in comparison to the thermolysis of **^{i}Bu ZDDP** in isolation (Fig. 5.1) the rate of thermolysis is enhanced over 2 fold, with full thermal degradation having occurred after 30 h (*cf*. **^{i}Bu ZDDP** required 77 h at 160 °C for full degradation). The observed thermolysis rate enhancement supports the conjecture that the presence of a more nucleophilic species, *i.e.* anionic DTP, promotes the thermal degradation of ZDDP. That said, in this case two degradation products are clearly observed by ^{31}P NMR spectroscopy (Fig. 5.8), and while one is assigned to the previously observed *O,O,S*-triisobutyldithiophosphate (δ_P 97.4), the nature of the second species was unknown (δ_P 97.0).

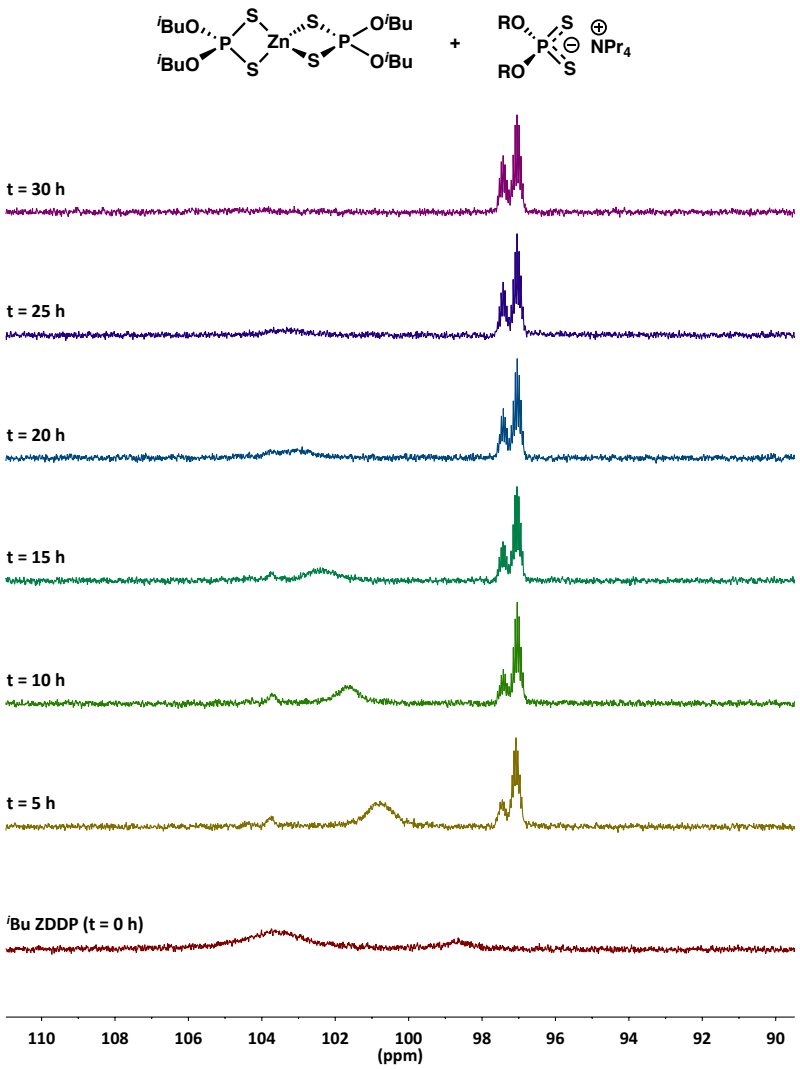

Figure 5.8: Evolution of the $^{31}P[^{1}H]$ NMR (162 MHz, mineral oil) spectrum of ***i*Bu ZDDP**-ADTP (1:1) upon heating at 160 °C. 0.28 wt.% P, C_6D_6 insert spiked with PPh_3 to provide lock. Chemical shifts were referenced against PPh_3 in C_6D_6 (lit. -5.0 ppm[176]).

To gain further insight into the nature of the unknown degradation product, the degradation sample (160 °C, 30 h) obtained from the NMR-scale degradation reaction was passed through a short silica column (hexane/toluene 95:5) to remove the mineral oil solvent and enable the acquisition of a suitable ^{1}H NMR spectrum. Subsequent analysis of the ^{1}H NMR spectrum collected (consisting of both *O,O,S*-triisobutyldithiophosphate and the unknown degradation product which were not separable) (Fig. 5.9), revealed the presence of three extra resonances in addition to the known resonances arising from *O,O,S*-triisobutyldithiophosphate. These additional spectroscopic resonances were consistent with a propylated sulfur residue. Subsequent high resolution mass spectrometric

analysis (undertaken directly from the degraded sample in mineral oil) [HRMS (ASAP) *m/z* calc. for $[M+H]^+$ $C_{11}H_{26}O_2PS_2$: 285.1112. Found: 285.1118] corroborated the NMR spectroscopic data and confirmed the unknown degradation product to be *O,O*-diisobutyl-*S*-propyldithiophosphate. Peak assignments for the *S*-propyl group are depicted in Figure 5.9, though it should be noted that the terminal *S*-CH_3 triplet resonance of *O,O*-diisobutyl-*S*-propyldithiophosphate overlaps with the terminal *S*-CH_3 doublet from *O,O,S*-triisobutyldithiophosphate.

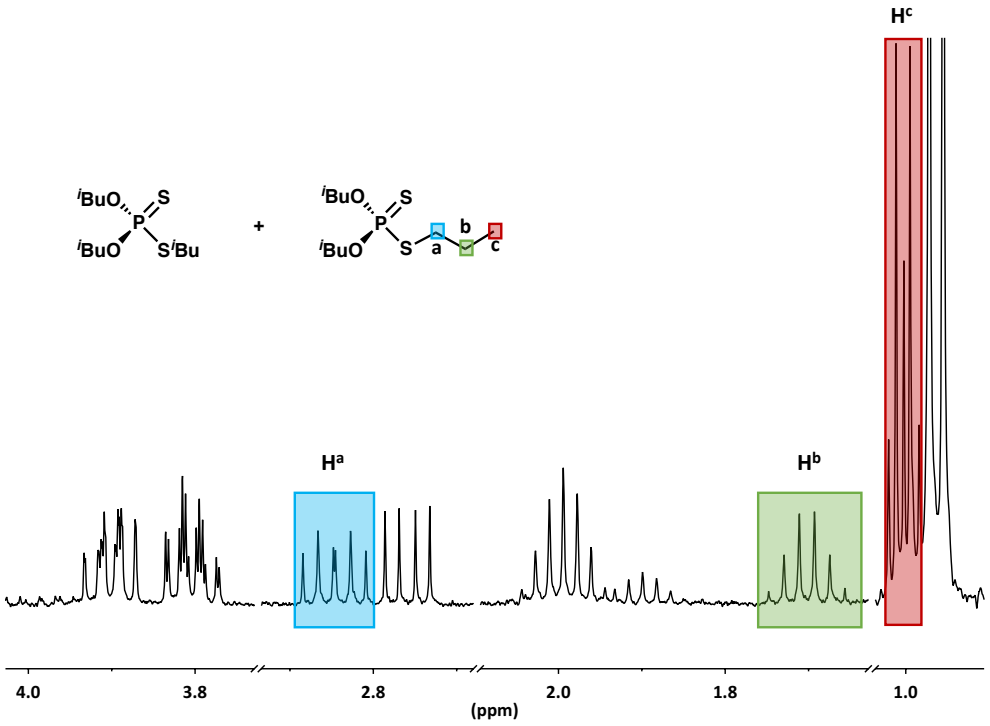

Figure 5.9: ^{1}H NMR (400 MHz, $CDCl_3$) spectrum of **^{i}Bu ZDDP**-ADTP (1:1) degradation mixture (150 °C, 3 h) post silica column.

The *S*-propyl group of *O,O*-diisobutyl-*S*-propyldithiophosphate must originate from the tetrapropylammonium cation and drawing similarities to the known alkyl transfer degradation mechanism of ZDDPs (Scheme 5.2), it is expected that *O,O*-diisobutyl-*S*-propyldithiophosphate forms *via* a similar mechanism, but with alkyl transfer from nitrogen to sulfur, rather than oxygen to sulfur (Scheme 5.4).

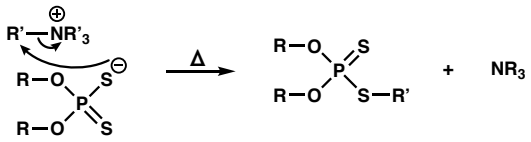

Scheme 5.4: Proposed nitrogen to sulfur alkyl transfer mechanism.

Analogies from this proposed reaction pathway can be drawn and applied to the aforementioned **^{i}Bu ZDDP-OFM5** (1:2) thermolysis, which displayed four oil soluble P-containing degradation products by $^{31}P\{^{1}H\}$ NMR spectroscopy (Fig. 5.6, inset). Having observed that alkyl groups can be transferred from an ammonium-based cation to DTP species, when sufficiently nucleophilic DTP is present, by extension, it is feasible that a similar reaction may occur for the **^{i}Bu ZDDP-OFM5** (1:2) system, in which anionic DTP has previously been identified as a side product. High resolution-mass spectrometric analysis undertaken directly on the degraded **^{i}Bu ZDDP-OFM5** (1:2) sample in mineral oil, identified five possible degradation products including the previously identified *O,O,S*-triisobutyldithiophosphate (Fig. 5.10).

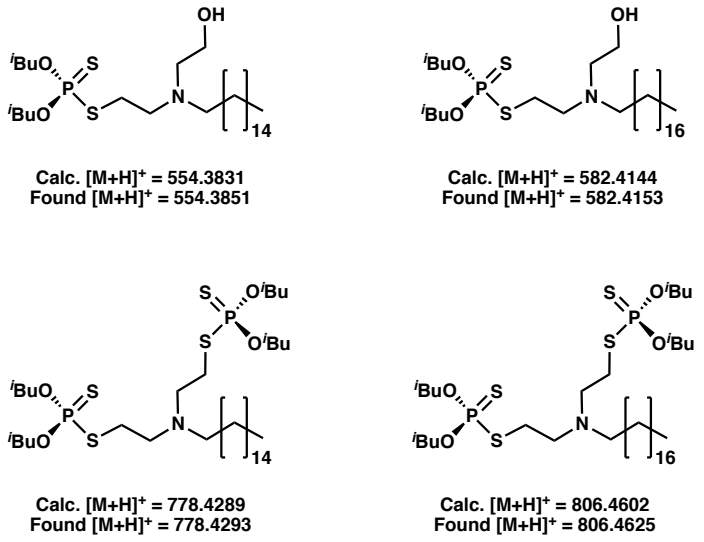

Figure 5.10: Possible thermal degradation products identified by HRMS (ASAP) after thermolysis of a **^{i}Bu ZDDP-OFM5** (1:2) sample (150 °C, 3 h).

While *O,O,S*-triisobutyldithiophosphate is known to form *via* "conventional" oxygen to sulfur alkyl transfer between DTP species (Scheme 5.2), the other species are believed to form, not by nitrogen to sulfur transfer as found for the ADTP containing system, but by a related process involving nucleophilic attack at the β-carbon of the pendant ethanol

branches (Scheme 5.5). The observation of the two, single- and double-substitution reaction products (Fig. 5.10), that differ only in the length of the alkyl chain is consistent with the known composition of the commercial product **OFM5**, which contains around 35% and 65%, C_{16} and C_{18} ethoxylated amine, respectively. Of course, with only HRMS data to support the formation of the given products it is possible that the observed ions are formed simply as a consequence of the mass spectrometry-induced ionisation processes. As such, further work would be necessary to definitively confirm their presence in the degraded mineral oil sample.

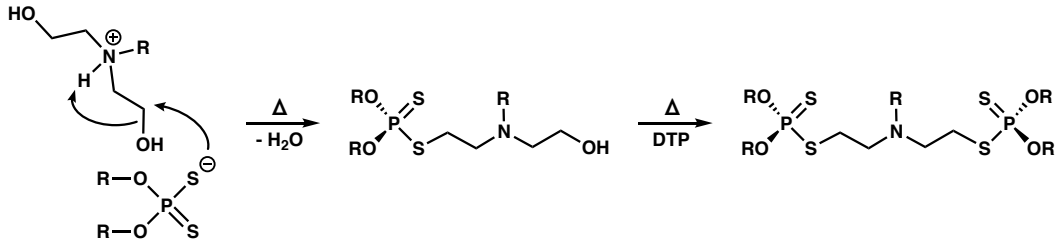

Scheme 5.5: Proposed mechanism for the formation of the single and double substitution products, identified by HRMS, involving nucleophilic attack at the β-carbon of a pendant ethanol branch.

Overall, the thermolysis studies performed have identified the ability of amine-functional OFMs to enhance the rate of thermal degradation in ZDDP-OFM systems. The relative thermal stabilities observed are highly dependent on the DTP binding configuration, something that is dictated by strength of the ZDDP-amine interaction in solution (Fig. 5.11)

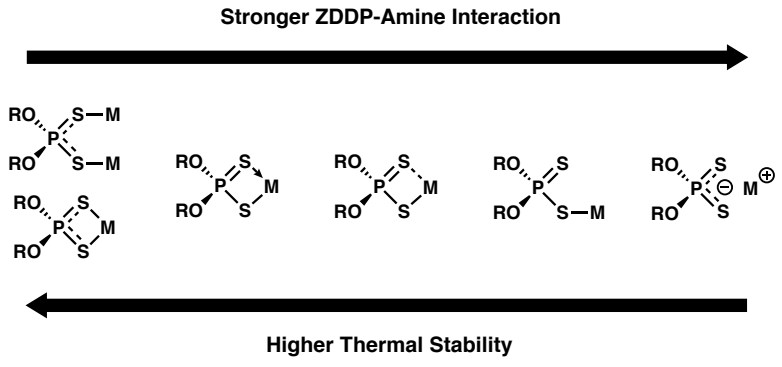

Figure 5.11: Relationship observed between the strength of ZDDP-amine interaction, the resulting DTP binding mode and the thermal stability observed for ZDDP-amine systems.

For ZDDP systems with 1° and 3° amines, a common degradation product is observed, thus suggesting a common degradation mechanism. Based on the known degradation mechanisms of alkyl ZDDPs, the degree of the rate enhancement observed is rationalised based on the strength of ZDDP-amine interaction in solution. A stronger ZDDP-amine interaction causes greater change in DTP binding mode, which increases both the nucleophilicity and the basicity of the DTP moieties of ZDDP.

When the change in DTP binding mode is taken to the extreme case and the DTP ligands are fully ionised to produce anionic DTP, an even greater rate enhancement is observed. This was postulated to occur due to the greater nucleophilicity of anionic DTP, something that was subsequently verified by adding an ammonium-based DTP salt to ZDDP and studying the thermal degradation. This study revealed an additional degradation product, *O,O*-diisobutyl-*S*-propyldithiophosphate, which must form *via* nitrogen to sulfur, rather than oxygen to sulfur, alkyl transfer. For the ethoxylated amine system studied, a more complex degradation mixture was observed by $^{31}P\{^{1}H\}$ NMR spectroscopy. HRMS studies identified several possible degradation products, which form *via* a subtly different mechanism that involves nucleophilic attack at the β-carbon of the pendant ethanol branches of the ethoxylated amine.

5.2.2 Tribological Behaviour of ZDDP-OFM systems

With a greater understanding of the effect of amine-functional OFMs on the thermal behaviour of ZDDP-OFM systems, it was then necessary to assess, and subsequently rationalise, the tribological performance observed in such systems. To achieve this aim, various techniques were employed to investigate the growth kinetics, physical (thickness, morphology), chemical (composition), and tribological properties (friction, wear) of tribofilms generated from ZDDP-OFM systems.

Tribological tests were performed at AkzoNobel in Stenungsund, Sweden using a Mini Traction Machine (MTM2) in a sliding-rolling ball-on-disk setup. The MTM2 is fitted with a 3D Spacer Layer Imaging Method (SLIM) attachment, which enables the *in situ* capture of optical interference images of the tribofilm formed on the steel ball (Fig.

5.12); subsequent analysis yields the tribofilm thickness (see experimental for more details).

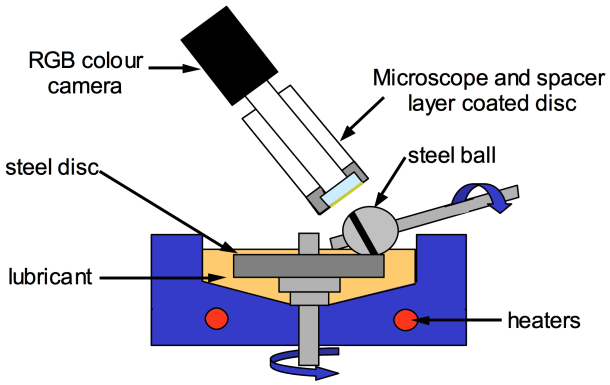

Figure 5.12: Diagram of MTM-SLIM set up.

MTM-SLIM conditions used in this thesis are summarised in Table 5.1, with a typical MTM-SLIM test procedure consisting of several stages:

1. Firstly, in the "film-forming" stage, the ball and disk were rubbed together in the mixed or boundary regime (low entrainment speed) to generate a tribofilm on the rubbed track of the ball and disk.

2. After a predetermined length of time at a set temperature, motion was halted, the rubbed track of the ball was loaded against the coated glass window and an optical interference image was captured ("tribofilm measurement"). The ball was then withdrawn and the film-forming process was resumed.

3. After the desired test duration (2 h), a "Stribeck curve" was acquired, in which friction was measured over a range of entrainment speeds at a fixed slide-roll ratio.

Table 5.1: MTM-SLIM test conditions.

Film-Forming Phase	
Temperature	120 °C
Load	20 N
Entrainment Speed	0.1 m/s
Slide-roll Ratio	50%
Stribeck Curve Phase	
Temperature	120 °C
Load	20 N
Entrainment Speed	3 to 0.005 m/s
Slide-roll Ratio	50%

5.2.2.1 ^{i}Bu ZDDP Tribofilm Formation and Properties

So as to provide a baseline for comparison to ZDDP-OFM mixtures, MTM-SLIM tests were initially performed on mineral oil and **^{i}Bu ZDDP** mineral oil (0.5 wt.% ZDDP) solutions. For **^{i}Bu ZDDP**, optical interferometry images collected periodically during the course of the MTM test displays the evolution of the ZDDP growth indicated by the dark areas within the contact (Fig. 5.13). Graphically, this evolution is also displayed versus rubbing time, where tribofilm growth can be characterised by initial rapid growth (0-30 mins), which then slows down and stabilises at a thickness around 120 nm. These results are consistent with previous reports of ZDDP tribofilm growth.[59,73,119] It should be noted however, in this work a single-component ZDDP is used, rather than a commercial ZDDP sample made up of a mixture of ZDDPs, which are normally used in the bulk of the ZDDP literature.

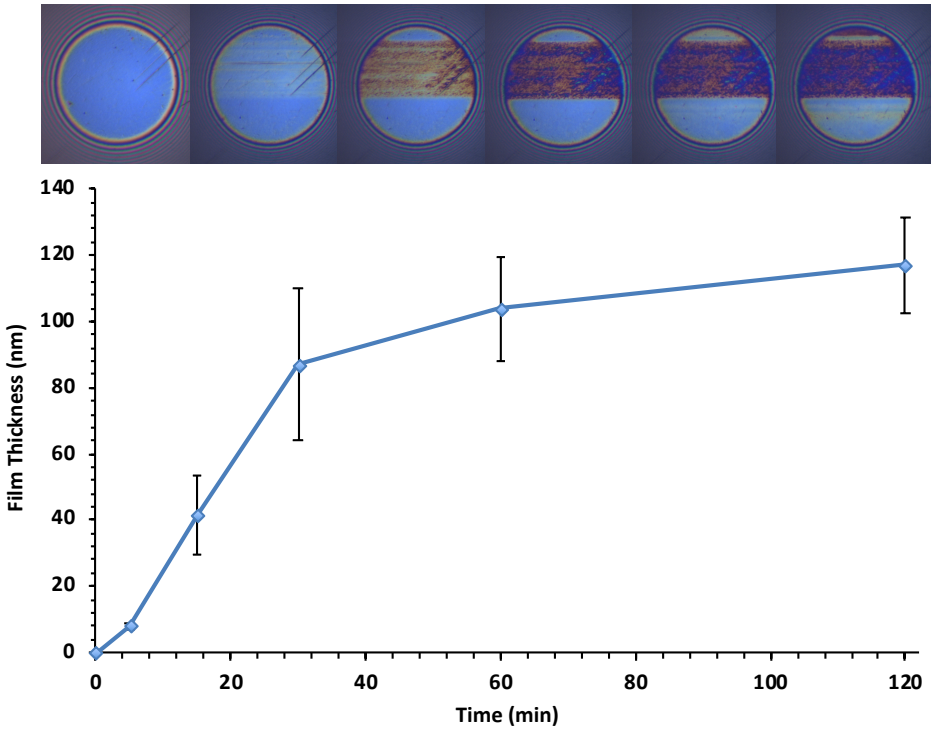

Figure 5.13: Optical interference images and average film thicknesses plotted against rubbing time for **^{i}Bu ZDDP**. Film thicknesses quoted are the average values from two independent tests and error bars depict the standard deviation.

It might be expected that the growth plateau observed for ZDDP tribofilms after extended rubbing is based on a balance of tribofilm formation and removal. This possibility has been investigated by replacing a ZDDP solution after the tribofilm growth has plateaued with a mineral oil solution. Negligible tribofilm removal was observed and therefore suggests ZDDP tribofilm growth is self-limiting, something that is in agreement with the stress-promoted thermal activated model proposed for tribofilm growth (see Section 1.2.2.8.2).[59,73]

Subsequently, after tribofilm formation (at the end of the 2 h film-forming stage), friction coefficient measurements were performed over a range of entrainment speeds at a fixed slide-roll ratio to produce Stribeck curves, which can be related to the performance of the tribofilms formed. The data presented in Figure 5.14 show how friction varies and generally decreases as the entrainment speed is increased. This corresponds to the transition away from the boundary lubrication regime at low entrainment speeds, to the fluid lubrication regime at high speeds. Specifically, for a mineral oil sample containing

no additives, after 2 h rubbing the Stribeck curve presented shows an almost linear decrease in friction coefficient with increasing entrainment speeds. However, for the ZDDP-containing mineral oil solution, the Stribeck curve profile is distinctly different. Overall, there is a clear increase in friction across all entrainment speeds investigated, though the greatest increase in friction is observed in the mixed lubrication regime (intermediate speeds), where the high friction values typical in the boundary regime (low speeds) are extended and persist to much higher speeds, before a linear drop in friction at high speeds is observed.

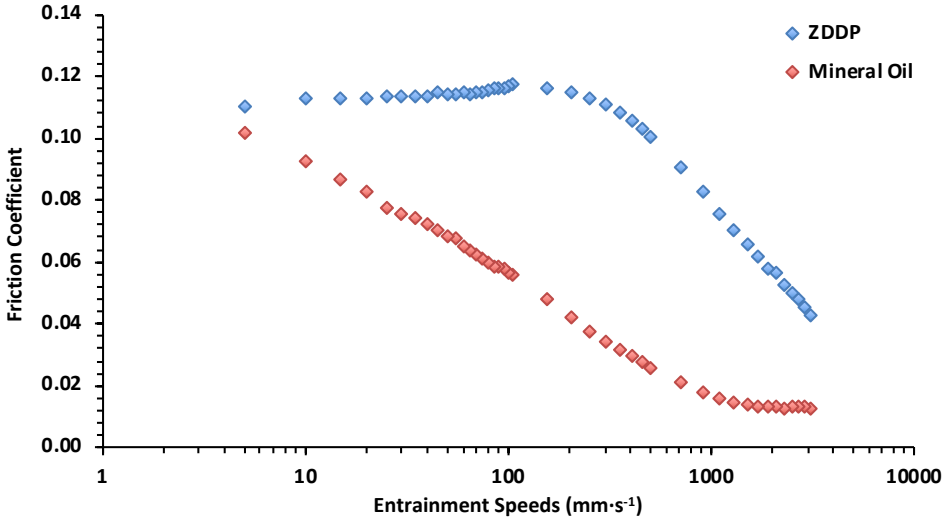

Figure 5.14: Stribeck curves for **^{i}Bu ZDDP** and neat mineral oil solutions after 2 h rubbing. The results presented are the average plots obtained from two independent tests.

This frictional response caused by ZDDP tribofilms, that essentially shifts the Stribeck curve to the right (to higher entrainment speeds), has been recognised for a long time and for this reason the additional of a compatible and synergistic FM is essential for fuel economy improvements in an engine lubricant formulation.[73] The origin of ZDDPs' frictional performance is believed to be caused by the extremely rough topology of ZDDP tribofilms that allows lubricant to drain from the contact and inhibits fluid entrainment to higher speeds.[71]

Based on the results presented, the following conclusions were drawn, before tests with OFMs were performed:

- **^{i}Bu ZDDP** forms thick (~120 nm) films on rubbing steel surfaces.
- Tribofilm growth was observed to be rapid in the first 30 minutes of rubbing, before the growth slows and the tribofilm reaches its critical thickness.
- The **^{i}Bu ZDDP**-derived tribofilm increases friction, especially in the mixed lubrication regime (intermediate speeds).

5.2.2.2 Film Formation and Properties of ZDDP-OFM Blends

MTM-SLIM tests were performed on solutions containing **^{i}Bu ZDDP** (0.5 wt.%) and the selected OFM in the desired ZDDP:OFM molar ratio, in order to investigate the extent to which the presence of OFMs affected tribofilm growth and friction. Initial tests were performed with the straight chain primary amine, octadecylamine (**OFM1**) studied in two ZDDP:OFM molar ratios, specifically 1:1 and 1:2.

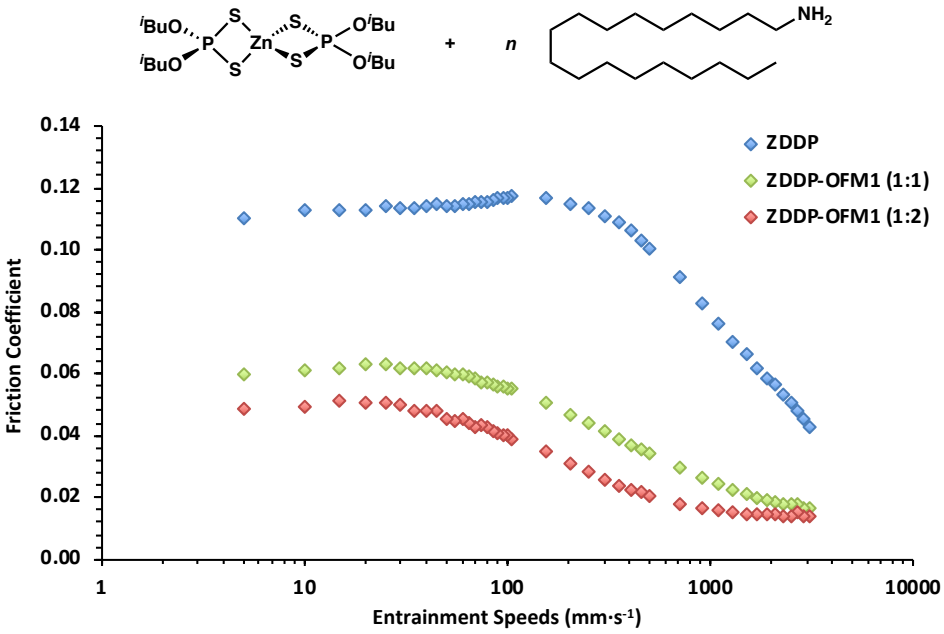

Figure 5.15: Stribeck curves for **^{i}Bu ZDDP-OFM1** solutions (ratio 1:1 and 1:2) produced after 2 h rubbing. The Stribeck curve for **^{i}Bu ZDDP** is given comparison. The results presented are the average plots obtained from two independent tests.

In terms of frictional performance, from the Stribeck curves obtained it can be seen that a significant reduction in friction is observed for both 1:1 and 1:2 systems across all entrainment speeds, in comparison to **^{i}Bu ZDDP** (Fig. 5.15). This result is very much

expected and consistent with the known function of OFMs.[73,120] Particularly it is apparent that the extension of high friction values to higher speeds observed for **^{i}Bu ZDDP**, is no longer present in the case of the **OFM1**-containing systems, suggesting significant modification and/or inhibition of ZDDP tribofilm growth. Increasing the concentration of **OFM1** from 1 to 2 equivalents leads to a slightly greater friction reduction, something likely to be due to increased OFM surface adsorption and/or ZDDP tribofilm inhibition.

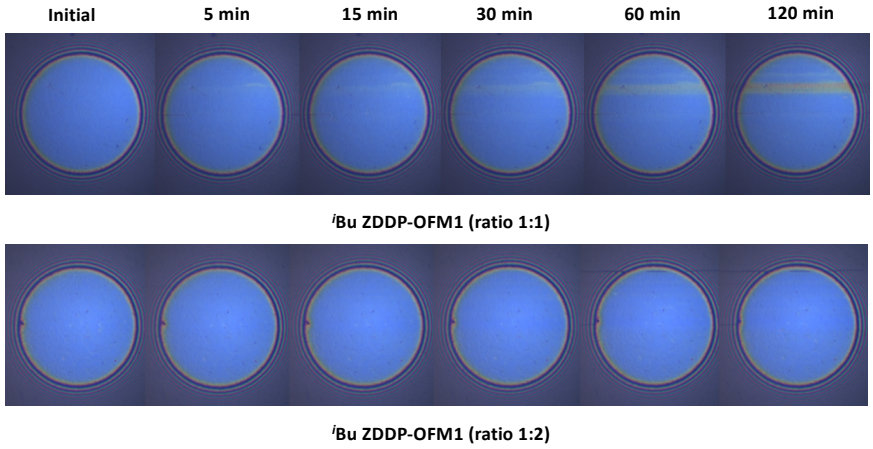

Figure 5.16: Optical interference images obtained for **^{i}Bu ZDDP-OFM1** systems (ratio 1:1 and 1:2) upon progressive rubbing during MTM tests.

From the SLIM images presented in Figure 5.16 it can seen that the rate of tribofilm growth is indeed significantly suppressed when **OFM1** is added to ZDDP-containing solutions. The film formation observed is dependent on the ZDDP:OFM molar ratio, where at a molar ratio equal to 1:2, tribofilm growth is suppressed to the point that no measurable tribofilm is formed on the surface after 2 h under the test conditions used (*cf.* detection limit of SLIM is ~ 5 nm[119]). In contrast, for the lower 1:1 ZDDP-OFM ratio, some visible tribofilm begins to form after approximately 30 minutes, though the thickness is considerably is reduced in comparison to **^{i}Bu ZDDP** in isolation (Fig. 5.13). The lack of tribofilm observed in the SLIM images for the **^{i}Bu ZDDP-OFM1** systems is consistent with *ex situ* SEM-EDX analysis performed on the wear track of the MTM disk. The elemental compositions obtained from both the **OFM1**-containing systems closely resembles that of the MTM disk substrate outside the contact zone (data not presented); in particular, the lack of zinc content is especially diagnostic in identifying the absence of a significant ZDDP-based tribofilm (Table 5.2).

Table 5.2: Average elemental compositions of a 5 mm area of the wear tracks of MTM disks post MTM-SLIM testing obtained *via* SEM-EDX analysis. Standard deviations are given in parentheses.

Formulation	%C	%O	%P	%S	%Cr	%Fe	%Zn
^{i}Bu ZDDP	12.3 (*0.1*)	9.7 (*0.3*)	1.5 (*0.05*)	0.7 (*0.05*)	1.3 (*0.05*)	65.5 (*0.4*)	6.3 (*0.1*)
^{i}Bu ZDDP-OFM1 (1:1)	12.4 (*0.5*)	1.7 (*0.05*)	0.2 (*0.05*)	0.2 (*0.1*)	1.6 (*0.1*)	82.9 (*0.4*)	0.7 (*0.1*)
^{i}Bu ZDDP-OFM1 (1:2)	12.0 (*0.3*)	1.0 (*0.4*)	0.1 (*0.1*)	0.1 (*0.05*)	1.6 (*0.05*)	84.6 (*0.2*)	0.1 (*0.1*)

Tribofilm growth suppression has been reported previously for amine-based OFMs with ZDDPs and is typically rationalised as either a consequence, or combination of, ZDDP-amine complexation and OFM surface adsorption, thus blocking surface sites.[73,118,120] Relating to this, our thermal studies (Section 5.2.1) identified that in terms of thermal behaviour, amine complexation increased the rate of ZDDP thermolysis, and is something therefore that might be expected to translate to faster tribofilm formation, as proven for ZDDPs when studied in isolation.[144] The fact that the opposite is true suggests some other growth suppression mechanism is operative and dominant, which is not related to thermal stability.

One possibility for the observed growth suppression can be deduced from the fact that the presence of a friction modifier inherently reduces friction, and thus also reduces the applied shear stress. Given the thermally-activated, stress-assisted rate model recently proposed for ZDDP tribofilm formation (see Section 1.2.2.8.2),[57,70] a reduction in shear stress therefore reduces a significant driver for tribofilm formation and could explain the slower growth kinetics observed. This idea is consistent with the observation that ZDDP solutions in group III or group IV base oils intermittently fail to form tribofilms even in thin-film sliding/rolling conditions, something that is suspected to be caused by the low friction and hence shear stress in these systems.[57]

Another plausible mechanism of tribofilm growth suppression is based on the availability

of network-forming zinc cations. If amine-functional OFMs effectively sequester the zinc cations and make them less available and/or leach them from preformed ZDDP tribofilms, the tribofilm thickness will be effectively reduced, in spite of the faster thermal degradation of the ZDDP-OFM system.

To test the validity of the hypothesis that the availability of zinc cations could be limiting tribofilm formation, MTM-SLIM tests were performed on the previously observed thermal degradation product, *O,O,S*-triisobutyldithiophosphate (formulated at a wt.% P to match that of a 0.5 wt.% ZDDP solution). This species possesses very similar chemical functionality to a ZDDP, but lacks the potentially crucial zinc cation. The optical interference images collected during MTM testing for this species show evidence to suggest the beginning of tribofilm formation, but with only a very thin tribofilm being present after 2 h rubbing time (Fig. 5.17).

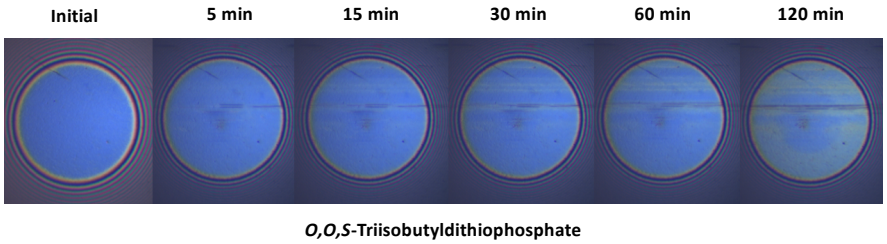

Figure 5.17: Optical interference images obtained for *O,O,S*-triisobutyldithiophosphate upon progressive rubbing during MTM tests.

This result supports the idea that amine-functional OFMs can sequester or leach zinc from the ZDDP tribofilm, which contributes to the slower ZDDP tribofilm growth kinetics observed. Further to this, the optical interference results obtained for tests involving *O,O,S*-triisobutyldithiophosphate are also consistent with reports regarding other metal-free species.[35] For these compounds, tribofilms are reported to form, but at a much slower rate than for ZDDPs. Suitable network-forming cations are reported to be eventually provided by iron from the steel surface, generated with prolonged rubbing.

To summarise, several mechanisms have been proposed to explain the slower tribofilm growth kinetics observed for the **^{i}Bu ZDDP-OFM1** systems studied and will be summarised below, though in fact, it is possible and perhaps likely that a combination of

mechanisms contributes to the tribofilm growth behaviour observed, rather than a single process.

- Amine-functional OFMs sequester network-forming zinc cations and make them less available and/or leach them from preformed ZDDP tribofilms
- Inherent friction reduction caused by OFMs, which in turn reduces the applied shear stress in the system - shear stress being recently identified as a key driver for ZDDP tribofilm formation.
- Adsorption of OFMs to the steel surface thus blocking surface sites for tribofilm growth.

5.2.2.2.1 Steric Effects on Tribofilm Formation and Properties

Previously in this thesis, we have identified a correlation between the steric demands and the strength of ZDDP-amine complexation, initially for pyridine-based ligands (Chapter 3) and subsequently for amine-based OFMs (Chapter 4). Additionally, as outlined above, we subsequently investigated the effect of steric demands of the amine-based OFM on the thermal properties of ZDDP-OFM systems. Here it was found that stronger OFM complexation reduced the thermal stability of ZDDP causing faster thermal degradation. With this understanding in hand, we then investigated the tribological performance of octadecyldimethylamine (**OFM3**) with **^{i}Bu ZDDP** to assess and rationalise any differences observed compared to the previously studied **OFM1** system.

MTM-SLIM tests were performed for **^{i}Bu ZDDP** with **OFM3** in two ZDDP:OFM molar ratios, 1:2 and 1:4, the resulting friction and film thickness results are presented in Figure 5.18.

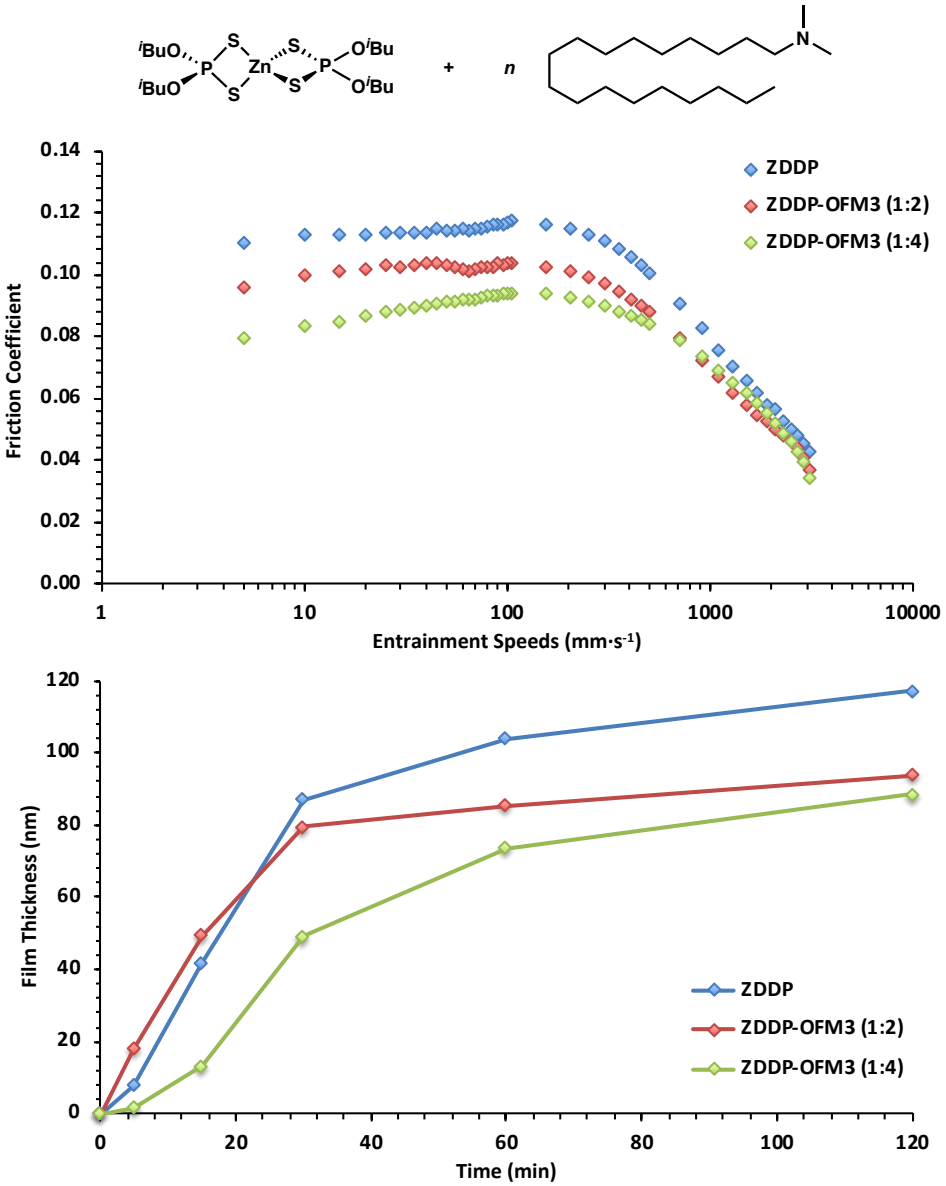

Figure 5.18: Stribeck curves produced after 2 h rubbing (top) and film thickness development (bottom) for **^{i}Bu ZDDP-OFM3** solutions (ratio 1:2 and 1:4). Results are the average from two independent tests. Individual film thickness error bars are omitted for clarity (average standard deviation, $\bar{\sigma}$ = 7 nm).

Initially focussing on the 1:2 **OFM3** ratio studied, a modest friction reduction is observed in comparison to that from the **^{i}Bu ZDDP** solution alone. Additionally, a further friction reduction is observed with increased OFM loading (1:4 ZDDP:OFM ratio), particularly in the boundary/mixed regimes (low/medium speeds) (Fig. 5.18, top). The friction reduction observed for **OFM3** is far less efficient than for **OFM1** (Fig. 5.15), and can be attributed to a combination of reduced surface adsorption and less efficient OFM surface

packing caused by increased steric demands at nitrogen.

In terms of tribofilm thickness, it is apparent that with increased **OFM3** concentrations the tribofilm thickness decreases, as observed previously for **OFM1** (Fig. 5.16). However, the degree of ZDDP tribofilm growth suppression observed for the two OFMs is notably different. For **OFM1** at a ZDDP:OFM ratio of 1:2, tribofilm growth is completely precluded, while at a 1:1 ratio the tribofilm is less than 20 nm thick after 2 h rubbing. Under otherwise identical conditions, for **OFM3** at a ZDDP:OFM ratio equal to 1:2, a tribofilm thickness of approximately 90 nm is observed, whilst even at the highest OFM loading (1:4 ZDDP:OFM ratio) a tribofilm thickness of greater than 85 nm is formed.

Finally, to check the origin and composition of the tribofilms formed, tribofilm elemental compositions of the MTM disk wear tracks were obtained by SEM-EDX measurements (Table 5.3). The elemental analyses data confirms the origin of the tribofilms to be ZDDP-based (significant zinc content), and that the composition is similar to that obtained with pure **^{i}Bu ZDDP** solutions.

Table 5.3: Average elemental compositions of a 5 mm area of the wear tracks of MTM disks post MTM-SLIM testing. Standard deviations are given in parentheses.

Formulation	%C	%O	%P	%S	%Cr	%Fe	%Zn
^{i}Bu ZDDP	12.3 (*0.1*)	9.7 (*0.3*)	1.5 (*0.05*)	0.7 (*0.05*)	1.3 (*0.05*)	65.5 (*0.4*)	6.3 (*0.1*)
^{i}Bu ZDDP-OFM3 (1:2)	14.1 (*0.3*)	9.6 (*0.3*)	1.5 (*0.1*)	1.2 (*0.1*)	1.3 (*0.05*)	62.2 (*0.4*)	7.9 (*0.4*)
^{i}Bu ZDDP-OFM3 (1:4)	13.2 (*0.6*)	7.5 (*0.3*)	1.0 (*0.1*)	0.9 (*0.05*)	1.4 (*0.05*)	67.8 (*0.4*)	6.3 (*0.2*)

In the context of the previously-proposed mechanisms for ZDDP tribofilm growth suppression (Section 5.2.2.2), one might expect all of three of the mechanisms proposed to contribute to the difference in tribofilm growth rates observed for **OFM1** *versus* **OFM3** in ZDDP solutions as follows:

- Firstly, based on the increased steric demands of **OFM3** compared to **OFM1**, less

efficient surface adsorption and packing will result in more surface sites available for ZDDP adsorption and tribofilm formation.

- Somewhat related to the first point, the reduced surface adsorption and less efficient packing of **OFM3**, results in a less effective friction reduction. Higher shear stress results as a consequence of higher friction in the system and shear stress is believed to drive tribofilm formation.

- Finally, the greater steric demands of **OFM3** reduces its propensity to bind ZDDP and sequester network-forming zinc cations. This means the zinc cations are more available to form a tribofilm.

5.2.2.2.2 Multiple Donor Sites – Effect on Tribofilm Formation and Properties

As discussed in Chapters 4 and 5, the presence of additional OFM donor sites can have a drastic impact on the solution and thermal behaviour in ZDDP-OFM systems. Specifically for ethoxylated amine-based OFMs, our solution studies suggested that **^{i}Bu ZDDP-OFM5** complexation resulted in the formation of a tetranuclear zinc cluster and fully ionised DTP ligands. The presence of anionic DTP was subsequently attributed to cause drastic increases in the rate of ZDDP thermal degradation for this system.

In terms of tribological performance, MTM-SLIM tests were performed for **^{i}Bu ZDDP** with **OFM5** in two ZDDP:OFM molar ratios, 1:2 and 1:4; the results are displayed in Figure 5.19.

The Stribeck curves obtained for the two **^{i}Bu ZDDP-OFM5** ratios studied are not particularly striking, only a modest friction reduction is observed in comparison to that obtained for an **^{i}Bu ZDDP** solution (Fig. 5.19, top), and is somewhat comparable to that obtained using **OFM3** (Fig. 5.18, top). Although one might expect the ethoxylated OFM to be better 'anchored' to a steel surface given the presence of multiple donor sites, the OFM packing efficiency will be low based on the steric requirements of the additional donor groups, and thus accounts for the relatively small friction reductions observed.

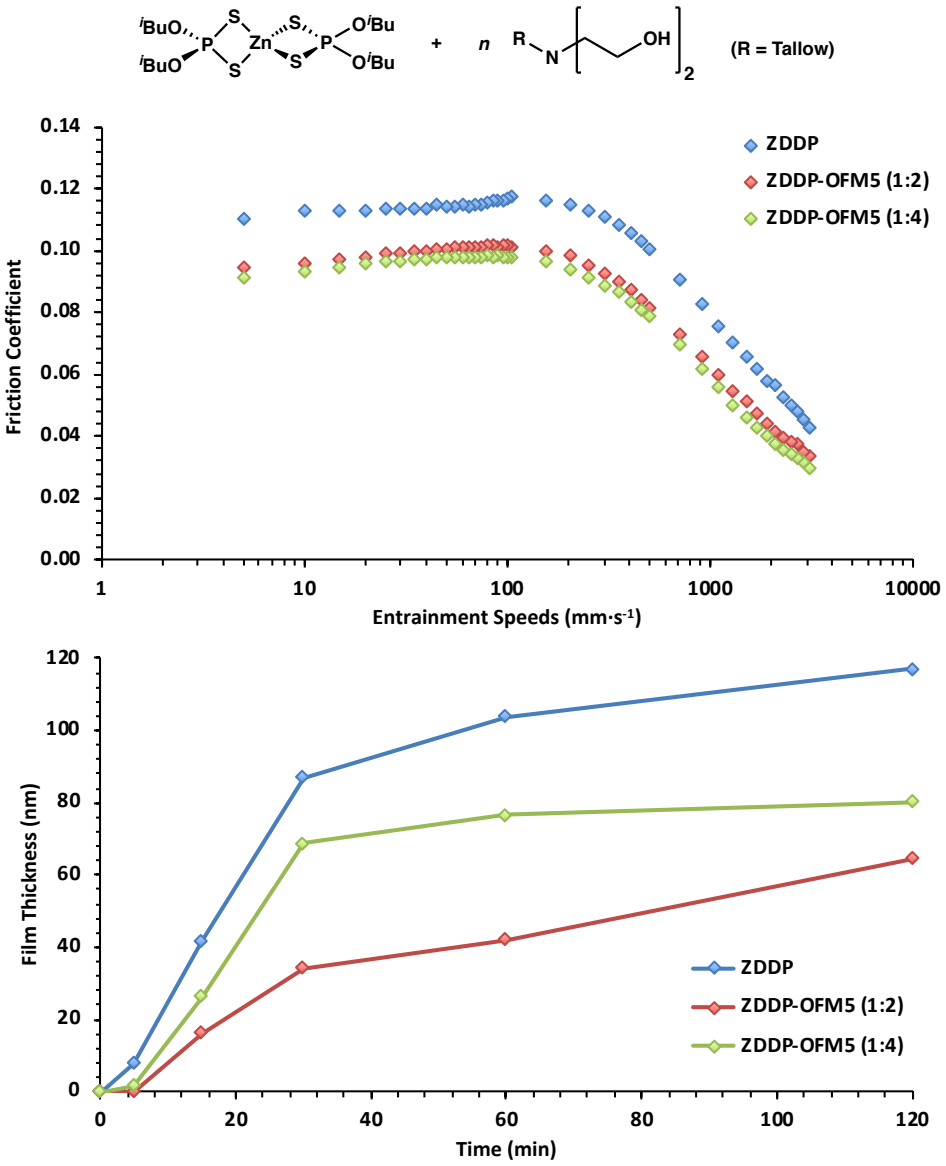

Figure 5.19: Stribeck curves produced after 2 h rubbing (top) and film thickness development (bottom) for **^{i}Bu ZDDP-OFM5** solutions (ratio 1:2 and 1:4). Results are the average from two independent tests. Individual film thickness error bars are omitted for clarity (average standard deviation, $\bar{\sigma}$ = 10 nm).

In contrast to the friction performance, the tribofilm growth trends observed for the two **^{i}Bu ZDDP-OFM5** ratios are particularly interesting (Fig. 5.19, bottom). The data show that while tribofilm growth is suppressed for both the 1:2 and 1:4 ZDDP:OFM ratios studied in comparison to **^{i}Bu ZDDP**, the higher 1:4 ratio **OFM5** system produces a notably thicker tribofilm than the 1:2 ratio. This increasing tribofilm thickness with increasing OFM concentration directly contradicts the trends observed for all other ZDDP-OFM systems studied in this thesis. Subsequently, to help explain the contradictory tribofilm

growth trend observed for **^{i}Bu ZDDP-OFM5** systems elemental compositions of the tribofilms formed on the MTM disk were determined by SEM-EDX analysis (Table 5.4).

Table 5.4: Average elemental compositions of a 5 mm area of the wear tracks of MTM disks post MTM-SLIM testing obtained *via* SEM-EDX analysis. Standard deviations are given in parentheses.

Formulation	%C	%O	%P	%S	%Cr	%Fe	%Zn
^{i}Bu ZDDP	12.3 (*0.1*)	9.7 (*0.3*)	1.5 (*0.05*)	0.7 (*0.05*)	1.3 (*0.05*)	65.5 (*0.4*)	6.3 (*0.1*)
^{i}Bu ZDDP-OFM5 (1:2)	12.2 (*0.4*)	2.5 (*0.3*)	0.2 (*0.05*)	0.4 (*0.05*)	1.6 (*0.05*)	82.4 (*0.3*)	0.0 (*0.05*)
^{i}Bu ZDDP-OFM5 (1:4)	14.2 (*0.9*)	2.1 (*0.8*)	0.1 (*0.05*)	0.2 (*0.05*)	1.6 (*0.05*)	81.2 (*0.1*)	0.0 (*0.05*)

From the elemental analyses data presented, particularly the absence of any zinc content for **OFM5**-containing systems, demonstrates that the tribofilms formed are not ZDDP-based, but rather OFM-based. The fact that the tribofilms are OFM-based, provides an explanation for the trend observed whereby greater OFM loading results in a thicker tribofilm.

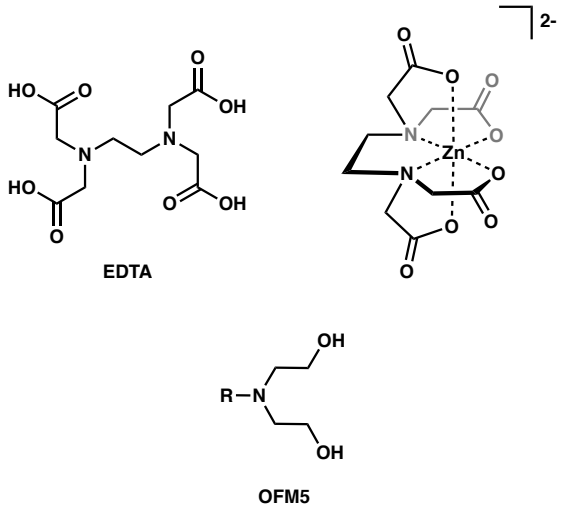

Figure 5.20: Chemical structure and binding of EDTA to a zinc cation, top, and the chemical structure of **OFM5** (R = tallow), bottom.

The reason behind the complete absence of a ZDDP-based tribofilm is thought to be two-fold. Firstly the multiple donor sites present in **OFM5** are expected to anchor the

OFM to the surface more effectively and hence more effectively block surface sites and promote OFM tribofilm formation. In addition, earlier in this thesis (Section 4.2.6.2) the tridentate **OFM5** was shown to bind zinc more strongly than other monodentate OFMs, and hence is expected to sequester network-forming zinc cations extremely effectively. In fact, work by Spikes and co-workers,[177] demonstrated that ethylenediaminetetraacetic acid (EDTA) is extremely effective in dissolving ZDDP tribofilms by complexing to Zn^{II} and Fe^{III} cations. The structural motifs of EDTA are very similar to those of **OFM5** (Fig. 5.20), and therefore it would be expected that these similar chemical functionalities would significantly hinder the formation of ZDDP-based tribofilms, especially when present in solution during the film-forming process.

5.3 Conclusions

In this chapter, the thermal stability of selected ZDDP and ZDDP-OFM systems were studied using ^{31}P NMR spectroscopy. Here it was demonstrated that the presence of amine-functional OFMs enhanced the rate of thermal degradation in ZDDP-OFM solutions, with the extent of this rate enhancement being dependent on the structure of the OFM present. For the monodentate amine-functional OFMs studied (**OFM1** and **OFM3**), it was found that decreasing OFM steric demands favoured ZDDP degradation. This behaviour was attributed to the stronger ZDDP-OFM solution interaction that resulted in a greater change in DTP binding mode (chelating to monodentate) and ultimately increases the nucleophilicity/basicity of the ZDDP-based DTP moieties.

When **^{i}Bu ZDDP** was studied in the presence of an ethoxylated OFM (**OFM5**) an even greater thermolysis rate enhancement was observed. This faster thermal degradation was rationalised based on the presence of the extremely nucleophilic, anionic DTP ligands, which were believed to form as a result of ZDDP-OFM complexation, as discussed in Chapter 4. The degradation mixture obtained for the ethoxylated amine system is much more complex and is believed to be a result of a competing nucleophilic pathway, which involved nucleophilic attack by DTP ligands at the β-carbon of the pendant ethanol branches of the ethoxylated amine OFM.

In terms of tribological performance, MTM-SLIM studies demonstrated that OFM structure plays a key role in dictating both tribofilm formation and properties. Decreased OFM steric demands for monodentate amine-functional OFMs studied with ZDDP results in a greater friction reduction, but also coincides with severely inhibited tribofilm formation, despite the lower thermal stability previously demonstrated for all ZDDP-OFM systems. Similarly, the combination of an ethoxylated OFM with ZDDP in solution completely inhibited the formation of a ZDDP-based tribofilm, though an OFM-based tribofilm was apparent and confirmed by SEM-EDX analysis.

Overall, a key result obtained in this chapter was that lower thermal stability in ZDDP-OFM systems does not correlate to faster ZDDP-tribofilm formation in amine-functional OFM-containing systems, a correlation that has been long established for ZDDPs when studied in isolation. Rather than thermal stability dictating the rate of tribofilm formation, it is apparent that the propensity of an OFM to complex to network-forming zinc cations, to adsorb to and thus block surface sites, and to reduce friction (and hence shear stress), dictates tribofilm formation and properties.

5.4 Experimental

5.4.1 General Considerations

Solvent purification and compound characterisation was performed as detailed in Chapter 3. All commercial OFMs and the Group III mineral oil, Nexbase 3043 (Neste), were kindly supplied by AkzoNobel, while all other chemicals were purchased and used as received from commercial suppliers, unless otherwise stated.

5.4.2 Synthetic Procedures

O,O,S-Triisobutyldithiophosphate

Isobutyl bromide (0.98 g, 7.13 mmol) was added to a solution of potassium diisobutyl dithiophosphate (2.00 g, 7.13 mmol) in ^{i}BuOH (75 cm^3) and the mixture heated at reflux for 16 hours. Volatile components were removed *in vacuo* before the addition of

water and the product extracted into ether (3×20 cm^3). Subsequent removal of volatile components yielded the title compound as a clear liquid (1.21 g, 57% yield).

^{1}H NMR (600 MHz, Chloroform-*d*) δ 3.92 – 3.77 (m, 4H, OCH_2CH(CH$_3$)$_2$), 2.75 (dd, $^3J_{PH}$ = 14.7 Hz, $^3J_{HH}$ = 6.8 Hz, 2H, SCH_2CH(CH$_3$)$_2$), 1.99 (nonet, $^3J_{HH}$ = 6.8 Hz, 2H, OCH$_2$CH(CH$_3$)$_2$), 1.90 (nonet, $^3J_{HH}$ = 6.8 Hz, 1H, SCH$_2$CH(CH$_3$)$_2$), 1.00 (d, $^3J_{HH}$ = 6.8 Hz, 6H, SCH$_2$CH(CH_3)$_2$), 0.96 (d, $^3J_{HH}$ = 6.8 Hz, 12H, OCH$_2$CH(CH_3)$_2$).

^{31}P{^{1}H} NMR (243 MHz, Chloroform-*d*) δ 95.8 (s).

^{13}C{^{1}H} NMR (151 MHz, Chloroform-*d*) δ 73.8 (d, $^2J_{CP}$ = 7.2 Hz, OCH$_2$CH(CH$_3$)$_2$), 42.1 (d, $^2J_{CP}$ = 4.0 Hz, SCH$_2$CH(CH$_3$)$_2$), 29.4 (d, $^3J_{CP}$ = 5.7 Hz, SCH$_2$$C$H(CH$_3$)$_2$), 29.0 (d, $^3J_{CP}$ = 8.5 Hz, OCH$_2$$C$H(CH$_3$)$_2$), 21.9 (SCH$_2$CH($CH_3$)$_2$), 19.0 (OCH$_2$CH($CH_3$)$_2$).

HRMS (ASAP) *m/z* Calc. for [M+H]$^+$ $C_{12}H_{28}O_2PS_2$ 299.1268; Found 299.1275.

(Calc.: C, 48.30; H, 9.12. Found: C, 48.10; H, 9.03).

S,S,S-Triisobutyltetrathiophosphate

In a dried, nitrogen-flushed three-necked round bottom flask fitted with a condenser, dry, degassed triethylamine (5.37 g, 53.1 mmol) was added to a solution of degassed isobutyl mercaptan (4.79 g, 53.1 mmol) in dry, degassed THF (80 cm^3). The resulting solution was cooled to 0 °C before dropwise addition of a solution of $PSCl_3$ (3.00 g, 17.7 mmol) dissolved in dry, degassed THF (50 cm^3). Upon complete addition, the mixture was allowed to warm to room temperature and stirred overnight. The white solid was removed *via* filtration and volatile components removed from the filtrate *in vacuo* to yield a yellow liquid. Vacuum distillation (116-120 °C / 0.005 mmHg) yielded the title compound as a clear liquid (2.41 g, 41% yield).

^{1}H NMR (400 MHz, Chloroform-*d*) δ 2.88 (dd, $^3J_{PH}$ = 15.3 Hz, $^3J_{HH}$ = 6.8 Hz, 6H, SCH_2CH(CH$_3$)$_2$), 2.01 (nonet, $^3J_{HH}$ = 6.8 Hz, 3H, SCH$_2$CH(CH$_3$)$_2$), 1.03 (d, $^3J_{HH}$ = 6.8 Hz, 18H, SCH$_2$CH(CH_3)$_2$).

^{31}P{^{1}H} NMR (162 MHz, Chloroform-*d*) δ 95.4 (s).

^{13}C{^{1}H} NMR (101 MHz, Chloroform-*d*) δ 43.7 (d, $^2J_{CP}$ = 4.2 Hz, SCH$_2$CH(CH$_3$)$_2$),

29.1 (d, $^3J_{CP}$ = 5.5 Hz, $SCH_2CH(CH_3)_2$), 22.1 ($SCH_2CH(CH_3)_2$).

HRMS (ASAP) *m/z* Calc. for $[M+H]^+$ $C_{12}H_{28}PS_4$ 331.0812; Found 331.0814.

(Calc.: C, 43.60; H, 8.23. Found: C, 44.01; H, 8.27).

Tetrapropylammonium Diisobutyldithiophosphate

Tetrapropylammonium bromide (0.95 g, 3.57 mmol) was added to an aqueous solution (20 cm^3) of potassium diisobutyldithiophosphate (1.00 g, 3.57 mmol) and the reaction mixture stirred for 2 hours. The solvent volume was reduced *in vacuo* (50 °C, water bath) until some solid material was visible, before allowing the solution to cool slowly to room temperature to yield colourless crystals of the title compound (1.21 g, 79% yield).

^{1}H NMR (700 MHz, Chloroform-*d*) δ 3.74 (dd, $^3J_{PH}$ = 7.7 Hz, $^3J_{HH}$ = 6.7 Hz, 4H, $OCH_2CH(CH_3)_2$), 3.38 – 3.33 (m, 8H, $NCH_2CH_2CH_3$), 1.93 (nonet, $^3J_{HH}$ = 6.7 Hz, 2H, $OCH_2CH(CH_3)_2$), 1.82 – 1.74 (m, 8H, $NCH_2CH_2CH_3$), 1.05 (t, $^3J_{HH}$ = 7.3 Hz, 12H, $NCH_2CH_2CH_3$), 0.91 (d, $^3J_{HH}$ = 6.7 Hz, 12H, $OCH_2CH(CH_3)_2$).

^{31}P{^{1}H} NMR (283 MHz, Chloroform-*d*) δ 113.0 (s)

^{13}C{^{1}H} NMR (176 MHz, Chloroform-*d*) δ 71.9 (d, $^2J_{CP}$ = 8.0 Hz, $OCH_2CH(CH_3)_2$), 61.1 ($NCH_2CH_2CH_3$), 29.2 (d, $^3J_{CP}$ = 8.9 Hz, $OCH_2CH(CH_3)_2$), 19.5 ($OCH_2CH(CH_3)_2$), 16.1 ($NCH_2CH_2CH_3$), 11.1 ($NCH_2CH_2CH_3$).

HRMS (ASAP) *m/z* Calc. for $[M+H]^+$ $C_{20}H_{47}N\,O_2PS_2$ 428.2786; Found 428.2788.

(Calc.: C, 56.17; H, 10.84; N, 3.28. Found: C, 55.58; H, 10.72, N; 3.18).

5.4.3 Thermolysis Experiments

Thermal degradation experiments were performed on 2.5 wt.% **^{i}Bu ZDDP** samples in a 1:2 ZDDP-amine ratio, unless otherwise stated. Samples were formulated and stirred at 40-50 °C for ~ 30 mins to ensure complete additive dissolution and sample homogeneity. Approximately 0.7 cm^3 of the formulated sample was placed into an NMR tube and an initial (t = 0) ^{31}P NMR spectrum collected (C_6D_6 insert spiked with PPh_3 to provide lock). The NMR sample was then heated periodically at 150 or 160 °C (sample

fully immersed in oil bath) for the desired time interval, before being quenched in cold water, allowed to return to room temperature and another ^{31}P NMR spectrum collected. This heating/NMR spectrum collection process was repeated until full degradation was observed by ^{31}P NMR spectroscopy.

5.4.4 MTM

The Mini Traction Machine (MTM2; PCS Instruments, Acton, UK) consists of a steel ball loaded against the flat surface of a steel disc. The ball and disk are driven independently to allow for any combination of rolling/sliding conditions. The steel disc is fully submerged in the desired test fluid in a temperature-controlled reservoir. When a test is in progress, the lateral force on the ball generated from friction is detected and recorded, while curves of entrainment *versus* friction coefficient (Stribeck curves) can be programmed to be collected as desired. Stribeck curves were acquired from high speeds to low speeds in order to protect the formed tribofilm by avoiding its damage at low speeds (boundary regime).

5.4.4.1 Test Specimens

Test specimens used for MTM tests were a 3/4 inch ball and a 46 mm diameter disk, both made of AISI 52100 steel (hardness 750-700 HV) and supplied by PCS instruments. The root-mean-square roughness of both balls and disks was 11 ± 3 nm, giving a composite surface roughness of ~16 nm. New specimens were used for each test and were cleaned with solvents in an ultrasonic bath before use.

5.4.5 MTM-SLIM

The principle of the Space Layer Interferometry Mapping (SLIM) is shown in Figure 5.21. A flat glass disk is surface coated with a thin, semi-reflective chromium layer, on top of which is a 'spacer-layer' of transparent silicon dioxide. White light is shone into the contact, some light is reflected from the chromium layer while some passes through the semi-reflective layer, the silicon dioxide layer and any lubricant film present on the ball before being reflected back from the steel surface. The phase difference created

by the different distances travelled by the two beams means upon recombination they interfere, constructively or destructively. The result is a coloured interference image of the contact, which is captured by a digital camera; based on the red, green and blue colour of each pixel can be converted into a map of the path difference and hence the film thickness separating the ball and the glass disk.

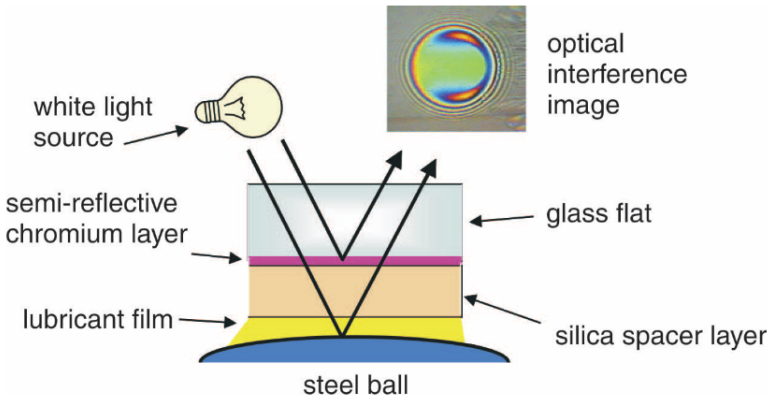

Figure 5.21: Basic principles of SLIM.

This method is applied to study ZDDP tribofilms *in situ* within a MTM tribometer, *i.e.* outside of the contact but within the test apparatus. This is achieved by periodically halting the motion in the MTM and capturing an interference image from the stationary ball surface (see Fig. 5.12). The thickness directly calculated from the image gives the thickness of the tribofilm and the silica spacer layer. The thickness of the spacer layer is determined by capturing an optical interference image at the beginning of each test and subsequently subtracted. Further details on the MTM-SLIM method can be found in ref. 58.

The tribofilm thicknesses were calculated from the optical interference images obtained using the associated SLIM offline analysis software (PCS Instruments) by averaging thickness values obtained from circular regions across the entire of the width of tribofilm formed.

5.4.6 SEM-EDX

After MTM-SLIM testing the MTM disk specimens were rinsed with heptane to remove excess oil and dried in air prior to SEM imaging. SEM imaging was performed by B. D. Rossenaar (AkzoNobel) on a Zeiss Sigma FEG-SEM equipped with an Oxford Instruments X-Max EDX detector of 80 mm^2.

Chapter 6

Alternative Synthetic Routes for the Preparation of Zinc Dialkyl Diselenophosphates (Se-ZDDPs)

6.1 Introduction

Earlier in this thesis, we have demonstrated the ability to monitor changes in dithiophosphate (DTP) binding mode that occurs as a result of amine or amine-functional OFM coordination to the zinc atom of **^{i}Bu ZDDP**, using ^{31}P NMR spectroscopy. This method indirectly indicates a change in DTP binding mode based on a change in ^{31}P chemical shift. The resulting DTP binding configuration can be assigned using chemical shift generalisations previously reported in the literature.[126] Although very useful generalisations, exceptions to the chemical shift guidelines reported are only too apparent, thus meaning an alternative, complementary spectroscopic handle or technique is highly desirable. To gain an additional spectroscopic handle, we decided to investigate the selenium analogues of ZDDPs, zinc dialkyl diselenophosphates (Se-ZDDP). With ^{77}Se being NMR active, the study of Se-ZDDPs would provide an additional spectroscopic handle and would greatly aid in elucidating any structural changes and the binding mode of the diselenophosphate (DSP) ligands in solution. The results and understanding obtained from the Se-ZDDP systems could then be compared and correlated back with the ZDDP equivalents.

Preparation of dialkyl diselenophosphoric acids has been reported previously *via* the reaction of diphosphorus pentaselenide (P_2Se_5) with an alcohol, in a reaction akin to that used for the preparation of dialkyl dithiophosphoric acids used in the synthesis of ZDDPs. The diselenophosphoric acids prepared however, were unstable and could not be isolated, though their preparation is inferred from the isolation of the potassium salts.[178] Similarly, ammonium DSP salts have been reported more recently, that were subsequently complexed to zinc to form Se-ZDDPs (Scheme 6.1).[179]

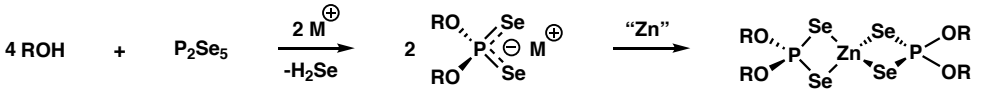

Scheme 6.1: Synthesis of Se-ZDDPs using P_2Se_5.[179]

Solid state structures of ethyl and isopropyl Se-ZDDP derivatives have been shown to possess polymeric and dimeric configurations, respectively, and thus match that of their ZDDP equivalents (Fig. 6.1).

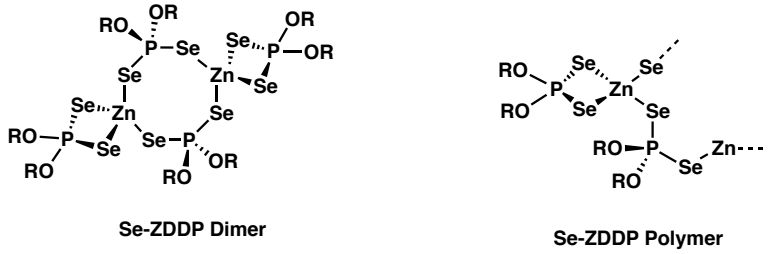

Figure 6.1: Dimeric (R = ^{i}Pr) and polymeric (R = Et) structures of Se-ZDDPs.

In addition, both Se-ZDDPs (R = ^{i}Pr and Et) were shown to partake in a monomer-dimer equilibrium in solution, something that also resembles the behaviour of ZDDPs in solution (Scheme 6.2).[179]

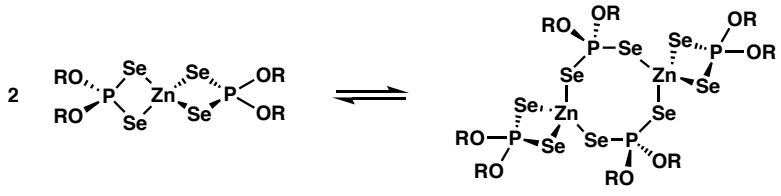

Scheme 6.2: Monomer-dimer equilibrium for Se-ZDDPs.[179]

6.2 Preparation of Dialkyl Diselenophosphate (DSP) Salts

In our initial attempts to make the isobutyl Se-ZDDP derivative, using the literature methods described above, we experienced very poor conversion of P_2Se_5 to the resulting diselenophosphate (DSP) salt. Furthermore, subsequent isolation/purification was difficult based on the unstable nature of these compounds. Subsequent reaction of the crude diselenophosphate salt appeared successful based on multinuclear NMR spectroscopic analysis, though subsequent purification attempts were again not successful. Attempts to grind P_2Se_5 (synthesised by heating the required elements in the correct stoichiometric ratio at 460 °C under static vacuum for using 24 hours) to improve conversions were unsuccessful using a pestle and mortar, while other methods of grinding were hindered by the air/moisture sensitivity of P_2Se_5, its extremely strong odour and the formation of toxic H_2Se in air. With the aforementioned problems in mind, and the general difficulties in making and handling P_2Se_5, we sought an alternative method for the synthesis of DSP salts, and subsequently Se-ZDDPs, which did not require the synthesis and subsequent use of P_2Se_5.

6.2.1 Synthesis of DSP Salts *via* a Dialkoxyphosphine-Borane

The first alternative preparation investigated involved the initial synthesis of diisobutoxyphosphine-borane from diisobutyl chlorophosphite. This could be synthesised in good yield using a modification of the procedure reported by Montchamp *et al.,* for the related diethoxy derivative (Scheme 6.3).[180] The dialkoxyphosphine-borane adduct was a particularly attractive intermediate as it served as an air stable, protected P^{III} species that was easily accessible.

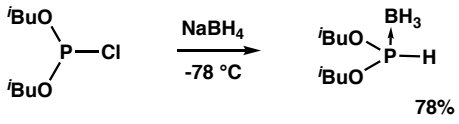

Scheme 6.3: Synthesis of diisobutoxyphosphine-borane.

Once isolated, it was envisaged that borane deprotection and deprotonation using an

amine, followed by selenation of diisobutoxyphosphine-borane, using elemental selenium, should lead to the desired diselenophosphate salt, with the protonated amine serving as the counter cation (Scheme 6.4). The amine of choice for this reaction was selected to be pyrrolidine, based on its reported efficacy in deprotecting phosphine-borane adducts.[181]

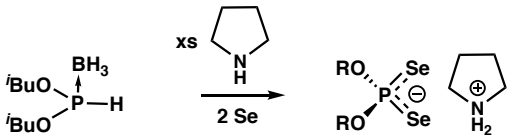

Scheme 6.4: Proposed synthesis of pyrrolidinium diisobutyldiselenophosphate.

After heating at 60 °C for 72 hours, analysis of the crude reaction mixture by ^{31}P NMR spectroscopy was very promising and revealed the presence of a pentet resonance {δ_P 84.9, (^{i}BuOH)} flanked by selenium satellites (J_{SeP} = 730 Hz). From this crude reaction mixture a clear oil could be isolated, and the ^{31}P NMR spectrum revealed a similar pentet resonance {δ 82.5 ($CDCl_3$)} flanked by selenium satellites (J_{SeP} = 720 Hz) (Fig. 6.2). The pentet resonance and J_{SeP} coupling agrees favourably with the two ammonium dialkyl diselenophosphate salts previously reported {δ_P 82 (isopropyl) and 88 (ethyl), J_{SeP} = 720 Hz}.[182] Unfortunately however, some impurities remained, notably a boron-containing impurity that displays a broad ^{31}P NMR spectroscopic resonance {δ_P 154.2 ($CDCl_3$)}, which may appear insignificant due to its broad nature, but ^{31}P NMR integrations actually reveal it was present in approximately a 1:3 ratio with the desired diselenophosphate salt.

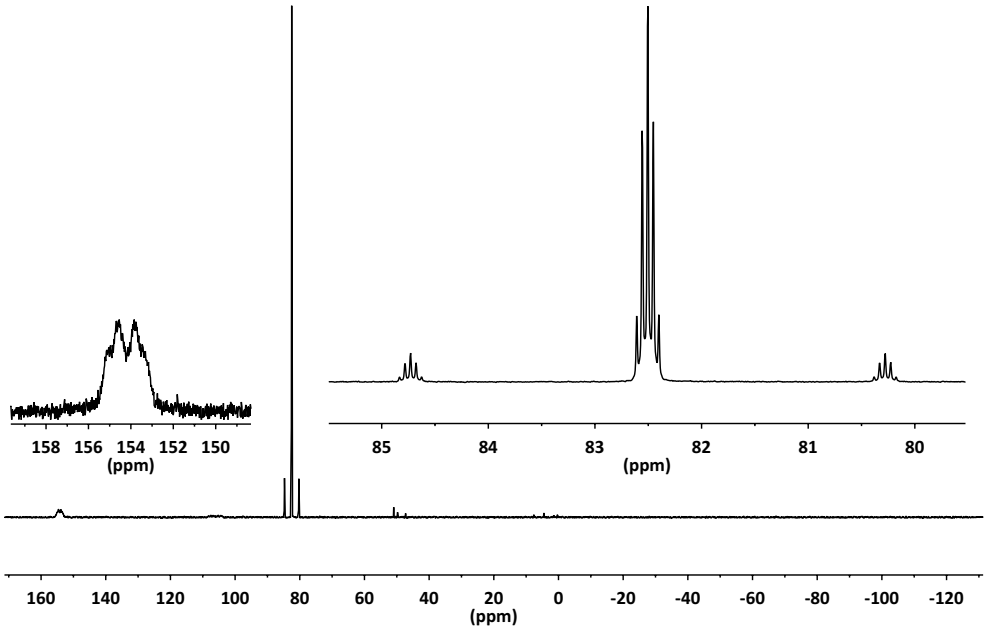

Figure 6.2: $^{31}P[^{1}H]$ NMR (162 MHz, $CDCl_3$) spectrum of crude pyrrolidinium diisobutyldiselenophosphate. Insets show expansions of notable resonances.

All attempts to crystallise or precipitate the diselenophosphate salt were, to our surprise, completely unsuccessful. Failure to precipitate or crystallise the diselenophosphate salt could be due to the impurities present, which inhibit crystallisation, or from the fact that the product is simply an ionic liquid. Continued manipulation of the crude diselenophosphate oil was not desirable given its instability, and therefore was subsequently used in its crude form.

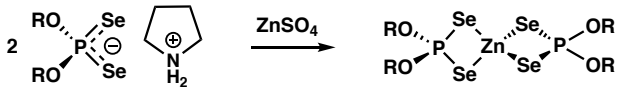

Scheme 6.5: Synthesis of zinc diisobutyl diselenophosphate.

With the crude diselenophosphate salt in hand, subsequent reaction with zinc sulphate in degassed water (Scheme 6.5), yielded full conversion of the diselenophosphate salt, as observed by ^{31}P NMR spectroscopy (Fig. 6.3). In the displayed spectrum, a new broad resonance can be observed $\{\delta_P$ 64.2 ($CDCl_3$)$\}$ that is assigned to zinc diisobutyl diselenophosphate; a broad resonance being expected based on monomer-dimer interconversion in solution (Scheme 6.2). Alongside the isobutyl Se-ZDDP resonance, an additional resonance is apparent that arises from the boron-containing impurity, which carried through from the crude diselenophosphate starting material. In this spectrum,

given the broad nature of both resonances, the relative ratio of impurity to product (1:3) is much more easily observed. Unfortunately, all attempts to remove the undesired boron-containing impurity at this stage, or precipitate/crystallise the Se-ZDDP product, were also unsuccessful, much like purifications attempted at earlier stages in the Se-ZDDP synthesis.

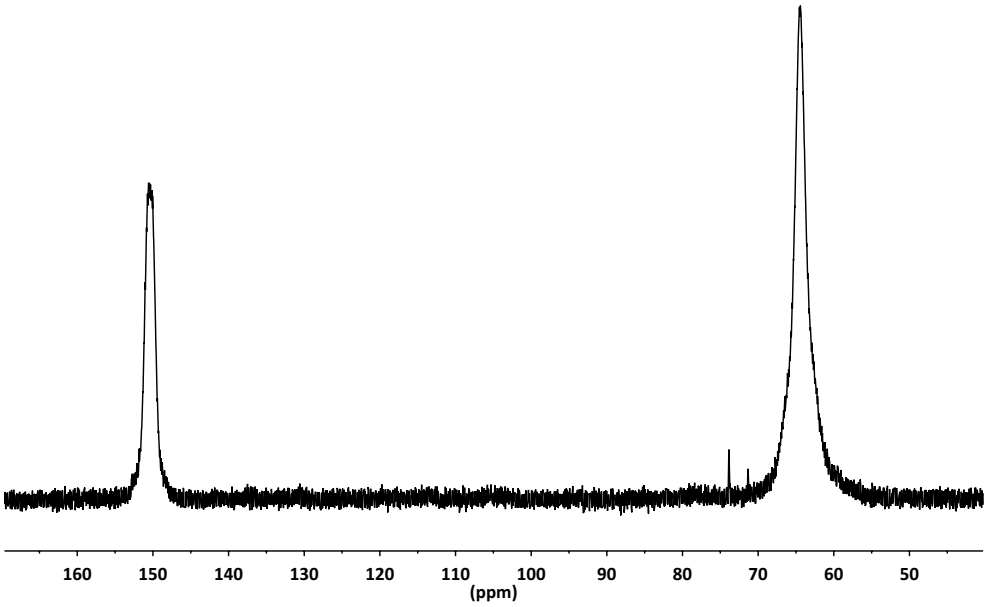

Figure 6.3: $^{31}P[^{1}H]$ NMR (162 MHz, $CDCl_3$) spectrum of crude isobutyl Se-ZDDP contaminated with a boron-containing impurity.

The problematic boron-containing impurity is postulated to be the pyrrolidinium salt of boranoselenophosphate $[(RO)_2P(Se)BH_3^-]$, and although there is no direct analogue reported in the literature, a sulfur derivative is known (Fig. 6.4).[183]

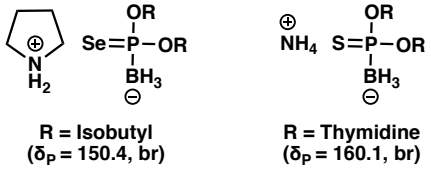

Figure 6.4: Proposed structure of boron-containing impurity and a known sulfur analogue reported in the literature.[183]

Although it might be expected that a boranoselenophosphate impurity would be sufficiently water soluble to be removed during reaction workup, the organic substituents and cation may render it sufficiently insoluble to persistent after reaction workup. Nevertheless, further investigations are needed to definitively assign this impurity, one of

which would be to selectively synthesise the boranoselenophosphate salt. This could be achieved *via* reaction of diisobutoxyphosphine-borane with potassium hydride and subsequent reaction with elemental selenium, as achieved for the related boranoselenophosphinate species (Scheme 6.6).[184]

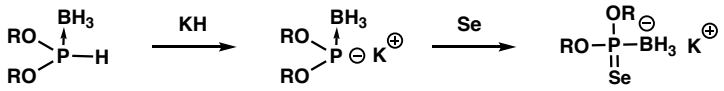

Scheme 6.6: Proposed synthetic pathway for the selective preparation of boranoselenophosphate salts.

Modification of the synthetic route, used in the synthesis of the diselenophosphate salt from the borane protected dialkoxyphosphine moiety (Scheme 6.4), to a stepwise borane deprotection-selenation procedure could potentially avoid the formation of the boron-containing impurity altogether (Scheme 6.7). This route would also allow for the convenient synthesis of mixed seleno/thio compounds *via* sequential addition of 1 equivalent of sulfur/selenium, followed by addition of a further equivalent of chalcogen with a suitable base.

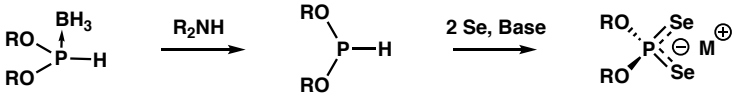

Scheme 6.7: Stepwise borane deprotection-selenation route toward diselenophosphate salts.

That said, simply the selection of an alternative amine, other than pyrrolidine, or alternative alkyl substituents, that produces a diselenophosphate salt that precipitates or crystallises easily could prove to be the simplest modification that allows easy purification at the selenophosphate stage, before reacting on to give pure Se-ZDDP. Alternatively, a cation exchange to substitute pyrrolidinium for an alternative cation, *e.g.* potassium, could be performed to aid crystallisation and hence purification.

6.2.2 Synthesis of DSP Salts *via* a Dialkyl Triethylsilylphosphite

Taking inspiration from the syntheses of triethylammonium salts of disubstituted diselenophosphinates reported by O'Brien and co-workers,[185] we attempted to use a similar approach for the synthesis of disubstituted diselenophosphates (Scheme 6.8). This

method uses excess triethylsilane and triethylamine with elemental selenium to yield the desired diselenophosphate species. Triethylsilane is preferred to trichlorosilane as the latter reacts to precipitate triethylammonium chloride.

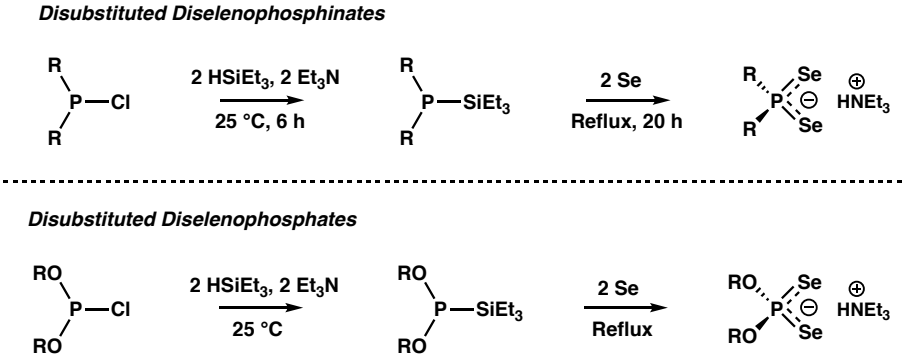

Scheme 6.8: Synthesis of dialkyl diselenophosphinates and proposed synthetic pathway for dialkyl diselenophosphates.

After the treatment of diisobutyl chlorophosphite with 2 equivalents of triethylsilane and triethylamine, subsequent addition of elemental selenium and heating at reflux (40 hours), ^{31}P NMR spectroscopy of the crude reaction mixture revealed the expected pentet resonance, flanked by selenium satellites, that can be assigned to the desired selenophosphate salt (Fig. 6.5).

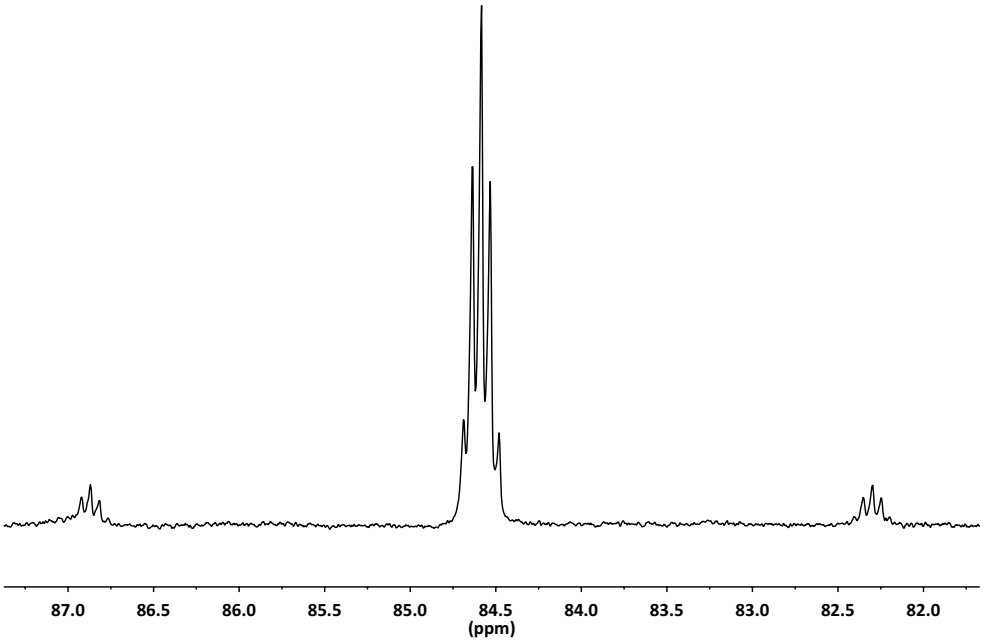

Figure 6.5: $^{31}P[^{1}H]$ NMR (162 MHz, toluene) spectrum of the crude reaction mixture after heating diisobutyl chlorophosphite with triethylsilane/triethylamine/selenium for 40 h at reflux. C_6D_6 insert used to provide lock.

Crystal growth by reducing the solvent volume and cooling to 0 °C, as achieved for the diselenophosphinate equivalents, was in this case unsuccessful. Though after volatile components were removed, a yellow precipitate was produced upon treatment with dry ether. However, upon adding dry $CDCl_3$ to obtain NMR spectra, sample decomposition occurred and the yellow precipitate instantaneously turned red. Early reports from Kudchadker *et al*. regarding the synthesis of diselenophosphate salts had previously noted that these species turn red upon storage, something that could arise due to separation of red selenium.[178]

A problem with the alternative synthetic pathways proposed for the synthesis of diselenophosphate derivatives (Schemes 6.8 and 6.4), is that only the diethyl chlorophosphite starting material is commercially available. Synthesis of dialkyl chlorophosphites using phosphorus trichloride however has been long known (Scheme 6.9),[186–188] although the yields of these reactions can be notably low after purification by vacuum distillation. Similarly, in our hands, we found that despite very good conversion to the desired dialkyl chlorophosphite species observed by ^{31}P NMR spectroscopy (Route B, Scheme 6.9),

after purification by vacuum distillation, yields of the diisobutyl chlorophosphite were poor and as a result hindered subsequent reaction screening due to constant need for more starting material. We believe the poor yields obtained are as a result of re-equilibration between mono-, di- and tri-alkoxy species during the distillation procedure, thus decreasing the yield of the desired chlorophosphite.

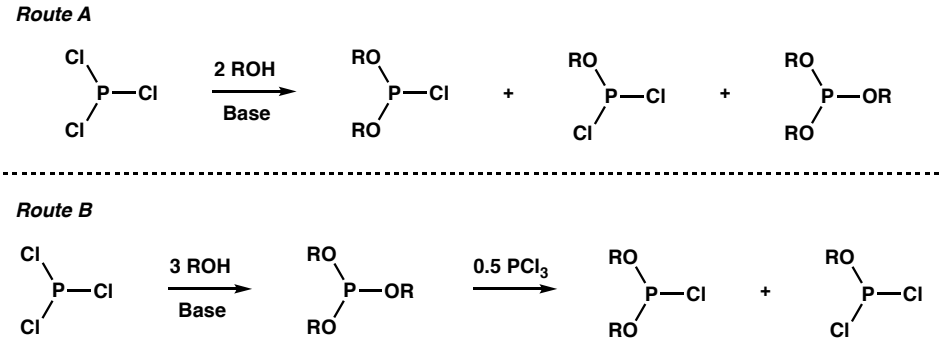

Scheme 6.9: Synthesis of dialkyl chlorophosphites by the direct reaction of 2 equivalents of alcohol with PCl_3 (Route A) or *via* the formation of trialkyl phosphite and subsequent reaction with PCl_3 (Route B).

To circumvent this problem, we attempted to synthesise the desired dialkyl chlorophosphite starting material *in situ* before reacting on with triethylsilane, triethylamine and selenium. To achieve this we reacted the commercially available diisobutyl phosphite with the commercially available chlorinating agent, dichlorotriphenylphosphorane (Scheme 6.10). Similar reactions have previously been performed by Wada *et al.* using tris(2,4,6-tribromophenoxy)dichlorophosphorane and showed excellent selectivity for dialkyl chlorophosphites.[189]

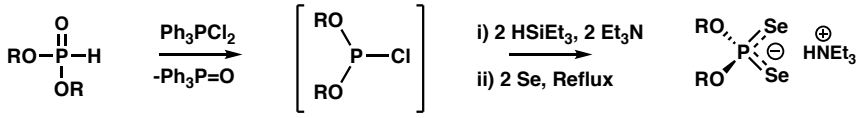

Scheme 6.10: Synthesis of diselenophosphate salts *via* the *in situ* synthesis of dialkylchlorophosphite using dichlorotriphenylphosphorane.

Upon carrying out this modified approach, ^{31}P NMR spectroscopic analysis of the crude reaction mixture displayed the characteristic pentet resonance {δ 85.1 (toluene)}, flanked by selenium satellites (J_{SeP} = 740 Hz), for the desired diselenophosphate salt as observed previously (Fig. 6.5). The triphenylphosphine oxide side product that forms during the

initial chlorination step (Scheme 6.10), can be selectively crystallised out and removed by reducing the solvent volume followed by cooling, to yield a yellow/orange oil. It was then envisaged that the diselenophosphate salt could be precipitated with dry ether, as achieved previously, to give the required product. This however, to our surprise, was not the case. X-Ray crystallographic analysis of the triphenylphosphine oxide isolated, revealed that the crystals formed where actually the monohydrate. This observation suggests that water had been unintentionally entered into the reaction and could explain the inability to precipitate the reaction product. Subsequently it was identified that the solvent purification facility was not functioning as required and solvents being used were not water free as expected.

6.2.3 Attempted Synthesis of Se-ZDDPs *via* Direct Sulfur/Selenium Exchange using Woollins' Reagent (WR)

Woollins' reagent (WR), $(PhPSe_2)_2$, is a selenium analogue of the well known Lawesson's reagent (LR), that has been identified as an effective selenating agent and as a useful tool for the synthesis of heterocycles containing phosphorus-selenium moieties.[190,191] (Fig. 6.6).

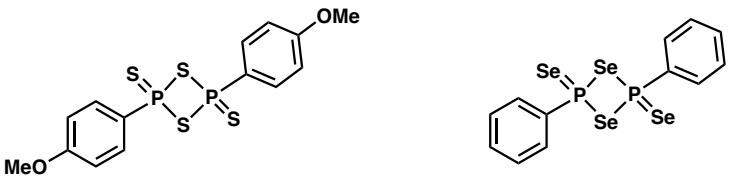

Figure 6.6: Chemical structures of Lawesson's reagent and the related Woollins' reagent.

Now available commercially from Sigma Aldrich, we attempted to use WR to achieve direct sulfur/selenium exchange in ZDDPs to afford the corresponding selenium-containing ZDDP analogue (Scheme 6.11).

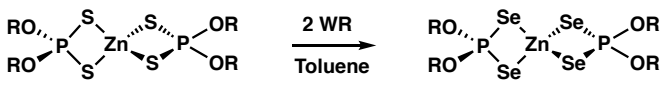

Scheme 6.11: Attempted selenium/sulfur exchange reaction of **^{i}Bu ZDDP** with WR.

To test the feasibility of the chalcogen exchange reaction proposed above, an NMR scale test reaction was performed in which **^{i}Bu ZDDP** was combined with 2 equivalents of WR in refluxing toluene-d_8 (due to the limited solubility of WR most synthetic procedures are carried out in refluxing toluene). The resulting ^{31}P NMR spectra, collected periodically after timed heating intervals, revealed extremely complex, intractable mixtures of phosphorus-containing products. Based on the observed complexity of the ^{31}P NMR spectra collected, this route was judged to be unfeasible and no further investigations were undertaken.

6.3 Conclusions

In this chapter alternative methods for the synthesis of dialkyl diselenophosphate salts, toward the easier synthesis of zinc dialkyl diselenophosphates, have been explored. Two promising alternative syntheses have been identified, one *via* a dialkoxy phosphine borane adduct and another *via* a dialkyl triethylsilylphosphite species. Both methods show promise in terms of a more convenient synthesis of diselenophosphate salts, over the conventional P_2Se_5 route, though purification remained problematic in both cases and further optimisation of both methods is required. The lack of commercial availability of the required dialkyl chlorophosphite starting materials can be addressed by their *in situ* synthesis from dialkyl phosphites using dichlorotriphenylphosphorane. Attempted direct sulfur/selenium exchange by reaction of **^{i}Bu ZDDP** with Woollins' reagent yielded an extremely complex mixture of phosphorus-containing products and proved unsuccessful.

6.4 Experimental

6.4.1 General Considerations

Unless otherwise stated, all manipulations were performed under an atmosphere of dry nitrogen using standard Schlenk line techniques with oven dried glassware. Solvent purification and compound characterisation was performed as detailed in Chapter 3. $CDCl_3$ was dried over P_2O_5 and subsequently distilled and degassed. Toluene-d_8 was dried over CaH_2prior to distillation and degassing. ^{i}BuOH was dried over $NaBH_4$ at reflux

and subsequently distilled and degassed. Diisobutyl chlorophosphite was synthesised using the method of Cook *et al.* with slight modifications and the purity assessed by ^{31}P and ^{1}H NMR spectroscopies.[186] All other chemicals were purchased from commercial suppliers and degassed before use.

6.4.2 Synthetic Procedures

Diisobutoxyphosphine-Borane

A stirred solution of $NaBH_4$ (0.32 g, 8.46 mmol) in THF (20 cm^3) was cooled to -78 °C three-necked round bottom flask. Diisobutyl chlorophosphite (1.00 g, 4.70 mmol) was added in a single portion, the mixture was stirred for 10 minutes, allowed to warm to room temperature, and then stirred for a further 3 hours. The reaction mixture was poured directly onto a mixture of conc. HCl (3 cm^3) and ice (20 g), extracted with ethyl acetate (3 × 15 cm^3). The combined organic layers were dried ($MgSO_4$), filtered and volatile components removed *in vacuo* from the filtrate to yield a mixture of a clear oil and white solid. An aliquot of DCM was added before filtration (celite) and the resulting solution was concentrated *in vacuo* to yield the title compound as a clear oil (0.70 g, 78% yield).

^{1}H NMR (400 MHz, Chloroform-*d*) δ 6.98 (d, 1H, $^{1}J_{HP}$ = 444.3 Hz, P*H*), 3.91 – 3.68 (m, 4H, OCH_2CH(CH_3)$_2$), 1.95 (nonet, 2H, $^{3}J_{HH}$ = 6.7 Hz, $OCH_2CH(CH_3)_2$), 0.95 (d, 12H, $^{3}J_{HH}$ = 6.7 Hz, $OCH_2CH(CH_3)_2$), 0.55 (br. qd, 3H, $^{1}J_{HB}$ = 96.2 Hz, $^{2}J_{HP}$ = 13.5 Hz, BH_3)*.

^{31}P{^{1}H} NMR (162 MHz, Chloroform-*d*) δ 129.1 (q, $^{1}J_{PB}$ = 75 Hz).

^{13}C{^{1}H} NMR (101 MHz, Chloroform-*d*) δ 75.3 (d, $^{2}J_{CP}$ = 7.8 Hz, $OCH_2CH(CH_3)_2$), 29.5 (d, $^{3}J_{CP}$ = 5.6 Hz, $OCH_2CH(CH_3)_2$), 18.8 (s, $OCH_2CH(CH_3)_2$).

^{11}B {^{1}H} NMR (Chloroform-*d*, 128 MHz): δ -41.8 (d, $^{1}J_{BP}$ = 75 Hz).

HRMS (ASAP) *m/z* Calc. for $[M\text{-}H]^-$ $C_8H_{21}BO_2P$: 190.1409. Found: 190.1397.

* Peak partially masked by doublet at δ = 0.95 ppm

Pyrrolidinium Diisobutyldiselenphosphate

A Schlenk flask was charged with elemental selenium (0.27 g, 3.44 mmol) and evacuated with vacuum and nitrogen cycles. Subsequently, ^{i}BuOH (50 cm^3) and then pyrrolidine (0.27 g, 3.78 mmol) were added and the mixture heated at 60 °C for 40 hours to give a red solution. Volatile components were removed *in vacuo* to give a red solid and clear oil. The clear oil was extracted with ether (3 × 10 cm^3) and after volatile components were removed *in vacuo*, crude pyrrolidinium diselenophosphate was obtained as a clear oil. All attempts to precipitate or crystallise the desired product, to enable further purification, were unsuccessful and so characterisation beyond ^{31}P NMR spectroscopy was not performed.

^{31}P{^{1}H} NMR (162 MHz, Chloroform-*d*) δ 82.5 (s, $^{1}J_{\mathrm{SeP}}$ = 720 Hz).

Zinc Diisobutyl Diselenophosphate

Method A – Synthesis from Crude Pyrrolidinium Diisobutyldielenophosphate

$ZnSO_4{\cdot}7H_2O$ (0.13 g , 0.45 mmol) dissolved in degassed water (20 cm^3) was transferred *via* cannula to a flask containing crude pyrrolidinium diisobutyldiselenophosphate (0.35 g, 0.86 mmol) and the mixture stirred for 2 hours. A waxy white precipitate formed that was isolated by filtration and dried *in vacuo* overnight. All attempts to recrystallise and purify the product were unsuccessful and so characterisation beyond ^{31}P NMR spectroscopy was not performed.

^{31}P{^{1}H} NMR (162 MHz, Chloroform-*d*) δ 64.2 (br. s).

Method B – Attempted Sulfur/Selenium Exchange using Woollins' Reagent

A J. Young's NMR tube was charged with **^{i}Bu ZDDP** (10.3 mg, 0.018 mmol), Woollins' reagent (20.0 mg, 0.038 mmol) and purged with vacuum and nitrogen cycles. Dry toluene-d_8 (0.7 cm^3) was subsequently added before the mixture was heated at 110 °C. ^{31}P NMR spectra were collected periodically over the period of 4 days, revealing the formation of an intractable mixture of phosphorus-containing products and thus no product was isolated for further analysis.

Triethylammonium Diisobutyldiselenophosphate

Method A – Synthesis from Diisobutyl Chlorophosphite

Diisobutyl chlorophosphite (0.8 g, 3.76 mmol) and triethylsilane (0.87 g, 7.52 mmol) were dissolved in toluene (35 cm^3) followed by the addition of triethylamine (0.76 g, 7.52 mmol). The mixture was stirred at room temperature overnight forming a white precipitate. Grey selenium (0.59 g, 7.52 mmol) was added and the solution heated at reflux for 40 hours. Volatile components were removed *in vacuo* to yield an orange oil. A yellow solid was precipitated with ether (20 cm^3) and subsequently isolated by filtration. Addition of $CDCl_3$ caused immediate sample decomposition and the yellow solid turned red. Based on the obvious decomposition no further analysis was performed.

Method B – Synthesis from Diisobutyl Phosphite

To a slurry of dichlorotriphenylphosphorane (3.22 g, 9.65 mmol) in toluene (35 cm^3), triethylamine (10 cm^3) followed by diisobutyl phosphite (1.25 g, 6.44 mmol) were added and the reaction mixture stirred for 2 hours. After 2 hours, triethylsilane (1.50 g, 12.9 mmol) was added and the reaction mixture stirred for a further 1 hour. Grey selenium (1.27 g, 16.1 mmol) was then added and the mixture heated at reflux for 60 hours. The resulting yellow solution was filtered *via* cannula, before the solvent volume was reduced and the solution placed in the fridge overnight. Triphenylphosphine oxide monohydrate crystallised from solution and was removed by filtration to yield crude triethylammonium diisobutyldiselenophosphate as a yellow oil. Attempts to precipitate the reaction product were unsuccessful, something believed to be inhibited by residual water.

Chapter 7

Summary and Outlook

7.1 Introduction

This chapter seeks to draw the preceding chapters' work together, to highlight key areas of overlap and assess the extent to which the thesis aims (Section 2.2) have been met. Initially an overview of the key findings obtained in each chapter will be outlined before more generalised conclusions are drawn from the results as a whole. Particular emphasis is given to the potential impact in automotive lubrication. Finally, possible areas for future research are suggested and discussed.

7.2 Thesis Summary and Key Findings

This thesis aimed to provide a fundamental understanding of any solution interactions, and the consequences thereof, between ZDDPs and friction modifier (FM) additives, with a particular focus on organic friction modifiers (OFMs) bearing an amine functionality. This understanding is necessitated by ever-stringent legislation imposed on automotive lubricant formulators that demands greater fuel economy, lower emissions and extended drain intervals. To achieve these aims, the solution-phase interactions, and resulting coordination-, thermo- and tribo-chemistry of single-component ZDDP/OFMs formulations were studied. Alongside the commercial amine-based OFMs, several model amine alternatives were investigated, where applicable, to aid chemical understanding and provide grounding for subsequent discussions regarding commercial OFMs.

Chapter 3 initially investigated ZDDP-amine interactions more generally, and reported the interaction between ZDDP and several substituted pyridine derivatives, with the pyridine moiety serving as an easily tuneable amine scaffold. In these studies it was identified that complexation occurred *via* a zinc-nitrogen interaction, where greater steric demands ($\%V_{bur}$) and attenuated Lewis basicity (pK_{aH}) reduced the propensity for complex formation in solution, something that was quantified by obtaining binding constants (K_a) from ^{31}P NMR spectroscopic NMR data. Meanwhile, complexation is accompanied by a significant change in the coordination behaviour of the associated dithiophosphate (DTP) ligands; a change that could be monitored and assigned using Raman spectroscopy.

Building on the understanding gained in Chapter 3 regarding the ZDDP-Py' systems investigated, Chapter 4 subsequently identified ZDDPs interact with OFMs in a similar manner (*via* a nitrogen-zinc reaction pathway accompanied by a change in DTP binding mode). X-Ray crystallographic analysis of the first isolated ZDDP-OFM complex, unequivocally confirmed the zinc-nitrogen interaction and provided a structure to validate the use of Raman spectroscopy as a diagnostic tool in determining DTP binding mode in ZDDP-OFM complexes relevant to engine oil formulations (Fig. 7.1).

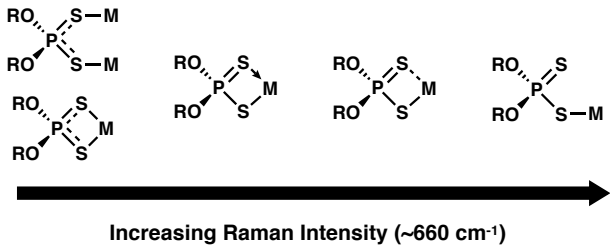

Figure 7.1: Relative intensity of the Raman band at ~660 cm^{-1} as a function of DTP binding mode.

The method was subsequently extended to encompass the assignment of anionic DTP ligands, when applied in combination with previously-established ^{31}P NMR spectroscopic generalisations. The application of both techniques should aid the unambiguous assignment of DTP binding modes in any zinc-DTP complex where crystal structure data is not attainable/available.

The propensity of ZDDP-OFM complex formation (for monodentate amines) was demonstrated to be strongly dependent on the steric demands of the complexing amine (as found for the related Py' systems), following the substitution trend, 1° > 2° > 3°. Multi-donor amines/OFMs were shown to interact more strongly than their monodentate equivalents, where both diamine and ethoxylated OFMs (at commercially relevant loadings) were shown to effectively sequester the zinc atoms of ZDDP and produce anionic DTP ligands (though *via* subtly different pathways).

The thermal stability of selected ZDDP-OFM systems were then studied in Chapter 5, were it was found that the presence of amines/amine-functional OFMs enhance the rate of ZDDP thermal degradation. The extent of this rate enhancement could be directly related to the assigned DTP binding modes and was rationalised based on the relative nucleophilicity/basicity of the ascribed DTP ligands (Fig. 7.2).

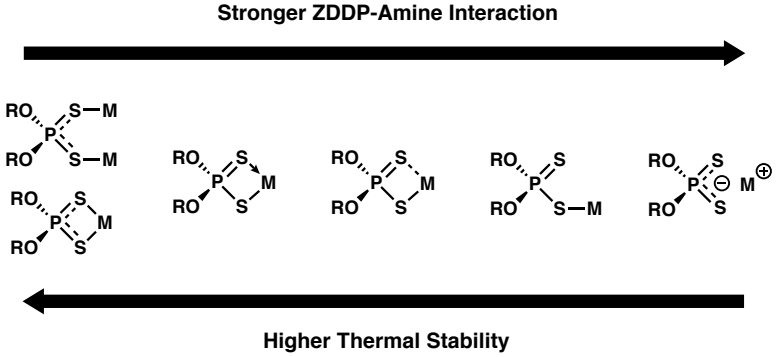

Figure 7.2: Relationship observed between the strength of ZDDP-amine interaction, the resulting DTP binding mode and the thermal stability observed for ZDDP-amine systems.

The tribological performance, assessed by MTM-SLIM testing, demonstrated that amine structure is key in dictating tribofilm formation and the associated friction in the tribocontact. Decreased steric demands for monodentate amine-based OFMs corresponds to lower friction values, but also cause severely inhibited ZDDP tribofilm growth in spite of the lower thermal stability previously observed for such ZDDP-OFM systems. Similarly, for the ZDDP-ethoxylated OFM system investigated, complete ZDDP-tribofilm inhibition was observed and rationalised based on the ability of the multi-donor OFM to sequester zinc cations extremely effectively. In this case, an OFM-based tribofilm

was observed however (identified by SEM-EDX analysis), and therefore highlights the need for detailed tribofilm analysis when studying more complex ZDDP formulations. An important question that arises from these results is whether the reduction in ZDDP-tribofilm thicknesses observed, and the formation of an OFM-based tribofilm, rather than a ZDDP-based film, is detrimental to antiwear properties.

Overall, a key result obtained from Chapter 5 is that lower thermal stability of ZDDP-OFM systems does not correlate to faster ZDDP-tribofilm formation, the latter being a variable that is often related to antiwear performance. This is in stark contrast to that known for ZDDPs when studied in isolation, where the relationship between lower thermal stability and faster tribofilm formation (and hence quicker antiwear protection) has been long known. Rather than thermal stability dictating the rate of tribofilm formation for ZDDP-OFM formulations (and presumably fully formulated engine oils), it is apparent that the propensity of an OFM to sequester network-forming zinc cations, to adsorb to and block surface sites, and to reduce friction (and hence shear stress), dictates tribofilm formation and properties.

Together, the results in this thesis identify and demonstrate the importance of understanding how key additives in engine lubricant formulations interact in solution. A small change in the nature of the complexing OFM has been shown to have a drastic impact on the solution behaviour in ZDDP-OFM systems, something that subsequently affects their thermal and tribological performance. Some relationships between OFM structure and the strength and nature of ZDDP-OFM interactions have been identified and discussed, a knowledge of which could help in selecting or designing future additive combinations. In addition, reliable methods for studying the solution interactions between ZDDPs and lubricant additives more generally have been outlined, alongside the development of a Raman spectroscopic method for reliably assigning changes in DTP binding modes.

7.3 Outlook and Future Work

7.3.1 Extension of the Raman Spectroscopic Method Developed for Identifying DTP Binding Modes

In Chapter 3 and subsequently Chapter 4 the use of Raman spectroscopy as a diagnostic tool for assigning DTP binding modes has been highlighted. Although currently this analysis is qualitative in nature, future work will seek to correlate the relative intensity of $\nu(PS_2)$asym/ν(P=S) vibrations to the binding mode for compounds of known structure, to provide quantitative guidelines akin to that previously performed using ^{31}P NMR spectroscopy. Naturally, this process will be significantly aided by the isolation and characterisation of a bigger library of ZDDP-amine complexes possessing variable DTP binding modes. In the same vein, although not explored in this thesis, there is potential scope to expand the diagnostic method for use with any DTP-containing species or complex.

7.3.2 Further MTM-SLIM Testing

In the current study only a selection of representative ZDDP-amine systems were studied using the MTM-SLIM method. Several experiments would greatly aid overall understanding and in rationalising and confirming the trends observed in this thesis:

1. MTM-SLIM tests of OFMs in isolation - this would demonstrate which OFMs potentially have the ability to form relatively thick tribofilms in the absence of ZDDP.

2. Modify test parameters such as load and test duration to determine if tribofilm formation is just slowed or is inhibited indefinitely for certain ZDDP-OFM systems.

3. Sequential MTM-SLIM experiments that involve:

   (a) the formation of a ZDDP tribofilm in a ZDDP-containing oil

(b) replacement of the ZDDP-containing oil with an OFM-containing lubricant (with or without ZDDP)

These tests would help to elucidate the influence of OFMs on ZDDP tribofilm removal and properties. Surface analysis before and after any OFM-induced tribofilm removal could be also applied to confirm the species/elements removed from the ZDDP tribofilm, as well as what remains.

4. Variation of lubricant parameters, *i.e.* absolute ZDDP and OFM concentrations, as well as the ZDDP:OFM ratio.

7.3.3 Wear Evaluation

One aspect of tribological performance not investigated for the ZDDP-OFM formulations studied in this thesis is wear (see Section 1.1.3). While from the tribofilm thickness and elemental composition results determined in Chapter 5, an important question that arises is whether the reduced tribofilm thicknesses and significantly different tribofilm compositions observed are detrimental to the wear protection observed in ZDDP-OFM systems.

Wear measurements could be performed using the known MTM reciprocating and/or the high frequency reciprocating rig (HFRR) test methods previously used in the literature,[73,119] both of which involve reciprocating motions that localise the resulting wear, thus make it easier to measure (Fig. 7.3). Subsequent surface analysis (scanning white light interferometry (SWLI) and AFM) of the rubbing surface and the wear track enables the quantification of wear volumes.

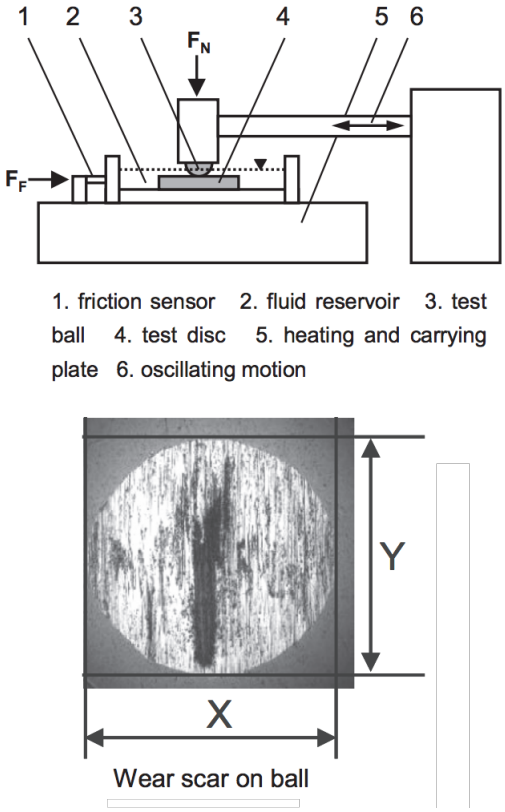

Figure 7.3: HFRR test schematic and typical HFRR ball wear scar. Adapted from ref. 192.

7.3.4 Other Alkyl ZDDPs

In this thesis, the entirety of the research presented has been focussed on the interaction of the single-component zinc diisobutyl dithiophosphate (**^{i}Bu ZDDP**). **^{i}Bu ZDDP** is a branched primary ZDDP of moderate alkyl chain length. The use of a single-component ZDDP in this thesis facilitated the detailed solution- and solid-state characterisations performed, which ultimately lead to a molecular level understanding of the nature and consequences of ZDDP-OFM interactions to be attained. However, other ZDDP alkyl chain types and lengths are also of commercial importance for engine lubricant formulations, particularly other 1°/2° ZDDPs and longer alkyl chain lengths. In addition to their effect on thermal stability (and subsequently antiwear effectiveness) when ZDDPs are studied in isolation, the nature of the DTP-bound organic substituents in ZDDPs have previously been reported to affect molecular structure in ZDDP-amine complexes. For example, in ZDDP-dipyridyl systems, the steric demands of the ZDDP organic substituents contribute to the degree of aggregation in the resulting ZDDP-amine species.[127–129]

Future work would therefore seek to investigate alternative, single-component ZDDPs, *i.e.* *n*-butyl, *sec*-butyl and 2-ethylhexyl (Fig. 7.4), in combination with amine-based OFMs using similar methods to that outlined in this thesis.

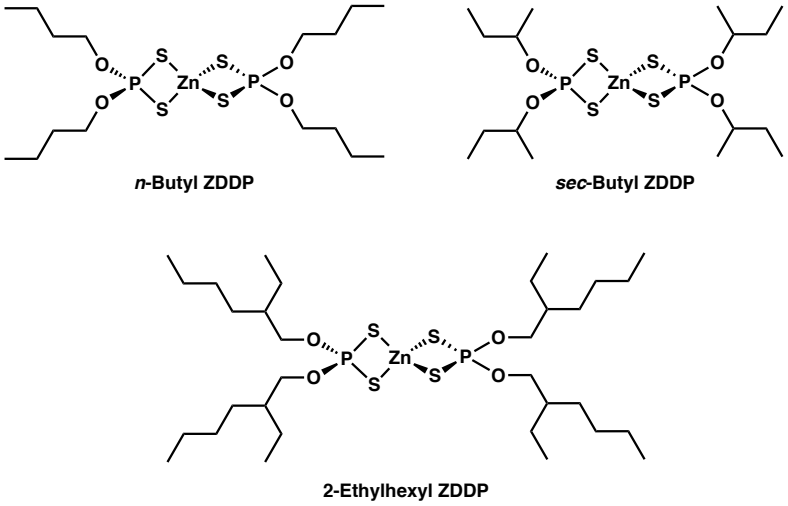

Figure 7.4: Chemical structures of other alkyl ZDDPs of commercial interest.

The synthesis of a range of single-component ZDDPs with different alkyl architectures, would also aid in determining if it is the alkyl groups ability to transmit shear to the rest of the molecule that contributes to the rate of ZDDP tribofilm formation.[57]

7.3.5 Final Comments

While the work in this thesis has focussed predominantly on binary ZDDP-OFM systems in mineral oil, it is realised that engine oil additive packages and subsequent lubricant formulations are much more complex. Even so, there is a fundamental need to fill the knowledge gap regarding additive-additive interactions in simple binary additive systems relevant to engine lubricant formulations. This would begin to enable the selection and design of optimal/synergistic additive combinations, to which, additional components/complexities can be progressively added to move closer to a fully formulated engine lubricant formulation.

References

[1] *Jost Report, Lubrication (Tribology) - Education and Research: A Report on the Present Position and Industry Needs*, Department of Education, HMSO, London, 1966.

[2] M. Torbacke, Å. K. Rudolphi and E. Kassfeldt, *Lubricants: Introduction to Properties and Performance*, John Wiley & Sons, Ltd, Chichester, 2014.

[3] S. Q. A. Rizvi, *A Comprehensive Review of Lubricant Chemistry, Technology, Selection, and Design*, ASTM International, West Conshohocken, PA, 2009.

[4] K. Holmberg, P. Andersson and A. Erdemir, *Tribol. Int.*, 2012, **47**, 221–234.

[5] G. Fontaras and Z. Samaras, *Energy Policy*, 2010, **38**, 1826–1833.

[6] *Global Transport Scenarios 2050*, World Energy Council, London, 2011.

[7] B. J. Hamrock, S. R. Schmid and B. O. Jacobson, *Fundamentals of Fluid Film Lubrication*, Marcel Dekker Inc, New York, 2nd edn., 2004.

[8] T. Mang, in *Lubricants and Lubrication*, ed. T. Mang and W. Dresel, Wiley-VCH Verlag GmbH & Co. KGaA, Weinheim, Germany, 2nd edn., 2007, pp. 7–22.

[9] S. Basu, in *Encyclopedia of Lubricants and Lubrication*, ed. T. Mang, Springer, Berlin, Heidelberg, 2014, pp. 700–707.

[10] Y. Wang and Q. J. Wang, in *Encyclopedia of Tribology*, ed. Q. J. Wang and Y.-W. Chung, Springer US, Boston, MA, 2013, pp. 2110–2113.

[11] K. Kato and K. Adachi, in *Modern Tribology Handbook*, ed. B. Bhushan, CRC Press, Boca Raton, 2000, pp. 273–300.

[12] W. M. Needelman and P. V. Madhavan, *SAE Tech. Pap. 881827*, 1988.

[13] D. Kramer, B. Lok and R. Krug, in *Turbine Lubrication in the 21st Century*, ed. W. R. Herguth and T. M. Warne, ASTM International, West Conshohocken, PA, 2001, pp. 25–38.

[14] T. Yoshida and H. Watanabe, US Pat., 4737297, 1988.

[15] *Lubricant Additives: Use and Benefits*, ATC Document 118, 2016.

[16] G. C. Smith, *J. Phys. D. Appl. Phys.*, 2000, **33**, R187–R197.

[17] S. Rizvi, in *Lubricant Additives: Chemistry and Applications*, ed. L. Rudnik, CRC Press, Boca Raton, 2nd edn., 2009, pp. 123–141.

[18] R. H. Ottewill, E. Sinagra, I. P. MacDonald, J. F. Marsh and R. K. Heenan, *Colloid Polym. Sci.*, 1992, **270**, 602–608.

[19] J. Mansot, M. Hallouis and J. Martin, *Colloids Surf. A Physicochem. Eng. Asp.*, 1993, **71**, 123–134.

[20] J.-P. Roman, P. Hoornaert, D. Faure, C. Biver, F. Jacquet and J.-M. Martin, *J. Colloid Interface Sci.*, 1991, **144**, 324–339.

[21] D. Atkinson, A. J. Brown, D. Jilbert and G. Lamb, in *Chemistry and Technology of Lubricants*, ed. R. Mortimer, M. Fox and S. Orszulik, Springer Netherlands, Dordrecht, 2010, pp. 293–324.

[22] S. Rizvi, in *Lubricant Additives: Chemistry and Applications*, ed. L. Rudnik, CRC Press, Boca Raton, 2nd edn., 2009, pp. 143–170.

[23] R. E. Kornbrekke, P. Patrzyk-Semanik, T. Kirchner-Jean, M. G. Raguz and E. A. Bardasz, *SAE Tech. Pap. 982665*, 1998.

[24] M. J. Covitch, B. K. Humphrey and D. E. Ripple, *SAE Tech. Pap. 852126*, 1985.

[25] J. Dong and C. Migdal, in *Lubricant Additives: Chemistry and Applications*, ed. L. Rudnik, CRC Press, Boca Raton, 2nd edn., 2009, pp. 3–50.

[26] A. M. Barnes, K. D. Bartle and V. R. Thibon, *Tribol. Int.*, 2001, **34**, 389–395.

[27] T. Colclough, *Ind. Eng. Chem. Res.*, 1987, **26**, 1888–1895.

[28] M. E. Hunter, in *Encyclopedia of Lubricants and Lubrication*, ed. T. Mang, Springer, Berlin, Heidelberg, 2014, pp. 1681–1702.

[29] H. Spikes, *Tribol. Lett.*, 2004, **17**, 469–489.

[30] E. Bardasz and G. Lamb, in *Lubricant Additives: Chemistry and Applications*, ed. L. Rudnik, CRC Press, Boca Raton, 2nd edn., 2009, pp. 457–491.

[31] D. Thong and P. A. Hutchinson, in *Encyclopedia of Lubricants and Lubrication*, ed. T. Mang, Springer, Berlin, Heidelberg, 2014, pp. 1393–1397.

[32] D. Thong, P. A. Hutchinson, C. Wincierz and T. Schimmel, in *Encyclopedia of Lubricants and Lubrication*, ed. T. Mang, Springer, Berlin, Heidelberg, 2014, pp. 2292–2316.

[33] A. Martini, U. S. Ramasamy and M. Len, *Tribol. Lett.*, 2018, **66**, 58.

[34] M. A. Nicholls, T. Do, P. R. Norton, M. Kasrai and G. Bancroft, *Tribol. Int.*, 2005, **38**, 15–39.

[35] H. Spikes, *Lubr. Sci.*, 2008, **20**, 103–136.

[36] J. J. Dickert and C. N. Rowe, *J. Org. Chem.*, 1967, **32**, 647–653.

[37] J. F. Ford, *J. Inst. Pet.*, 1968, **54**, 198–210.

[38] G. J. J. Jayne and J. S. Elliot, *J. Inst. Pet.*, 1970, **56**, 42–49.

[39] T. Ito, T. Igarashi and H. Hagihara, *Acta Crystallogr. Sect. B*, 1969, **25**, 2303–2309.

[40] S. L. Lawton and G. T. Kokotailo, *Inorg. Chem.*, 1969, **11**, 2410–2421.

[41] S. Menzer, J. R. Phillips, A. M. Z. Slawin, D. J. Williams and J. D. Woollins, *J. Chem. Soc. Dalt. Trans.*, 2000, 3269–3273.

[42] P. G. Harrison and T. Kikabhai, *J. Chem. Soc. Dalt. Trans.*, 1987, 807–814.

[43] J. J. Harrison, C. Y. Chan, A. Onopchenko, A. R. Pradhan and M. Petersen, *Magn. Reson. Chem.*, 2008, **46**, 115–124.

[44] E. S. Yamaguchi, R. L. Primer, S. R. Aragón and E. Q. Labrador, *Tribol. Trans.*, 1997, **40**, 330–338.

[45] E. S. Yamaguchi, P. R. Ryason, E. Q. Labrador and T. P. Hansen, *Tribol. Trans.*, 1996, **39**, 220–224.

[46] M. Fuller, Z. Yin, M. Kasrai, G. Bancroft, E. S. Yamaguchi, P. Ryason, P. A. Willermet and K. H. Tan, *Tribol. Int.*, 1997, **30**, 305–315.

[47] E. S. Yamaguchi, A. Onopchenko, M. M. Francisco and C. Y. Chan, *Tribol. Trans.*, 1999, **42**, 895–901.

[48] L. O. Farng, in *Lubricant Additives: Chemistry and Applications*, ed. L. Rudnik, CRC Press, Boca Raton, 2nd edn., 2009, pp. 213–249.

[49] I. Sieber, K. Meyer, H. Kloss and A. Schöpke, *Wear*, 1983, **85**, 43–56.

[50] T. Sakamoto, H. Uetz, J. Föhl and M. Khosrawi, *Wear*, 1982, **77**, 139–157.

[51] M. Masuko, T. Hanada and H. Okabe, *Lubr. Eng.*, 1994, **50**, 972–977.

[52] R. B. Jones and R. C. Coy, *ASLE Trans.*, 1981, **24**, 91–97.

[53] R. C. Coy and R. B. Jones, *ASLE Trans.*, 1981, **24**, 77–90.

[54] R. J. Ellis, P. J. Lake and R. A. G. Marshall, *J. Chem. Technol. Biotechnol.*, 1980, **30**, 602–610.

[55] N. J. Mosey and T. K. Woo, *J. Phys. Chem. A*, 2003, **107**, 5058–5070.

[56] N. J. Mosey and T. K. Woo, *J. Phys. Chem. A*, 2004, **108**, 6001–6016.

[57] J. Zhang and H. Spikes, *Tribol. Lett.*, 2016, **63**, 24.

[58] H. Fujita and H. A. Spikes, *Proc. IMechE Part J: J. Eng. Tribol.*, 2004, **218**, 265–278.

[59] H. Fujita, R. P. Glovnea and H. A. Spikes, *Tribol. Trans.*, 2005, **48**, 558–566.

[60] M. L. Fuller, M. Kasrai, G. Bancroft, K. Fyfe and K. H. Tan, *Tribol. Int.*, 1998, **31**, 627–644.

[61] G. Bancroft, M. Kasrai, M. Fuller, Z. Yin, K. Fyfe and K. Tan, *Tribol. Lett.*, 1997, **3**, 47–51.

[62] J. Palacios, *Tribol. Int.*, 1986, **19**, 35–39.

[63] M. Suominen Fuller, L. Rodriguez Fernandez, G. Massoumi, W. Lennard, M. Kasrai and G. Bancroft, *Tribol. Lett.*, 2000, **8**, 187–192.

[64] M. Aktary, M. T. McDermott and G. A. McAlpine, *Tribol. Lett.*, 2002, **12**, 155–162.

[65] Z. Yin, M. Kasrai, M. Fuller, G. Bancroft, K. Fyfe and K. H. Tan, *Wear*, 1997, **202**, 172–191.

[66] J. M. Martin, C. Grossiord, T. Le Mogne, S. Bec and A. Tonck, *Tribol. Int.*, 2001, **34**, 523–530.

[67] M. Eglin, A. Rossi and N. D. Spencer, *Tribol. Lett.*, 2003, **15**, 199–209.

[68] S. Bec, A. Tonck, J. M. Georges, R. C. Coy, J. C. Bell and G. W. Roper, *Proc. R. Soc. A Math. Phys. Eng. Sci.*, 1999, **455**, 4181–4203.

[69] A. Morina and A. Neville, *J. Phys. D. Appl. Phys.*, 2007, **40**, 5476–5487.

[70] N. N. Gosvami, J. A. Bares, F. Mangolini, A. R. Konicek, D. G. Yablon and R. W. Carpick, *Science*, 2015, **348**, 102–106.

[71] H. Spikes, *Lubr. Sci.*, 2006, **18**, 223–230.

[72] L. J. Taylor and H. A. Spikes, *Tribol. Trans.*, 2003, **46**, 310–314.

[73] K. T. Miklozic, T. R. Forbus and H. A. Spikes, *Tribol. Trans.*, 2007, **50**, 328–335.

[74] *API Engine Oil Classifications*, https://www.infineum.com/media/80723/api-engine-oil-classifications.pdf, (accessed August 2018).

[75] Z. Tang and S. Li, *Curr. Opin. Solid State Mater. Sci.*, 2014, **18**, 119–139.

[76] D. Kenbeek, T. Buenemann and H. Rieffe, *SAE Tech. Pap. 2000-01-1792*, 2000.

[77] H. Spikes, *Tribol. Lett.*, 2015, **60**, 5.

[78] K. T. Miklozic, J. Graham and H. Spikes, *Tribol. Lett.*, 2001, **11**, 71–81.

[79] C. Grossiord, K. Varlot, J.-M. Martin, T. Le Mogne, C. Esnouf and K. Inoue, *Tribol. Int.*, 1998, **31**, 737–743.

[80] A. Kuc, in *Chemical Modelling: Volume 11*, The Royal Society of Chemistry, 2015, pp. 1–29.

[81] E. S. Yamaguchi, S. H. Roby and S. W. Yeh, *Tribol. Trans.*, 2005, **48**, 57–68.

[82] A. Morina, A. Neville, M. Priest and J. Green, *Tribol. Lett.*, 2006, **24**, 243–256.

[83] C. Grossiord, J. Martin, K. Varlot, B. Vacher, T. Le Mogne and Y. Yamada, *Tribol. Lett.*, 2000, **8**, 203–212.

[84] K. Komvopoulos, S. A. Pernama, E. S. Yamaguchi and P. R. Ryason, *Tribol. Trans.*, 2006, **49**, 151–165.

[85] A. Morina and A. Neville, *Tribol. Int.*, 2007, **40**, 1696–1704.

[86] K. Yagishita and J. Igarashi, *Prepr. JAST Tribol. Meeting*, Fukuoka, 1991, pp. 673–676.

[87] R. K. Jensen, M. D. Johnson, S. Korcek and M. J. Rokosz, *Lubr. Sci.*, 1998, **10**, 99–120.

[88] R. K. Jensen, S. Korcek and M. D. Johnson, *Lubr. Sci.*, 2001, **14**, 25–42.

[89] S. Korcek, R. Jensen, M. D. Johnson and J. Sorab, *Tribol. Ser.*, 1999, **36**, 13–24.

[90] S. Korcek, R. Jensen and M. Johnson, *Tribol. Ser.*, 2000, **38**, 399–407.

[91] J. Graham, H. Spikes and R. Jensen, *Tribol. Trans.*, 2001, **44**, 637–647.

[92] M. Muraki, Y. Yanagi and K. Sakaguchi, *Tribol. Int.*, 1997, **30**, 69–75.

[93] M. De Barros Bouchet, J. Martin, T. Le Mogne, P. Bilas, B. Vacher and Y. Yamada, *Wear*, 2005, **258**, 1643–1650.

[94] Y. Sogawa, N. Yoshimura and H. Iwasaki, *R&D on New Friction Modifier for Lubricant for Fuel Economy Improvement*, Japan Petroleum Energy Centre, E1.1.5, 2000.

[95] D. N. Khaemba, A. Neville and A. Morina, *RSC Adv.*, 2016, **6**, 38637–38646.

[96] F. P. Bowden and L. Leben, *Philos. Trans. R. Soc. A Math. Phys. Eng. Sci.*, 1940, **239**, 1–27.

[97] D. D. Dominguez, R. L. Mowery and N. H. Turner, *Tribol. Trans.*, 1994, **37**, 59–66.

[98] E. Hutchinson and E. K. Rideal, *Trans. Faraday Soc.*, 1947, **43**, 435–438.

[99] H. A. Spikes and A. Cameron, *Proc. R. Soc. A Math. Phys. Eng. Sci.*, 1974, **336**, 407–419.

[100] G. W. Stachowiak and A. W. Batchelor, *Engineering Tribology*, Elsevier Butterworth-Heinemann, Oxford, 4th edn., 2014.

[101] V. Anghel, C. Bovington and H. A. Spikes, *Lubr. Sci.*, 1999, **11**, 313–335.

[102] M. Ratoi, H. A. Spikes and C. Bovington, *Tribol. Trans.*, 2003, **46**, 24–30.

[103] M. Ratoi, C. Bovington and H. Spikes, *Tribol. Lett.*, 2003, **14**, 33–40.

[104] H. Liang, G. Totten and G. Webster, in *Fuels and Lubricants Handbook: Technology, Properties, Performance, and Testing*, ed. G. Totten, ASTM International, West Conshohocken, PA, 2003, pp. 909–961.

[105] G. Koltsakis and A. Stametelos, *Prog. Energy Combust. Sci.*, 1997, **23**, 1–39.

[106] P. Granger and V. I. Parvulescu, *Chem. Rev.*, 2011, **111**, 3155–3207.

[107] W. B. Williamson, J. Perry, R. L. Goss, H. S. Gandhi and R. E. Beason, *SAE Tech. Pap. 841406*, 1984.

[108] S. Nemoto, Y. Kishi, K. Matsuura, M. Miura, S. Togawa, T. Ishikawa, T. Hashimoto and T. Yamazaki, *SAE Tech. Pap. 2004-01-1887*, 2004.

[109] J. Franz, J. Schmidt, C. Schoen, M. Harperscheid, S. Eckhoff, M. Roesch and J. Leyrer, *SAE Tech. Pap. 2005-01-1097*, 2005.

[110] K. Inoue, T. Kurahashi, T. Negishi, K. Akiyama, K. Arimura and K. Tasaka, *SAE Tech. Pap. 920654*, 1992.

[111] S. V. Kumar, J. Rogalo, M. Deeba, P. L. Burk and V. Ferrari, *SAE Tech. Pap. 2003-01-3735*, 2003.

[112] J. Li, J. Theis, W. Chun, C. Goralski, R. Kudla, J. Ura, W. Watkins, M. Chattha and R. Hurley, *SAE Tech. Pap. 2001-01-2503*, 2001.

[113] T. Asanuma, S. Hirota, M. Yanaka, Y. Tsukasaki and T. Tanaka, *SAE Tech. Pap. 2003-01-1865*, 2003.

[114] T. W. Selby, *Tribotest*, 2005, **11**, 247–268.

[115] T. W. Selby, *Tribotest*, 2005, **11**, 355–370.

[116] L. O. Farng and T.-C. Jao, in *Lubricant Additives: Chemistry and Applications*, ed. L. Rudnik, CRC Press, Boca Raton, 3rd edn., 2017, pp. 117–156.

[117] U. D. Schwarz, *Science*, 2015, **348**, 40–41.

[118] S. Soltanahmadi, A. Morina, M. C. P. van Eijk, I. Nedelcu and A. Neville, *J. Phys. D. Appl. Phys.*, 2016, **49**, 505302.

[119] J. Zhang, E. Yamaguchi and H. Spikes, *Tribol. Trans.*, 2014, **57**, 57–65.

[120] M. Ratoi, V. B. Niste, H. Alghawel, Y. F. Suen and K. Nelson, *RSC Adv.*, 2014, **4**, 4278–4285.

[121] I. Haiduc, D. Sowerby and S.-F. Lu, *Polyhedron*, 1995, **14**, 3389–3472.

[122] R. Mehrotra, G. Srivastava and B. Chauhan, *Coord. Chem. Rev.*, 1984, **55**, 207–259.

[123] M. Shiomi, M. Tokashiki, H. Tomizawa and T. Kuribayashi, *Lubr. Sci.*, 1989, **1**, 131–147.

[124] M. G. B. Drew, M. Hasan, R. J. Hobson and D. A. Rice, *J. Chem. Soc. Dalt. Trans.*, 1986, 1161–1166.

[125] P. G. Harrison, M. J. Begley and T. Kikabhai, *J. Chem. Soc. Dalt. Trans.*, 1986, 929–938.

[126] P. G. Harrison and A. Sebald, *J. Chem. Res.*, 1991, (Synopsis) 340–341, (Miniprint) 3128–3136.

[127] C. S. Lai, S. Liu and E. R. T. Tiekink, *CrystEngComm*, 2004, **6**, 221–226.

[128] C. S. Lai and E. R. T. Tiekink, *J. Mol. Struct.*, 2006, **796**, 114–118.

[129] D. Chen, C. S. Lai and E. R. T. Tiekink, *CrystEngComm*, 2006, **8**, 51.

[130] V. Mark, C. H. Dungan, M. M. Crutchfield and J. R. Van Wazer, in *Top. Phosphorus Chem.*, ed. M. Grayson and E. J. Griffith, Interscience, New York, vol. 5, 1967, pp. 227–457.

[131] D. Dakternieks and D. Graddon, *Aust. J. Chem.*, 1970, **23**, 1989–1995.

[132] *Bindfit*, www.supramolecular.org, (accessed August 2018).

[133] J. S. Summers and A. M. Stolzenberg, *J. Am. Chem. Soc.*, 1993, **115**, 10559–10567.

[134] A. W. Addison, T. N. Rao, J. Reedijk, J. van Rijn and G. C. Verschoor, *J. Chem. Soc., Dalt. Trans.*, 1984, 1349–1356.

[135] H. Clavier and S. P. Nolan, *Chem. Commun.*, 2010, **46**, 841–861.

[136] L. Falivene, R. Credendino, A. Poater, A. Petta, L. Serra, R. Oliva, V. Scarano and L. Cavallo, *Organometallics*, 2016, **35**, 2286–2293.

[137] C. R. Groom, I. J. Bruno, M. P. Lightfoot and S. C. Ward, *Acta Crystallogr. Sect. B*, 2016, **72**, 171–179.

[138] *CRC Handbook of Chemistry and Physics*, ed. W. M. Haynes, D. R. Lide and T. J. Bruno, CRC Press, Boca Raton, 97th edn., 2016.

[139] R. J. L. Andon, J. D. Cox and E. F. G. Herington, *Trans. Faraday Soc.*, 1954, **50**, 918.

[140] *Scifinder*, www.scifinder.cas.org, (accessed August 2018).

[141] B. E. Smart, *J. Fluor. Chem.*, 2001, **109**, 3–11.

[142] H. C. Brown and D. H. McDaniel, *J. Am. Chem. Soc.*, 1955, **77**, 3752–3755.

[143] C. F. Macrae, P. R. Edgington, P. McCabe, E. Pidcock, G. P. Shields, R. Taylor, M. Towler and J. van de Streek, *J. Appl. Crystallogr.*, 2006, **39**, 453–457.

[144] P. A. Willermet, *Tribol. Lett.*, 1998, **5**, 41–47.

[145] C. N. McEwen, R. G. McKay and B. S. Larsen, *Anal. Chem.*, 2005, **77**, 7826–7831.

[146] P. G. Harrison and T. Kikabhai, *Wear*, 1987, **116**, 25–31.

[147] C. Glidewell, *Inorganica Chim. Acta*, 1977, **25**, 159–163.

[148] R. Constantinescu, F. Martinas and I. Haiduc, *Inorganica Chim. Acta*, 1976, **19**, 105–108.

[149] B. P. Singh, G. Srivastava and R. C. Mehrotra, *Synth. React. Inorg. Met. Chem.*, 1982, **12**, 105–121.

[150] J. L. Paddy, N. C. J. Lee, D. N. Waters and W. Trott, *Tribol. Trans.*, 1990, **33**, 15–20.

[151] A. J. Burn, I. Gosney, P. S. G. Tan and J. P. Wastle, *J. Chem. Soc. Perkin Trans. 2*, 1992, 1725–1729.

[152] F. Menges, *Spekwin32 - optical spectroscopy software*, Version 1.72.2, 2016, http://www.effemm2.de/spekwin/.

[153] M. J. Frisch, G. W. Trucks, H. B. Schlegel, G. E. Scuseria, M. A. Robb, J. R. Cheeseman, G. Scalmani, V. Barone, B. Mennucci, G. A. Petersson, H. Nakatsuji, M. Caricato, X. Li, H. P. Hratchian, A. F. Izmaylov, J. Bloino, G. Zheng, J. L. Sonnenberg, M. Hada, M. Ehara, K. Toyota, R. Fukuda, J. Hasegawa, M. Ishida, T. Nakajima, Y. Honda, O. Kitao, H. Nakai, T. Vreven, J. A. Montgomery, Jr., J. E. Peralta, F. Ogliaro, M. Bearpark, J. J. Heyd, E. Brothers, K. N. Kudin, V. N. Staroverov, R. Kobayashi, J. Normand, K. Raghavachari, A. Rendell, J. C. Burant, S. S. Iyengar, J. Tomasi, M. Cossi, N. Rega, J. M. Millam, M. Klene, J. E. Knox, J. B. Cross, V. Bakken, C. Adamo, J. Jaramillo, R. Gomperts, R. E. Stratmann, O. Yazyev, A. J. Austin, R. Cammi, C. Pomelli, J. W. Ochterski, R. L. Martin, K. Morokuma, V. G. Zakrzewski, G. A. Voth, P. Salvador, J. J. Dannenberg, S. Dapprich, A. D. Daniels, O. Farkas, J. B. Foresman, J. V. Ortiz, J. Cioslowski and D. J. Fox, *Gaussian 09*, Revision A.02, Gaussian, Inc, Wallingford CT, 2009.

[154] E. Pasquinet, P. Rocca, F. Marsais, A. Godard and G. Quéguiner, *Tetrahedron*, 1998, **54**, 8771–8782.

[155] Y. Matsui, S. Aoki and M. Masuko, *Tribol. Trans.*, 2018, **61**, 220–228.

[156] P. G. Harrison, P. Brown and J. McManus, *Wear*, 1992, **156**, 345–349.

[157] P. Harrison, P. Brown, M. Hynes, J. Kiely and J. McManus, *J. Chem. Res.*, 1991, (Synopsis) 174–175, (Miniprint) 1636–1693.

[158] P. Thordarson, *Chem. Soc. Rev.*, 2011, **40**, 1305–1323.

[159] W. Kemp, *NMR in Chemistry*, Macmillan Education UK, London, 1986.

[160] J. T. Sheff, A. L. Lucius, S. B. Owens and G. M. Gray, *Organometallics*, 2011, **30**, 5695–5709.

[161] K. Inoue and H. Watanabe, *ASLE Trans.*, 1983, **26**, 189–199.

[162] N. Lowther, P. Crook and C. D. Hall, *Phosphorus Sulfur Silicon Relat. Elem.*, 1995, **102**, 195–204.

[163] M. D. Gordon and L. D. Quin, *J. Magn. Reson.*, 1976, **22**, 149–153.

[164] R. I. Taylor, R. Mainwaring and R. M. Mortier, *Proc. IMechE Part J: J. Eng. Tribol.*, 2005, **219**, 331–346.

[165] F. Ulatowski, K. Dąbrowa, T. Bałakier and J. Jurczak, *J. Org. Chem.*, 2016, **81**, 1746–1756.

[166] G. De and N. R. Chaudhuri, *Thermochim. Acta*, 1983, **69**, 349–359.

[167] R. Hayami, N. Endo, T. Abe, Y. Miyase, T. Sagawa, K. Yamamoto, S. Tsukada and T. Gunji, *J. Sol-Gel Sci. Technol.*, 2018, **87**, 743–748.

[168] E. Conterosito, G. Croce, L. Palin, E. Boccaleri, W. van Beek and M. Milanesio, *CrystEngComm*, 2012, **14**, 4472.

[169] T. Shibahara and H. Akashi, *Inorg. Synth.*, 1992, **29**, 254–260.

[170] F. A. Schultz, V. R. Ott, D. S. Rolison, D. C. Bravard, J. W. McDonald and W. E. Newton, *Inorg. Chem.*, 1978, **17**, 1758–1765.

[171] D. Kenbeck and T. Bunemann, in *Lubricant Additives: Chemistry and Applications*, ed. L. Rudnik, CRC Press, Boca Raton, 2nd edn., 2009, pp. 195–210.

[172] J. Parada-Aliste, A. Megia-Fernandez, D. De La Torre-Gonzalez, F. Hernandez-Mateo and F. Santoyo-Gonzalez, *Eur. J. Org. Chem.*, 2013, **2013**, 3758–3763.

[173] D. Wu, A. Chen and C. Johnson, *J. Magn. Reson. Ser. A*, 1995, **115**, 260–264.

[174] A. Jerschow and N. Müller, *J. Magn. Reson.*, 1997, **125**, 372–375.

[175] F. Malz, in *NMR Spectrosopy in Pharmaceutical Analysis*, Elsevier, 2008, pp. 43–62.

[176] J. S. Valentine, J. P. Coliman, E. C. Niederhoffer, J. H. Timmons, A. E. Martell, L. Dahlenburg, R. J. Nast, L. Vaska, H. J. Lawson, J. D. Atwood, R. R. Schrock, J. D. Fell-Mann, R. D. Temple, Y. Tsuno, J. E. Leffler, H. R. Hays and D. J. Peterson, *J. Am. Chem. Soc*, 1989, **111**, 346.

[177] K. Topolovec-Miklozic, T. R. Forbus and H. A. Spikes, *Tribol. Lett.*, 2007, **26**, 161–171.

[178] M. V. Kudchadker, R. A. Zingaro and K. J. Irgolic, *Can. J. Chem.*, 1968, **46**, 1415–1424.

[179] B. K. Santra, B.-J. Liaw, C.-M. Hung, C. W. Liu and J.-C. Wang, *Inorg. Chem.*, 2003, **42**, 8866–8871.

[180] Y. Belabassi, M. I. Antczak, J. Tellez and J.-L. Montchamp, *Tetrahedron*, 2008, **64**, 9181–9190.

[181] G. C. Lloyd-Jones and N. P. Taylor, *Chem. Eur. J.*, 2015, **21**, 5423–5428.

[182] C. W. Liu, I.-J. Shang, C.-M. Hung, J.-C. Wang and T.-C. Keng, *J. Chem. Soc. Dalt. Trans.*, 2002, **10**, 1974–1979.

[183] J. Lin and B. R. Shaw, *Chem. Commun.*, 1999, 1517–1518.

[184] F. Dornhaus, M. Bolte, H.-W. Lerner and M. Wagner, *Eur. J. Inorg. Chem.*, 2006, **2006**, 5138–5147.

[185] C. Q. Nguyen, M. Afzaal, M. A. Malik, M. Helliwell, J. Raftery and P. O'Brien, *J. Organomet. Chem.*, 2007, **692**, 2669–2677.

[186] H. G. Cook, J. D. Ilett, B. C. Saunders, G. J. Stacey, H. G. Watson, I. G. E. Wilding and S. J. Woodcock, *J. Chem. Soc.*, 1949, 2921.

[187] W. Gerrard, M. J. D. Isaacs, G. Machell, K. B. Smith and P. L. Wyvill, *J. Chem. Soc.*, 1953, 1920–1926.

[188] D. Collins, P. Drygala and J. Swan, *Aust. J. Chem.*, 1983, **36**, 2517–2536.

[189] T. Wada, H. Hotoda, M. Sekine and T. Hata, *Tetrahedron Lett.*, 1988, **29**, 4143–4146.

[190] G. Hua and J. D. Woollins, *Angew. Chemie Int. Ed.*, 2009, **48**, 1368–1377.

[191] J. D. Woollins, *Synlett*, 2012, **23**, 1154–1169.

[192] M. Matzke, A. Jess and U. Litzow, *Fuel*, 2015, **140**, 770–777.

Appendix A

X-Ray Crystallographic Data

Table A.1: Selected bond lengths and angles of the isolated mononuclear complexes [Zn{κ^2-*S*,*S*-$S_2P(O^iBu)_2$}$_2$(L)] {L = Py (**1**), 2-MePy (**2**), 2-EtPy (**3**) and 2-^{i}PrPy (**4**)} and [Zn{κ^1-*S*-$S_2P(O^iBu)_2$}$_2$(4-MeOPy)$_2$] (**6**).

Complex	Zn-N (Å)	Zn-N-C (°)	Zn-S (Å)	P-S (Å)	Zn-S-P (°)	S-P-S (°)	S-Zn-S (°)	P-O (Å)	O-P-O (°)
1	2.014(3)	120.77(18)	2.3226(7) 2.7085(7)	1.9988(11) 1.9703(10)	86.74(3) 77.24(3)	113.16(4)	81.98(2)	1.585(2), 1.588(2)	100.01(12)
2	2.021(6)	112.3(7), 126.5(5)[a]	2.3332(13) 2.7288(12)	1.9898(12) 1.9625(16)	87.33(6) 77.45(5)	113.24(8)	80.87(4)	1.572(4), 1.598(4)	100.6(2)
3[b]	2.0408(17)	116.78(16), 123.72(17)[a]	2.3347(7) 2.7121(3)	1.9989(7) 1.9663(4)	87.07(3) 77.807(13)	112.66(4)	81.298(16)	1.5826(9), 1.5926(9)	100.21(5)
4[c]	2.0369(14)	115.41(12), 125.63(12)[a]							
		Ligand 1:	2.3184(9) 2.7862(12)	2.0014(14) 1.9694(13)	89.16(4) 77.38(4)	112.39(5)	79.96(3)	1.5795(18), 1.5980(16)	99.21(10)
		Ligand 2:	2.3653(5) 2.6060(6)	1.9961(7) 1.9741(6)	84.71(2) 78.91(2)	112.28(3)	82.933(17)	1.5798(13), 1.5867(13)	100.43(7)
5[d]	2.034(2)	117.35(16), 123.65(17)	2.285(4), 2.351(4) 2.896(3), 2.525(3)	1.9957(9) 1.9770(9)	81.66(7), 91.27(8) 77.66(8), 75.38(6)	113.55(4)	85.86(12), 78.82(10)	1.5863(18), 1.5916(18)	100.26(10)
6	2.0328(8)	118.54(6), 124.20(6)	2.3340(3)	2.0197(3) 1.9414(3)	100.649(12)	118.679(15)		1.5961(7), 1.5997(7)	104.97(4)

[a] Substituted carbon of 2-alkylpyridine ligand.
[b] Two equivalent dithiophosphate ligands with S2 atoms disordered over two positions with equal occupancy. Bond lengths and angles are defined using a centroid between the two positions.
[c] Disorder on one dithiophosphate ligand (occupancy 0.15) omitted.
[d] Disorder on both dithiophosphate ligands (occupancy 0.07) omitted.

	[Zn{κ²-S,S-S₂P(O^{i}Bu)₂}₂(Py)] (1)	[Zn{κ²-S,S-S₂P(O^{i}Bu)₂}₂(2-MePy)] (2)	[Zn{κ²-S,S-S₂P(O^{i}Bu)₂}₂(2-EtPy)] (3)
Empirical formula	$C_{21}H_{41}NO_4P_2S_4Zn$	$C_{22}H_{43}NO_4P_2S_4Zn$	$C_{23}H_{45}NO_4P_2S_4Zn$
Formula weight	627.1	641.12	655.15
Temperature/K	120	200	120
Crystal system	monoclinic	monoclinic	monoclinic
Space group	C2/c	C2/c	C2/c
a /Å	29.3284(15)	28.6306(13)	28.4133(16)
b/Å	9.3124(5)	9.2468(4)	9.1961(5)
c/Å	11.5284(6)	12.3443(6)	12.5332(7)
α/°	90	90	90
β/°	93.524(2)	95.4804(19)	95.454(2)
γ/°	90	90	90
Volume/Å^3	3142.7(3)	3253.1(3)	3260.0(3)
Z	4	4	4
ρ_{calc}g/cm^3	1.325	1.309	1.335
μ/mm^{-1}	1.174	1.136	1.135
F(000)	1320	1352	1384
Crystal size/mm^3	0.437 × 0.336 × 0.136	0.275 × 0.274 × 0.224	0.594 × 0.487 × 0.411
Radiation	MoKα (λ = 0.71073)	MoKα (λ = 0.71073)	MoKα (λ = 0.71073)
2Θ range for data collection/°	4.59 to 60	4.632 to 52.998	4.658 to 62.462
Index ranges	-41 ≤ h ≤ 41, -13 ≤ k ≤ 12, -16 ≤ l ≤ 16	-35 ≤ h ≤ 35, -11 ≤ k ≤ 11, -15 ≤ l ≤ 15	-41 ≤ h ≤ 41, -13 ≤ k ≤ 13, -18 ≤ l ≤ 18
Reflections collected	26848	22375	37353
Independent reflections	4578 [R_{int} = 0.0342, R_{sigma} = 0.0311]	3370 [R_{int} = 0.0386, R_{sigma} = 0.0298]	5306 [R_{int} = 0.0298, R_{sigma} = 0.0187]
Data/restraints/parameters	4578/14/160	3370/156/190	5306/167/208
Goodness-of-fit on F^2	1.019	1.052	1.019
Final R indexes [I>=2σ (I)]	R_1 = 0.0490, wR_2 = 0.1209	R_1 = 0.0560, wR_2 = 0.1433	R_1 = 0.0264, wR_2 = 0.0658
Final R indexes [all data]	R_1 = 0.0667, wR_2 = 0.1348	R_1 = 0.0847, wR_2 = 0.1761	R_1 = 0.0336, wR_2 = 0.0694
Largest diff. peak/hole / e Å^{-3}	1.03/-0.62	0.69/-0.43	0.44/-0.41

	[Zn{κ²-S,S-S₂P(O^{i}Bu)₂}₂(2-^{i}PrPy)] (4)	[Zn{κ²-S,S-S₂P(O^{i}Bu)₂}₂(3-FPy)] (5)	[Zn{κ¹-S-S₂P(O^{i}Bu)₂}₂(4-MeOPy)₂] (6)
Empirical formula	$C_{24}H_{47}NO_4P_2S_4Zn$	$C_{21}H_{40}FNO_4P_2S_4Zn$	$C_{28}H_{50}N_2O_6P_2S_4Zn$
Formula weight	669.17	645.09	766.25
Temperature/K	180	180	120
Crystal system	triclinic	monoclinic	monoclinic
Space group	P-1	C2/c	C2/c
a /Å	9.3776(4)	29.1820(13)	19.3562(9)
b/Å	13.4873(6)	9.3715(4)	11.5935(5)
c/Å	15.3390(6)	11.5773(5)	16.0884(8)
α/°	111.6069(15)	90	90
β/°	103.0544(15)	93.8325(17)	92.1600(18)
γ/°	98.2042(15)	90	90
Volume/Å^3	1701.59(13)	3159.1(2)	3607.8(3)
Z	2	4	4
ρ_{calc}g/cm^3	1.306	1.356	1.411
μ/mm^{-1}	1.089	1.174	1.042
F(000)	708	1352	1616
Crystal size/mm^3	0.435 × 0.373 × 0.34	0.412 × 0.295 × 0.158	0.469 × 0.203 × 0.164
Radiation	MoKα (λ = 0.71073)	MoKα (λ = 0.71073)	MoKα (λ = 0.71073)
2Θ range for data collection/°	4.604 to 61.292	4.566 to 60.2	4.096 to 71.23
Index ranges	-13 ≤ h ≤ 13, -19 ≤ k ≤ 19, -21 ≤ l ≤ 21	-41 ≤ h ≤ 41, -13 ≤ k ≤ 13, -16 ≤ l ≤ 16	-31 ≤ h ≤ 31, -18 ≤ k ≤ 18, -25 ≤ l ≤ 24
Reflections collected	33622	34005	48476
Independent reflections	10480 [R_{int} = 0.0280, R_{sigma} = 0.0325]	4646 [R_{int} = 0.0307, R_{sigma} = 0.0200]	7731 [R_{int} = 0.0340, R_{sigma} = 0.0285]
Data/restraints/parameters	10480/359/392	4646/158/188	7731/0/205
Goodness-of-fit on F^2	1.015	1.04	1.042
Final R indexes [I>=2σ (I)]	R_1 = 0.0378, wR_2 = 0.0859	R_1 = 0.0410, wR_2 = 0.1143	R_1 = 0.0275, wR_2 = 0.0578
Final R indexes [all data]	R_1 = 0.0590, wR_2 = 0.0944	R_1 = 0.0585, wR_2 = 0.1254	R_1 = 0.0406, wR_2 = 0.0614
Largest diff. peak/hole / e Å^{-3}	0.73/-0.38	0.45/-0.45	0.47/-0.33

	[Zn{κ¹-*S*-$S_2P(O^iBu)_2$}$_2$(C_{18}-NH_2)$_2$] (7)	[Zn{κ¹-*S*-$S_2P(O^iBu)_2$}$_2$(κ²-EDA)] (8)	[Zn(EDA)$_3$][$S_2P(O^iBu)_2$]$_2$ (9)
Empirical formula	$C_{52}H_{114}N_2O_4P_2S_4Zn$	$C_{18}H_{44}N_2O_4P_2S_4Zn$	$C_{22}H_{60}N_6O_4P_2S_4Zn$
Formula weight	1087	608.1	728.31
Temperature/K	120	120	120
Crystal system	triclinic	triclinic	triclinic
Space group	P-1	P-1	P-1
a /Å	11.8542(9)	6.2953(8)	9.9094(4)
b/Å	15.7138(12)	12.6560(17)	11.7222(5)
c/Å	17.9814(14)	19.614(3)	16.4021(7)
α/°	97.533(4)	99.017(4)	96.7224(16)
β/°	91.613(4)	96.771(5)	90.3854(16)
γ/°	108.834(4)	93.067(5)	98.2287(16)
Volume/Å^3	3133.9(4)	1528.5(3)	1872.15(14)
Z	2	2	2
ρ_{calc}g/cm^3	1.152	1.321	1.292
μ/mm^{-1}	2.568	1.205	0.998
F(000)	1192	644	780
Crystal size/mm^3	0.548 × 0.164 × 0.066	0.67 × 0.151 × 0.044	0.595 × 0.175 × 0.056
Radiation	CuKα (λ = 1.54184)	MoKα (λ = 0.71073)	MoKα (λ = 0.71073)
2Θ range for data collection/°	6.008 to 149.392	4.178 to 66.284	4.568 to 60.066
Index ranges	-13 ≤ h ≤ 14, -19 ≤ k ≤ 19, -22 ≤ l ≤ 22	-9 ≤ h ≤ 9, -19 ≤ k ≤ 19, -30 ≤ l ≤ 30	-13 ≤ h ≤ 13, -16 ≤ k ≤ 16, -23 ≤ l ≤ 23
Reflections collected	38440	48077	41292
Independent reflections	11685 [R_{int} = 0.0482, R_{sigma} = 0.0446]	11647 [R_{int} = 0.0560, R_{sigma} = 0.0526]	10916 [R_{int} = 0.0562, R_{sigma} = 0.0566]
Data/restraints/parameters	11685/465/631	11647/0/312	10916/0/368
Goodness-of-fit on F^2	1.078	1.039	1.062
Final R indexes [I>=2σ (I)]	R_1 = 0.0389, wR_2 = 0.0883	R_1 = 0.0362, wR_2 = 0.0721	R_1 = 0.0432, wR_2 = 0.0944
Final R indexes [all data]	R_1 = 0.0530, wR_2 = 0.1063	R_1 = 0.0590, wR_2 = 0.0791	R_1 = 0.0640, wR_2 = 0.1011
Largest diff. peak/hole / e Å^{-3}	0.77/-0.58	0.52/-0.48	0.88/-0.49

	[Zn(DAP)$_2$][S$_2$P(O^{i}Bu)$_2$]$_2$ (10)	**[Zn{κ^1-*S*-S$_2$P(O^{i}Bu)$_2$}$_2$(μ-DAB)]$_n$ (11)**	**[Zn{κ^1-*S*-S$_2$P(O^{i}Bu)$_2$}$_2$(κ^2-MDAP)] (12)**
Empirical formula	$C_{22}H_{56}N_4O_4P_2S_4Zn$	$C_{20}H_{48}N_2O_4P_2S_4Zn$	$C_{20}H_{48}N_2O_4P_2S_4Zn$
Formula weight	696.25	636.15	636.15
Temperature/K	120	120	120(2)
Crystal system	tetragonal	monoclinic	triclinic
Space group	P-42$_1$c	P2$_1$/c	P-1
a /Å	16.4144(10)	18.1265(7)	12.3299(7)
b/Å	16.4144(10)	10.0858(4)	16.1120(10)
c/Å	13.0506(9)	18.6276(8)	16.5289(10)
α/°	90	90	75.242(2)
β/°	90	109.097(2)	89.991(2)
γ/°	90	90	83.281(2)
Volume/Å^3	3516.3(5)	3218.1(2)	3152.0(3)
Z	4	4	4
ρ_{calc}g/cm^3	1.315	1.313	1.341
μ/mm^{-1}	4.306	4.639	1.172
F(000)	1488	1352	1352
Crystal size/mm^3	0.656 × 0.054 × 0.048	0.156 × 0.145 × 0.057	0.449 × 0.354 × 0.148
Radiation	CuKα (λ = 1.54184)	CuKα (λ = 1.54184)	MoKα (λ = 0.71073)
2Θ range for data collection/°	7.616 to 133.016	5.16 to 133.32	3.986 to 50.25
Index ranges	-18 ≤ h ≤ 17, -19 ≤ k ≤ 17, -15 ≤ l ≤ 11	-21 ≤ h ≤ 18, -11 ≤ k ≤ 10, -20 ≤ l ≤ 22	-14 ≤ h ≤ 14, -19 ≤ k ≤ 19, -19 ≤ l ≤ 19
Reflections collected	19432	26309	45908
Independent reflections	3037 [R_{int} = 0.1277, R_{sigma} = 0.0844]	5387 [R_{int} = 0.0699, R_{sigma} = 0.0589]	11221 [R_{int} = 0.0553, R_{sigma} = 0.0735]
Data/restraints/parameters	3037/6/168	5387/350/361	11221/311/614
Goodness-of-fit on F^2	1.062	1.024	1.063
Final R indexes [I>=2σ (I)]	R_1 = 0.0625, wR_2 = 0.1504	R_1 = 0.0627, wR_2 = 0.1157	R_1 = 0.1157, wR_2 = 0.2925
Final R indexes [all data]	R_1 = 0.0906, wR_2 = 0.1644	R_1 = 0.1120, wR_2 = 0.1363	R_1 = 0.1437, wR_2 = 0.3160
Largest diff. peak/hole / e Å^{-3}	0.65/-0.48	0.49/-0.82	4.90/-1.68

	$Zn_4(MDEA)_2\{S_2P(O^iBu)_2\}_4$(14)	$[Mo_2O_2S_2(2\text{-}EH_2DTC)_2]$	$[NPr_4][S_2P(O^iBu)_2]_2$
Empirical formula	$C_{42}H_{94}N_2O_{12}P_4S_8Zn_4$	$C_{34.25}H_{68.5}Cl_{0.5}Mo_2N_2O_2S_6$	$C_{20}H_{46}NO_2PS_2$
Formula weight	1461.03	942.37	427.67
Temperature/K	150	120	120
Crystal system	triclinic	monoclinic	monoclinic
Space group	P-1	P2/c	$P2_1/c$
a /Å	10.0339(9)	19.5808(12)	9.0904(4)
b/Å	11.9672(11)	12.3960(8)	11.9494(5)
c/Å	15.5674(15)	18.9327(11)	24.1649(10)
α/°	107.586(4)	90	90
β/°	98.081(4)	102.853(2)	99.7501(15)
γ/°	104.513(3)	90	90
Volume/Å^3	1677.0(3)	4480.3(5)	2586.99(19)
Z	1	4	4
ρ_{calc}g/cm^3	1.447	1.397	1.098
μ/mm^{-1}	1.807	0.899	0.281
F(000)	764	1970	944
Crystal size/mm^3	0.32 × 0.2 × 0.16	0.182 × 0.08 × 0.025	0.244 × 0.17 × 0.168
Radiation	MoKα (λ = 0.71073)	MoKα (λ = 0.71073)	MoKα (λ = 0.71073)
2Θ range for data collection/°	4.568 to 55.996	4.258 to 52.044	4.546 to 56.998
Index ranges	$-13 \le h \le 13, -15 \le k \le 15, 0 \le l \le 20$	$-24 \le h \le 24, -15 \le k \le 15, -23 \le l \le 23$	$-12 \le h \le 12, -16 \le k \le 16, -32 \le l \le 32$
Reflections collected	7982	71676	51702
Independent reflections	7982 [Rint = ?, Rsigma = 0.0687]	8831 [R_{int} = 0.0592, R_{sigma} = 0.0403]	6542 [R_{int} = 0.0467, R_{sigma} = 0.0301]
Data/restraints/parameters	7982/33/330	8831/55/478	6542/0/252
Goodness-of-fit on F^2	1.022	1.059	1.025
Final R indexes [I>=2σ (I)]	R1 = 0.0630, wR2 = 0.1276	R_1 = 0.0404, wR_2 = 0.0914	R_1 = 0.0333, wR_2 = 0.0782
Final R indexes [all data]	R1 = 0.1078, wR2 = 0.1503	R_1 = 0.0665, wR_2 = 0.1010	R_1 = 0.0506, wR_2 = 0.0846
Largest diff. peak/hole / e Å^{-3}	1.48/-0.76	0.77/-0.62	0.29/-0.25